Ship Collision and Grounding Performances

Anuar Bin Abu Bakar
CEng, CMarEng, MIMarEST

Submitted for the degree of
Doctor of Philosophy

9 December 2014

School of Marine Science and Technology
Faculty of Science, Agriculture and Engineering
Newcastle University
Newcastle upon Tyne, UK

enneeur@yahoo.com

School of Marine Science and Technology

Armstrong Building

Newcastle University

NE1 7RU United Kingdom

Abstract

This present thesis investigates the accidental load of ship collision and grounding performances. To achieve this objective the thesis is composed of several main tasks. The main tasks comprise the rupture prediction, validation of material failure, ship grounding analysis and ship collision analysis.

To predict material rupture, FLD material failure was used and validated with available experimental and FEA data. The FLD was extended to established material failure scaling laws which consider onset failure at plane strain in relation to mesh sizes. This was accomplished by running mesh convergence studies at different mesh sizes and at different FLD_0. The linear material damage evolution is adopted in this case until the convergence results were satisfied. The material damage was used for all of further analysis in ship collision and grounding and employed mild steel and high tensile steel material properties. The ship grounding structure damage was investigated by deploying conical rocks at different locations of the ship's double bottom structure. The analysis focused on vertical penetration and horizontal penetration which contributed to significant damage to the structure. The ship collision analysis was investigated in various types of structures arrangement and diverse ship striking scenarios to penetrate struck ship and collide rigid wall.

Furthermore, the prediction of ship collision and grounding were extended by using simplified approaches that were capable to predict ship collision to rigid wall, rigid body striking ship collided with deformable struck ship and deformable collision of striking and struck ship.

Finally, this substantial amount of research work achieved the objectives of the study when the results of accidental load were validated and correlate well with experimental, empirical and FEA simulations at more than a satisfactory level.

Acknowledgements

Table of Contents

List of Figures

List of Tables

Nomenclature

a_i	The added mass of the installation
a_s	Added mass for striking ship
C	Nodal damping matrix / Equivalent stiffness (N/m)
C_{bs}	Coefficient of bow shape
dM	Added mass
DWT	Ship deadweight in tones
e	Coefficient of restitution
E_{cr}	Deformation energy at critical speed (KJ)
E_{imp}	Energy to be absorbed by plastic deformations
E_t	Tangent modulus for plastic deformation
$\dot{\varepsilon}_o$	Strain rate
$\dot{\varepsilon}_f$	Fracture strain
$\dot{\varepsilon}_1$	Minor principal strain rate
$\dot{\varepsilon}_2$	Major principal strain rate
ε_1	Major strain
ε_2	Minor strain
$\dot{\bar{\varepsilon}}^{pl}$	Equivalent plastic strain rate
$\bar{\varepsilon}_D^{pl}$	Stress triaxiality and strain rate
ε_{plat}	Plateau strain
F	External forces
F_{max}	Maximum crushing force
F_η , F_ξ	Impact forces,
I_a^z	Virtual moment of inertia in yaw of the struck
K	Nodal stiffness matrix
Lpp	Length of the vessel (m)
m_1	Mass of striking ship, including 10% of added mass (Tones)
m_2	Mass of struck ship, including 40% of added mass (Tones)
M_a	Mass struck ship
m_i	The mass of installation
m_s	Ship displacement

m_x	Mass plus added mass (5%) w.r.t longitudinal position (10^6 kg)
M_a^y	Virtual mass of the struck ship including added mass in sway
M_b^x	Virtual mass of the striking ship including added mass in surge
M	Nodal matrix / Ship displacement (kg)
ξ_{max}, η_{max}	Relative penetration
$\ddot{\eta}$, $\ddot{\xi}$	Relative accelerations
τ_{max}	Maximum shear stress
m,n	Strain hardening number power law
P_{bow}	Maximum collision load (MN)
P_o	Reference collision load equal to 210 MN
r_ε	Strain ratio
R	Rigidity ratio
R_b	Rigidity ratio for deformable bow of striking ship
R_s	Rigidity ratio for deformable side shell of struck ship
σ_m	Hydrostatic stress
σ_u	Ultimate Stress
σ_y	Yield Stress
σ_{eq}	Von-Mises equivalent stress
θ_{melt}	Melting temperature
θ	Current temperature
u	Nodal displacement
$\dot{u}$	Nodal displacement
$\ddot{u}$	Nodal Acceleration
V	Ship collision speed (m/s)
V_a	Velocity of struck ship
V_b	Velocity of striking ship
V_i	The velocity of installation
V_s	Collision speed of striking ship
V_0	Initial speed of the vessel in (m/s)
V_2	Initial velocity of striking ship
V_{cr}	Critical speed (Knots)
V_a^x	Final velocity of struck ship in the sway direction
V_b^x	Final velocity of striking ship in the sway direction of the struck ship

ω_a^x Final angular velocity of struck ship

X_a Impact point to the midship point of struck ship.

Abbreviations

CQD	Come Quick Danger
COLREGS	The International Regulation for Preventing Collisions at sea
FEA	Finite Element Analysis
FEM	Finite Element Method
FLD	Forming Limit Diagram
HAZ	Heat Affected Zone
IIP	International Ice Patrol
IMO	International Maritime Organization
MCA	Maritime and Coastguard Agency
MSRC	Marine Spill Response Corporation
OPA	Oil Pollution Act
SAR	Maritime Search and Rescue
SOLAS	The International Convention for the Safety of Life at Sea
STCW	Standards of Training, Certification and Watch keeping for Seafarers

CHAPTER 1: INTRODUCTION

1.1. Motivation of research

Currently, the growing public demand to reduce the risk of human lives and oil spillage at sea as well as to minimize the damage caused by ship collisions and grounding is always a priority. Besides that, collision and grounding events still continue to occur despite the continuous efforts to prevent them. Each year hundreds of vessels and thousands of lives are lost at sea worldwide, most of them involving short sea vessels (Tørnqvist, 2003). 1912, RMS Titanic hit an iceberg and sank with the loss of 1503 lives. December 1976, the Argo Merchant ran aground carrying 27,000 tons of oil and caused huge public concern as the oil slick threatened New England resorts and Georges Bank fishing ground(IMO). 1978 The Amoco Cadiz the supertanker runs aground three miles off the coast of Brittany, spilling 227,000 tonnes of oil. 1989, Exxon Valdez runs aground on Bligh Reef in Prince William Sound, Alaska, killing countless birds and animals.

Ship safety and sea pollution are closely related and the protection of the environment from disasters such as oil spillage is rather complex. The means to protect the environment and human lives are generally by improvement of "pre-collision" and "post-collision" safety. Where "pre-collision" are mainly active approaches such as vessels equipped with new technology of navigation equipments, competent crew training, efficient traffic control system and etc. "Post-collision" is a passive approach that tries to minimize the damage after collision by improving the crashworthiness of structure integrity of the vessel, improving rescue operation procedures and etc.

The crashworthiness of ship collision and grounding performance analysis is a highly nonlinear complex process and mainly involves large plastic deformation, high collision energy and rupture failure. It is very important to establish reliable material failure to predict structural damage and validate with available experimental and empirical data. This is a very complex

mechanism involving in ship collision and grounding, and very high costs when developing actual ship models for experiments, simulation ship collision and grounding dynamics become more and more important in the product development process.

1.2. Research Objectives

The main objectives of this thesis are to predict accidental load of ships during collision and grounding. To achieve the main objective, the study proposed to cover some of the aspects of small objectives as below:

I. To understand ship safety and the stake holders involved throughout the ship safety developments.

II. To investigate nonlinear behavior of marine grade steel using FLD material failure.

III. To investigate the effect of mesh sizes in relation with initial damage initiation and rupture of FLD material failure approach.

IV. To validate the material failure with available experimental and FE analysis data.

V. To investigate the behavior of ship grounding at different locations of double bottom grounding on rock.

VI. To investigate the deformable of ship bow collision with rigid wall

VII. To investigate the rigid and deformable bow collision with deformable double skin of side shell using displacement control.

VIII. To investigate the rigid and deformable bow collision with deformable double skin of side shell using energy dissipation approach.

IX. To predict the accidental load of ship collision using simplified approach.

The stipulated objectives are briefly explained in the section 1.3

1.3. Organization of the thesis

Chapter 2 discuss the chronology of ship history toward maritime safety, directly and indirectly as it relates to ships and maritime as a whole. The safety and statistics, especially involving in ship accidents which are collision and grounding, and also some of the regulatory bodies that are directly involved in the shipping industry. The overview will help to understand the big picture of ship safety as it has evolved throughout history.

Chapter 3 presents the work done from previous researchers. The chapter is divided into several main sections. Firstly, a brief review of material background, development of high strength ship plate, code and standards and ship collision and grounding mechanics. The material background and the development of high strength ship plate discusses some of the material grade used in ship construction and their properties. The codes and standards mainly focus on the review code and standards for ship collision and grounding. The external mechanics and internal mechanics of ship collision and grounding.

Chapter 4 will discuss the characteristics and parameters for finite element analysis. The topics included a basic understanding of stress-strain curve, material properties of material used, the technique and formula used to generate the strain hardening curve, material constitutive failure methods that are capable to predict rupture, finite element modeling technique and procedure. This chapter lays down the basis of common aspects used for finite element analysis for later chapters.

Chapter 5 provides FEA simulation results and compares with available experiment data to validate the material failure mentioned in chapter 4 that used FLD damage criteria. The analyses consists of penetration damage of stiffened panels with several setup configurations and lateral crushing of simplified buffer bow. An investigation of mesh convergence study is observed to capture better localized stress and rupture prediction point. The FEA results obtained were compared with actual experiment data and FEA

results published in (Alsos et al., 2009) for penetration damage, grounding experiment by Naval Surface Warfare Center, USA, NSWC (Rodd, 1996) and (Endo et al., 2001) for lateral ship bow collision to rigid wall. The scaling of mesh convergence study is established where the effect of FLD_0 in relation of mesh sizes is plotted to reduce CPU time to simulate bigger structures.

Chapter 6 focuses on grounding damage of double bottom structure and is divided into two parts. Firstly the analysis of vertical grounding to a typical double bottom application using the same material failure model as discussed in previous chapters and secondly the analysis looks at extended longitudinal movement along the compartment. The result is compared to available data from (Samuelides et al., 2007; Zilakos et al., 2009) that looking at fully plastic and rupture effect of material employed.

Chapter 7 is very challenging, where most of the simulation was very costly in terms of simulation time, processers and memory used capacity. The incidence of ship collisions and grounding has a significant contribution to oil spills, loss of life and environmental damage at sea. The costs incurred due to these accidental scenarios and the time taken for the polluted environmental area to recover to its original state is significantly large. In this paper the accidental loads and damage mechanism incurred on a ship's bow during a ship collision are analyzed using Nonlinear Finite Element methods in order to investigate the capability of the ship's bow to absorb the force and energy generated during a collision event. The study investigates the effect of collision angle and ship speed, when looking at an extreme collision event of a ship striking a rigid wall, a full ship model is employed in this investigation.

In this study, the capability of ship bow absorbing the impact force and energy during collision is investigated by introducing ship bow rigidity ratio which mainly focuses on the forward part of potential damage bow. The analysis involved using a full scale sized ship with velocity applied at center of mass of ship with 6 degrees of freedom allowed at all axis impact on rigid wall. The numerical simulation findings are used as the basis of a new simplified procedure for predicting damage response of the bow structure during

collision events. The numerical results are also compared with more simple analytical calculations.

In chapter 8, eighteen analyses were performed and is an extension of the study from chapter 7. The studies are divided into 3 main sections;

      i) Control displacement of rigid bow collision to deformable ship side,

      ii) Energy dissipation of rigid body of ship collision to ship side and

      iii) Deformable of ship bow collision to deformable of ship side.

The control displacement collision is a setup where the displacement and time of bow penetration is set prior simulation analysis. The energy dissipation of ship-ship collision is further divided into two categories where lateral collision and angle collision of ship-ship interaction. This collision study mainly monitor the force and energy dissipation until the kinetic went to zero. The deformable ship-ship collision is simulated only for lateral collision and at 50 degrees on inclination angle and was a very expensive simulation.

Chapter 9 is a case study of a box girder ultimate strength and residual strength after damage, solved using dynamic and static approaches. The chapter is divided into two sections which are damage analysis and progressive collapse analyses of the damaged structures due to indentation of an artificial indenter.

The results of damage analysis will be focused on the load of the indenter that punches into the box girder with constant velocity. The progressive collapse analyses is to compare the predictions of damaged box girder ultimate strength with and without residual stress using dynamic and static analysis and available methods.

The analysis will enable the author to understand the behavior of the FE solvers adopted and the reliability of the methods and techniques for FE analysis. The contents are already discussed and published in (Benson et al., 2013).

Chapter 10 provides overall conclusions of the research and recommendations for future research.

1.4. Contribution of work

The main contribution of work in this thesis, contains several research fields of rupture prediction using FLD material failure, ship collision and grounding accidental load prediction. The following provides a brief overview of the main research efforts.

The validation of material failure using FLD method in comparison with available experimental data. The establishment of FLD_0 in relation with mesh sizes to predict material rupture were a signification contribution to reduce the cost of analysis for larger structure models.

Detailed analysis of ship collision and grounding, involves a variety of simulation analysis parameters such as ship grounding on rock in different locations for double bottom cases, deformable bow collision with rigid wall, rigid bow collision with deformable side shell, displacement control of rigid bow collision with deformable side shell, displacement control of deformable bow collision with deformable side shell and investigation of near actual incident of ship collision where both, bow and side shell are deformed.

An extension of the study, the methodology of prediction of material rupture for steel ship using FLD approaches and simplified formulae to predict the performance of ship collision is proposed and validated. The methodologies are very useful for FEA simulation and the prediction of accidental load of ship collision and grounding.

CHAPTER 2: SHIP SAFETY

2.1. Introduction

This chapter will discuss the chronology of ship history toward maritime safety, directly and indirectly to ships and maritime as a whole. The safety and statistics, especially involving ship accidents which are collision and grounding, and also some of the regulatory bodies that are directly involved in the shipping industry. The overview will help to understand the big pictures of ship safety as it has evolved throughout history.

2.2. The Development of Ship Accident Safety

2.1.1. Plimsoll Load Line

By the mid-1800's, the overloading of cargo ships had become a major problem. By 1836 public concern about the loss of ships and crews reached the point where Parliament was forced to appoint a committee to investigate the growing number of shipwrecks. In 1850 legislation was passed to create the Marine Department of the Board of Trade: one of its duties was to enforce the laws governing the manning, crew competence and operation of merchant vessels. Despite calls for regulation, the British government avoided direct interference with ship operators until 1870 when Samuel Plimsoll (1824-1898), a member of Parliament from Derby, headed a campaign to require that vessels bear a load line marking indicating when they were overloaded, hence ensuring the safety of crew and cargo. Plimsoll exposed what he described as "coffin ships" created by overloading. He drafted a bill to improve conditions on merchant vessels. Gladstone's government set up a Royal Commission to investigate merchant marine practices and conditions; the report exposed many malpractices committed by unscrupulous owners. A Bill introduced in 1875 was defeated. Plimsoll's violent speeches aroused the House of Commons and his book, *Our Seamen*, shocked the public. It also earned him the hatred of many shipowners who started a series of legal battles against him. Undeterred, Plimsoll fought until finally, in 1876,

Parliament was forced to pass the Unseaworthy Ships Bill into law. The Act required a series of 'lines' to be painted on the ship to show the maximum loading point. Unfortunately, the Act allowed the shipowners to paint the line where they saw fit and some chose to paint it on the funnel of the ship. It was not until 1890 that Board of Trade officials applied the regulations that Plimsoll had intended. (Bloy, 2002)

This Plimsoll line (see Figure 1)is for the starboard side of a vessel; on the port side, the markings are reversed. The centre of the disk is placed at the middle of the loadline. The lines are one inch thick.
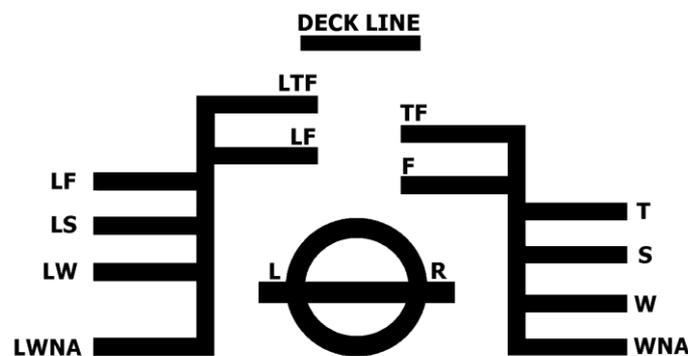
Figure 1: Plimsoll Line

The letters indicate cargo, season and location:

LTF - Lumber, Tropical, Fresh   TF - Tropical Fresh Water Mark

LF - Lumber, Fresh   F - Fresh Water Mark

LT - Lumber, Tropical   T - Tropical Load Line

LS - Lumber, Summer   S - Summer Load Line

LW - Lumber, Winter   W - Winter Load Line

LWNA - Lumber, Winter, North Atlantic   WNA - Winter Load Line, North Atlantic

    LR - Lloyds Register of Shipping

2.1.2. Radio Distress Signal

In 1904,the first radio distress signal 'CQD' adopted. By 1904 there were many trans-Atlantic British ships equipped with wireless communications. The wireless operators came from the ranks of railroad and postal telegraphers. In the same year the Marconi company suggested the use of "CQD" for a distress signal. Although generally accepted to mean, "Come Quick Danger," that is not the case. It is a general call, "CQ," followed by "D," meaning distress. A strict interpretation would be "All stations, Distress." and it is a conventional signal which was introduced originally to express a state of danger or peril of a ship that sends it. At the second Berlin Radiotelegraphic Conference 1906, the subject of a danger signal was again addressed. Considerable discussion ensued and finally SOS was adopted. The thinking was that three dots, three dashes and three dots "...---..." could not be misinterpreted. It was to be sent together as one string. In 1908 'SOS' is ratified as the international distress signal at a conference in Berlin and used for first time in 1909 when RMS Republic and SS Florida collide off Nantucket 2(Johnson, 1999, McEwen, 1999).

2.1.3. The Collision of RMS Titanic

Figure 2 shows 1912 RMS Titanic hits an iceberg and sinks with the loss of 1,503 lives. The impact of the TITANIC sinking on maritime safety legislation and naval architecture are legend. Needless to say, sufficient floatation and lifeboat space for each passenger, mandatory lifeboat drills and provisioning of lifeboats was immediately instituted. On the design front, we have the TITANIC tragedy to thank for the rapid development of watertight compartmentalization (as opposed to watertight bulkheads); sluice valves between bulkheads for bilge pumps, so these could be connected in unison; damage control training which emphasized pumping and counter-flooding measures; increased maneuverability (larger rudders and voluminous hull skegs forward of the propulsion screws); reversible Parson's turbines; double hulls; and a host of other technical innovations, which saved thousands of

lives during the First and Second World Wars. Damage control training became routine in the world's modern navies.(Rogers)

Figure 2 : RMS titanic berthing (Left) and resting on sea bed after collision with iceberg (Right)

2.1.4. International Ice Patrol

In 1913, the International Ice Patrol (IIP) was formed after the RMS Titanic sank on 15 April 1912. Since 1913, except for periods of World War, Ice Patrol has monitored the iceberg danger near the Grand Banks of Newfoundland and has broadcast the Iceberg Limit to mariners. The activities and responsibilities of IIP are delineated in the U.S. Code, Title 46, Section 80302, and the International Convention for the Safety of Life at Sea (SOLAS), 1974. (USCG, 2011)

2.1.5. The International Convention for the Safety of Life at Sea (SOLAS)

1914, Maritime states develop the first global safety agreement for shipping, the International Convention for the Safety of Life At Sea (SOLAS), which was signed by 13 countries on 20 January 1914. Ittook into account many of the lessons learned from the Titanic disaster - but more than that, it laid down internationally applicable rules for the first time. The Convention included eight chapters(IMO., 1998).

- Chapter I - Safety of Life at Sea - Article 1 (in which Parties undertake to give effect to the convention);
- Chapter II - Ships to which this Convention applies - Articles 2-4 (Article 2 states that the Convention applies to mechanically-propelled merchant ships carrying more than 12 passengers on international voyages);
- Chapter III - Safety of Navigation - Articles 5-15 (includes the establishment of the North Atlantic ice patrol);
- Chapter IV - Construction - Articles 16-30 (includes requirements for watertight bulkheads);
- Chapter V - Radiotelegraphy - Articles 31-38 (includes requirement for a continuous watch on radio frequencies during navigation);
- Chapter VI - Life-saving appliances and fire protection Articles 39-56; · Chapter VII - Safety Certification - Articles 57-63 (requires ships to obtain a safety certificate);
- Chapter VIII - General Articles 64-74 (covers entry into force, accession by other States, modification of the Convention); and · The 1914 SOLAS also included a section of Regulations, covering technical details and expanding on the Articles.

2.1.6. The First International Convention on Load Lines

1930, The first International Convention on Load Lines, adopted and was based on the principle of reserve buoyancy, although it was recognized then that the freeboard should also ensure adequate stability and avoid excessive stress on the ship's hull as a result of overloading. It has long been recognized that limitations on the draught to which a ship may be loaded make a significant contribution to her safety. These limits are given in the form of freeboards, which constitute, besides external weather tight and watertight integrity, the main objective of the Convention. In the 1966 Load Lines convention, adopted by IMO, provisions are made determining the freeboard of ships by subdivision and damage stability calculations. The regulations take

into account the potential hazards present in different zones and different seasons. The technical annex contains several additional safety measures concerning doors, freeing ports, hatchways and other items. The main purpose of these measures is to ensure the watertight integrity of ships' hulls below the freeboard deck. All assigned load lines must be marked amidships on each side of the ship, together with the deck line. Ships intended for the carriage of timber deck cargo are assigned a smaller freeboard as the deck cargo provides protection against the impact of waves.(IMO, 1966)

2.1.7. The Morro Castle ship Accident

In 1934, a fire aboard the passenger ship Morro Castle caused 134 casualties (see Figure 3). The investigation of the Morro Castle fire, and the lessons learned from it, played a major part in the development of the non-combustible construction regulations which today form the basis of the fire safety regulations for passengers ships.(Bramfitt, 2012)
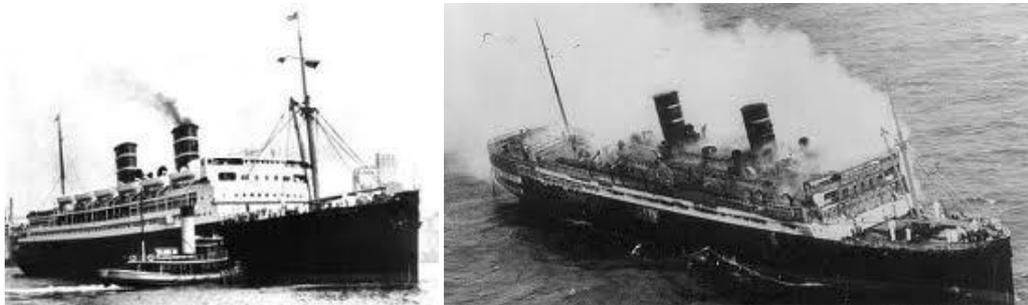
Figure 3: The ship of Morro Castle at port (left) and on fire (right)

2.1.8. The Establishment of International Maritime Organization (IMO)

1948, The United Nations holds the Geneva Conference which leads to the establishment of Inter-Governmental Maritime Consultative Organization. The Organization later changed its name to International Maritime Organization (IMO) to draw up the blueprint for an international organization that would develop standards for shipping - for adoption and universal implementation throughout the entire industry. (IMO)

1959 International Maritime Organization (IMO) begins business. It adopts a new version of SOLAS, the most important treaty dealing with maritime safety. Over time it widens its remit to assume responsibility for all pollution related matters, maritime search as well as rescue and tonnage regulations. It was recognized at the first Assembly that IMO's initial task was to establish a comprehensive body of conventions and other treaty instruments relating to maritime safety and pollution prevention. This task involved updating a number of existing treaties, notably the International Convention for the Safety of Life at Sea (SOLAS) and it had always been intended that IMO would take over responsibility for it when the Organization came into being. IMO also accepted responsibilities regarding the International Regulations for Preventing Collisions at Sea, the International Code of Signals and the International Convention for the Prevention of Pollution of the Sea by Oil (OILPOL), which was adopted in 1954. (IMO).

2.1.9. The Explosion of British Crown

1960, BP, which was experiencing very rapid tank corrosion in their ships carrying high sulphur Mideast crude, became interested in inerting as a corrosion control method. 1963, on all new BP crude carriers were fitted with inert gas systems at build. The program did not extend to most existing tankers. On 8th August 1966, the 1952 built, 28,598 DWT British Crown(see Figure 4)was just finishing loading crude at Umm Said, Qatar when she exploded killing 19 and badly injuring 8. The ship was non-inerted, fitted with gauze flame screens (Devanney, 2010).
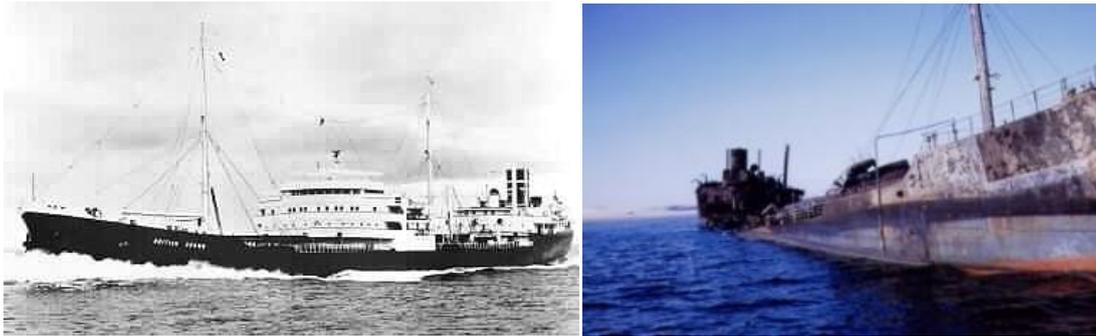
Figure 4 : The British Crown on Service (Left) and after explosion (Right)

2.1.10. The Torrey Canyon Oil Spill

1967, the damage of Torrey Canyon (see Figure 5) and oil spill in the English Channel is often regarded as the key incident for international improvement. It led to the creation by the ITOPF (the International Tanker Owners Pollution Federation Ltd) of TOVALOP (Tanker Owners' Voluntary Agreement for Liability For Oil Pollution), and later, the cargo owners founded CRISTAL (Contract Regarding A Supplement to Tanker Liability for Oil Pollution). Both TOVALOP and CRISTAL relate to issues of liability and compensation arrangements, ensuring adequate compensation is provided to persons suffering pollution damage from accidents involving oil tankers. This disaster is the turning point for the IMO as it expands its activities in the environmental and legal fields. (Ritchie, 1995)
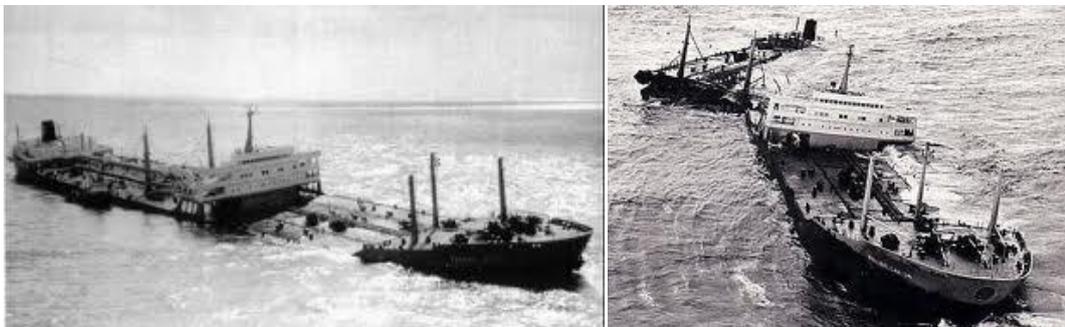
Figure 5: The grounded of Torrey Canyon (left) and brake apart at midship (Left)

2.1.11. Convention on The International Regulations for Preventing Collisions at sea (COLREGS)

1972,Convention on the International Regulations for Preventing Collisions at Sea (COLREGS), the Convention was designed to update and replace the Collision Regulations of 1960 which were adopted at the same time as the 1960 SOLAS Convention. One of the most important innovations in the 1972 COLREGs was the recognition given to traffic separation schemes - Rule 10 gives guidance in determining safe speed, the risk of collision and the conduct of vessels operating in or near traffic separation schemes. The first such traffic separation scheme was established in the Dover Strait in 1967. It was operated on a voluntary basis at first but in 1971 the IMO Assembly adopted a resolution stating that that observance of all traffic separation schemes be made mandatory - and the COLREGs make this obligation clear. (IMO, 1972).

2.1.12. The Major Event of Tanker Accidents

1976-1977, a series of tanker accidents, mostly in or near United States waters and including the stranding of the Argo Merchant(see Figure 6), led to demands for more stringent action to curb accidental and operational oil pollution. The Argo Merchant ran aground off Massachusetts in December 1976. It was a small tanker, carrying 27,000 tons of oil, but caused huge public concern as the oil slick threatened New England resorts and Georges Bank fishing ground.(IMO)

Figure 6: The Agro Merchant run aground (left) and sank into sea (right)

1978, Conference on Tanker Safety and Pollution Prevention, adopted a protocol to the 1973 MARPOL Convention, absorbing the parent Convention and expanding on the requirements for tankers to help make them less likely to pollute the marine environment. The Protocol expanded the requirements for segregated ballast tanks to all new crude oil tankers of 20,000 DWT and above and all new product carriers of 30,000 DWT and above. The Protocol also required segregated ballast tanks to be protectively located, in other words, placed in areas of the ship where they will minimise the possibility of an amount of oil outflow from cargo tanks after a collision or grounding. These included the requirement for inert gas systems (whereby exhaust gases, which are low in oxygen and thus incombustible, are used to replace flammable gases in tanks) on all new tankers over 20,000 DWT and specified existing tankers. The SOLAS Protocol also included requirements for steering gear of tankers; stricter requirements for carrying of radar and collision avoidance aids; and stricter regimes for surveys and certification.(IMO)

1978, The Amoco Cadiz(see Figure 7) accident was the world's largest oil tanker accident causing the developing of the first regional port state control Paris MoU. The super tanker runs aground three miles off the coast of Brittany, spilling 227,000 tonnes of oil. The disaster followed an argument over salvage rights. (Luoma, 2009).

Figure 7:The grounded and oil spill of Amoco Cadiz

2.1.13. The International Convention on Standards of Training, Certification and Watch keeping for Seafarers (STCW)

1978, The International Convention on Standards of Training, Certification and Watch keeping for Seafarers (STCW) is established. It sets requirements on training, certification and watch keeping for seafarers to international levels. (IMO, 1978)

2.1.14. The International Convention on Maritime Search and Rescue (SAR Convention)

1979, International Convention on Maritime Search and Rescue (SAR Convention) obliges State Parties to ensure that assistance be provided to any person in distress at sea, regardless of the nationality or status of such a person or the circumstances in which that person is found and provide for their initial medical or other needs, and deliver them to a place of safety. (IMO, 2012a)

1985 Oil Spill Response Limited is formed by the oil majors in the UK to focus on responding to spills, maintaining spill response equipment and providing training.(Smith and Mead, 2005)

2.1.15. The Grounding of the Exxon Valdez

1989, Figure 8, shows the ship, Exxon Valdez ran aground on Bligh Reef in Prince William Sound, Alaska. Oil eventually pollutes 1,100 miles of non-continuous coastline making this the largest oil spill to date in US waters. The spilled oil sullied over one thousand miles of coastline, killing countless birds and animals. To this date, two billion dollars have been spent on cleanup efforts; however, only three to four percent of the oil has been recovered.(Torem, 1991, Harrison, 1991, Paine et al., 1996)

Figure 8: The oil pollution of Exxon Valdez at Prince William, Alaska

2.1.16. Oil Pollution Act (OPA)

1990 Oil Pollution Act (OPA) is signed into law in the United States, which included numerous provisions designed to improve our ability to prevent and respond to oil spills in U.S. waters. OPA included provisions that:.

- Created an Oil Spill Liability Trust Fund, to compensate victims of oil spills; provide quick, efficient cleanup; and minimize damage to fisheries, wildlife and other natural resources. The fund serves to pay for containment and oil spill removal activities and prevent or mitigate substantial threats of oil discharge among its many functions.

- Required owners of oil tankers and localities where oil is extracted, stored or transported to develop detailed contingency spill response plans.

- Required stockpiling of chemical dispersants and equipment for cleaning or containing spills to ensure that adequate resources would be on hand to respond to emergencies

2.1.17. Marine Spill Response Corporation (MSRC)

1990 Marine Spill Response Corporation (MSRC) is formed in the US by oil and marine transportation companies to meet not only regulatory requirements imposed by the Oil Pollution Act of 1990 (OPA-90), but also the private needs of companies demanding a robust response to any spills that might occur.(MSRC, 2012)

2.1.18. Double Hull Requirement

In 1992 the double hull requirement was adopted, MARPOL was amended to make it mandatory for tankers of 5,000 DWT and more ordered after 6 July 1993 to be fitted with double hulls, or an alternative design approved by IMO (regulation 19 in Annex I of MARPOL). The requirement for double hulls that applies to new tankers has also been applied to existing ships under a programme that began in 1995 (under old regulation 13G (now regulation 20 in Annex I of MARPOL). All tankers would have to be converted (or taken out of service) when they reached a certain age (up to 30 years old). This measure was adopted to be phased in over a number of years because shipyard capacity is limited and it would not be possible to convert all single hulled tankers to double hulls without causing immense disruption to world trade and industry (IMO, 2011).

2.1.19. International Management Code for Safe Operation of Ship and Pollution Prevention.

1993   IMO adopts International Management Code for the Safe Operation of Ships and for pollution Prevention in response to major accidents at sea in the 1980s. The ISM Code aims to ensure safety at sea, prevent human injury and loss of life and avoid damage to the marine environment.(Moore and Roberts, 1995).

2.1.20. Maritime and Coastguard Agency (MCA)

1998   UK Maritime Safety Agency and Coastguard Agency are merged into the Maritime and Coastguard Agency (MCA) with a remit to promote high standards of safety at sea. Its main functions are to develop, promote and enforce high standards of marine safety, to minimize loss of life amongst seafarers and coastal users, and to minimize pollution from ships of the sea and coastline. (UK-HSE, 2009)

2.1.21. The Erika and Prestige Disaster

1999, Figure 9 shows the Erika a 25 year old single hulled tanker breaks up off southern Brittany, spilling 15,000 tons of heavy fuel oil. The European Commission blames the poor condition of the ship for the spill. The incident results in the IMO adopting faster, stricter phase out schedules for single hulled tankers from 2003.

Figure 9 : The Erika oil pollution (Left) and sank into sea (Right)

2002,Figure 10, shows the Prestige, a 26 year old single hulled tanker breaks up and sinks 150 miles off the coast of Spain while carrying 20 million gallons of heavy fuel oil, devastating large sections of the northern Spanish coastline. This spill leads to further amendments to the phase out of single hulled tankers.

Figure 10: The Prestige and her structure failure

2.1.22. International Convention for the Control and Management of Ship's Ballast Water and Sediments.

2004, The IMO has adopted the International Convention for the Control and Management of Ship's Ballast Water and Sediments The purpose of the Convention is to prevent, minimize and ultimately eliminate the risk of introduction of Harmful Aquatic Organisms and Pathogens which use the ballast water as a hub. Ballast Water Management includes exchange of ballast water and ballast water treatment. – For the later, technical solutions by mechanical, physical, chemical or biological processes are possible, either singularly or in combination.(IMO, 2004)

2.3. Ship Accident Statistics

Throughout the shipbuilding industry, the demand of reducing the cost of operation, has led ship owners to greatly increased in size and numbers (see Figure 11). Since often the cargoes often contain hazardous materials, safe navigation is required to prevent accidents leading to increased risk to life, property and environment. According to Faulkner (Faulkner, 2004), there are two main sources causing ship loss. About 60% are due to operational causes (e.g. fire, collision, machinery damage), while the remaining 40% are characterized by design and maintenance causes (i.e. water ingress, hull breaking in two, and

capsizing). Although many incidents may be related to human errors, accidents still occur due to unexpected and dangerous sea states, which can result in an inability to keep the ship under proper control(Toffoli et al., 2005).

	1980	1985	1990	1995	2000	2005	2006	2007	2008	2009	2010	2011
Container	102	160	246	389	628	1 020	1 134	1 264	1 319	1 201	1 347	1 477
Other dry	935	918	1 039	1 131	1 905	1 852	2 032	2 066	2 109	1 921	1 976	2 105
Five major bulks	796	857	968	1 082	1 288	1 701	1 836	1 957	2 059	2 094	2 333	2 477
Crude oil and products	1 871	1 459	1 755	2 049	2 163	2 422	2 698	2 747	2 742	2 642	2 752	2 820
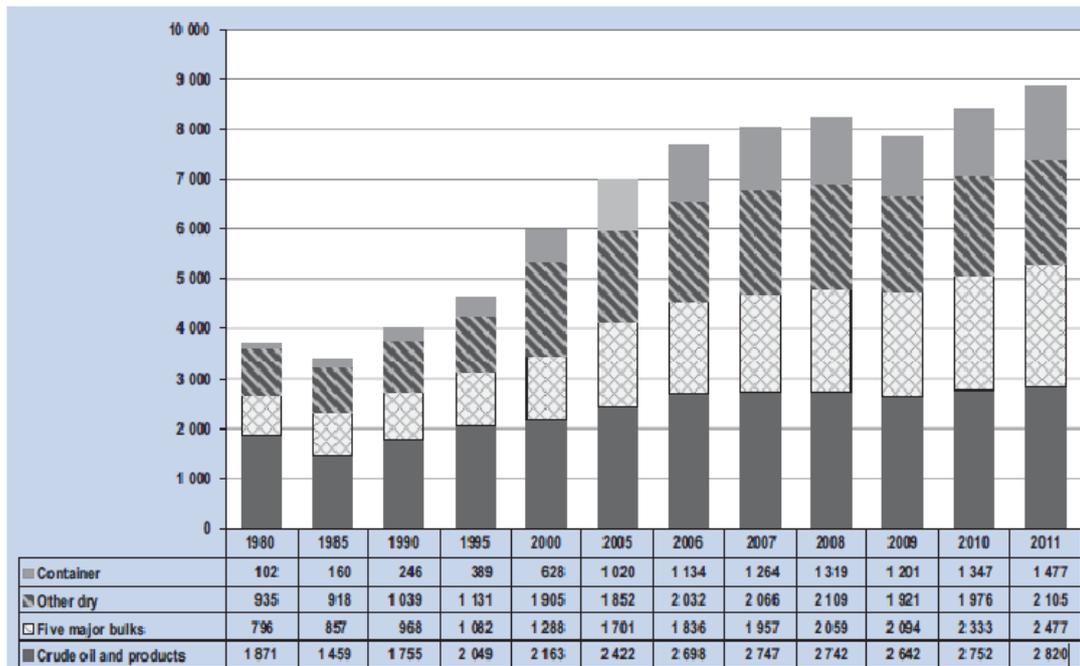
Figure 11: The development of world fleet by millions of DWT(IMO, 2012b)

With the increase of ship speeds and the total number of ships sailing at sea, collisions and grounding accidents seem inevitable. At the same time, the public is becoming less tolerant towards the environmental pollution caused by the associated oil spills. The judgment of maritime safety often rely on The Lloyd's Marine Information Service (LMIS) that produces a ship accident database, regarded as the most consistent and trustworthy. According to (Toffoli et al., 2005), all reported casualties due to bad weather including total losses to all propelled sea-going merchant ships in the world of about 100 gross tonnage and above(see Figure 12). The classification of the accidents applies to the first event that has occurred and hence does not include other consequences that may have happened in the same accident(Guedes Soares et al., 2001).
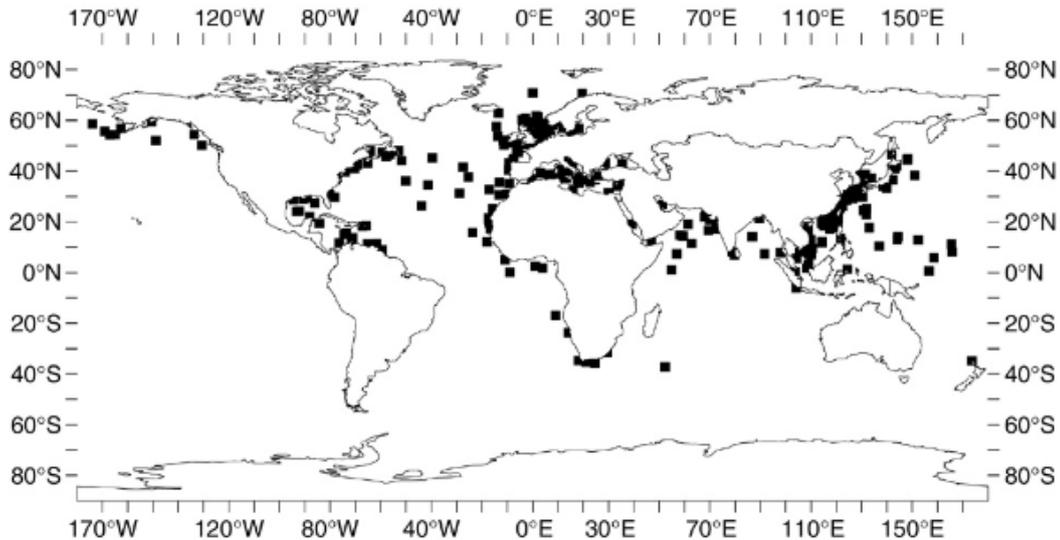
Figure 12: Distribution of shipping accidents (1995–1999). Accidents were collected from Lloyd's Marine Information Service (LMIS)(Toffoli et al., 2005).

According to WMO, climate analysis should be preferably based on 30 years of data. (Toffoli et al., 2005), generated long-term statistics for a whole 45 year period of the ERA-40 project as well as over the period from January1995 to April 1999 covered by the accidents database. The accident area focuses on those areas prone to shipping accidents which are Western North Pacific, Western Central Pacific; Indochina, Western North India, South Africa, Mediterranean, Eastern North Atlantic, Western North Atlantic, Equatorial Atlantic, Caribbean, Gulf of Mexico and Eastern North Pacific (see Figure 12).

According to the report from the IOPCF (International Oil Pollution Compensation Fund), collisions and grounding accidents were responsible for about 50 percent of all major oil spills in its member states from 1970 to 2005 (see Figure 13). Lately, there is more awareness towards adopting more-rational design procedures for collisions and groundings, aside from prescriptive regulations. Numerous innovative concepts and methods have been proposed and adopted in ship-design procedures. Among these inventions, a procedure based on ALS (accidental-limit state) design concept was brought forward by(Amdahl and Kavlie, 1995). The rational-design procedure: scenario definition, assessment of global and local structural performance, post-accident evaluation, and acceptance criteria are

embedded in whole process of ship design and ship building. This may be a useful tool in the preliminary stages of ship design(Wang et al., Paik et al.).
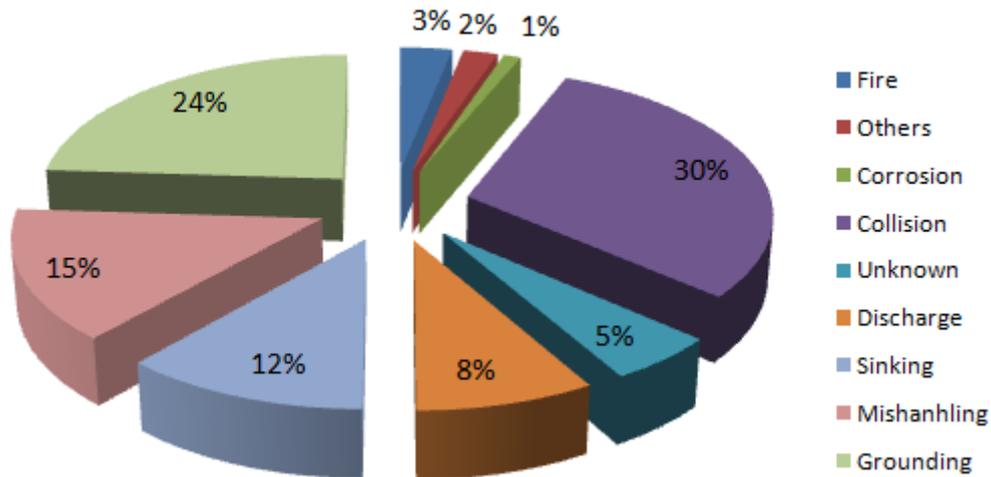
Figure 13: Cause of major oil spills from tankers compensated by the IOPCF(Zhiqiang et al., 2011, IOPCF, 2005).

Figure 13, also shows that collision and grounding contributed to about 54% of the oil spills and directly damaged our environment that takes a long time to recover to its original state.

2.4. Summary

This chapter mostly covered basic understanding of ship safety and ship accident statistic and also some regulatory bodies that are involved in determining maritime safety. Most of the counter action by regulation on forming new respective bodies is based on the major casualties and big events of accidents that gave significant effect to loss of life, environmental pollution and economic impact.

Later chapters will discuss and focus on some previous work and recent developments of ship collision and grounding and the rules of ship classification society on determining standards for ship collision and grounding.

CHAPTER 3: REVIEW OF LITERATURE

3.1. Introduction

This chapter presents the work done by previous researchers. The chapter is divided into several main sections. Firstly, a brief review of material background is discussed including the development of high strength ship plate, code and standards and ship collision and grounding mechanics. The material background and the development of high strength ship plate discusses some of the material grades used in ship construction and their properties. The codes and standards mainly focus on the review code and standards for ship collision and grounding. The ship collision and grounding mechanics is crucial information for FEA comparison in later chapters where are discuss available tools to predict energy absorption, penetration forces, penetration distance, etc. The methods discussed are divided into two categories namely external mechanics and internal mechanics of ship collision and grounding.

3.2. Material Background

(Romhanji and Popović, 2006) Steel is a prominent material used for over one and half century in the shipbuilding industries due to its excellent mechanical properties and relatively low manufacturing costs compared to others materials available. (HIROTA et al., 2007) Along with the rapid increase in the size of container ships, the steel plates used for ship hulls have increased in thickness as the toughness of steel plates generally tends to decrease for thicker plates(see Figure 14). In order to address this challenge, Mitsubishi Heavy Industries, Ltd. (MHI) has jointly developed with Nippon Steel Corporation steel plates with the yield strength of 470MPa, which is an increase of about 20% in comparison with conventional steel plates for general commercial ship hulls. This steel possesses both high strength and high toughness, which has made it possible to substantially improve the reliability of the hull structure of mega container ships against

brittle fractures through reduced plate thickness and appropriate plate layout design based on good use of its special characteristics. In addition, its weight-reducing effect has also contributed to improvement in propulsive performance and cargo loading efficiency. This steel has already been used for the first time in the world on an 8100 TEU container ship constructed by MHI and has gained the deep appreciation of the customer both for its safety and performance.

(Zhang, 2011)In the field of material used in the twenty-first century, steel production technology keeps developing at a high speed especially after finance crisis. In 2010, the steel yield reached 600 million tons in China which means China has become the biggest steel production country in the world. If the steel strength were increased from 400 to more than 800 MPa, the steel consumption would be reduced greatly.

3.3. The Development of High Strength Ship Plate

(Zhang, 2011) Ansteel has developed shipbuilding steel for a long time and now has the largest yield in producing the most variant dimensions and the highest grade of shipbuilding steels in China. Ansteel is also a pioneering steelmaker in the production of ultra-high strength steel for shipbuilding and offshore structures in the world. In 2008, Nickel alloy steels containing 3.5, 5, and 9% Ni for cryogenic service were successfully produced at Ansteel and certificated by DNV, LR, and CCS Societies. In 2009, the steel plates for high heat input welding were successfully developed with a maximum thickness of 100 mm and the weld heat input of 100 kJ/cm and were certificated by ABS, CCS, DNV, GL, NK classification societies.

(Willms and der Dillinger Hüttenwerke, 2009) The field of application for high strength steel extends from offshore and hydropower constructions to ship- and bridge building. Steels with very high strength (up to 1,100 MPa) are generally produced by a quenching and tempering process (Q+T). Extremely high strength is always associated with higher amounts of alloying elements

and tends to result in higher hardenability which leads to a higher risk for brittle fracture and hydrogen induced cracking in welded constructions. The thermo-mechanically controlled process (TMCP) is employed to address issues such as weldability and allows the choice of efficient and cost-savings in the welding processes.

(Suzuki et al., 2004) The shipbuilding industry has energetically promoted the high performance of ships and improved productivity in construction in response to vessel diversification (trend toward exclusive-use ships). The JFE Steel adopted TMCP (thermo-mechanical control process) and introduced six products which were developed by JFE Steel in response to these needs. In the field of plate, they include new TMCP steel plates for high heat input welding for container ships, which contribute to improved productivity by greatly reducing welding working time, and LP steel plates (longitudinally profiled plates, also called taper plates), new anti-corrosion steel plates for crude oil tankers, NAC5, which contributes to higher performance in ships through improved corrosion resistance, and clad steel plates for chemical tankers. Tubular products include JFE-MARINE-COP for crude oil tankers, which improves corrosion wear performance in onboard oil receiving pipes used in loading and unloading crude oil. Among shape steels, JFE Steel has developed TMCP technologies for shapes for shipbuilding which provide weldability equal to that of plates.
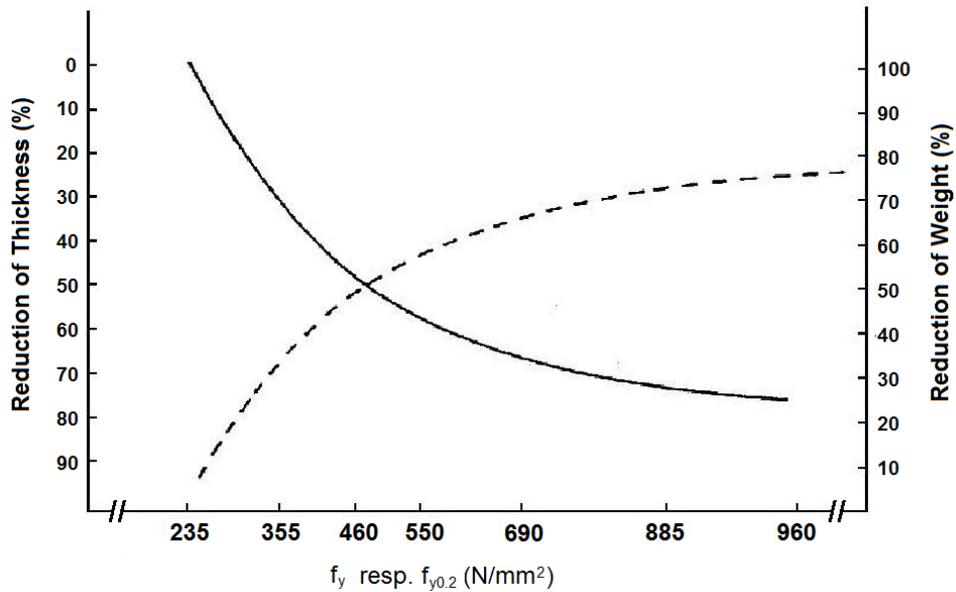
Figure 14: The weight, thickness and steel strength relationship (Sedlacek and Müller, 2001).

(Willms and der Dillinger Hüttenwerke, 2009, Sedlacek and Müller, 2001) The evolution in steel production in the heavy plate sector over the last decades is determined by the development of quenched and tempered (Q+T) steels with very high yield strengths (S690Q, S890Q, S960Q and S1100Q) and on the by thermo-mechanically rolled (TMCP) steels with a more moderate yield strength, but higher toughness (S355M, S460M and S500M). The chronology of steel evolution, true stress and load deflection of structural steels is illustrated in Figure 15, Figure 16 and Figure 17.
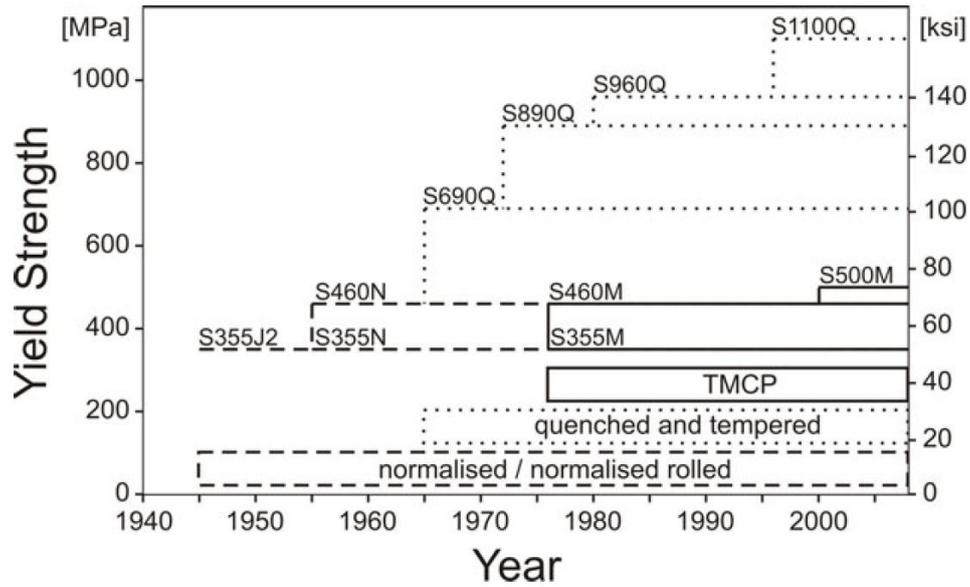
Figure 15: Shipbuilding steel grades and its evolution(Willms and der Dillinger Hüttenwerke, 2009).
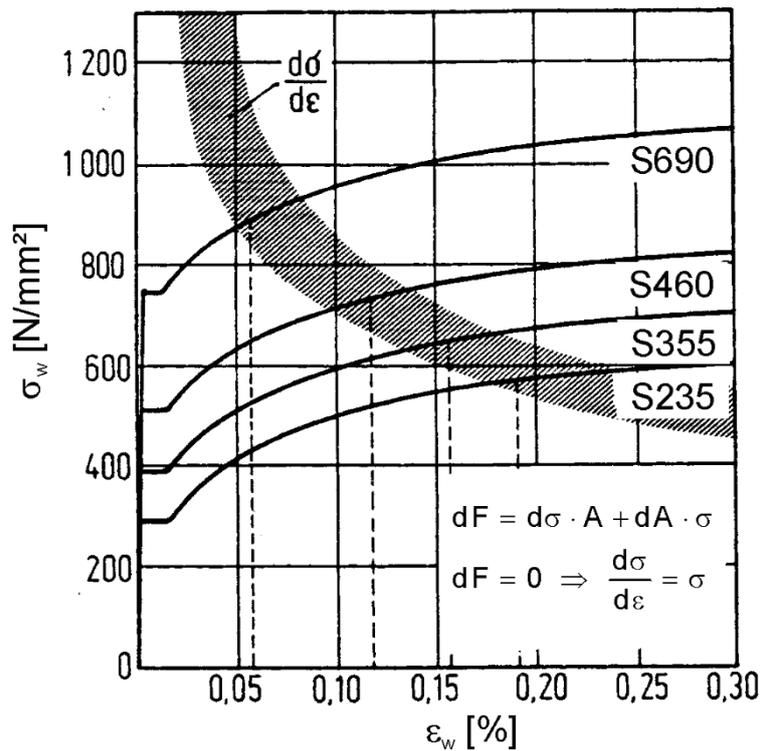
Figure 16: True stress strain for different steel grades (Sedlacek and Müller, 2001).
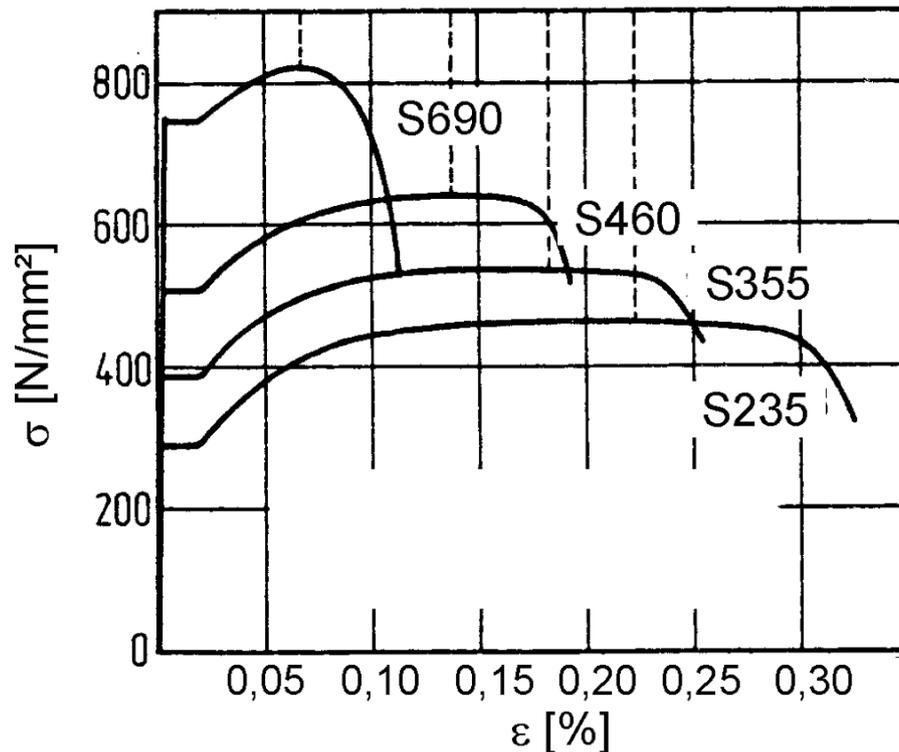
Figure 17 : Load deflection for different steel grades(Sedlacek and Müller, 2001).

3.4. Codes and Standards

The codes and standards is a guidance for the designer and it is a must for any party involved to adopt during design and construction of marine structures such as floating structures, ships, platforms etc. The codes are formed from various regulatory bodies, authorities and classification societies. This section will examine issues that related to ship collision and grounding that apply to some codes and standards.

The development of codes and standards begin in 1914 when SOLAS was established, 1948 the forming of IMO and 1972 COLREGS. The Norwegian Petroleum Directorate (NPD, 1990), requires all platforms to be designed to withstand impact from supply vessels of 5,000 tonnes displacement with a collision speed of 2 m/s yielding kinetic energy of 14MJ for beam impact and 11 MJ for bow impact. The rules are based on Det Norske Veritas(DNV,

1981, DNV, 1996, DNV, 1999) and share the same ideas of consideration. However, the DNV rules allowed the energy of impact to be shared between the platform structure and striking vessels (HSE, 1990).

The DNV code stated that the absorbed energy should be calculated using equation (3.1):

$$E = \frac{1}{2}(m + a)V^2 \qquad (3.1)$$

Where:

  m = Displacement of striking ship in tonnes

  a = Added mass of the vessel, 0.4m for sideways and 0.1m for bow or stern collision.

  V = Collision speed in m/s

The Lloyds Register of Shipping (LLOYDS, 1999), adopted some of the standard from (DNV, 1981, DNV, 1996, DNV, 1999, NPD, 1990), in the document of "Rules and regulation for the classification of floating offshore installation".

NORSOK (NORSOK, 1999), The code embedded both internal and external mechanics, it has a special section (Annex A: Design against accidental actions) devoted to ship collision design guidance. The absorbed energy can be calculated using equation (3.2):

$$E = \frac{1}{2}(m_s + a_i)V_s^2 \frac{\left(1 - \frac{V_i}{V_s}\right)}{1 + \left(\frac{m_s + m_a}{m_i + a_i}\right)} \qquad (3.2)$$

Where:

  m_s = Ship displacement

  a_s = Added mass for striking ship

  V_s = Collision speed of striking ship

  m_i = The mass of installation

  a_i = The added mass of the installation

  V_i = The velocity of installation

The internal energy is mainly focused on the distribution energy on the installation and striking ship. The code implies simplified plastic analysis techniques for the prediction of force deformation for stiffened plate as details can be accessed from the standard.

The(AASTHO, 1994, ENV, 1991), standards consider particulars on ship-bridge collision. Which can be calculated using equation (3.3) and (3.4):

$$P_{max} = 0.122V\sqrt{DWT} \qquad \text{for ASSTHO} \qquad (3.3)$$

$$P_{max} = \sqrt{KM} \cdot V \qquad \text{for Eurocode} \qquad (3.4)$$

Where:

P_{max} = Maximum impact force

K = Equivalent stiffness (N/m)

M = Ship displacement (kg)

V = Ship collision speed (m/s)

DWT = Ship deadweight in tones

The (Germanischer-Lloyd, 1997) is critical on tearing of cargo tank with oil or chemical leakage and water ingress into dry cargo hold. The code emphasizes critical speed at which the bow of the striking ship just touches the side shell of struck ship. The critical speed is determined by equation (3.5):

$$V_{cr} = 2.75\sqrt{\frac{E_{cr}}{m_2}\left(\frac{m_2}{m_1}\right)} \qquad (3.5)$$

Where:

V_{cr} = Critical speed (Knots)

E_{cr} = Deformation energy at critical speed (KJ)

m_1 = Mass of striking ship, including 10% of added mass (Tones)

m_2 = Mass of struck ship, including 40% of added mass (Tones)

The aims of these standards is to standardise the critical speed employed in design that is able to initiate the rupture of the side shell of a struck ship.

3.5. Ship collision and grounding mechanics

Ship collision and grounding analysis was initially discovered in the 1950s by Minorsky for ships transporting radioactive materials. Later it was adopt into a wide range of floating vessels. Ship Structure Committee, SOLAS, IMO ship classification societies, standard, etc. play an important role to make sure that crashworthiness of ships is acceptable and safe during their services.

Analysis of the ship collision and grounding mechanics can be categorized into two parts, namely external and internal mechanics. The external mechanics deal with the rigid body global motion of the ships under the external forces acting on ships while the hydrodynamic pressures on the wet surface of ships, mainly focuses on the inertia forces (added mass).

The internal accident mechanics is an evaluation of the structural failure of ships during an accident. It mainly, focuses on local damage to the ships and is a very complex problem to resolve and understand. A broad spectrum of methods has been developed for the analysis of internal mechanics as a result of recent extensive research. Generally, these methods can be grouped into four categories, simple formulae, simplified analytical methods, simplified finite element methods and non-linear FEM simulations. They differ in the complexity of modelling and calculation efforts. At one extreme (simple formulae) the calculations are easiest. Towards the other extreme, non-linear FEM, the accuracy and reliability of calculations improves, while the required time to perform the calculation increases substantially (Wang et al., 2002)

Various approaches, models of assessment and analysis of ship collision and grounding are discussed in further this section.

3.5.1. 1 DOF - Minorsky's Method

Minorsky was among the earliest scholar in the field of studying ship collisions. Minorsky's approach examined fifty major collision cases that occurred before 1959 and used rigid body mechanics together with the conservation of energy and momentum principles to estimate the kinetic energy lost during a collision between two vessels. This global approach relationship has been used over many years to derive estimates of absorbed energy during collision and grounding events.
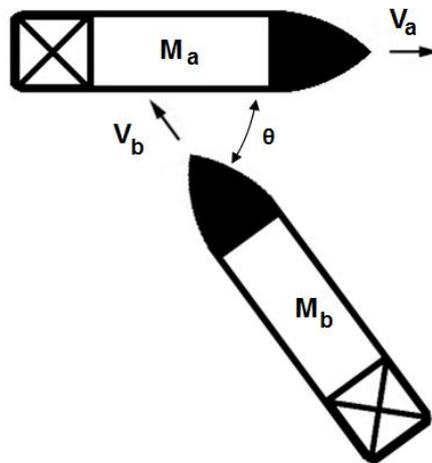
Figure 18 : The ships collision setup

Minorsky' approach is based on the following assumptions:

i. The collision is an inelastic state
ii. The effect of the system kinetic energy along the struck ship's longitudinal direction is small and assuming $V_a = 0$
iii. The rotations of the struck and striking ships (yaw) are small and can be neglected, therefore only added mass is considered due to the inertia effect.

The first two assumptions define the so-called "worse case". The third is based on the observation that only small rotations occur in actual collisions. With these assumptions, the motion is one-dimensional and the final

velocities of both striking and struck ships are derived as follows based on conservation of momentum (Paik and Pedersen, 1996, Brown, 2002).

$$(M_a + M_b + dM)V = M_a V_a + M_b V_b \qquad (3.6)$$

Where;

M_a = mass struck ship

V_a = velocity of struck ship

M_b = mass of striking ship

V_b = velocity of striking ship

dM = added mass

V = Final velocity

For simplicity, assuming normal penetration to the struck ship, the effect of the system kinetic energy along the struck ship's longitudinal direction is considered small, therefore $V_a = 0$ in that direction , thus;

$$V = \frac{M_b V_b}{M_a + M_b + dM} \qquad (3.7)$$

The conservation of kinetic energy of the collision;

$$\frac{1}{2}(M_a + M_b + dM)V^2 = \frac{1}{2}M_a V_a^2 + \frac{1}{2}M_b V_b^2 \qquad (3.8)$$

and the absorbed energy of the collision when assuming $V_a = 0$, hence;

$$\Delta KE = \frac{1}{2}M_b V_b^2 - \frac{1}{2}(M_a + M_b + dM)V^2 \qquad (3.9)$$

$$\Delta KE = \frac{1}{2}M_b V_b^2 - \frac{1}{2}(M_a + M_b + dM)\left(\frac{M_b}{M_a + M_b + dM}\right)^2 V_b^2 \qquad (3.10)$$

$$\Delta KE = \frac{M_b(M_a + dM)}{2(M_a + M_b + dM)}V_b^2 \qquad (3.11)$$

Let;

$$e = \frac{M_a + dM}{M_b} \qquad (3.12)$$

hence;

$$\Delta KE = \frac{1}{2}M_b V_b^2 \left(\frac{e}{e+1}\right) \qquad (3.13)$$

Base on Minorsky's approach, added mass can be taken approximately$0.4M_b$, therefore;

$$e = 1.4 \frac{M_a}{M_b} \qquad (3.14)$$

and,

$$\Delta KE = \frac{M_a M_b}{2M_a + 1.43 M_b} V_b^2 \tag{3.15}$$

The collision angle,$\emptyset$ is introduced and the absorbed kinetic energy in the struck ship is now;

$$\Delta KE = \frac{M_a M_b}{2M_a + 1.43 M_b} (V_b \sin \emptyset)^2 \tag{3.16}$$

For grounding case and rigid wall collision, the energy released be determined from letting $M_a \to \infty$ and $V_a = 0$, then, the formula become;

$$\Delta KE = \frac{1}{2} M_b V_b^2 \tag{3.17}$$

The method also found is not suitable for oblique angle collision and may underestimate the kinetic energy absorbed during collision.

3.5.2. 2 DOF - Damage Method

DAMAGE (Simonsen, 1999)is a two-degree of freedom (DOF) modeland was developed at MIT under the Joint MIT-Industry Program on Tanker Safety. Both sway and yaw are allowed motions of the struck ship, however the striking ship is only allowed one DOF, in surge direction only. DAMAGE is based upon the following assumptions:

   i. The collision is inelastic state

   ii. The lateral collision only is considered.

   iii. The struck ship is initially stand-still

   iv. The kinetic energy in surge direction of struck ship is negligible
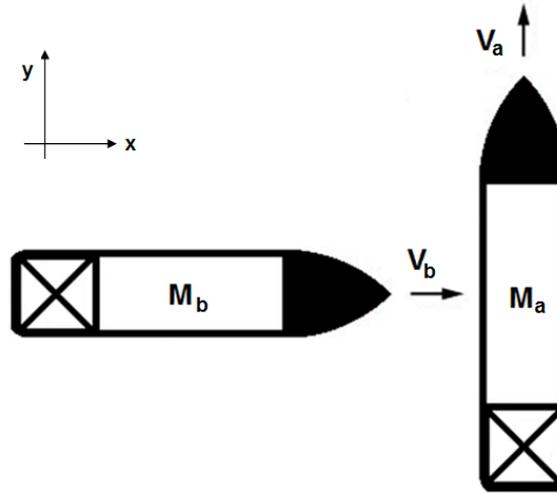
Figure 19: The ships collision parameters by (Paik and Pedersen, 1996).

The final speeds of both the striking and struck ships are found using the conservation of linear and angular momentum. From DAMAGE, the total kinetic energy absorbed within the collision as described by (Sajdak, 2004, Paik and Pedersen, 1996).

$$M_a^y V_a^x + M_b^x V_b^x = M_2^x V_2 \tag{3.18}$$

$$I_a^z \omega_a^x + M_b^x X_a V_b^x = M_b^x X_a V_2 \tag{3.19}$$

$$V_b^x = V_a^x + X_a \omega_a^x \tag{3.20}$$

$$V_a^x = V_2 \frac{1}{1 + \frac{M_a^y X_a^2}{I_a^z} + \frac{M_a^y}{M_b^x}} \tag{3.21}$$

$$\omega_a^x = V_2 \frac{\frac{M_a^y X_a}{I_a^z}}{1 + \frac{M_a^y X_a^2}{I_a^z} + \frac{M_a^y}{M_b^x}} \tag{3.22}$$

The kinetic energy absorbed in the collision then becomes:

$$\Delta KE = \frac{1}{2} M_a^y V_a^{x^2} + \frac{1}{2} M_b^x V_b^{x^2} + \frac{1}{2} I_a^z \omega_a^{x^2} - \frac{1}{2} M_b^x V_b^2 \tag{3.23}$$

Where:

M_a^y = virtual mass of the struck ship including added mass in sway

M_b^x = virtual mass of the striking ship including added mass in surge

I_a^z = virtual moment of inertia in yaw of the struck ship including yaw added mass (moment of inertia)

V_a^x =final velocity of struck ship in the sway direction

ω_a^x = final angular velocity of struck ship

V_2 = initial velocity of striking ship

V_b^x = final velocity of striking ship in the sway direction of the struck ship

X_a =impact point to the midship point of struck ship.

3.5.3. 3 DOF - Pedersen's Method

The (Terndrup Pedersen and Zhang, 1998) is a 3-DOF analysis of ship-ship collision. The method includes the effect of water pressure in the form of virtual added mass acting on a ship motions in yaw, surge and sway directions. The absorbed kinetic energy of ship collision is derived from solving force, moment equilibrium and conservation of momentum and energy. The method also considers the effect of friction during contact and is based upon the following assumptions;

   i.   The collision period occurs in a very short time, therefore the γ and α is consider constant during the event.
   ii. The procedure is based on rigid-body mechanics, where it is assumed that there is negligible strain energy for deformation outside the contact region and that the contact region is local and small.
   iii. The ratio between the collision forces parallel and perpendicular to the impacting surfaces F_η and F_ξ respectively, is constant during the collision.
   iv. The effect of roll motion is neglected.
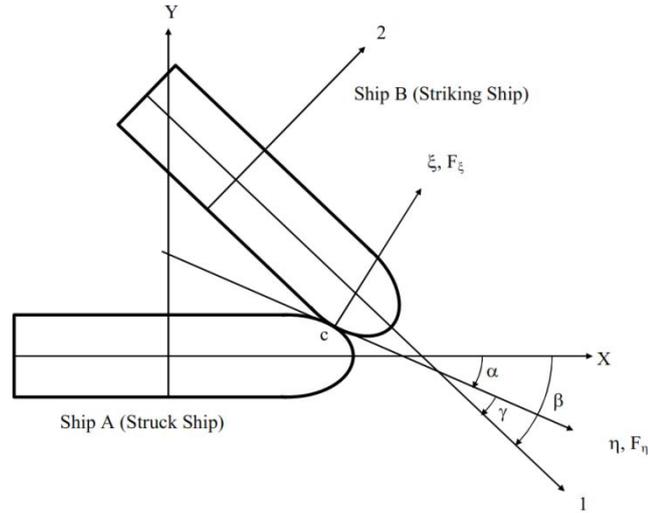
Figure 20: The ships collision parameter by (Terndrup Pedersen and Zhang, 1998).

Thus, the equation of motion when referring to Figure 20 for both ships at the impact point C between the striking ship (A) and the struck ship (B) from direction of η and ξ can be expressed as;

$$\begin{Bmatrix} F_\eta \\ F_\xi \end{Bmatrix} \begin{bmatrix} -K_\eta & -K_\xi \\ -D_\eta & -D_\xi \end{bmatrix} = \begin{Bmatrix} \ddot{\eta} \\ \ddot{\xi} \end{Bmatrix} \tag{3.24}$$

Where F_η and F_ξ are impact forces, $\ddot{\eta}$ and $\ddot{\xi}$ are relative accelerations, K_η, K_ξ, D_η, D_ξ are algebraic expressions that are a function of the ship masses, strike location, collision angle, and added mass coefficients in the η and ξ direction, respectively. Added mass coefficients are assumed to be 0.05 in surge, 0.85 in sway and 0.21 in yaw.

.

Hence, by simplifying the equation of impact force, the equation (3.24)become.

$$\begin{Bmatrix} F_\eta \\ F_\xi \end{Bmatrix} = \begin{bmatrix} -K_\eta & -K_\xi \\ -D_\eta & -D_\xi \end{bmatrix}^{-1} \begin{Bmatrix} \ddot{\eta} \\ \ddot{\xi} \end{Bmatrix} = \frac{1}{D_\xi K_\eta - D_\eta K_\xi} \begin{bmatrix} -K_\eta & -K_\xi \\ -D_\eta & -D_\xi \end{bmatrix} \begin{Bmatrix} \ddot{\eta} \\ \ddot{\xi} \end{Bmatrix} \tag{3.25}$$

Then, integrating the impact force with respect to time, the impulses in direction can be expressed as;

$$I_{\xi 0} = \int_0^T F_\xi \, dt = \frac{K_\xi \dot{\xi}(0)(1+e) - D_\eta \dot{\eta}(0)}{D_\xi K_\eta - D_\eta K_\xi} \tag{3.26}$$

$$I_{\eta 0} = \int_0^T F_\eta \, dt = \frac{D_\xi \dot{\eta}(0) - K_\xi \dot{\xi}(0)(1+e)}{D_\xi K_\eta - D_\eta K_\xi} \tag{3.27}$$

Where e denotes a coefficient of restitution in ξ direction of ship rebound and is defined as;

$$e = \frac{\dot{\xi}_T}{\dot{\xi}_0} \tag{3.28}$$

and, the ratio of the impact impulses can be expressed as;

$$\mu = \frac{I_{\eta 0}}{I_{\xi 0}} \tag{3.29}$$

In the event of collision, ships may slide against each other, if the collision angle is small or very large. Therefore, it is crucial to take into consideration an impact with friction effect included and the effective coefficient of friction between the ships is regarded as μ_0 and critical value is regarded as μ. The two ships will slide against each other If satisfied $|\mu_0| < |\mu|$ and the two ships will stick together after collision if satisfied $|\mu_0| \geq |\mu|$. The μ is determined from the ratio of impact impulse.

Hence, ξ_{max} and η_{max} are the relative penetrations in the η and ξ direction at the end of collision, respectively. Therefore, the total absorbed energy is $E_{total} = E_\eta + E_\xi$ and the impulses in η and ξ direction are determined as;

i.   Sliding case, when $|\mu_0| < |\mu|$

$$E_\xi = \int_0^{\xi_{max}} F_\xi \, d\xi = \frac{1}{2} \frac{1}{D_\xi + \mu D_\eta} (1 - e^2) \big[\dot{\xi}(0)\big]^2 \tag{3.30}$$

$$E_\eta = \int_0^{\xi_{max}} F_\eta \, d\eta = \frac{1}{2} \frac{1}{\left(\frac{1}{\mu}\right) K_\xi + K_\eta} [\dot{\eta}(0)]^2 \tag{3.31}$$

$$I_\xi = \int_0^T F_\xi \, dt = \frac{1}{D_\xi + \mu D_\eta} (1 - e^2) \dot{\xi}(0) \tag{3.32}$$

40

$$I_\eta = \int_0^T F_\eta \, dt = \frac{1}{\left(\frac{1}{\mu}\right)K_\xi + K_\eta} [\dot{\eta}(0)]^2 \qquad (3.33)$$

ii.   Sticking case, when $|\mu_0| \geq |\mu|$.

$$E_\xi = \int_0^{\xi_{max}} F_\xi \, d\xi = \frac{1}{2} \frac{1}{D_\xi + \mu_0 D_\eta} (1 - e^2)\big[\dot{\xi}(0)\big]^2 \qquad (3.34)$$

$$E_\eta = \int_0^{\xi_{max}} F_\eta \, d\eta = \frac{1}{2} \frac{1}{\left(\frac{1}{\mu_0}\right)K_\xi + K_\eta} [\dot{\eta}(0)]^2 \qquad (3.35)$$

$$I_\xi = \int_0^T F_\xi \, dt = \frac{1}{D_\xi + \mu_0 D_\eta} (1 - e^2)\dot{\xi}(0) \qquad (3.36)$$

$$I_\eta = \int_0^T F_\eta \, dt = \frac{1}{\left(\frac{1}{\mu_0}\right)K_\xi + K_\eta} [\dot{\eta}(0)]^2 \qquad (3.37)$$

For the case where the striking ship (A) collides with a rigid wall, the energy released and impact impulses can also be determined when $M_b \rightarrow \infty$, $\alpha = \beta$, $V_{b1} = 0$, $V_{b1} = 0$, and $V_{b2} = 0$.

3.5.4. Empirical formulae -Minorsky Method

The Minorsky empirical method (Minorsky, 1959) is replicate of formulae derived from available data of an actual accidents. The data is based on an investigation of 26 ship-ship collisions. The method correlate the volume of damaged structural to the energy absorbed during the collision as shown in Figure 21.

The slope of the straight line in Figure 21 is the correlation of the damaged volume of ship structure and absorbed energy and calculated as below:

$$\text{ET} = 414.5\text{RT} + 121{,}900 \qquad (3.38)$$

where:

ET - energy absorbed (tons. knots^2)

RT - resistance factor or damaged volume $(\text{ft}^2.\,\text{in})$.
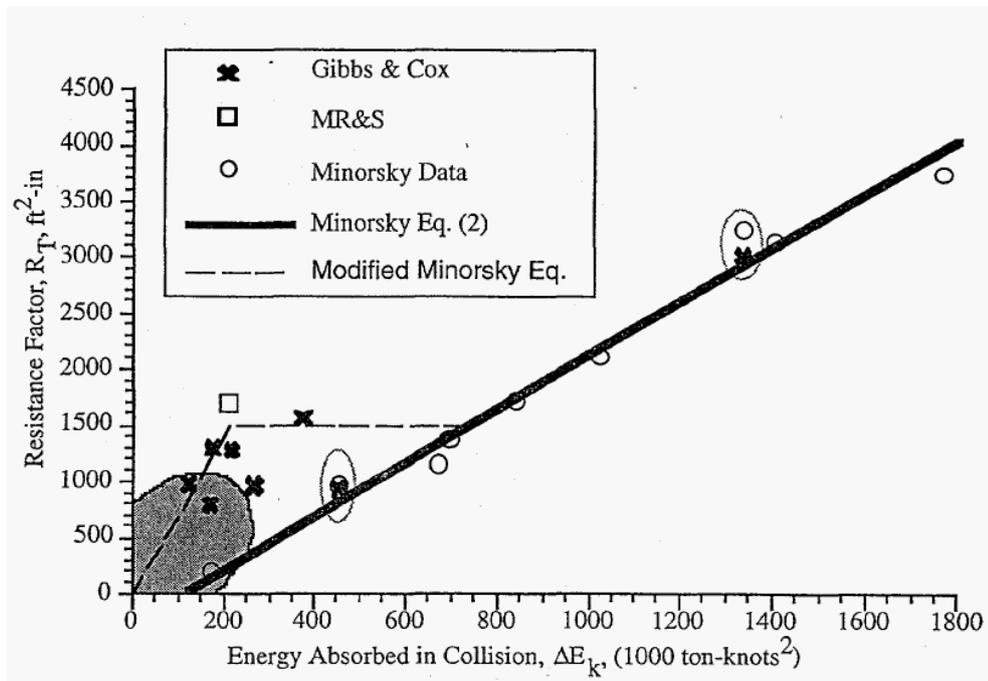
Figure 21: Minorsky's Correlation (Reardon and Sprung, 1996).

(Reardon and Sprung, 1996) revisited and revalidated Minorsky's approach by including statistical data from 16 additional collisions and proposed a new formulation in metric units as below;

$$DKE = (47.1 \pm 8.8)RT + 28.4 \hspace{3cm} (3.39)$$

where:

      DKE - Lost kinetic energy in (MJ)

      RT - Resistance factor in (m^3)

Low energy collisions are not modelled well with the Minorsky method. The intercept term, 121,900 ltons-knots2, in the original Minorsky's formula, and 28.4 MJ, in (Reardon and Sprung, 1996), is the energy expended bending, stretching, puncturing and tearing the shell of the struck ship. This value varies significantly in the collision data reflecting different designs and dependence on variables other than damage volume (Brown, 2002).

3.5.5. Soft bows - Woisin Method

(Woisin, 1979.) replicated and analyzed the structural design of nuclear ships to reduce damage from collision in a series of tests by GKSS in Germany. Twelve pairs of collision models were tested in Hamburg from 1967 to 1976. Figure 22 shows a schematic diagram of the dynamic collision model tests performed in Hamburg. These tests used deformable bows. He proposes a theory of "soft bows" to minimize penetration into other ships. The test stand consists of a carriage of up to 25 tonnes with a fore-ship model attached to its forward end, which rams a ship's side model attached to a rigid counter bearing (Woisin, 1979.)

The impact energy was achieved by released bow model from inclination structure and collided with side shell model. The damage is clearly shown in Figure 22. The model was adopted by using model scales of 1:12 and 1:7.5. The results showed a significant difference in impact force for both experiments.
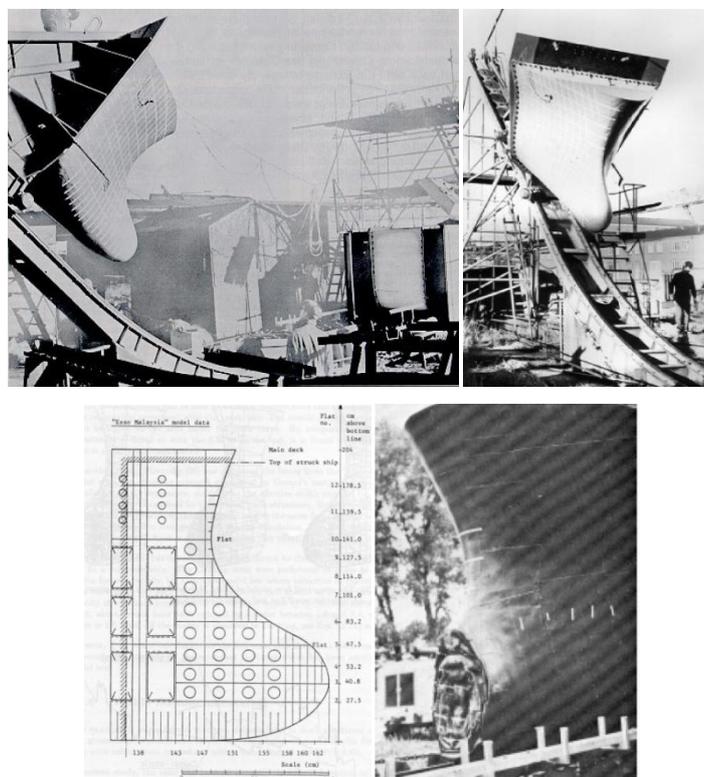
Figure 22 : Bow model- ESSO Malaysia (Kierkegaard, 1993).

Based on the experiments, (Woisin, 1979.) proposes a number of potential methods for designing soft bows that are capable of absorbing energy during collision and can reduce damage of the struck ship. The proposal included using transverse framing instead of longitudinal stiffeners, water filling, fewer breast hooks and reduced stem plate thickness, no hard points, design of bulbous bows and raking parts above water as crushable zones.
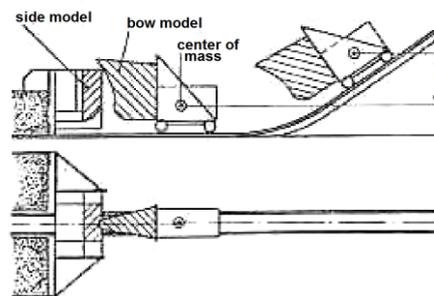
Figure 23: Schematic Diagram of Test Techniques in Hamburg (Woisin, 1979.).

$$P_{max} = 0.88\sqrt{DWT} \mp 50\% \qquad (3.40)$$

(Woisin, 1979.) introduced an equation capable of predicting the maximum collision force P_{max} for typical bow structures, as a function of the DWT of the striking ship.

3.5.6. Pedersen Method

(Terndrup Pedersen et al., 1993a) presents a method for estimating the impact forces between ship and large volume offshore structures. The study focused on the impact loads generated from the forward part of ship structures on fixed offshore structures during collision. The impact loads are determined as a function of vessel size, vessel speed, bow profile, collision angles and eccentric impacts. The method also takes into consideration modified (Amdahl, 1983, Yang and Caldwell, 1988) as shown in Figure 24.
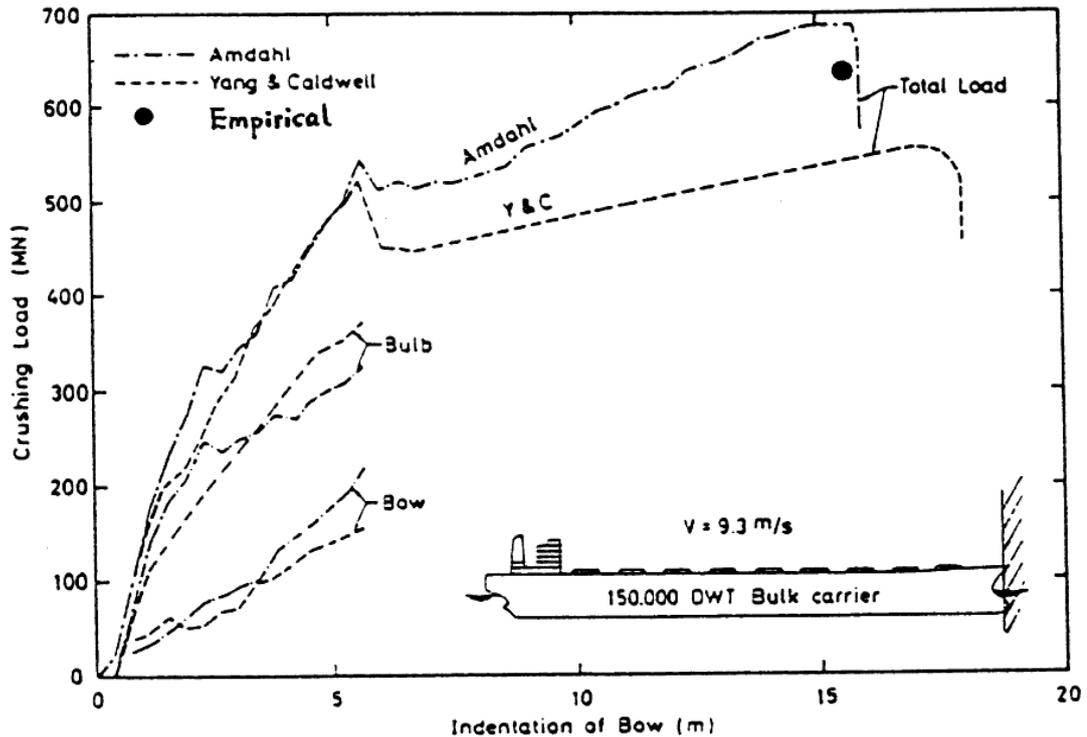
Figure 24: Force- indentation curves for 150,000 DWT Bulk Ship (Terndrup Pedersen et al., 1993a).

Figure 24 shows the calculated crushing load-indentation curves using (Amdahl, 1983) modified method and (Yang and Caldwell, 1988) method for the 150,000 DWT bulk vessel in a fully loaded condition, striking head-on with a rigid wall at an initial impact speed of 18 knots. Similar results are obtained for the 40,000 DWT container vessel for a head-on collision with a rigid wall at a speed of 12.9 m/s also discussed in (Brown, 2002).

(Terndrup Pedersen et al., 1993a) suggests that the force-penetration curve can be approximated using a sine curve, the peak of which represents the maximum bow crushing force and the quarter period is the impact duration as given in Equation (3.43) and Equation (3.44). Based on these six ships, an empirical expression is derived to estimate maximum bow collision load, as a function of strain rate, impact velocity, vessel displacement and vessel length. For a vessel between 500 DWT and 300,000 DWT the crushing load is given by:

$$P_{bow} = P_o \bar{L}[\bar{E}_{imp} + (5.0 - \bar{L})\bar{L}^{1.6}]^{0.5} \qquad \text{for } \bar{E}_{imp} \geq \bar{L}^{2.6} \qquad (3.41)$$

$$P_{bow} = 2.24 P_o [\bar{E}_{imp} \bar{L}]^{0.5} \qquad \text{for } \bar{E}_{imp} < \bar{L}^{2.6} \qquad (3.42)$$

Where , $\bar{L}$ = Lpp/275m, $\bar{E}_{imp}$ = E_{imp}/1425MN and $E_{imp} = \frac{1}{2}m_x V_o^2$

The maximum indentation;

$$S_{max} = \frac{\pi}{2}\frac{E_{imp}}{P_{bow}} \qquad (3.43)$$

The impact duration:

$$T_0 = 1.67\frac{s_{max}}{V_0} \qquad (3.44)$$

Where:

P_{bow} = maximum collision load (MN)

P_o = reference collision load equal to 210 MN;

E_{imp} = energy to be absorbed by plastic deformations;

Lpp = length of the vessel (m);

m_x = mass plus added mass (5%) w.r.t longitudinal position (10^6kg)

V_0 = initial speed of the vessel in (m/s)

3.5.7. Other available methods

Others prominent methods discussed and published by (Chen, 2000, McDermott et al., 1974, Terndrup Pedersen et al., 1993a, Simonsen, 1997b, Simonsen, 1997c, SUZUKI et al., 1999, Wang and Ohtsubo, 1997, Wang et al., 1998, WANG and OHTSUBO, 1999, Wierzbicki, 1991, Yang and Caldwell, 1988) use simplified analytical approaches as a basis of understanding global and local effects during ship collision and grounding. The areas of study range from head-on collision on rigidwalls, ship-ship collision, ship platform collision, ship-bridge collision, bottom ranking and ship

stranding. The non-linear FEM is a costly tool to simulate ship collision and grounding and has recently become popular among researchers. Some of the publication include(Amdahl et al., 1995, Egge and Böckenhauer, 1991, Kitamura, 1997, Kuroiwa, 1996, Paik et al., 1998). The FEM approaches are capable of investigating and replicating near actual ship-ship collision and grounding.

3.6. Summary

The content discussed in this chapter is related to chapter 7 and 8 for energy and forces absorbed with comparison to the present method. The history of material has evolved and their properties has been discussed briefly. The code and standards in general have touched overall regulatory bodies as the main player in marine structure safety. The external and internal mechanics of ship collision have been discussed directly and indirectly and includes Minorsky, Pederson, Gerard, Yang & Caldwell, and Woisin methods.

The chapter gave an overview for some prediction methods available and was comprised of 1-DOF, 2-DOF, 3-DOF and empirical methods based on actual statistical data. This chapter also helped the author to understand and workout a new prediction in later chapters and progressively discusses material properties in chapter 4.

CHAPTER 4:MATERIAL CHARACTERISTICS AND FINITE ELEMENT MODELLING PROCEDURES FOR COLLISION AND GROUNDING ANALYSIS

4.1. Introduction

This chapter will discuss the characteristics and parameters for finite element analysis. The topics included a basic understanding of stress-strain curve, material properties of material used, the techniques and formula used to generate the strain hardening curve, material constitutive failure methods that are capable of predicting rupture, finite element modeling techniques and procedures. This chapter lays down the basis of common aspects used for finite element analysis for later chapters.

4.2. Material Characterization

4.2.1. Stress-Strain Diagram

The basic mechanical properties of steel material can be extracted from the stress-strain diagram. Figure 25 shows normal mild steel behavior and deformable phases occurring under loading before failure. These properties are able to be determined bybasic tensile experiment test.
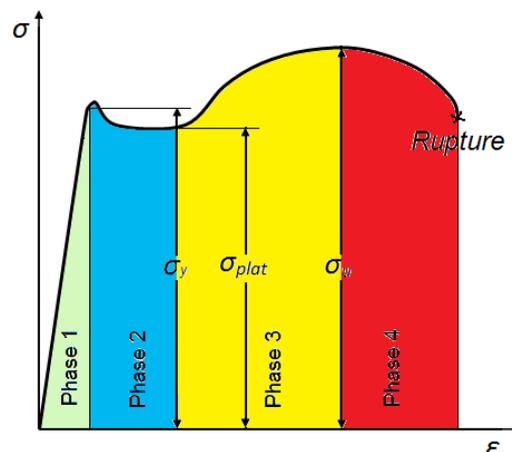
Figure 25: The Stress-strain Diagram (Stone, 2012).

- Phase 1 – The elastic region where material experiences a linear stress-strain relationship up to a stress level known as the proportional limit just below yield strength (σ_y) that follows Hooke's law of linearity behavior.

- Phase 2 – The material experience yielding phenomena where there is an increase in elongation without additional external load. This phenomenon is common to mild steel and not for high tensile steel.

- Phase 3 – The Strain hardening region where material experiences increase in strength due to resistance of further mechanical deformation and permanent deformation after being unloaded.

- Phase 4 – The necking region where material experiences localized deformation relatively in reducing the cross-sectional area before failure.

- Plateau Stress (σ_{plat})– The region where stress remains approximately unchanged and strain experiences some increment. This behavior understand only occur only for steel among common structural material.

- Yield Strength (σ_y)- The maximum load that can be applied without permanent set of deformation after being unloaded.

- Ultimate Strength (σ_U)- The maximum load that material can withstand before necking occurs.

- Rupture Point – Where the material totally fails.

4.2.2. Material Properties

The materials used in this analysis were mild steel (S235JR-EN10025) and high strength steel (S355NH-EN10210) the material properties are described in Table 1. The properties in this table were obtained experimentally.

A mild steel and high tensile steel tensile test result for force-displacement using dog-bone specimens is compared side by side by (Ehlers, 2009b, AbuBakar et al., 2010) and is shown in Figure 26. Theoretical comparisons were carried out using a 4.4mm mesh size and FLD material failure model.

The results give good correlation between both approaches and experiments for mild steel S235JR-EN10025.

Table 1: The properties of steel were taken from (Alsos and Amdahl, 2009, Alsos et al., 2009) and were obtained experimentally.

Material Grade	K (MPa)	n	ε_{plat}	ε_f	σ_y (MPa)	σ_u (MPa)
S235JR-EN10025	740	0.24	*Nil*	0.35	285	416
S235JR-EN10025	760	0.225	0.015	0.35	340	442
S355JR-EN10210	830	0.18	0.01	0.28	390	495
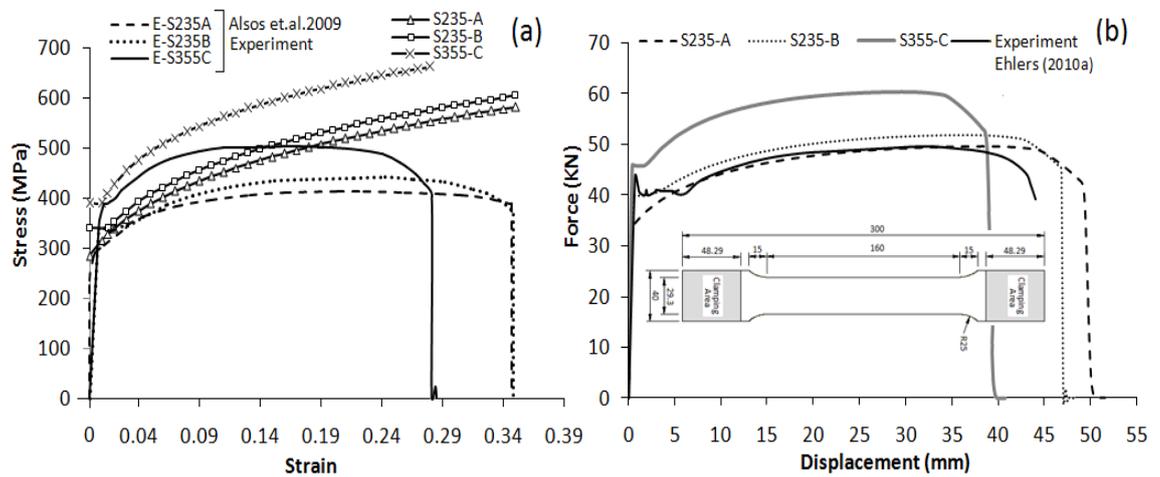
Figure 26 : (a) The stress-strain curve. (b) The tensile test force-displacement.

4.2.3. Material Model

The material is assumed to be isotropic and to exhibit strain hardening properties as described by Ludwik's strain hardening power law;

$$\sigma = K\varepsilon^n \tag{4-1}$$

To describe the time dependence of the material response, the following true stress-natural strain relation was employed using deformation theory. Where K, m and n are material parameters, where m lies between 0 and 0.05 from (Hutchinson and Neale, 1978).

$$\sigma = K\varepsilon^n \dot{\varepsilon}^m \qquad\qquad (4\text{-}2)$$

Hence, the true stress-strain relation is approximated by the equation below assuming isotropic material properties, where ε_{plat} is the plateau strain proposed by (Alsos et al., 2009).

$$\sigma = \begin{cases} \sigma_y \, \mathbf{if} \varepsilon \le \varepsilon_{plat} \\ K(\varepsilon + \varepsilon_0)^n \mathbf{otherwise} \end{cases} \qquad\qquad (4\text{-}3)$$

and

$$\varepsilon_0 = \left(\frac{\sigma_y}{K}\right)^{1/n} - \varepsilon_{plat} \qquad\qquad (4\text{-}4)$$

and

ε_{plat} is the plateau strain.

Where a quasi-linear stress-strain relationship as described in (Jie et al., 2009)can be approximately written as:

$$\dot{\varepsilon} = \left[\frac{\varepsilon}{(m+n)} - s(\sigma, \varepsilon)\right]\frac{\dot{\sigma}}{\sigma} + \left(\frac{\sigma}{K\varepsilon^n}\right)^{1/m} \qquad\qquad (4\text{-}5)$$

Where

$$s(\sigma, \varepsilon) = \frac{-c\sigma}{\varepsilon^{n/m}} \qquad\qquad (4\text{-}6)$$

and

$$\dot{\sigma} = E_t \dot{\varepsilon} \qquad\qquad (4\text{-}7)$$

Where, E_t is tangent modulus for plastic deformation and C is integration constant, which can be determined from uniaxial testing at various strain rates. In cases where the collision and grounding event occurs at relatively low speeds, the strain rate effect described in equation (4-3) is usually ignored. This was the procedure applied in the analysis carried out in this study, this means that the equation is reduced to that proposed by (Hill, 1991).

4.2.4. Material Failure

In general there are many types of material failures that are capable to model progressive damage. These are depending on the complexity and availability of data to validate the material failure for such simulation using ether commercial FEA codes or open source codes. The common material failures used for modeling progressive damage and failure in ductile metals are Johnson-Cook, Ductile Damage, Shear Damage, forming limit diagram (FLD), forming limit stress diagram (FLSD), Müschenborn-Sonne forming limit diagram (MSFLD), and Marciniak-Kuczynski (M-K) criteria. The progressive damage models permit for a soft degradation of the material stiffness, which suitable for both quasi-static and dynamic application, a huge benefit over the dynamic failure models. The failure mechanisms can cause the rupture (see Figure 27);

i.   Ductile failure due to the nucleation, growth, and coalescence of voids
ii.   Shear failure due to shear band localization.
iii. Brittle failure is typically rapid crack propagation with low energy release and without huge plastic deformation.

The ductile and shear failure mechanisms of the criteria for the onset of damage discussed in (Hooputra et al., 2004).
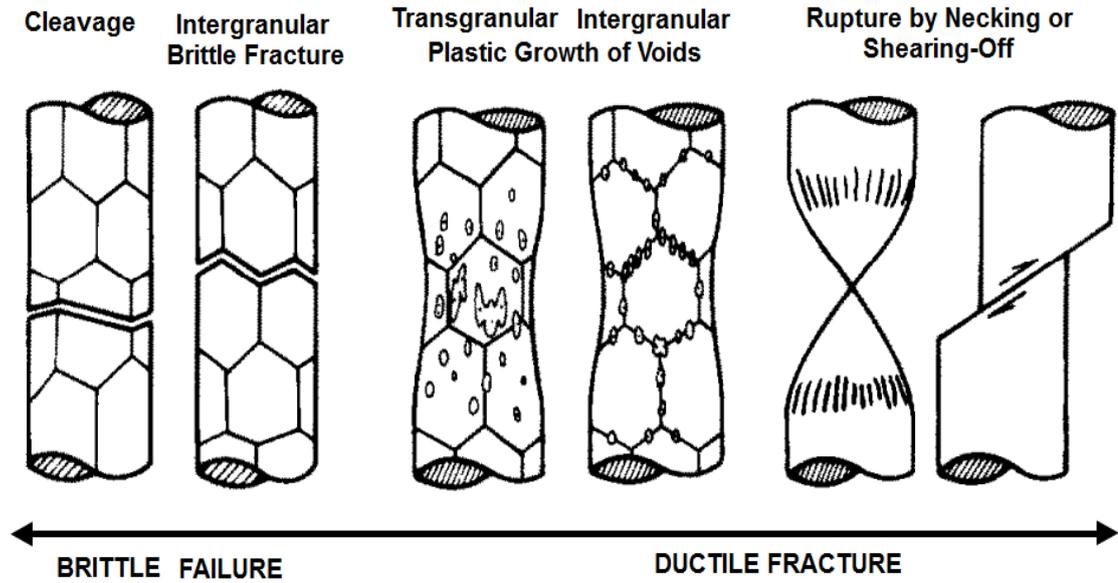
Figure 27: Fracture Mechanism (Ashby et al., 1979).

4.2.5. Ductile Failure

The ductile failure is a model for predicting the onset of damage due to nucleation, growth, and coalescence of voids. The model assumes that the equivalent plastic strain at the onset of damage, $\bar{\varepsilon}_D^{pl}$, is a function of stress triaxiality and strain rate:

$$\bar{\varepsilon}_D^{pl}(\eta, \dot{\bar{\varepsilon}}^{pl}) \qquad (4\text{-}8)$$

Where, $\eta = \dfrac{\sigma_m}{\sigma_{eq}}$, is the stress triaxiality, σ_m is the hydrostatic stress, σ_{eq} is the Mises equivalent stress, and $\dot{\bar{\varepsilon}}^{pl}$ is the equivalent plastic strain rate. The criterion for damage initiation is achieved when the following situation is satisfied:

$$\omega_D = \int \frac{d\bar{\varepsilon}^{pl}}{\bar{\varepsilon}_D^{pl}(\eta, \dot{\bar{\varepsilon}}^{pl})} = 1 \qquad (4\text{-}9)$$

where ω_D is a state of a variable that increases monotonically in conjunction with plastic deformation. For all increments during the analysis every incremental increase in ω_D is computed as;

$$\Delta\omega_D = \frac{\Delta\bar{\varepsilon}^{pl}}{\bar{\varepsilon}_D^{pl}(\eta,\dot{\bar{\varepsilon}}^{pl})} \geq 0 \qquad (4\text{-}10)$$

4.2.6. Johnson-Cook Failure

The Johnson-Cook criterion (available only in ABAQUS/Explicit) is a special case of the ductile failure where equivalent plastic strain at the onset of damage, $\bar{\varepsilon}_D^{pl}$, is consider to be of the form;

$$\bar{\varepsilon}_D^{pl} = [d_1 + d_2\exp(-d_3\eta)]\left[1 + d_4\ln(\frac{\dot{\bar{\varepsilon}}^{pl}}{\dot{\varepsilon}_o})\right](1 + d_5\hat{\theta}) \qquad (4\text{-}11)$$

Where, $d_1 - d_5$ are failure parameters and $\dot{\varepsilon}_o$ = strain rate. This expression differs from the original formula published by (Johnson and Cook, 1985) in the sign of the parameter d_3. This difference is motivated by the fact that most materials experience a decrease in $\bar{\varepsilon}_D^{pl}$ with increasing stress triaxiality; therefore, d_3 in the above expression will usually take positive values. $\hat{\theta}$ is the non-dimensional temperature defined as

$$\hat{\theta} \equiv \begin{cases} 0 & \text{for } \theta < \theta_{transition} \\ (\theta - \theta_{transition})/(\theta_{melt} - \theta_{transition}) & \text{for } \theta_{transition} \leq \theta \leq \theta_{melt} \\ 1 & \text{for } \theta > \theta_{melt} \end{cases} \qquad (4\text{-}12)$$

Where, θ = current temperature, θ_{melt} = melting temperature, and $\theta_{transition}$ = temperature at or below which there is no temperature dependence on the expression of the damage strain $\bar{\varepsilon}_D^{pl}$. The material parameters should be calculated at or below the transition temperature.

4.2.7. Shear Failure

Shear failure is a model for predicting the onset damage due to shear band localization. The model assumes that the equivalent plastic strain at the onset of damage, $\bar{\varepsilon}_s^{pl}$, is a function of the shear stress ratio and strain rate:

$$\bar{\varepsilon}_s^{pl}(\theta_s, \dot{\bar{\varepsilon}}^{pl}) \qquad\qquad (4\text{-}13)$$

Where, $\theta_s = \frac{q + k_s p}{\tau_{max}}$ is the shear stress ratio, τ_{max} = maximum shear stress, and k_s = material parameter. Damage initiation is satisfied when the following condition is achieved:

$$\omega_s = \int \frac{d\bar{\varepsilon}^{pl}}{\bar{\varepsilon}_s^{pl}(\theta_s, \dot{\bar{\varepsilon}}^{pl})} = 1 \qquad\qquad (4\text{-}14)$$

Where, ω_s is a variable that increases monotonically in conjunction with plastic deformation proportional to the increase of equivalent plastic strain. Every increment during the analysis the increment of ω_s is computed as;

$$\Delta\omega_s = \frac{\Delta\bar{\varepsilon}^{pl}}{\bar{\varepsilon}_s^{pl}(\theta_s, \dot{\bar{\varepsilon}}^{pl})} \geq 0 \qquad\qquad (4\text{-}15)$$

4.2.8. RCTL Failure

Briefly, the RCTL damage criterion is a combination of modified Rice Tracey and Cockcroft-Latham damage failure. Both of these functions are based on hydrostatic stress state, express by the stress triaxiality:

$$T = \frac{\sigma_m}{\sigma_{eq}}, \qquad \text{where}$$

σ_m is hydrostatic stress and

σ_{eq} is the equivalent stress.

The value of η lies between -1/3 <T< 1/3, damage ceases when *T*< -1/3, which is referred to as the cut-off value, where rupture is believed not to occur below this value.

The RTCL failure expressed as;

$$\dot{D} = \begin{cases} 0 & \text{if } T < \frac{1}{3} \\ \frac{\sigma_1}{\sigma_{eq}} \dot{\varepsilon}_{eq} & \text{if } -\frac{1}{3} \leq T < \frac{1}{3} \\ \exp\left(\frac{3T-1}{2}\right) \dot{\varepsilon}_{eq} & \text{Otherwise} \end{cases}$$

(4- 16)

Where :

$\dot{D}$= Rate of damage

σ_1= Principal stress

$\dot{\varepsilon}_{eq}$= Equivalent plastic strain rate

4.2.9. BWH Failure

The BWH failure based on stress failure and determining onset of local necking. The BWH is combination of (Hill, 1952, Bressan and Williams, 1983) using FLD failure concept and mathematical expression as below:

$$\sigma_1 = \begin{cases} \frac{2K}{\sqrt{3}} \frac{1+\frac{1}{2}r_\varepsilon}{\sqrt{r_\varepsilon^2+r_\varepsilon+1}} \left(\frac{2}{\sqrt{3}} \frac{n}{1+r_\varepsilon} \sqrt{r_\varepsilon^2 + r_\varepsilon + 1}\right)^n & \text{if } r_\varepsilon \leq 0 \\ \frac{2K}{\sqrt{3}} \frac{\left(\frac{2}{\sqrt{3}}n\right)^n}{\sqrt{1-\left(\frac{r_\varepsilon}{2+r_\varepsilon}\right)^2}} & \text{otherwise} \end{cases}$$

(4- 17)

Where σ_1= Principal stress, K,n are power law parameters that can be found in Table 1. $r_\varepsilon = \frac{\dot{\varepsilon}_2}{\dot{\varepsilon}_1}$, $\dot{\varepsilon}_1$ and $\dot{\varepsilon}_2$ are minor and major principle strain rates.

Both of RTCL and BWH failure models are described in detail in (Alsos et al., 2009, Alsos et al., 2008).

4.2.10.   FLD Failure

The material failure employed in the analysis has to be coupled with material failure model to predict the plastic deformation and onset rupture. In this work the authors have adopted the Forming Limit Diagram (FLD) approach to predict the onset of rupture. The Forming Limit Diagram (FLD) method, for predicting material failure is a concept introduced by (Keeler and Backofen, 1963b) to determine the amount of deformation that a material can withstand prior to the onset of necking instability. The maximum strains that a sheet material can sustain prior to the onset of necking are referred to as the forming limit strains.

When considering the forming limit strains including rate-dependant effects in FLD, (details of which can be found in (Jie et al., 2009), the following relationships are used;

$$\varepsilon_1 = \begin{cases} \frac{(m+n)}{1+r_\varepsilon} + \frac{\sqrt{3}(m+n)s(\sigma_{eq},\varepsilon_{eq})}{2\sqrt{1+r_\varepsilon+r_\varepsilon^2}} & \text{if } r_\varepsilon \leq 0 \\ \frac{3r_\varepsilon^2+(m+n)(2+r_\varepsilon)^2}{2(2+r_\varepsilon)(1+r_\varepsilon+r_\varepsilon^2)} + \left(\frac{(m+n)s(\sigma_{eq},\varepsilon_{eq})}{2(2+r_\varepsilon)(1+r_\varepsilon+r_\varepsilon^2)}\right)\left[(2+r_\varepsilon)\sqrt{3(1+r_\varepsilon+r_\varepsilon^2)}\ \varepsilon_{eq} - 3r_\varepsilon^2\right] & \text{if } r_\varepsilon > 0 \end{cases}$$

(4- 18)

Where ε_{eq} is the equivalent strain which, for the Von Misses, criterion defined as;

$$\varepsilon_{eq} = \frac{2}{\sqrt{3}}\varepsilon_1\sqrt{1+r_\varepsilon+r_\varepsilon^2}$$

(4- 19)

where: $r_\varepsilon = \frac{\varepsilon_2}{\varepsilon_1}$ is the strain ratio ($r_\varepsilon = 0$ for plain strain, $r_\varepsilon = -0.5$ for simple tension and $r_\varepsilon = 1$ biaxial tension) which is the basis for localized necking failure. This FLD material failure has been compared with experimental results, RCTL and BWH failure models in predicting the resistance of stiffened panels to penetration damage.

The FEA analysis conducted ignored the strain rate effect, where m = 0 and s = 0 in Eq. (8). Then the FLD failure model as expressed in Eq. (8) becomes:

57

$$\varepsilon_1 = \begin{cases} \dfrac{n}{(1+r_\varepsilon)} & \text{if} \quad r_\varepsilon \leq 0 \\[2mm] \dfrac{3r_\varepsilon^2 + (2+r_\varepsilon)^2 n}{2(2+r_\varepsilon)(1+r_\varepsilon + r_\varepsilon^2)} & \text{if} \quad r_\varepsilon > 0 \end{cases} \tag{4-20}$$
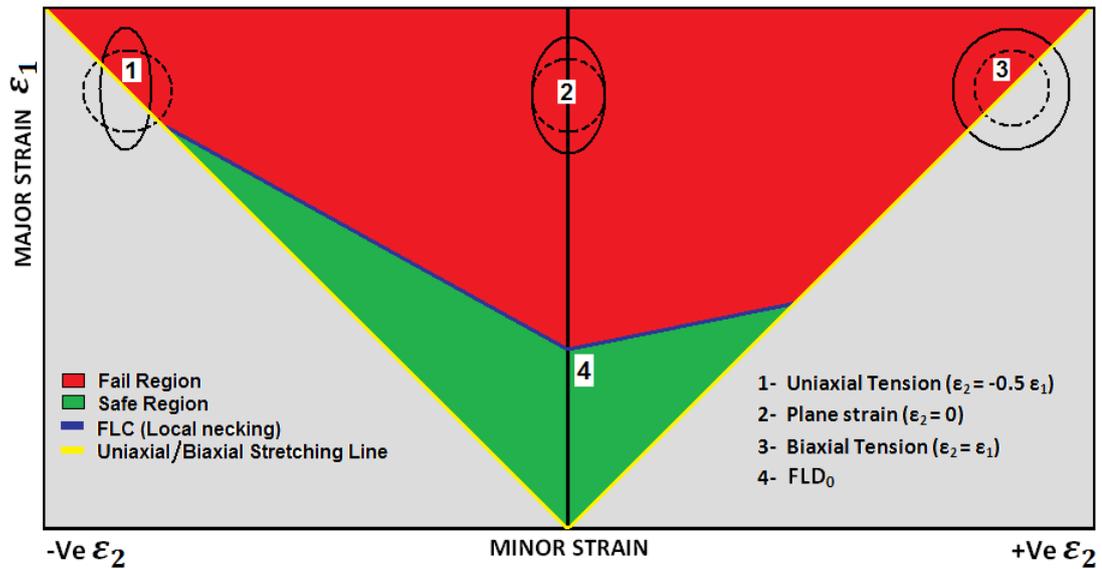
Figure 28 : Forming Limit Diagram.

Figure 28 shows the FLD_0 at minimum point for local necking before rupture occurs and Forming Limit Curve (FLC) that local necking point occurs for deferent strain ratio for different failure paths(Semiatin, 2006). Figure 28 also shows the safe region in green and the failure region in red where rupture occurs when mesh element are eliminated.

4.3. Finite Element Modelling

4.3.1. Introduction

Principally when solving nonlinear problems, the solution are not calculated by a single system of equations, as is common for linear problems. Normally

several iterations are required to solve for the nonlinear analysis. These problems are using implicit time integration, which ABAQUS/standard uses to solve, and the explicit way, used in the ABAQUS/explicit solver. The main principles of both strategies clarified by (Hilber et al., 1977, Quek and Liu, 2003, Wilson, 2002, Wriggers, 2008) will be explained in the following sections.

Mainly, the general approach for solving the dynamic response of structural systems is direct numerical integration of the dynamic equilibrium equations. This involves the attempt to satisfy dynamic equilibrium at discrete points in time after the solution has been defined at time zero. Most methods use equal time interval sat Δt, 2Δt, 3Δt…NΔt .Many different numerical techniques are used; however, all approaches can fundamentally be classified as either explicit or implicit integration methods(Wilson, 2002, Hilber et al., 1977). Most FEA commercial code is designated by these two methods (seeTable 2).

I. Explicit methods do not involve the solution of a set of linear equations at each step. Basically, those methods use the differential equation at time "t" to predict a solution at time "t + Δt". For most real structures, which contain stiff elements, a very small time step is required to obtain a stable solution. Therefore, all explicit methods are conditionally stable with respect to the size of the time step.

II. Implicit methods attempt to satisfy the differential equation at time "t" after the solution at time "t - Δt" has been found. Those methods require the solution of a set of linear equations at each time step; however, larger time steps may be used. Implicit methods can be conditionally or unconditionally stable. Thus the time step size is not limited. Implicit approaches are usually more stable numerically but less efficient computationally than explicit approaches.

The selection of time step sizes discussed in (Wriggers, 2008), used either in explicit or implicit algorithms, has to be justified by physics. In the case of impact problems (e.g. car-crash analysis) or shock waves moving through a

solid, small time steps have to be selected to resolve high frequency parts and travelling waves in order to capture the correct physical behavior. Hence explicit methods are ideal for such engineering applications. Implicit methods are advantageous for problems where the response of the dynamical system depends mainly upon lower frequencies (e.g. simulation of engine vibrations or vibration of structures). Since both types of physical behavior occur frequently in engineering applications, explicit and implicit methods will be used and discussed in chapter 9 for comparison of results generated as a case study.

Table 2: Commercially available software packages (Quek and Liu, 2003).

Software packages	Methods used	Application problems
ABAQUS	FEM (implicit, explicit)	Structural analysis, acoustics, thermal analysis, etc.
I-deas	FEM (implicit)	Structural analysis, acoustics, thermal analysis, etc.
LS-DYNA	FEM (explicit)	Structural dynamics, computational fluid dynamics, Fluid-structural interaction, etc.
Sysnoise	FEM/BEM	Acoustics (frequency domain)
NASTRAN	FEM (implicit)	Structural analysis, acoustics, thermal analysis, etc.
MARC	FEM (implicit)	Structural analysis, acoustics, thermal analysis, etc.
MSC-DYTRAN	FEM + FVM (explicit)	Structural dynamics, computational fluid dynamics, Fluid-structural interaction, etc.
ANSYS	FEM (implicit)	Structural analysis, acoustics, thermal analysis, multi-physics, etc.
ADINA DIANA	FEM (implicit)	Structural analysis, computational fluid dynamics, Fluid-structural interaction, etc.

4.3.2. Implicit Time Integration

To solve nonlinear problems, the Newton-Raphson method is used, where the solution is found by applying the specified load gradually and incrementally working toward the final solution (following the load-displacement path). The simulation is broken into a number of load increments where the approximate equilibrium configuration is found at the end of each load increment. It is thus a combination of incremental and iterative procedures. The dynamic equilibrium equation at a certain time tn+1 (here exemplarily for a one-dimensional single degree of freedom single mass oscillator without damping)

$$\mathbf{m\ddot{u}_{n+1} + ku_{n+1} = F_{n+1}} \tag{4-21}$$

is integrated at the end of the time step (tn+Δt). By applying a forward difference scheme (implicit time integration), the following relations are obtained and visualized in Figure 29. (Schweizerhof et al., 1992a)
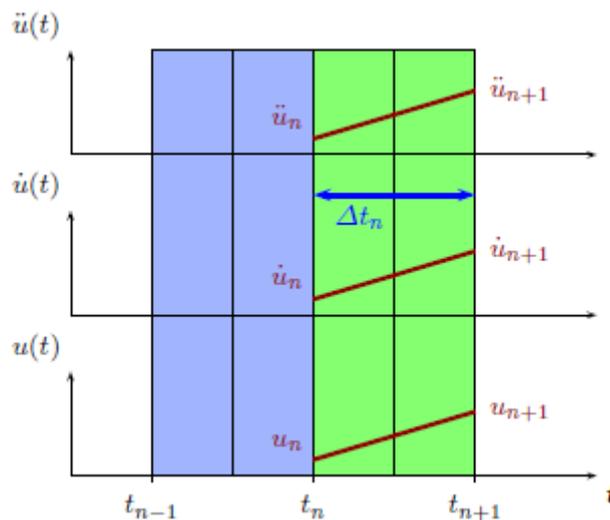
Figure 29: The Forward different method (Duddeck, 2008a)

$$\mathbf{\ddot{u}_{n+1} = \frac{\dot{u}_{n+1} - \dot{u}_n}{\Delta t}} \tag{4-22}$$

$$\mathbf{\dot{u}_{n+1} = \frac{u_{n+1} - u_n}{\Delta t}} \tag{4-23}$$

$$u_{n+1} = \frac{F_{n+1} + \frac{m}{\Delta t^2}(2u_n - u_{n-1})}{\frac{m}{\Delta t^2} + k}$$

(4- 24)

In (4.23) to (4.26), m is the mass, k the stiffness, F the external force, u the displacement, $\dot{u}$ the velocity and $\ddot{u}$ the acceleration at time tn+1. This scheme works independently of the time step size and is thus unconditionally stable. But as one can see in (4.26), the stiffness matrix has to be inverted and therefore the scheme requires many cost intensive iterations.(Duddeck, 2008a)

- A global stiffness matrix is calculated, inverted and applied to the nodal out of balance force to obtain a displacement increment
- Very Large mathematical iteration is required to form, factorize and store the stiffness matrix
- Most suitable for static and quasi-static simulations
- In general involves a fairly small number of expensive time steps
- Quasi -static analysis: "time" corresponds to a monotonically added to the parameter which characterizes the development of the loading

4.3.3. Explicit Time Integration

The Explicit method determines the solution to the dynamic equilibrium equation without iterating but by explicitly advancing the kinematic state from the previous increment.(Bathe, 1996, Duddeck, 2008b)

$$M\ddot{u} + C\dot{u} + Ku = F$$

(4- 25)

Where Internal force as $I = C\dot{u} + Ku$,
M = Nodal matrix
C = Nodal damping matrix
K = Nodal stiffness matrix
u = Nodal displacement
$\dot{u}$ = Nodal displacement

$\ddot{u}$ = Nodal Acceleration

F = External forces
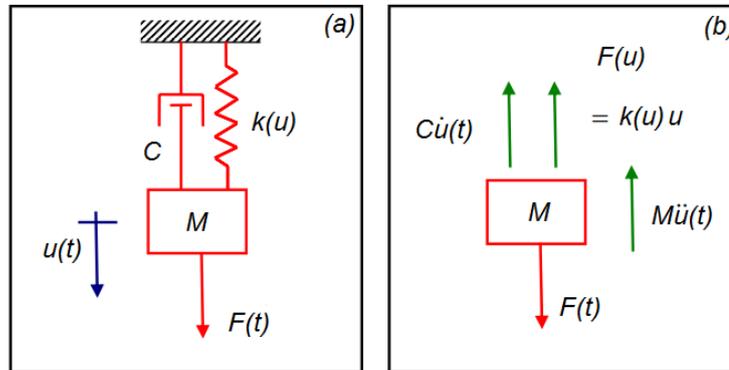
Figure 30: (a) Dynamic Model. (b) FBD of equilibrium (Duddeck, 2008a).

Since there is no necessary inversion of the stiffness matrix, the global set of equations does not have to be solved in each increment and even highly nonlinear procedures can be calculated easily with the explicit method. But unlike the implicit scheme, the explicit finite element method is only conditionally stable, that means that numerical stability is only guaranteed if the time increments are smaller than the time a material wave needs to cross the smallest element in the finite element mesh. The increment size depends solely on the highest natural frequency of the model and is independent of the type and duration of loading.

This indicates that the smaller the elements used, the smaller the time increments have to be and the more time is needed for the whole computation. The computational cost depends on;

- Element size: the smaller element is more expensive compared to the bigger size of elements, and

- Number of elements: The cost is proportional to the number of elements.

The explicit dynamics method was originally developed to analyze high-speed dynamic events, such as the crash problem at hand, where many small increments are required to obtain a high-resolution solution. As rapidly as the load is applied, the structure has to deform. Accurate tracking of stress waves through the metal sheet is important for capturing the dynamic response. Since stress waves are related to the highest frequencies of the system, obtaining an accurate solution requires many small time increments. By using the explicit method, also contact conditions are formulated more easily because this method can readily analyze problems involving complex contact interaction between many independent bodies.

The central difference method, like most explicit methods, is conditionally stable. This means that if the time step, 't' becomes too large to exceed a critical time step, 't' then the computed solution will become unstable and might grow without limit. The critical time step 't' should be the time taken for the fastest stress wave in the solids/structure to cross the smallest element in the mesh. Therefore, the time steps used in the explicit methods are typically 100 to 1000 times smaller than those used with implicit methods, outlined in the next subsection. The need to use a small time step, and especially its dependence on the smallest element size, makes the explicit codes lose out to implicit codes for some of the problems, especially for those of slow time variation (Quek and Liu, 2003) .

In the explicit solver, the central difference method is used to integrate the equations of motion explicitly through time, using the kinematic conditions at one increment to calculate the kinematic conditions at the next increment. That means the accelerations calculated at time t are used to advance the velocity solution to time $t + \frac{\Delta t}{2}$and the displacement solution to time $t + \Delta t$as described in the following, Figure 31. At the beginning of the increment the programme solves for dynamic equilibrium, which means solving

$$M\ddot{u}_n = F_n - Ku_n \tag{4-26}$$

for the nodal acceleration $\ddot{u}$ at the beginning of the current increment at time t. One then gets for the acceleration at time t:

$$\ddot{u}_n = M^{-1}(F_n - Ku_n) \tag{4-27}$$

This equation is easy to compute, since the explicit formula always uses a diagonal mass matrix (lumped mass approach). The acceleration of any node is determined completely by its mass and the net force acting on it. There are no equations to solve simultaneously. The accelerations are integrated through time using the central difference method, which calculates the change in velocity assuming that the acceleration is constant. The change in velocity is added to the velocity from the middle of the previous increment to determine the velocities at the middle of the current increment:

$$\dot{u}_{n+1/2} = \dot{u}_{n-1/2} + \Delta t_n \ddot{u}_n \tag{4-28}$$

The velocities are integrated through time and added to the displacements at the beginning of the increment to determine the displacements at the end of the increment:

$$u_{n+1} = u_n + \Delta t_{n+1/2}\dot{u}_{n+1/2} \tag{4-29}$$

Since the method integrates constant accelerations exactly, the elements are supposed to be quite small, such that the accelerations within an increment are nearly constant. The element stresses and consequently the internal forces are determined by applying material constitutive relationships on the determined element strains.
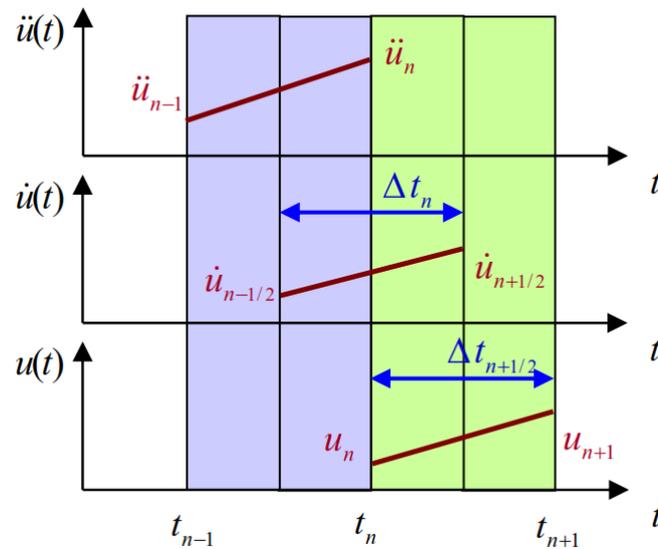
Figure 31: The central difference method, (Duddeck, 2008a).

The explicit approach is referring to the end of the increment and is based exclusively on the displacements, velocities and accelerations at the initial condition of the increment (Duddeck, 2008a).

- Internal and external forces are calculated at each point node and a nodal acceleration is computed by dividing the nodal mass.
- Solution is advanced by numerical integration of the above computed acceleration in time.
- Typically requires many relatively inexpensive time steps.
- Suitable for dynamic simulations such as impact and crash.

4.3.4. Stability Limit

The stability limit dictates the maximum time increment. For computational efficiency it is important to choose a time increment as close as possible to the stability limit, but without exceeding it. It is defined in terms of the highest frequency in the system ω_{max}, by the expression in (ABAQUS)

$$\Delta t_{stable} \leq (\sqrt{1 + \xi^2} - \xi) \qquad\qquad (4\text{-}30)$$

Where ξ is the fraction of critical damping in the mode with the highest frequency. According to (ABAQUS), it can be shown that the highest element frequency determined on an element-by-element basis is always higher than the frequency in the assembled finite element model. Due to the minor complexibility, it is thus more computationally feasible to calculate the stability limit based on an element-by-element estimate, where it can be defined by using the element length (L_e) and the wave speed (C_d) as a property of a linear elastic material with a Poisson's ratio of zero:

$$\Delta t_{stable} \approx \frac{L_e}{C_d} \qquad\qquad (4\text{-}31)$$

$$C_d = \sqrt{\frac{E}{\rho}} \qquad\qquad (4\text{-}32)$$

This estimate for Δt is only approximate and in most cases is not a conservative (safe) estimate. In general, the actual stable time increment chosen by ABAQUS/Explicit will be less than this estimate by a factor between $\frac{1}{\sqrt{3}}$ in a two-dimensional model and between $\frac{1}{\sqrt{2}}$ in a three-dimensionalmodel. The time increment chosen by ABAQUS/Explicit also accounts for any stiffness behavior in a model associated with penalty contact.

4.3.5. Computational Time

Despite advances in the computer industry, computer resources can still be one of the decisive factors on how complex a finite element model can be built. The CPU time required for a static analysis can be roughly estimated using the following simple relation (called the complexity of a linear algebraic system) (Liu, 2009):

$$\mathbf{t_{CPU}} \propto \mathbf{n_{dof}^{\propto}} \tag{4- 33}$$

where n_{dof} is the number of total degrees of freedom in the FE equation system, and a is a constant in the range of 2.0 to 3.0, depending on the different solvers used in the FEM package and the structure of the stiffness matrix. One of the very important factors that affects$\propto$ is the bandwidth of the stiffness matrix, as illustrated in Figure 11.2.
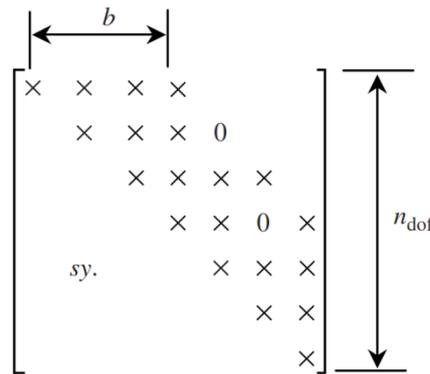
Figure 11.2. Schematic of the structure of the stiffness matrix.(Quek and Liu, 2003).

A smaller bandwidth leads to a smaller value of$\propto$, and hence a faster computation. The bandwidth can be changed even for the same FEM model by changing the global numbering of the nodes. Therefore, tools have been developed for minimizing the bandwidth through a re-numbering of nodes. Most FEM packages are equipped with one or more such tools. All the user needs to do is use the tool to minimize the bandwidth after meshing the problem domain. This simple operation can sometimes drastically reduce the CPU time. A very simple method for minimizing the difference of nodal numbers, and hence the bandwidth, can be found in (Liu, 2009).

Equation (4-33) clearly indicates that a finer mesh with a large number of Degrees of Freedom (DOFs) results in an exponentially increasing computational time and analysis should be aimed as;

I. To create an FEM model with minimum DOFs by using elements of as low a dimension as possible, and

II. To use as coarse a mesh as possible, and use fine meshes only for important areas. These have to be done without scarifying any accuracy in the results.

An evaluation between CPU time and model size for both approaches explicit and implicit is illustrated in Figure 32. Although for small models, the implicit method more convincing and for larger models the explicit method becomes is more cost attractive. This is even more suitable when disk storage and memory requirements are taken into consideration. As a general rule, large models are mainly controlled by the available memory and disk storage instead of the required computational time when using the implicit approach(Van der Vegte and Makino, 2004).

Implicit approach: The computational cost as a function of model size is rather difficult to predict, experience shows that for many problems, the CPU time is approximately proportional to the square of the number of degrees of freedom.

Explicit approach: The computational cost is proportional to the number of elements and roughly inversely proportional to the smallest element dimension.
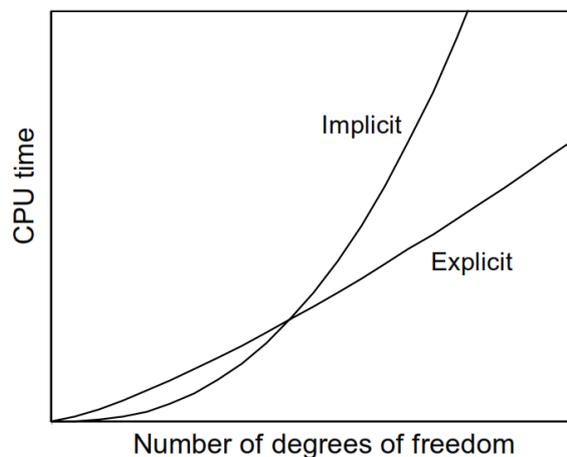
Figure 32: CPU time versus model size for the explicit and implicit methods (Van der Vegte and Makino, 2004).

4.3.6. Meshing

4.3.6.1. Element Type

In (ABAQUS, Systèmes, 2010), the elements are identified by their name. Element name, the type of element, and number of node are identified for each kind of element type. For example, the shell element name in ABAQUS starts with the letter "S". Furthermore, the axisymmetric shell begins with the letters "SAX". The 4-node shell element is called S4R.

ABAQUS/Explicit evaluates the material response at each integration point in each element. ABAQUS uses the letter R at the end of the element name to label reduced integration elements. For shell and beam elements, the cross-section of the element is integrated numerically so that nonlinear response can be computed accurately when needed. In this simulation, we used S4R. Element type S4R is a uniform strain 4-node shell element for three-dimensional problems. Shell element formulation follows the so-called 'degenerated' concept, which is closely related to Reissner-Mindlin theory for plates and shells.

Shell elements are based on the standard kinematical assumptions of shell theory:
  i.   Displacements in the shell are described by translations and rotations of mid-surface geometries.
  ii. Stresses perpendicular to the shell surface are neglected.

In shell theory, only two independent rotations are defined and rotation around the shell normally exists. For the shell finite elements used in explicit time integration, low order shape functions are preferred due to the time step limitations. The only element to be able to be used properly is the uniformly integrated element (S4R), which is very cost effective (Schweizerhof et al., 1992b).

70

4.3.6.2. Meshing Density

To reduce the DOFs, the varying density technique creates meshes along the model used. The mesh only needs to be finer in areas of importance, such as areas of interest, and expected zones of stress concentration, such as at corners, holes; slots; notches; or cracks. Hence, the regions that are not critical are set as coarse mesh. In using FEM packages, control of the mesh density is often performed by using so-called mesh seeds. The mesh seeds are created before meshing after the geometry has been created. (Quek and Liu, 2003).

4.3.6.3. Element Distortion

It is not always possible to have regularly shaped elements for irregular geometries. Irregular or distorted elements are acceptable in the FEM, but there are limitations, and one needs to control the degree of element distortion in the process of mesh generation. The distortions are measured against the basic shape of the element, which are;

  i. Square ⇒Quadrilateral elements
  ii. Isosceles triangle ⇒Triangle elements
  iii. Cube ⇒Hexahedron elements
  iv. Isosceles tetrahedron ⇒Tetrahedron elements

Five possible forms of element distortions and their rough limits are listed as follows (Quek and Liu 2003):

1. Aspect ratio distortion (elongation of element) (Figure 33a).
2. Angular distortion of the element (Figure 33b), where any included angle between edges approaches either 0 or 180 degrees (skew and taper).

3. Curvature distortion of element (Figure 33c), where the straight edges from the element are distorted into curves when matching the nodes to the geometric points.

Most FEM package preprocessors provide a tool for analyzing the element distortion rate after the mesh is generated. A report of the distortion rates will be generated for the analyst's examination. Users only need to redefine the distorted mesh before submitting the job.
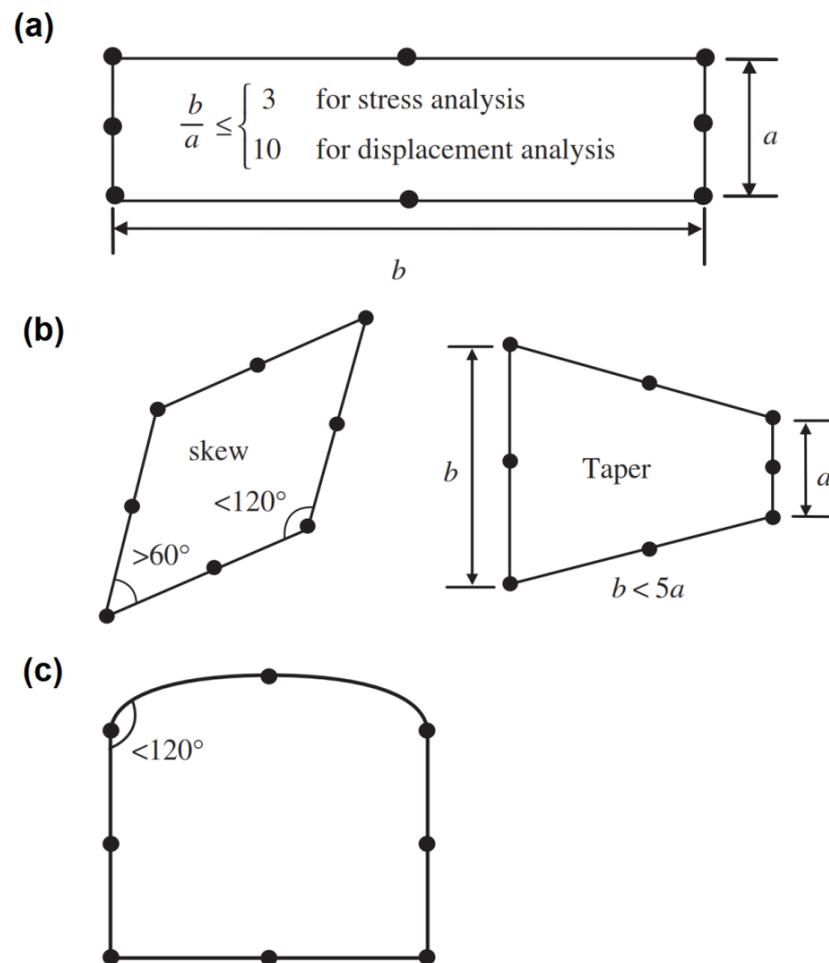
Figure 33 : Mesh Element distortion(a) Aspect distortion, (b) Angular distortion and (c) Curvature distortion(Quek and Liu, 2003).

4.3.7. Contact

By default, the contact pairs specified are added to the list of active contact pairs in the model. Initial penetrations should be avoided for contact pairs introduced after the first step, to avoid large nodal accelerations and severe element distortions which can result, and adjusting initial surface positions and specifying initial clearances for contact pairs in ABAQUS/Explicit is necessary. Redefining a contact pair by deleting it and adding it in the same step can also lead to problems, because the "state" information associated with the slave nodes in contact will be reinitialized. For example, a penalty contact slave node with a penetration past the mid-surface of a double-sided master surface would be allowed to pass through the master surface if the contact state were reinitialized.

Contact modeling in ABAQUS/Explicit was based on the concept of surfaces coming into contact with each other. The user must define surfaces based on the elements in the model and then define interactions between the surface or surfaces. Between the surfaces of almost any type, contact can be defined: a deformable surface can contact a rigid surface or another deformable surface, deformable surfaces can contact a rigid itself, or a set of nodes can contact a deformable or rigid surface.

4.3.8. The Element Characteristic length

Finite Element Analysis is an approximate solution technique, the accuracy of FEA analysis depends on a number of factors which include the mesh density. When considering material failure such as rupture, where the material will exhibit strain-softening and necking characteristics, mesh density can be an important factor for prediction of failure.

The damage evolution model included in the (ABAQUS) program allows the analyst to compensate for the strain softening effect that occurs in the

material between necking and rupture. In the context of an elastic-plastic material with isotropic hardening, the damage manifests itself in two forms: an effective reduction of the material yield stress coupled with degradation of material stiffness. Figure 34 represents the damaged stress-strain response, while the dashed curve is the response in the absence of damage. (ie. the true stress-strain curve.).
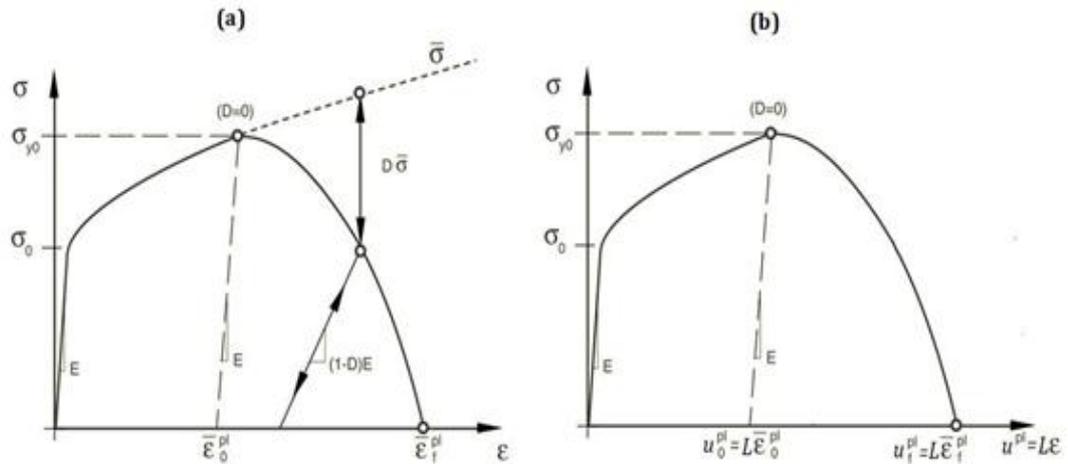
Figure 34: (a) ABAQUS documentation stress-strain curve with progressive damage degradation. (b) Stress–strain curve with progressive damage degradation dependent on mesh density (Yu and Jeong, 2010).

Material failure is normally expressed in terms of stress-strain relationships, see Figure 34a and b. During loading the material will undergo a damage processes which will follow a damage evolution law where damage will start to initiate at point D=0 and full damage degradation will occur when D reaches a maximum where $D_{max} \leq 1$. The equivalent plastic stress and strain at the onset of necking are denoted by σ_{y0}, $\bar{\varepsilon}_0^{pl}$ respectively where $\bar{\sigma}$ is a true stress curve in absence of damage or fully plastic condition and σ_0 is the yield stress. Finally, elements which fail are removed from the model when they satisfy the maximum damage evolution law as $D_{max} \leq 1$.

The evolution of the damage variable with the relative plastic displacement can be specified in tabular, linear, or exponential form. Instantaneous failure

will occur if the plastic displacement at failure, u_f^{pl}, is specified as 0; however, this choice is not recommended and should be used with care because it causes a sudden drop of the stress at the material point that can lead to dynamic instabilities.

Throughout this study a linear softening law was adopted for simplicity. The value of strain for the onset of damage is estimated as being $0.5\varepsilon_f$ this is a typical value which reflects the ultimate strength of steel before softening starts to take place. The softening or evolution of the damage is controlled by the gradient of material damage, where 0 is the sudden deletion of an element after FLD failure criterion is satisfied and 1 is fully plastic behavior (no elements deletion). The softening of the material will occur when the damage criteria is applied to initiate the local necking before rupture. For the purposes of this study the engineering fracture strain listed in Table1 have been adopted, ε_f = 0.35 and 0.28 for mild steel and high tensile steel respectively.

Additionally some further analyses were run with larger values of rupture strain (0.704) in the true stress/strain relationship modelled in ABAQUS. The results for this analysis demonstrated little effect on the local necking and fracture behavior observed in the analysis.

The available literature as reviewed comes to no real conclusion about the characteristic element length required for solution accuracy, hence the need for mesh convergence studies e.g. (Alsos et al., 2009, Wiśniewski and Kołakowski, 2003, Zhang and Suzuki, 2005). ABAQUS Explicit tries to resolve this problem by introducing an element characteristic length which is related to the element size.

Figure 34b shows the damage evolution law embedded with mesh dependency where u^{pl}, is the fracture work conjugate of the yield stress after the onset of damage (work per unit area of the crack), u_0^{pl} is damage initiation point, u_f^{pl} is fully degraded material where the elements will be removed from the model and L is mesh element characteristic length. The value of damage

evolution is estimated $D=0.5\bar{\varepsilon}_f^{pl}L$ where ε_f is fracture strain and for shell 2D elements, L is the square root of the integration area and for 3D elements, it is the integration of volume in unit meter, where $\bar{\varepsilon}_f^{pl}$ is determined from uniaxial tension tests and assumed to be the same as ε_f in Table 1.

4.3.9. Finite Element Procedure

The FE analysis was performed in ABAQUS explicit using S4R shell elements with general surface contact. Through thickness integration was carried out using Simpson rule with 5 integration points through the thickness. The modeling of the material plastic behavior was carried out using a power law expression as previously discussed in the material characterization section 4.4. The relationship between fracture strain and element size is discussed by various authors (Alsos et al., 2009, Ehlers, 2009a) using a scaling law applied to equation (3), neglecting the effect of strain rate, where the true stress strain curve is modified according to mesh size. (Lehmann and Peschmann, 2002) also use the same method where the material properties are modified using the scaling law where the critical fracture strain is calculated for different mesh sizes.

For the purpose of this study, material properties were generated using equation (4.4) and adopting the values listed in Table 1. The input parameter defining the onset necking using the FLD damage criterion is calculated using equation (4-18). The hardening number is adopted from Table 1 as 0.24, 0.225 and 0.18 for material type A, B and C respectively.

4.4. Summary

This topic has already laid down the information and methods that will be used in later chapter as a basic technique in running FEA analysis. The chapter discussed some aspect of material properties, material failure, solution technique (i.e. implicit and explicit) and some aspects need to be considered for running analysis in order to reduce costs.

This chapter also already affirmed that FLD material damage will be used as a foundation of FEA simulation throughout this thesis and will compare with other material failures in some chapters.

Material properties must be determined experimentally. Careful examination of the properties of most structural materials indicate that they are not isotropic or homogeneous. Nonetheless, it is common practice to use the isotropic approximation for most analyses. In the future of structural engineering, however, the use of composite, anisotropic materials will increase significantly. The responsibility of the engineer is to evaluate the errors associated with these approximations by conducting several analyses using different material properties(Wilson, 2002).

Remember the result obtained from a computer model is an estimation of the behavior of the real structure. The behavior of the structure is dictated by the fundamental laws of physics and is not required to satisfy the building code or the computer program's user manual.

CHAPTER 5: VALIDATION OF NUMERICAL MODELS FOR PENETRATION, COLLISION AND GROUNDING DAMAGE SIMULATION

5.1. Introduction

This chapter will discuss FEA simulation results and compare with available data from experiments to validate the material failure mentioned in chapter 4 that used FLD damage criteria. The analyses consists of penetration damage of stiffened panels with several setup configurations and lateral crushing of simplified buffer bow. An investigation of mesh convergence study is observed to capture better localized stress and rupture prediction point. The FEA results obtained were compared with actual experiment data and FEA results that published in (Alsos et al., 2009) for penetration damage, grounding experiment by Naval Surface Warfare Center, USA, NSWC (Rodd, 1996) and (Endo et al., 2001) for lateral ship bow collision to rigid wall. The scaling of mesh convergence study is established where the effect of FLD_0 in relation to mesh sizes is plotted to reduce CPU time to simulate bigger structures.

5.2. On Resistance of Stiffened Panels to Penetration Damage

A series of experimental tests were carried out by (Alsos and Amdahl, 2009) under quasi-static conditions, which were compared with FEA simulations (Alsos et al., 2009) using both RTCL and BWH damage evolution criteria. Their results are shown below in Figure 37a, b and c alongside those of the present FEA analysis using the FLD damage failure model. The current FEA simulations used an element mesh size of 15mm and only required simple damage input parameters. However the results produced are consistent and reliable when compared to the actual experimental results.

The FEA analysis conducted ignored the strain rate effect, where m=0 and s=0 in equation (4-18). Then the FLD failure model as expressed in equation (5-1)becomes:

$$\varepsilon_1 = \begin{cases} \dfrac{n}{(1+r_\varepsilon)} & \text{if } r_\varepsilon \leq 0 \\ \dfrac{3r_\varepsilon^2 + (2+r_\varepsilon)^2 n}{2(2+r_\varepsilon)(1+r_\varepsilon+r_\varepsilon^2)} & \text{if } r_\varepsilon > 0 \end{cases} \qquad (5\text{-}1)$$

5.2.1. Structure Geometry

The panels identified were manufactured and tested by (Alsos and Amdahl, 2009) in order to provide a simulation and analysis of the grounding scenario (see Figure 35a, b and c). The tests were carried out by laterally forcing an "indenter" to a depth of about 0.25m, as shown in Figure 35d, into the centre of a plate of the size 720 x 1200 x 5mm made from material type from Table 1.
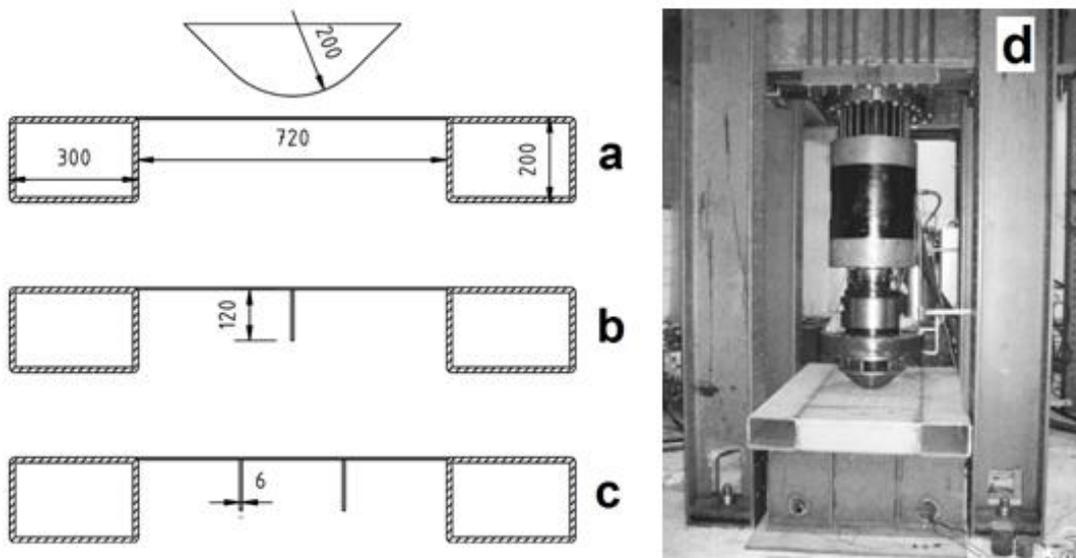
Figure 35: Flat panel, stiffened plate configurations and experimental setup from (Alsos and Amdahl 2009).

The configurations of the structure are as follows:

    a. Penetration of flat panel

    b. Penetration on stiffener of single stiffened panel

    c. Penetration of stiffened panel between two stiffeners.

(a)   **(b)**
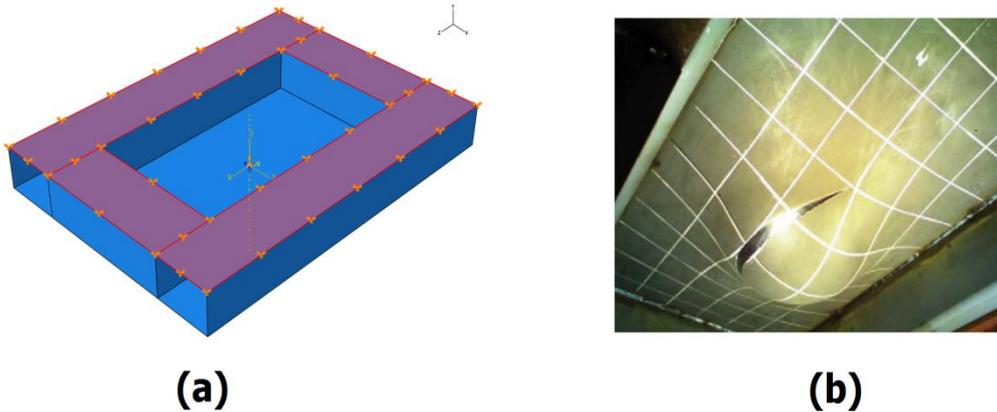
Figure 36: (a) The boundary condition for the penetration of stiffened plate and flat panel. (b) The rupture of flat panel after indentation (Alsos and Amdahl 2009).

For the stiffened panel cases, the plate stiffeners (120 x 6mm flat bars) were made from material Type B from Table 1and were evenly spaced as shown in Figure 35b and c. The 300 x 200 x 12.5mm hollow square frame supporting the test panels was assumed to be fully fixed as shown in Figure 35a. Figure 35d shows the penetration of the "indenter" in the experiment taken from (Alsos and Amdahl, 2009). Both the experiment and numerical simulations were carried out under quasi-static conditions.

5.2.2. Boundary Condition

Referring to Figure 35d, we should be able to determine the boundary condition for the analysis. The indenter was set moving downward and assumed no retraction during indentation and also no movement except in vertical down and up only. The column for the hydraulic press machine is also assumed as a rigid body where no elongation occurred. For the penetration

models, bottom plate that touched the base of the press machine in red color (see Figure 36a) was set as no movement in all directions where the base table is also assumes as a rigid plate.

5.2.3. Mesh Convergence Study

Mesh convergence studies were conducted in order to find the most suitable mesh for use in grounding damage studies for both stiffened panels and double bottom structures. The mesh chosen is always a compromise between the accuracy, computer resources and reasonable computational time.

For this problem, the load was applied in terms of the lateral displacement of the indenter which was applied at a uniform rate of 0.6m/s. When the speed of application of the load was slower than 2m/s (Yamada et al., 2005) or 10m/s (Ehlers, 2009a) then no significant inertia effects are apparent. The penetration depth was set at 0.234 meters and a friction coefficient of 0.3 was used.

The meshes chosen were 35mm, 25mm and 15mm. It was found that the best results for the FLD failure model, in terms of a good correlation with the experimental data from (Alsos and Amdahl, 2009), were achieved with a 15mm mesh size; see Figure 37a, b and c.

Although the results shown in Figure 37a, using a 35mm element gave the best agreement when compared with the experimental values, overall the 15mm element size gives the best correlation when considering all of the simulation results for the different structural models.

It can be observed in Figure 37that, for all mesh sizes, a good correlation is achieved up to where failure begins to occur. The prediction of failure/material rupture is most affected by the mesh size used to solve the problem, and hence mesh size appears to be directly related to the accurate prediction of failure.

It can also be observed in Figure 37that larger mesh sizes result in a delay in the onset of material failure, hence leading to an over-prediction of the maximum force. This is due to strain averaging occurring over a larger element area.
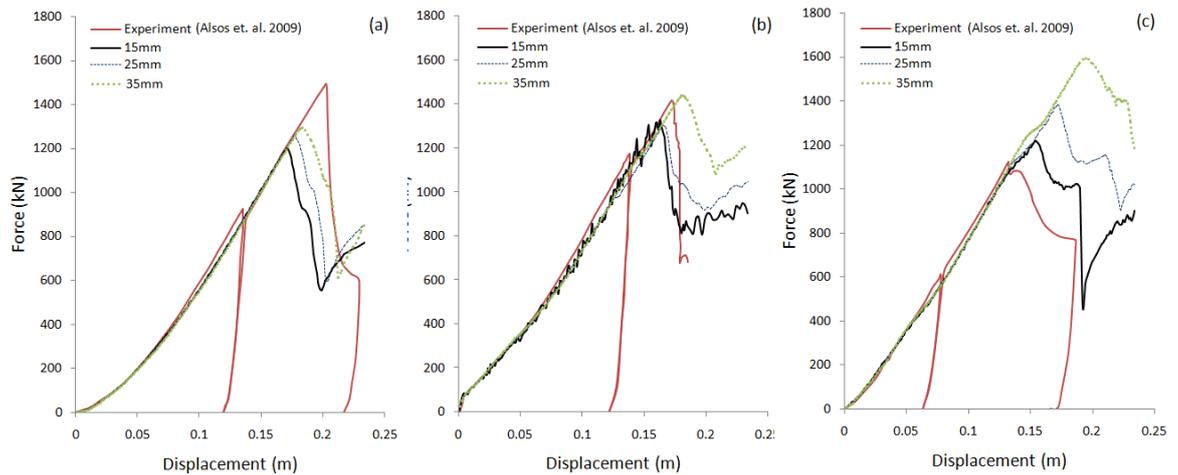
Figure 37: Mesh convergence studies, (a) no stiffener, (b) single stiffener, and (c) two stiffeners.

Mesh convergence studies were carried out for a range of different mesh sizes aligned with element characteristic length. For all of the simulations carried out the friction coefficient was set at 0.3 and the displacement at failure was considered to beε_uL. Where ε_u is ultimate strain, approximately $0.5\varepsilon_f$; ε_f is fracture strain and L is characteristic element length. In the post necking regime the element characteristic size has a significant influence on the accuracy of the results. For shell and 2D elements, L is square root of the integration area and for 3D elements, L is the cube root of the integration of volume.

5.2.4. The Scaling of Mesh Convergence Study

The scaling of mesh convergence study is investigated where large mesh sizes are applied ranging from 5-60mm on stiffened panels to penetration damage. The effect of FLD_0 is observed to predict rupture point as plotted in

Figure 40. The relation of mesh sizes is obtained by setting the value of n that local necking occurs where the point estimated is equivalent to FLD_0 in relation to mesh sizes.

Figure 38, shows the results of the scaling of mesh convergence study where the results are stable compare to Figure 37 that was simulated without the scaling convergence processes. Figure 38a, for un-stiffened panel, shows the converged results of indentation force which closed prediction for almost all sizes of mesh used. Figure 38b, the prediction of single stiffened panel for 60mm mesh, gave the lowest prediction of indentation force compared to other mesh sizes. Figure 38c, for two stiffened panels 5mm mesh projected the lowest result of penetration force and 10mm is close to the experimental result.
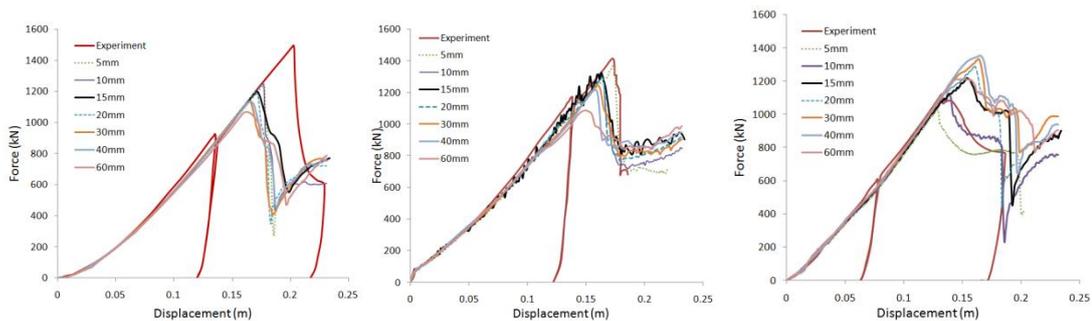
Figure 38: The scaling of mesh convergence study of stiffened panels to penetration damage: (a) no stiffener, (b) single stiffener, (c) two stiffeners.

Overall, the scaling of mesh convergence study gave a better prediction of indentation force and rupture point prediction, compared to without scaling technique. The technique is also coupled with damage evolution that was explained in chapter 4. Damage evolution is adopted from Figure 39 which shows mesh sizes proportional to damage evolution. Figure 39 also indicated that bigger meshes seemed to delay the evolution of damage where 0 is sudden rupture and 1 is fully plastic where no failure occurred in the analysis.
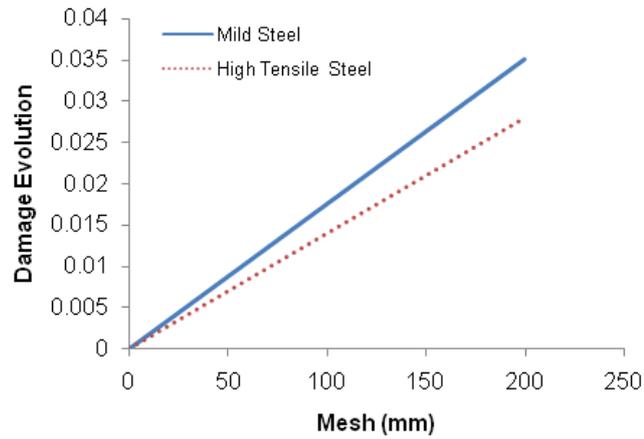
Figure 39: The Damage Evolution.

The results obtained by using scaling technique(AbuBakar et al., 2010) were plotted as element length against FLD0, where FLD0 is the local necking point which intercepts at y-axis when r=1. The results are shown in Figure 40a and b, where Figure 40a is FLD0 curve and Figure 40b shows the comparison of the failure strain trend line with (Ehlers and Varsta, 2009) which gives a good degree of correlation.
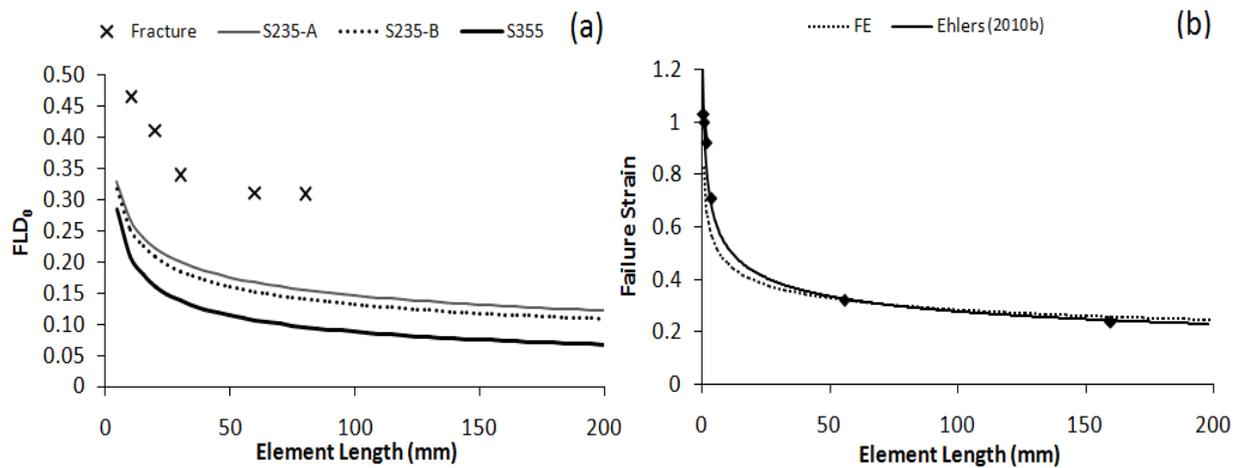
Figure 40: (a) The scaling of Forming Limit Diagram at onset necking versus Element Length (AbuBakar and Dow), (b) The failure strain versus element length.

5.2.5. Penetration of Flat Panel

The force-displacement results for the penetration of the flat panel using different damage criteria are shown Figure 41a and b. The current method using the FLD damage model coupled with the progressive failure model as previously discussed, predicted rupture at a vertical displacement of the penetrator of 180mm. This value is higher than those obtained using the BWH and most RTCL simulations. The BWH failure method predicted rupture at 175mm, which is constant for most element mesh sizes; whereas the RTCL failure method predicted a scattered rupture at 120, 170 and 190mm for mesh sizes of 18mm, 10mm and 5mm respectively. These predictions compare with the value of 200mm obtained in the experiment. The numerical simulations appeared to give a good prediction of rupture initiation when compared with the experimental results. Figure 44a shows the rupture damage predicted by the FE simulation which compares well with the experimental damage levels shown in Figure 36b for this panel. This predicted fracture pattern was constant for all of the failure models ie FLD, RTCL and BWH.
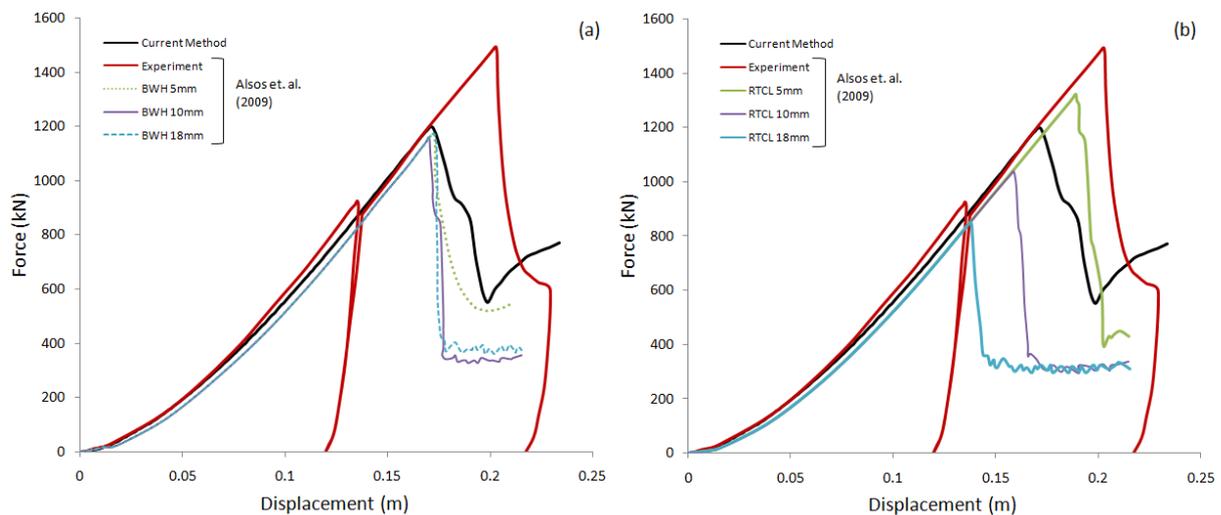
Figure 41: Penetration of flat panel.

5.2.6. Penetration on Stiffener Panel

The force-displacement results for the penetration of a single stiffened panel are shown in Figure 41a and b, where the current simulation predicts rupture at about the same level as the BWH and RTCL failure models. Depending on mesh size, rupture occurred at about 170mm for the current FLD failure method using 15mm mesh, and similar results were obtained for the BWH and RTCL failure models using 10mm mesh. The simulation using the current FLD method gave good agreement with the experimental results leading to the conclusion that a15mm mesh size is likely to be the most effective in this type of simulation using the progressive damage model described previously Figure 41b again shows the rupture damage pattern predicted by the FE solution.
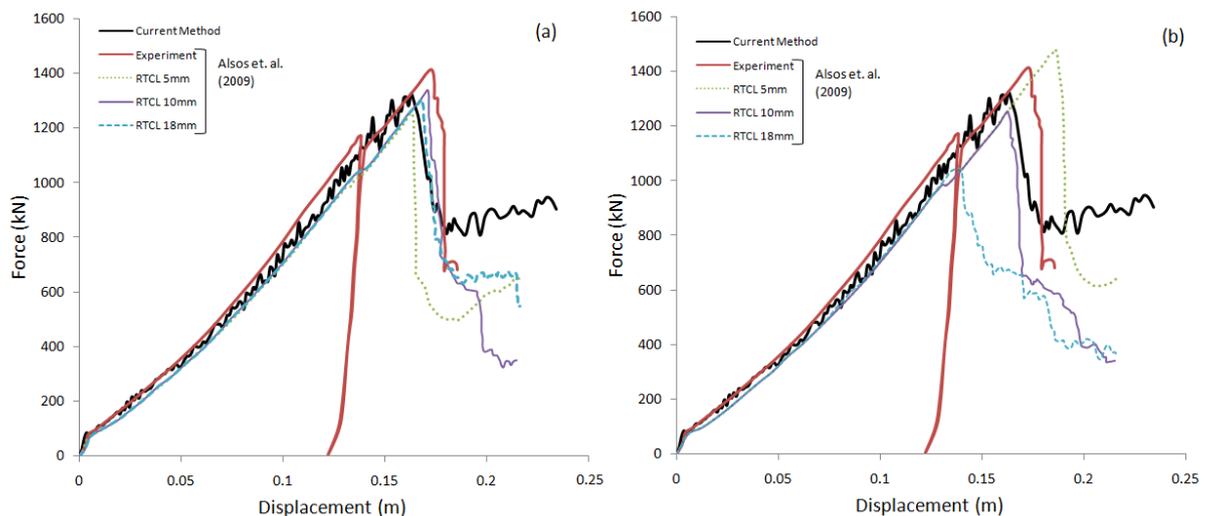
Figure 42: Penetration on stiffener of single stiffened panel.

5.2.7. Penetration of Stiffened Panel Between Two Stiffeners

Force-displacement results are shown in Figure 42a and b. These show curves for the case of the penetration of a stiffened panel between two stiffeners, with graphs of penetrator force vs. displacement comparisons for both RTCL and BWH failure models. The RTCL and BWH models give variable results depending on the mesh size used in the simulations. The figures compare numerical predictions with experiment results for both BWH and RTCL failure models using 5mm and 18mm element mesh sizes respectively.
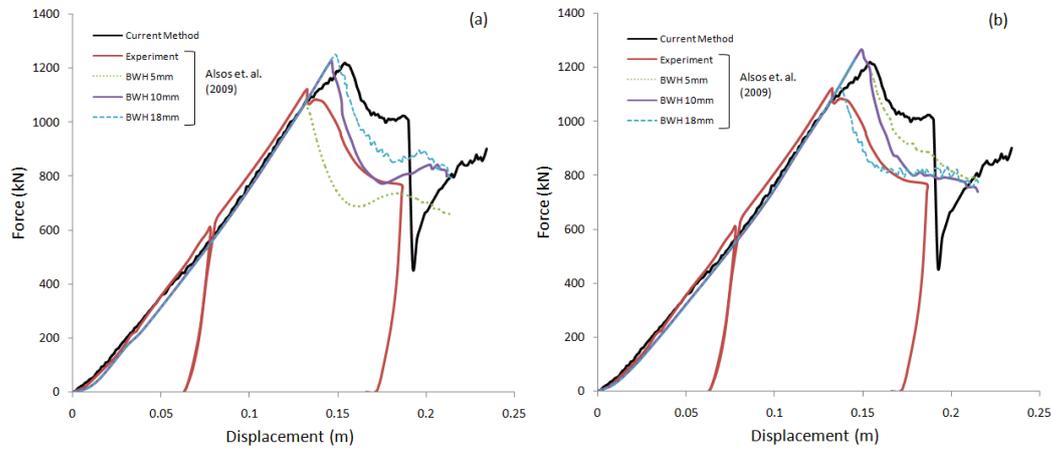
Figure 43: Penetration of stiffened panel between two stiffeners.

The rupture predicted by the current FLD method using the 15mm element size occurs at about 162mm penetration, which compares well with both the BWH and RTCL for 18mm and 5mm element sizes respectively. In the current simulation, as shown in Figure 44c, the stiffeners seem to be tripping in the opposite direction to that observed in the experiment. This could be because the current simulations fail to consider the effects of welding and HAZ on stiffened panels, or it could be caused by slight offsets in the position where the impactor strikes the plating in the experiments.
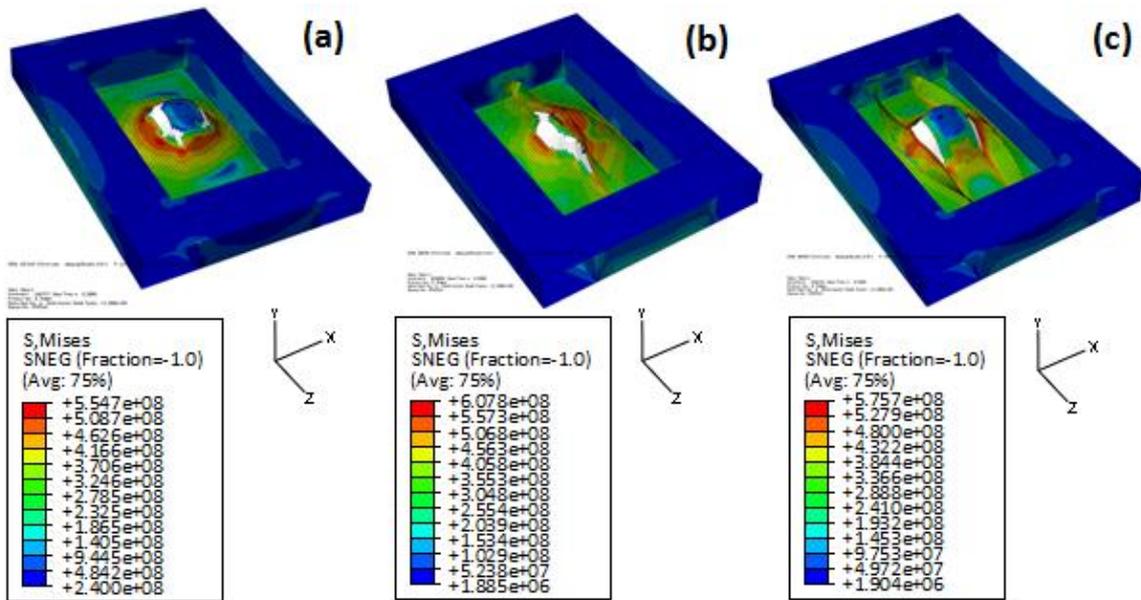
Figure 44: The simulation of resistance of stiffened panels to penetration damage: (a) no stiffener, (b) single stiffener, (c) two stiffeners.

5.3. Grounding Damage Experimental Validation

Material failure modelling as discussed in chapter 4 and the early part of chapter 5 is a crucial aspect of finite element analysis in producing reliable results for collision and grounding studies on steel ships for these cases. Therefore, further validation of the FE modelling technique was carried out using results from experimental studies that were performed at the Naval Surface Warfare Center, USA (Rodd, 1996). The configuration and scantling of the test is shown in Figure 45, Figure 46 and the properties involved are listed in Table 3.
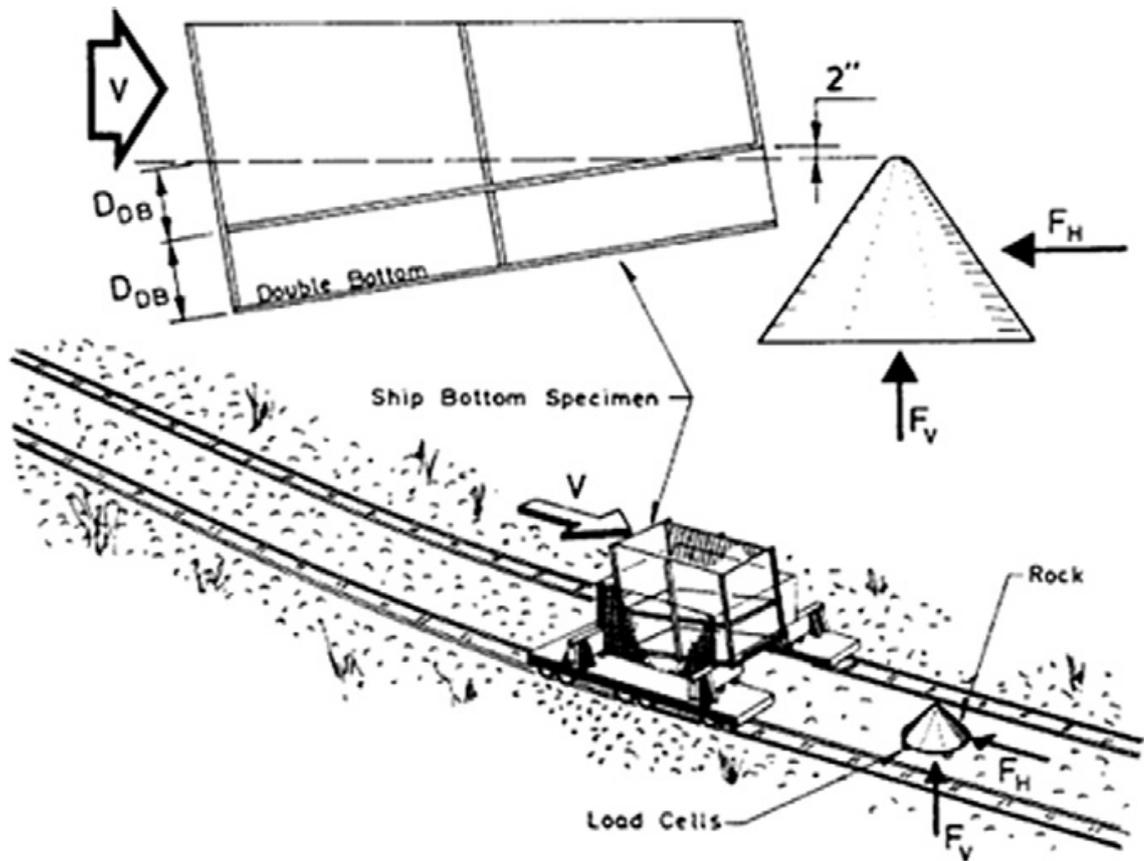
Figure 45: Experiment configuration at the Naval Surface Warfare Center, USA (Rodd, 1996).

Table 3: The setup experiment properties by Naval Surface Warfare Center, USA, NSWC (Rodd, 1996)

Property	Value
Weight of model	223 tons
Model speed (V)	6.173 m/s
Rock tip radius	0.17 m
Rock apex angle	90
Material	ASTM A569
Yield strength	283 MPa
Ultimate strength	345 MPa
Pitch angle (deg)	3.38
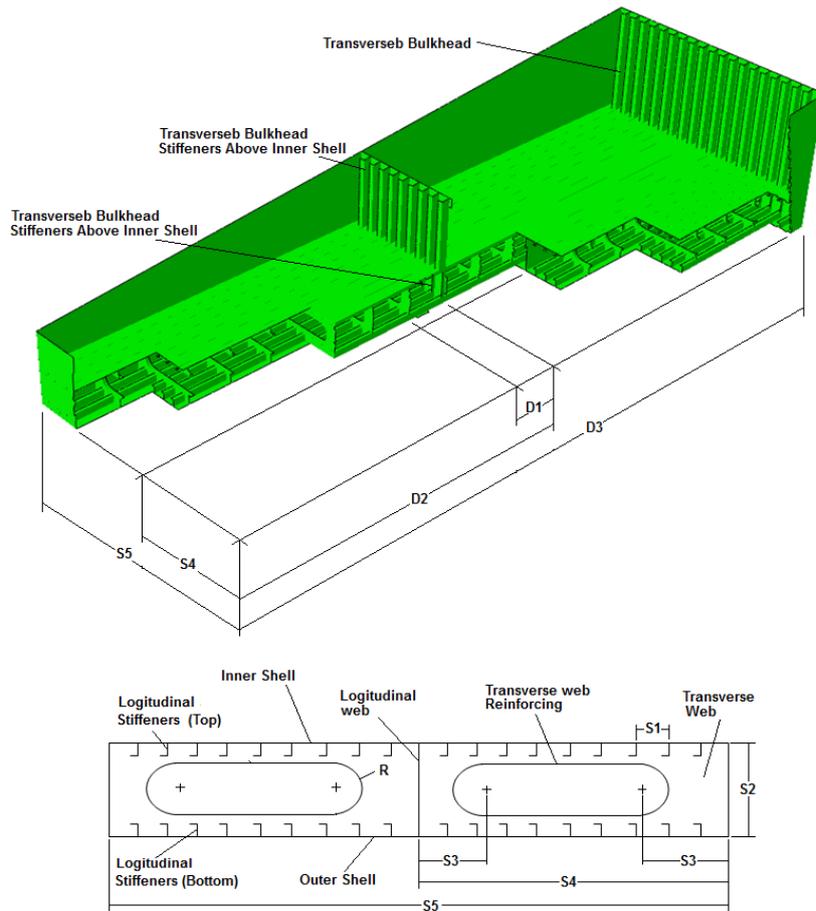
No	Item	Type	Size (mm)
1	Transverse Bulkhead - stiffener Above Inner Shell	L	8.9x5.1x3
2	Transverse Bulkhead - stiffener Below Inner Shell	FB	3.8
3	Longitudinal Stiffeners (bottom)	L	68.95x31.75x1.83
4	Longitudinal Stiffeners (Top)	L	34.92x34.92x2.59
5	Transverse Web - Reinforcing	FB	4.76x38
6	Transverse Bulkhead	Plate	6
7	Longitudinal web	Plate	2.3
8	Transverse Web	Plate	1.63
9	Outer Shell	Plate	3
10	Inner Shell	Plate	3
11	D1	-	160
12	D2	-	3600
13	D3	-	7320
14	S1	-	130
15	S2	-	330
16	S3	-	370
17	S4	-	1270
18	S5	-	2540
19	R	-	102

Figure 46 : The scantling of NSWC grounding Structure.

5.3.1. Simulation Results

The material employed for the finite element study is S235JREN10025 (B), where the strain hardening parameters used were 0.225 for FEA and 0.22 for the calculations carried out by (Simonsen, 1997a). The FE results were compared with these of the experiment carried out by (Rodd, 1996)and the calculations by (Simonsen, 1997a)and (Cerup-Simonsen et al., 2009) FE simulation which gave a very good correlation as shown in Figure 47.

Figure 48 shows the actual damage to the structure during the experiment and Figure 49shows the rupture of the structure from FEA using 15mm mesh. The figures show significant levels of tearing of the outer shell, inner shell and longitudinal bulkhead in both the FEA simulation and the experiment.

90

Figure 49 shows the damage of the grounding structure, comprise of the bottom structure includes internal structure, inner shell, outer shell, top longitudinal stiffeners and bottom longitudinal stiffeners. The observation of the FE simulation results found that there were two main categories of damage dictated in the processes, which are; rupture and plastic failure due to cripple and folding of structure members.
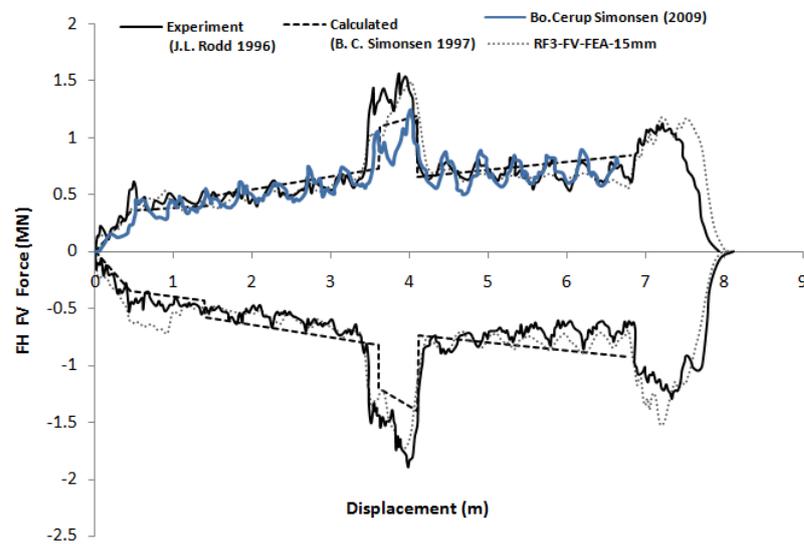
Figure 47: Force displacement of NSWC1 model by Naval Surface Warfare Center, USA, (Simonsen, 1997a, Rodd, 1996).

The rupture mainly occurred at the inner shell, outer shell and longitudinal bulkhead perpendicular to the strike by the rock in vertical and horizontal direction of the grounding structure movement. The plastic failure occurred at longitudinal members which rock strike to the parallel of the longitudinal members setting which allow the members to displace and deformed instead of tearing and cutting by rock. The details of the plastic and rupture failure can be seen in Figure 48 and Figure 49.
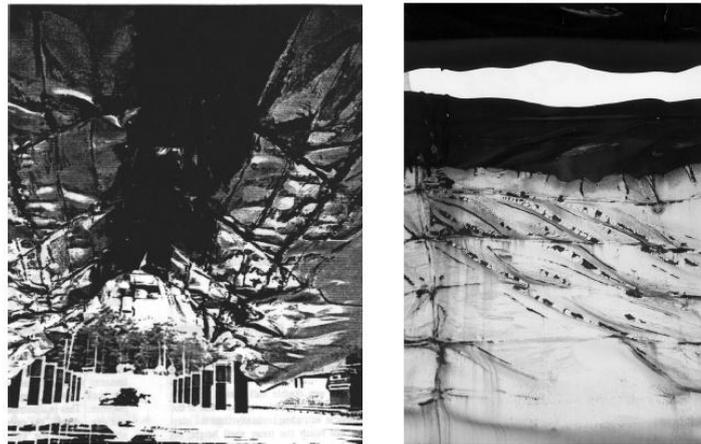
Figure 48: Experimental results from the Naval Surface Warfare Center, USA (Rodd, 1996, Simonsen and Pedersen, 1997).
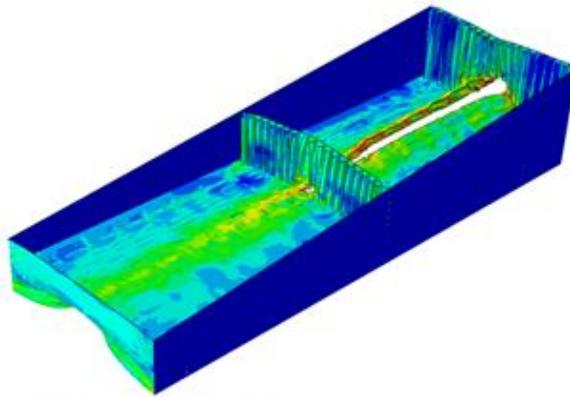
Damage Structure
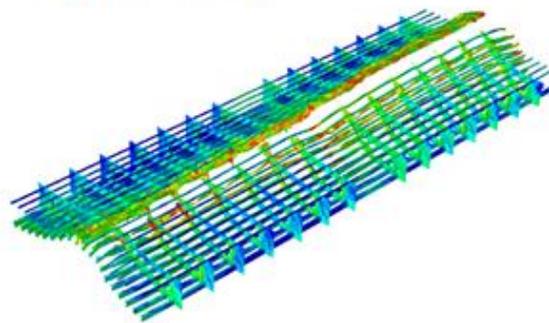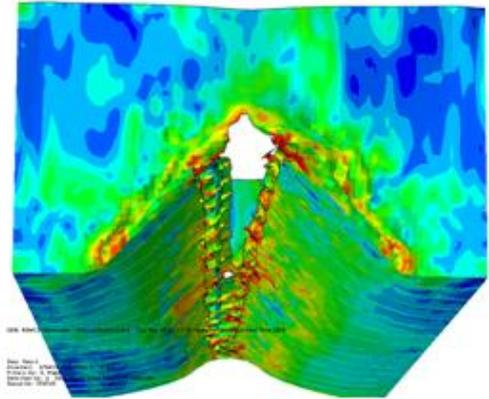
Internal Structure
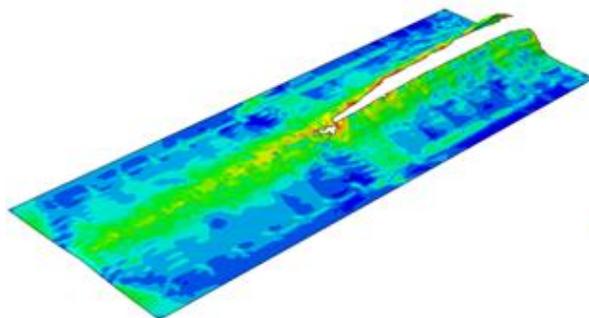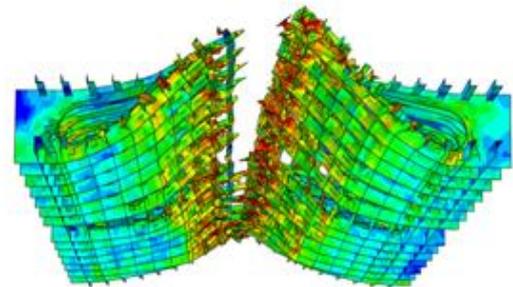
Inner Shell (Top)
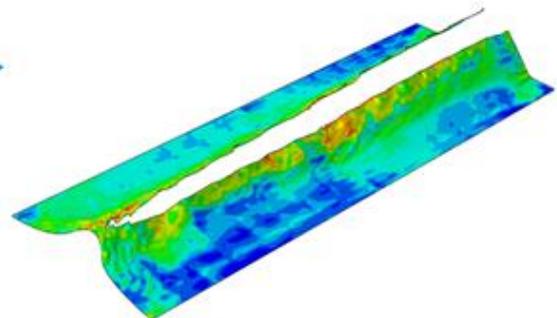
Outer Shell (Bottom)
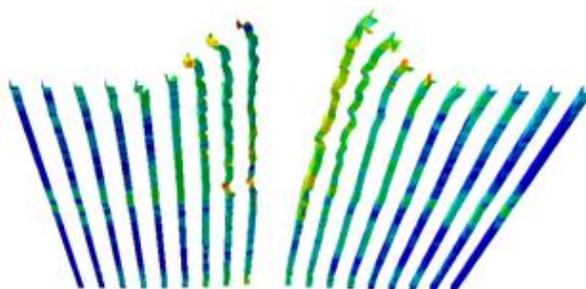
Logitudinal Stiffeners (Top)
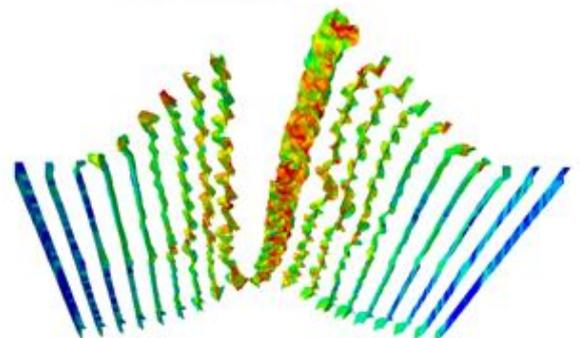
Longitudinal Stiffeners (Bottom)

Figure 49: The damage of grounding structure

5.4. Lateral Crushing of Buffer Bow

The simulation of lateral crushing of buffer bow using an experimental model used in a research project by ASIS launched in 2001. The project was sponsored by the Japanese Ministry of Land Infrastructure and Transport (MILT). The project was executed by the National Maritime Research Institute (NMRI) using several types of models. Due to the limited information published, only one structure model is used for the simulation analysis of lateral crushing (see Figure 50 and Figure 51).

5.4.1. Structure Geometry

The structure model was adopted from (Yamada and Endo, 2005). The model structure (see Figure 50) is in the form of conical shape and consists of:

i)   T- ring frame : 300 x 7mm and 100 x 10mm

ii)   Bulkhead : 7mm

iii)   Shell : 10mm

iv)   Side ring : 10mm
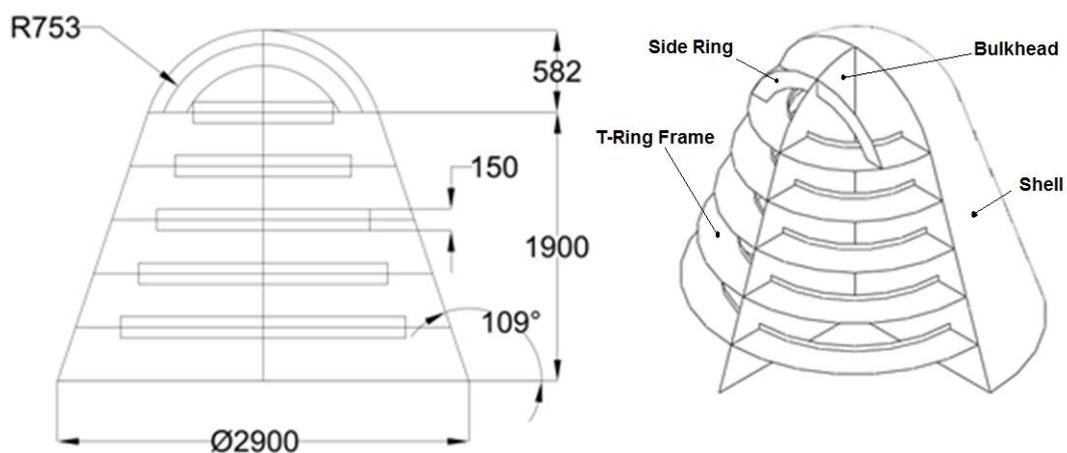
Figure 50: (a) The Schematic of simplified model of ship bow.

The material properties used in the experiment are combined from two batched of steel grades where yield stress = 226MPa, 361MPa, Ultimate

Strength=322MPa, 451MPa and fracture strain= 0.333, 0.283 for all parts except for shell respectively. In the simulation analysis the properties in Table 1 are adopted, using B-type steel for shell and others using A-type steel.
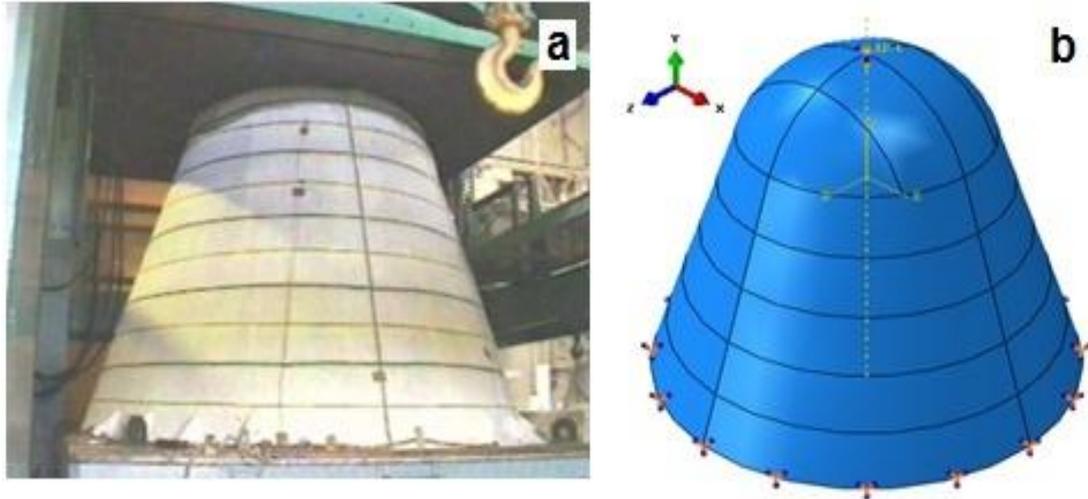
Figure 51: (a) The experimental setup (Yamada and Endo, 2005) (b) the boundary condition.

Figure 51a shows the experimental setup and Figure 51b shows boundary condition for simulation purposes where red marks are set at fixed in all directions. The simulation used 40, 50 and 60mm meshes. The chosen meshes are to observe the convergence of the result produced using damage evolution in Figure 39 and material failure in Figure 40 for larger meshes. The focus of the simulation was to use larger meshes. This is because the large mesh is a main critical concern when analyzing big structures which are able to reduce significantly the cost of analysis in terms of machine, CPU time and accuracy.

5.4.2. Results

Figure 52shows the comparison of experimental and simulation results from (Yamada and Endo, 2005) and FEA using damage evolution from Figure 39 and material failure adopted from Figure 40. The simulation of crushing speed is 5 m/s taken from (Yamada and Endo, 2005) simulation results. (Yamada

and Endo, 2005) running several simulation speeds and found that there was no significant effect of different speed on the results produced if the speed was less than 5m/s.

Figure 52a, b and c show the comparison of experimental and FEA results of (Yamada and Endo, 2005) simulation with current FEA approach using 40, 50 and 60mm mesh. The current FEA results generated a higher peak of crushing force due to a higher strength grade of steel being employed, compare to the experiment. It was found that the current FEA provided a balance and satisfactory results for mesh 40, 50 and 60mm where crushing force was approximately similar to the pattern is generated.

This phenomenon is shown in Figure 52d where the convergence results for different sizes of mesh was achieved. Figure 53 shows the phase of damage of simulation processes due to lateral crushing force against displacement of the crushing plate. The damage is mainly dictated by the plastic damage instead of rupture due the structure setup.

The FEA simulation by (Yamada and Endo, 2005) produce a tender curve of crushing force compared to experimental results at displacement 0-0.3m, this phenomenon occurs when soft or lower values of true stress-strain curve are deployed. As for comparison, the FEA results produced from (Yamada and Endo, 2005) and current FEA approach are closer to the experimental results when averaging the crushing force generated. The starting of lateral force shows very good correlation from 0 - 3.5m displacement where all meshes followed the same path compared to current FEA and experimental results.
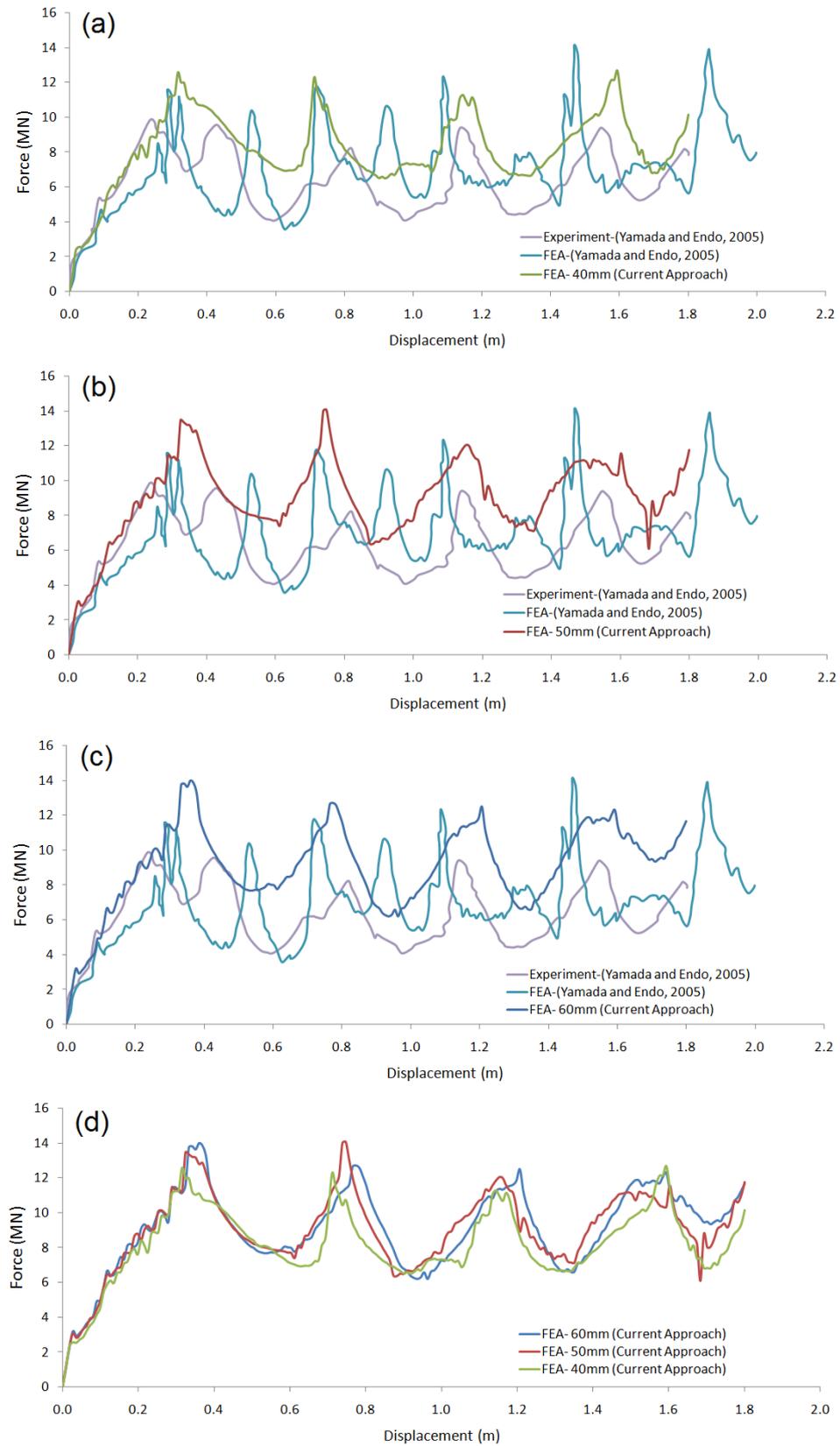
Figure 52: The lateral crushing force.

Time = 0.000s, Displacement = 0.000m

Time = 0.117s, Displacement = 0.585m

Time = 0.963s, Displacement = 0.963m

Time = 1.341s, Displacement = 1.341m

Time = 1.728s, Displacement = 1.728m
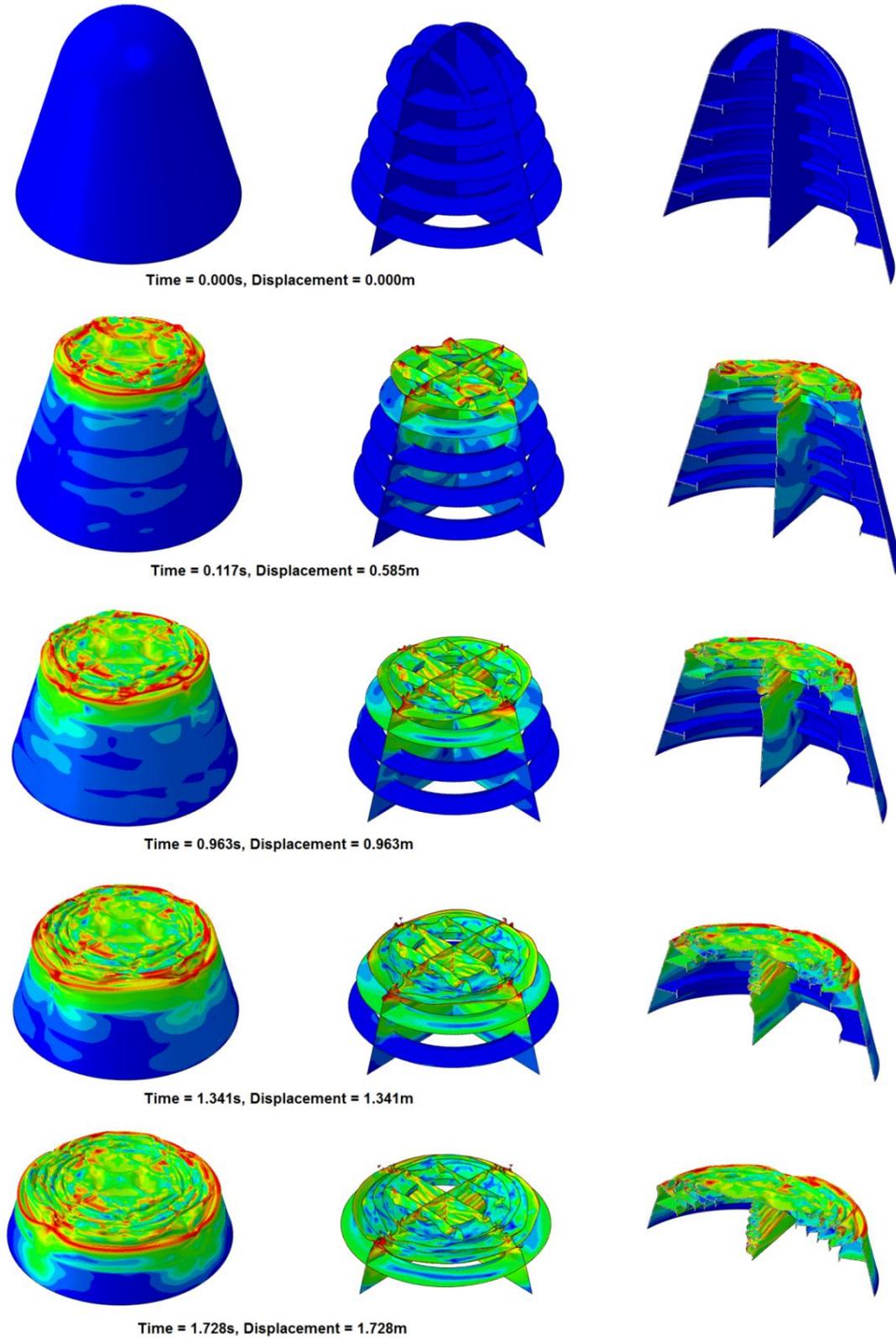
Figure 53 : The phase of bow damage.
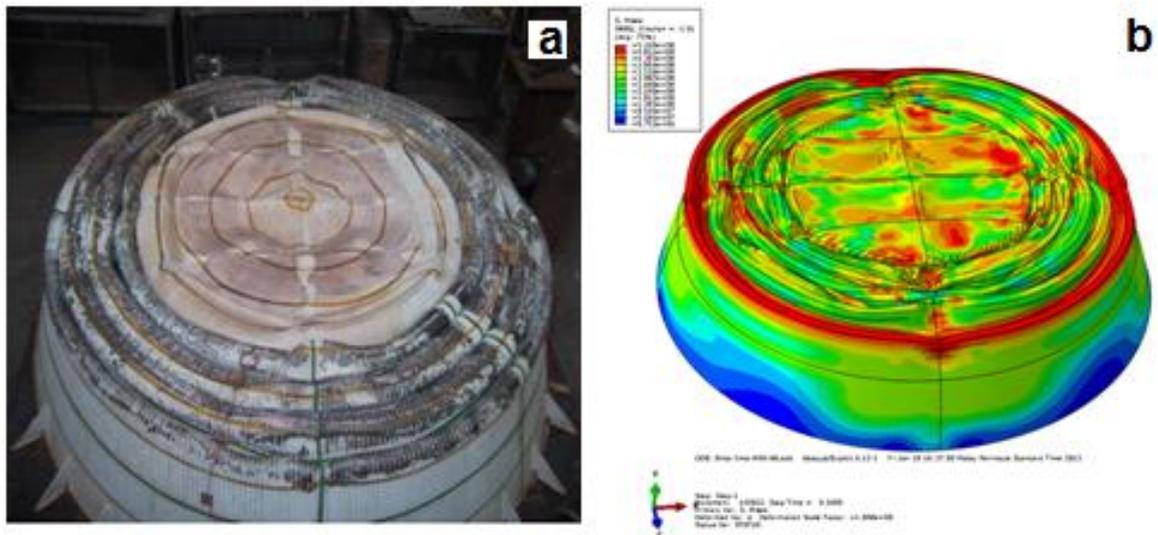
Figure 54: (a) The experimental result(Yamada and Endo, 2005) (b) The FEA result.

Figure 54a and b show the experimental and simulation results respectively. The dark color in Figure 54a and red color in Figure 54b is where the residual stress is concentrated after the crushing press. Both figures produce a similar collapse pattern where the collapse prediction using the current FEA method is very promising. The failure of the structure is dominated by plastic failure due to the structure folding on each other during the crushing processes and seemingly a smaller amount of rupture occurred at critical stress concentration which is at the welding area only for certain areas.

5.5. Summary

As is normal in FEA, the accuracy of the solution depends on the element type and mesh size. Given the limitations of the element formulations, finer meshes normally produced more realistic and accurate results. This is because a finer mesh usually gives a better representation of stress concentrations and also gives a better prediction of the strain in the element, hence providing a better prediction of the onset of failure.

In the stiffened panels numerical simulations this was not always the case. For the RTCL damage criterion, the finer mesh produced less accurate results than the coarser mesh in almost all the simulations carried out when compared with experimental results. The current FLD failure criteria and the BWH criterion produce consistently similar results, and roughly finer meshes give better correlation with experimental results as shown in Figure 37 and Figure 38.

The comparisons between numerical simulations and experimental results in this study are obviously valid for the mesh chosen and the material and rupture model used. Much more work needs to be carried out before any conclusion can be made about the applicability to other types of simulation.

It is easy for researchers to produce accurate results from numerical simulations when the answer we are trying to achieve is known. The mesh density can be varied as well as the modelling parameters until reliable results are achieved. Overall the current method demonstrates good convergence and a good correlation when compared to experimental results.

The attraction of the FLD approach to modeling material rupture is that it is very simple to construct the material failure diagram, which can account for both local necking and material rupture based on the simple tensile testing of materials.

CHAPTER 6: DOUBLE BOTTOM OF GROUNDING DAMAGE

6.1. Introduction

In the past, most studies of collisions and grounding were carried out using a combination of mathematical and experimental approaches. Since the late 1990s (Kitamura, 2002) the rapid progress of computer technology has made large-scale finite element analysis (FEA) practicle, while further progress in analytical methods has been relatively slow. In order to meet the increasing demands from the shipbuilding industry for reliability and cost efficiency, FEM approaches are now applied more often in the direct quantitative estimation of crashworthiness and also for the validation and verification of simplified analytical methods.

Previous studies have used either theoretical, experimental on numerical approaches. Currently there are a range of different approaches and codes available on the market that are capable of predicting damage to ship structures during grounding. These approaches include damage modelling, such as the Forming Limit Diagram (FLD) (Keeler and Backofen, 1963a, Jie et al., 2009) The Rice–Tracey and Cockcroft–Latham (RTCL) model (Alsos and Amdahl, 2007, Alsos et al., 2009), The Bressan, Williams and Hill (BWH) model (Alsos et al., 2008, Alsos et al., 2009) as well as other approaches. In this analysis the forming limit diagram method was used as a model of material failure for dynamic loading using the properties described below.

The present analysis is focused on grounding damage of double bottom structure and was divided into two parts. Firstly the analysis of vertical grounding to a typical double bottom application using the same material failure model as discussed in previous chapters and secondly the analysis was extended longitudinal movement along the compartment. The result is compared to available data from (Samuelides et al., 2007; Zilakos et al., 2009) that looking at the fully plastic and rupture effects of the material employed.

6.2. Grounding Damage of Double Bottom Structure

The use of FEA in crashworthiness analysis for double bottom structures has been considered by various authors (Amdahl and Kavlie, 1992, Naar et al., 2002, Wiśniewski and Kołakowski, 2003). Most of these studies use using both coarse and fine mesh densities to demonstrate convergence of results. Lately, (Samuelides et al., 2007a, J . Amdahl et al., 2009) carried out the analysis on a similar structure, but using flat bar stiffeners instead of angle bar stiffeners on the outer and inner shell of the double bottom, as used in the current model. However, those simulations did not consider rupture failure in the model, but instead only looked at the extreme condition of the strength of the structure using fully plastic deformation prediction.

In the current simulation, both Von-Mises plastic deformation and rupture damage models were considered when investigating vertical grounding and longitudinal crushing along the compartment. In the vertical grounding simulation, all of the complexity of the structure and impact location that mentioned in the previous numerical simulations was taken into consideration. For longitudinal crushing the whole structure, including all inner and outer stiffeners, was considered due to the very long simulation times.

6.2.1. Structure Geometry

A double bottom structure geometry was modelled as an idealised version of a real ship. Its particulars are as follows: LOA 265m, LBP 256m, Beam 42.5m draught 15.65m, GT (ITC 69) 72.449T, and DWT 126.355T. The midship compartment was selected with a length of 32 metres and a beam of 42.5 meters.
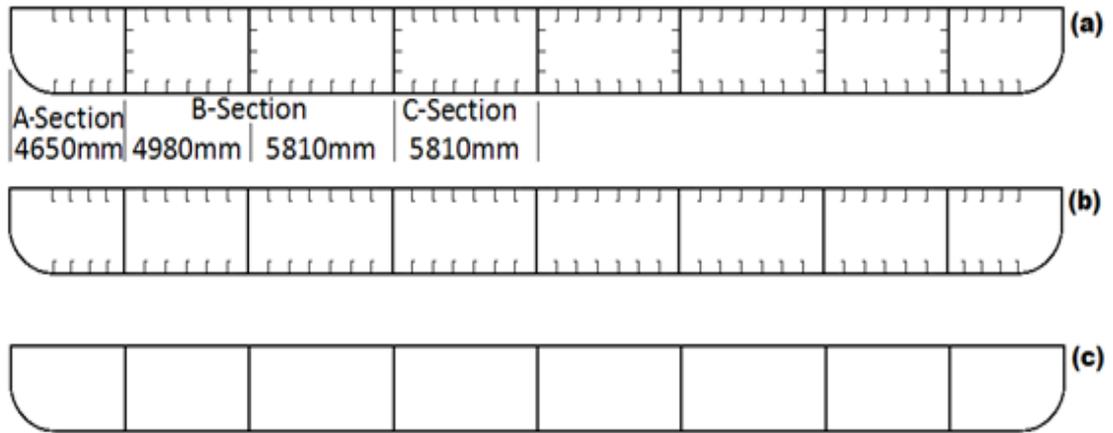
Figure 55: Simplified models of double bottom.

Nine transverse frames were included with a frame spacing of 4.0 meters being assumed as constant throughout the compartment. The height between outer plating and inner plating is 2.97 metres and spacing between vertical floors ranging from 4.65, 4.98, and 5.81 metres as shown in Figure 55. All structural members were included in the numerical models including: outer plating, inner plating, longitudinal floors, transverses, outer plating stiffeners, inner plating stiffeners and longitudinal floor stiffeners.
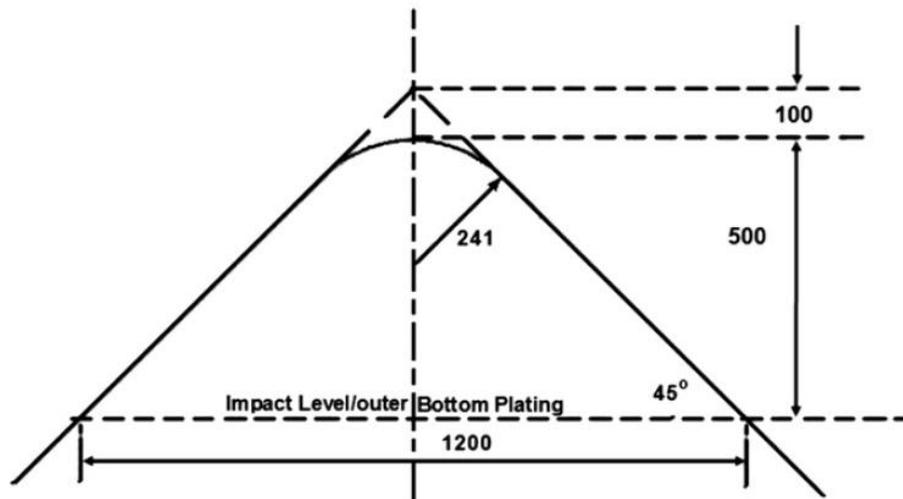
Figure 56: Simplified rock with conical shape from (J . Amdahl et al., 2009).

Three alternative FE models were used to carry out the numerical simulations and are shown in Figure 55, these were:

i. Model A: All longitudinal stiffeners included in the model (ALLSI) see Figure 55a

ii. Model B: All longitudinal stiffeners included except stiffeners on longitudinal floors (SI)- see Figure 55b

iii. Model C: No longitudinal stiffeners included (ALLSNI)- see Figure 55c

The details of the model arrangement and thickness of all plating and stiffeners are presented in Figure 55a, b and c and Table 4.The rock geometry model was taken from (J . Amdahl et al., 2009) and is shown in Figure 56.

Table 4: The thickness of the double bottom hull plating.

Types of Structure Member	Material	Thickness (mm)
Floor-1	C	15
Floor-2	C	15
Floor-3	C	15
Floor-4	C	16
Floor-5	C	15
Floor-6	C	15
Floor-7	C	15
A-Section Stiffeners-16 of 400x14mm	C	14
B-Section Stiffeners-44 of 430x15mm	C	15
C-Section Stiffeners-24 of 400x16mm	C	16
Floor Stiffeners-21 of 300x14mm	C	14
9 of Transverses	C	17
Inner Plate	A	17
Outer Plate	A	18

The details of the model arrangement and thickness of all plating and stiffeners are presented in Figure 55a, b and c and Table 4.The rock geometry model was taken from (J . Amdahl et al., 2009) and is shown in Figure 56.

6.2.2. Numerical Approach

A mesh size of 15mm was chosen based on the convergence study carried out in the previous simulation. The structure arrangement and location of crushing impact are both taken into consideration during the numerical simulations. The main impact locations considered were: impact on main transverse frame (IoMG)and (IbMG) impact between the main transverse frames as shown in Figure 57.
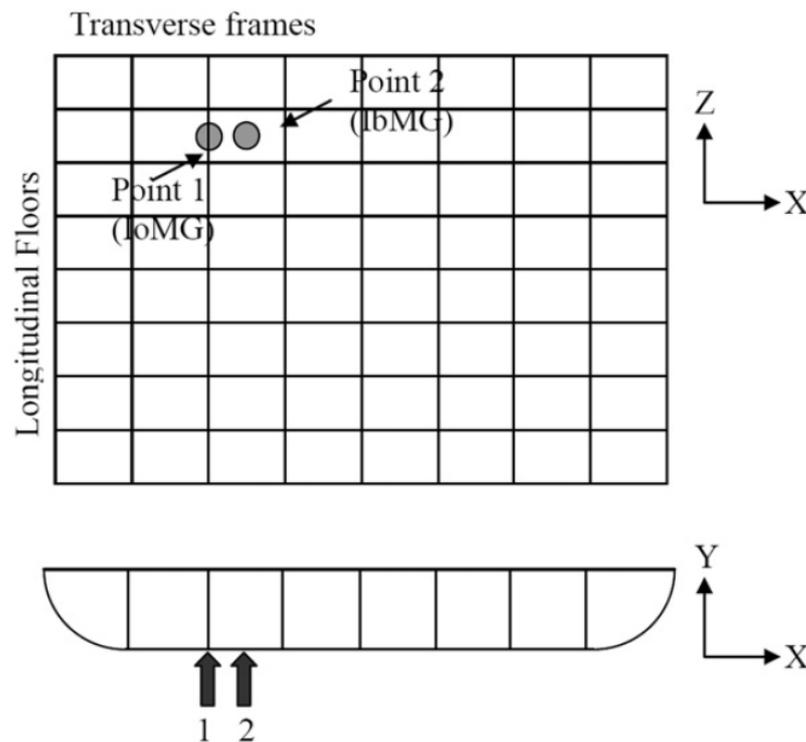
Figure 57: Impact location on midship compartment (42.5 x 32 m.).

For all the simulations the friction coefficient was set at 0.3 which is applicable for most cases of mild steel surface contact, the analyses utilised a structured quadrilateral dominated mesh for fine as well as coarse mesh regions and unstructured mesh for the transition region.

The speed of the vessel was taken as being a typical ship in service speed of 10m/s or 19.4 knots, and assumed to be constant during grounding simulation. This speed has been used by other researchers, (Samuelides et al., 2007b, Zilakos et al., 2009, J . Amdahl et al., 2009) in similar studies.

There are two different phases of impactor movement during these analyses: phase 1 is vertical movement or penetration of the double bottom of 0.5 metre depth in Y-direction, this is followed by phase 2, which is horizontal movement, travelling about 13 meters in Z direction (-ve). Phase 1simulated the early stage of rupture which happens during grounding of the double bottom. Phase 2 simulated the significant damage and rupture which occurs in the structure as the ships momentum moves it forwards.
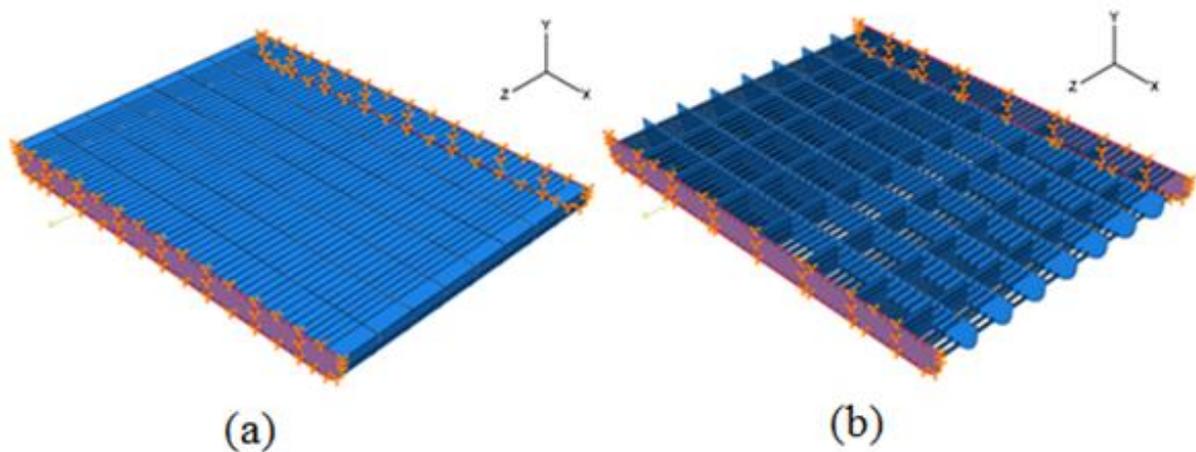
Figure 58: Boundary condition set as ECANSTRE in red color (a) midship compartment (42.5x32 m) and (b) internal structure members.

All the analysis was carried out using a strain based failure criterion as described previously in the material failure model. The boundary conditions were set as ESCANSTRE (fully fixed) for both ends of the transverse frames see Figure 58. This was modelled in this way due to the presence of transverse watertight bulkheads at these positions. The analysis was run without considering the effect of strain rate. For the cases considered here,

where the grounding speed is only 10m/s, this is a reasonable assumption to make.

The analysis were carried out by two types of desktop computers which were a using single processor Intel Core i7, 12 GB RAM, and dual Intel Xeon E5540, 24GB RAM systems. Most of the analyses generated file sizes ranging from 25-40 GB, running time between 300-360 hrs, and used a range of elements between 154229 and 254790 for the complete simulation; this includes vertical penetration and horizontal crushing during grounding. The dual Intel Xeon processor was faster during simulations compared to single processor when the same analysis was run on both machines.

6.3. Simulation Results

In this section, the progressive failure of the double bottom is discussed considering both, the effect of damage due to plastic deformation of the double bottom and also damage evolution including material rupture. In phase 1, the extreme grounding simulation vertical penetration of the double bottom was carried out by looking at force displacement and energy displacement relationships for all models. In phase 2, the main focus was looking at fully plastic deformation and material degradation against time due to grounding, only for model A (ALLSI).

6.3.1. Phase 1: Vertical Grounding
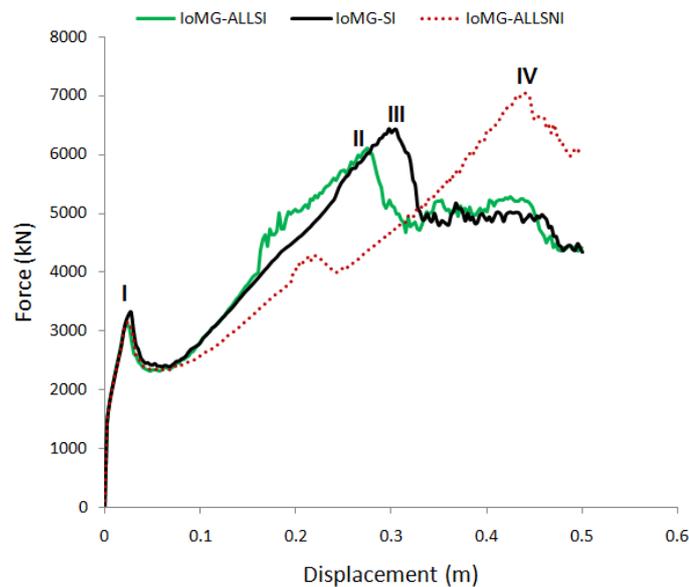
Figure 59: Impact on main floor: Force – penetrator displacement.

The results for impact on the main floor are shown in Figure 59 and Figure 60. Figure 59, shows that the structure for Model C was capable of resisting a higher force and displacement before rupture, followed by Model B and then Model A. Point I, indicate that the longitudinal main girder start to tripping which create less down force after that peak. The hump between point A and points I,II,III is where the main girder start to folded on each other and create some resistance to penetrator for Models A,B and C. Point I, II and III indicates that the main girder start to have second tripping which create less force for penetrator to push further after that points. The plateau region for Models A and B show that rupture occur at same event of penetrator keep pushing toward until reach point to stop at 0.5m penetration. Material rupture took place at 0.30m, 0.32m and 0.45m of penetration for models A, B and C respectively. The figure also indicates the significant effect of modelling stiffeners and their contribution to the failure during impact.

This shows that the stiffness of the structure plays an important part in the onset of rupture, a more rigid structure will give less crashworthiness capability compared to a more flexible structure from the point of view of hull rupture. Looking at Figure 60, we can see that the energy absorbed by the

structure is of a similar magnitude for all three models. The model without any longitudinal stiffeners, Model C, deviates slightly from Models A and B, but ended up at same point at 0.5m of displacement and 2.2MJ crushing energy.
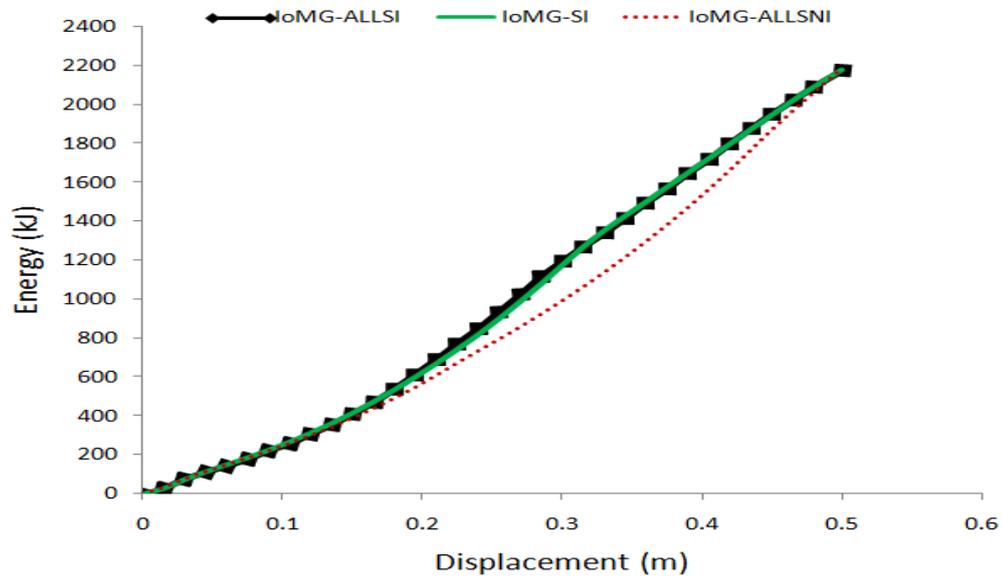
Figure 60: Impact on main floor: Energy – penetrator displacement.
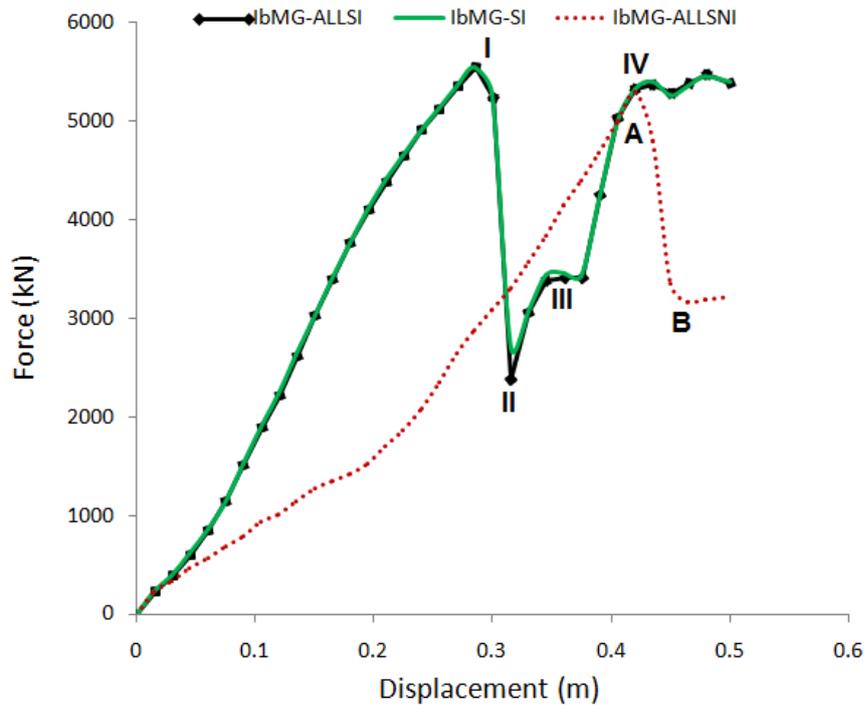
Figure 61: Impact between main floors: Force – penetrator displacement.
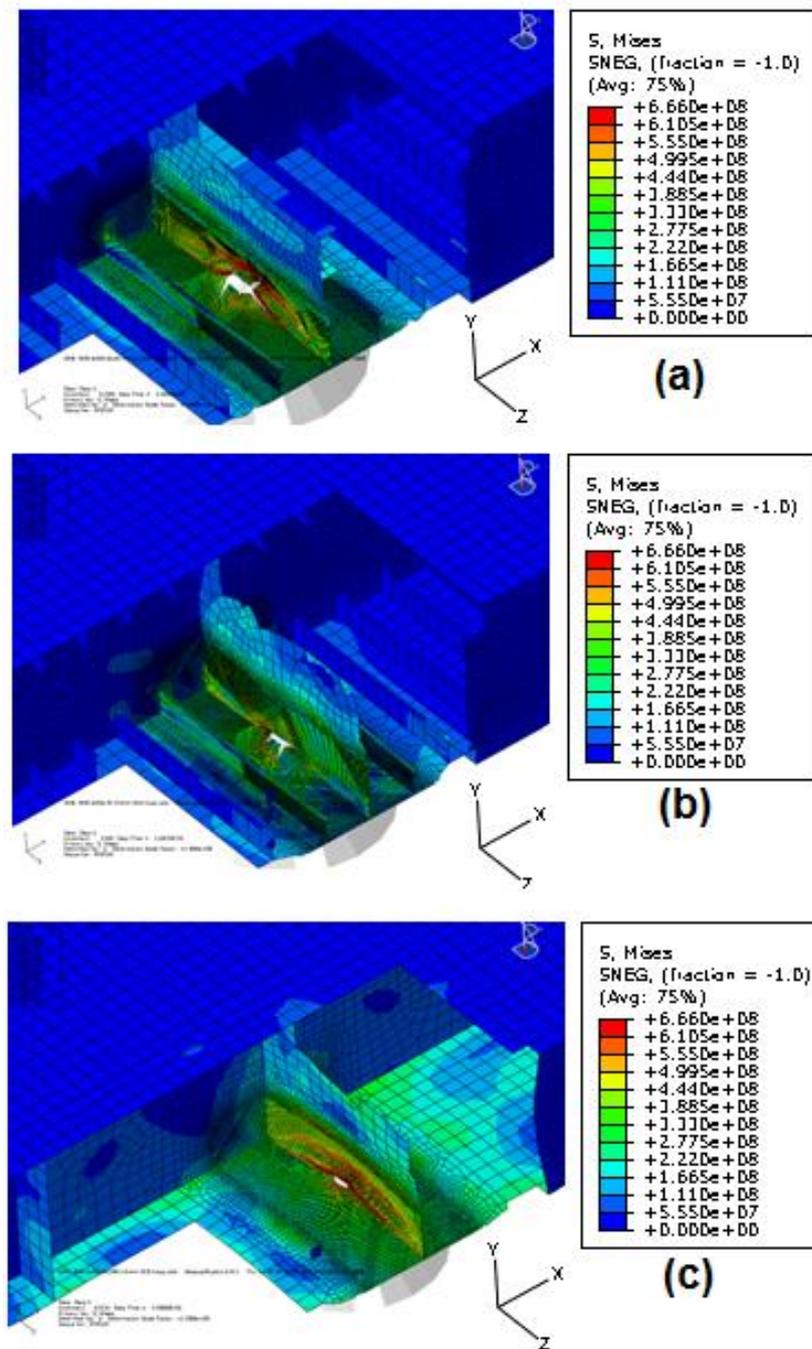
Figure 62: Phase 1. The simulation of vertical grounding displacement for Models A, B and C impact between main floors.

The response of the models to vertical grounding on the main transverse floor is shown in Figure 62a, b and c, these clearly show that damage started to occur on the bottom plating during grounding, mainly due to the large local deformation and strain being generated by the penetrator.

110

The forces generated during phase 1 grounding between the main transverse floors are shown in Figure 61 for Models A and B, and are almost identical, with rupture occurring at 0.31m vertical displacement and 5.6MN maximum force. This indicates that stiffeners on the main longitudinal floor do not appear to contribute significantly to the strength of the structure for this phase of grounding.

The first peak of point I for Model A and B, show that the plasticity of bottom shell plating reach at maximum strength and start to necking and break at point II. The force increase again due to more area of penetrator come into contact with bottom shell and start to tearing on side of shell at point III. The penetrator start to hit the bottom longitudinal stiffeners at both sides and lead to increase the penetration force until reach at point IV.

But, when all the stiffeners on the structure are removed the penetrator is able to cause greater deformation and bottom plate start degrading at point A. The bottom plate rupture initiates at point B, with rupture occurring at 0.44m vertical displacement. Figure 63 shows a similar pattern, where the energy for Models A and B are the same giving 1.78MJ at a vertical displacement of 0.5m. The energy for model C is lower than for models A and B giving 1.20 MJ at the same displacement.
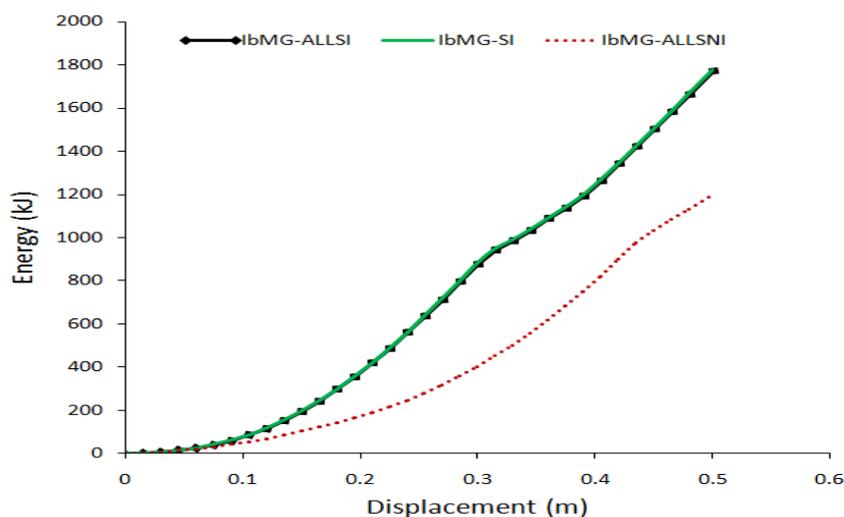
Figure 63: Impact between main floors: Energy – penetrator displacement.
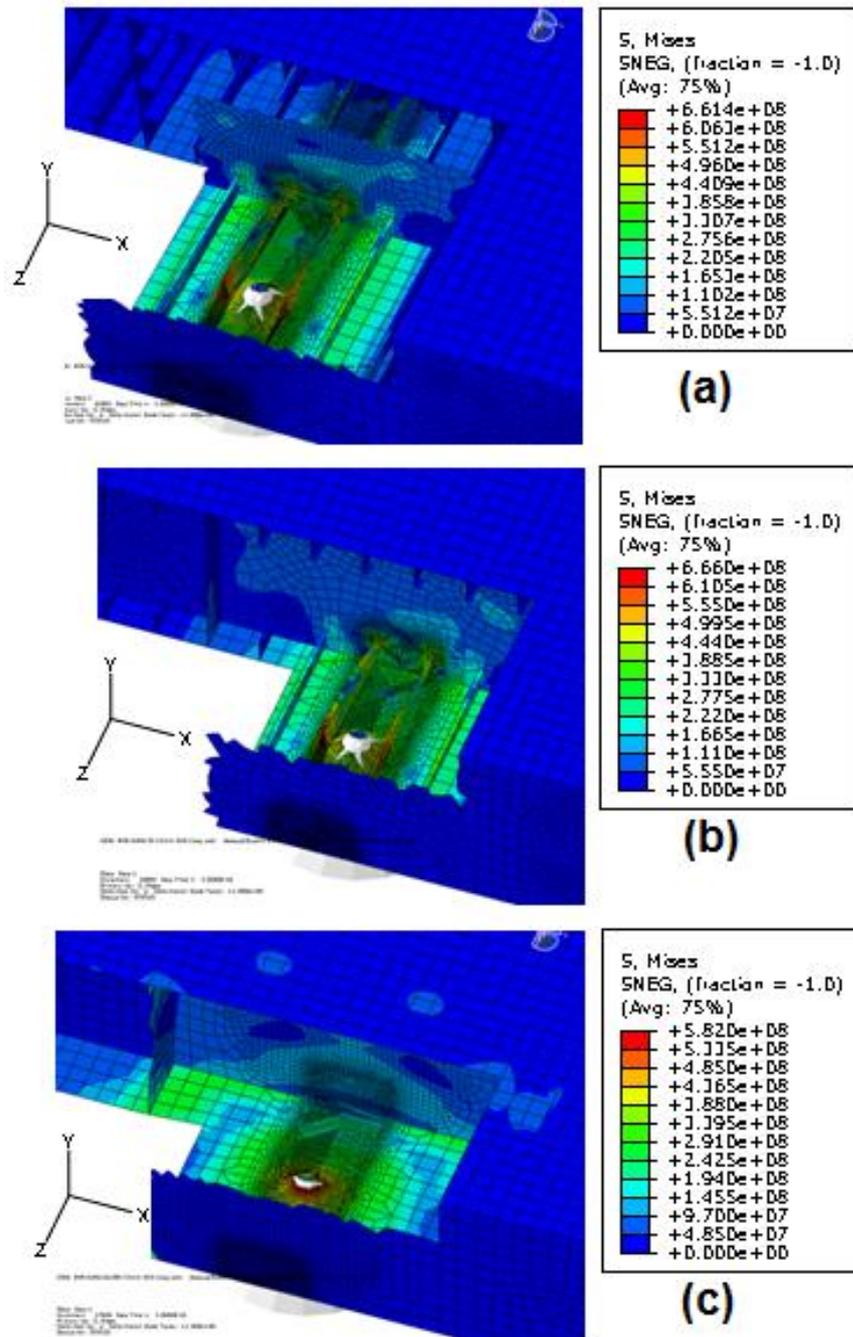
Figure 64: Phase 1. The simulation of vertical grounding displacement for Models A, B, and C impact between main floors.

The behaviour of the structure during the simulations are show in Figure 64a, b and c, where Models A and B again behave in the same manner and show similar rupture propagation tendencies. For model C the rupture pattern

displays similar patterns to that shown in the simplified experiment carried out by (Alsos and Amdahl, 2009).

The depth of penetration and subsequent grounding damage was chosen to be consistent with the result of (Samuelides et al., 2007b, Zilakos et al., 2009), since this is part of the same study.

6.4. Horizontal Crushing During Grounding

6.4.1. Phase 2: Horizontal Grounding

The next stage in the simulation was to investigate horizontal crushing of the double bottom, after rupture, due to the forward momentum of the ship. Both Figure 65a and b show the grounding force on the double bottom for the midship compartment. Both figures also show the fully plastic (FP) force which would be obtained if the simulation had been carried out without modelling material failure, this demonstrates that higher forces are produced for this simulation than when material failure (rupture) (WD) modelling is included in the simulation. In Figure 65a we can see that the maximum grounding forces during crushing of the transverse floors are: RFY: 10.4MN, RFZ: -14.6MN, for fully plastic, and RFY: 8.74MN, RFZ: -12MN when material failure properties are included.
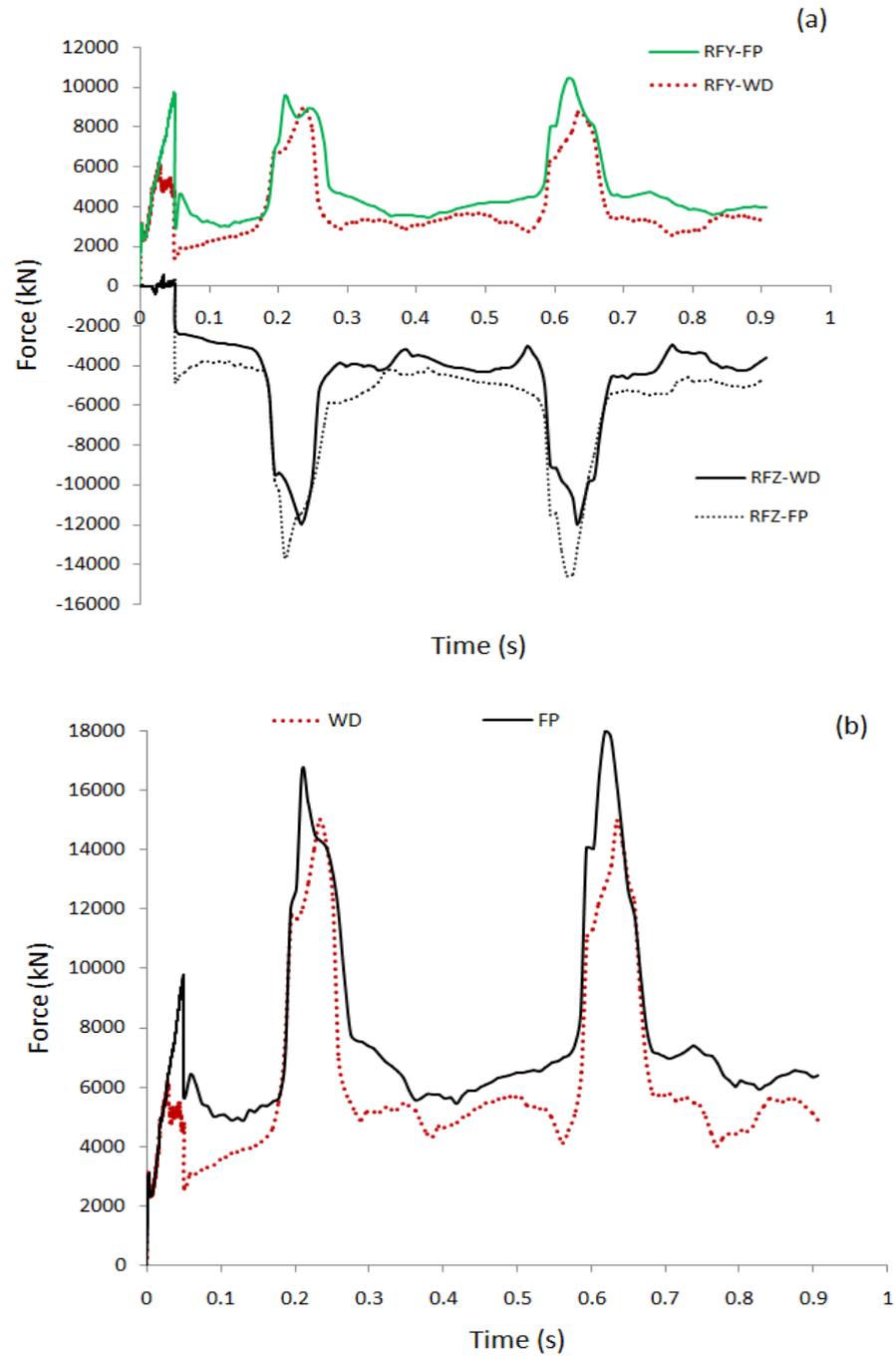
Figure 65: Impact on main floor (a) the grounding force in Y (RFY) and Z (RFZ) directions, and (b) the resultant force.
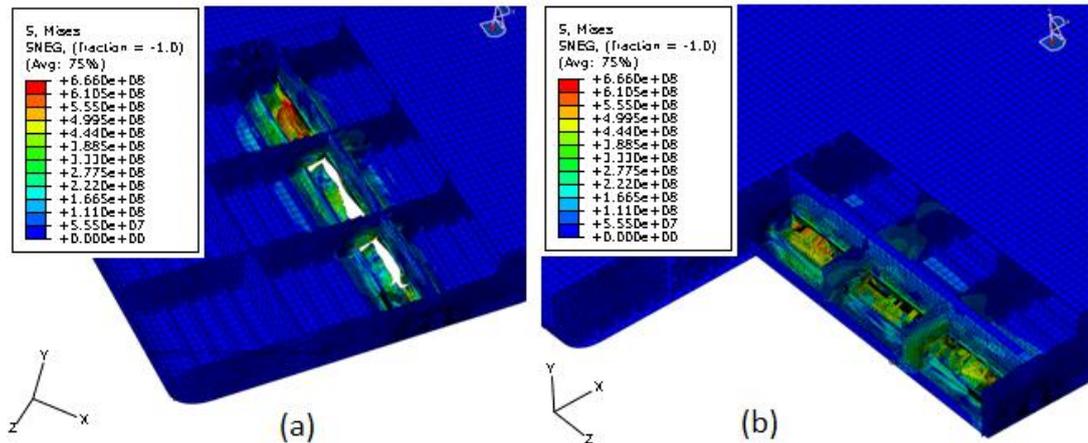
Figure 66: Impact on main floor (a) with damage (b) without damage.

When we look at the resultant crushing force on the double bottom as shown in Figure 65b, the grounding force when neglecting material failure (rupture) (FP) is always higher than when we include material rupture (WD). The difference between them is estimated at about 15-50%, the peak forces for phase 1 are 9.69MN, 17.96MN and for phase 2 are 6.18MN, 15.01MN for FP and WD failure models respectively. The performance of the structure, for both conditions, can be seen clearly in Figure 66a and b. In Figure 66a, tearing of plate during grounding due to high stress concentrations which occur at the joint of the plate between floor and bottom plate can be observed. In Figure 66b, the elements display only stretching without showing any tearing or rupture.
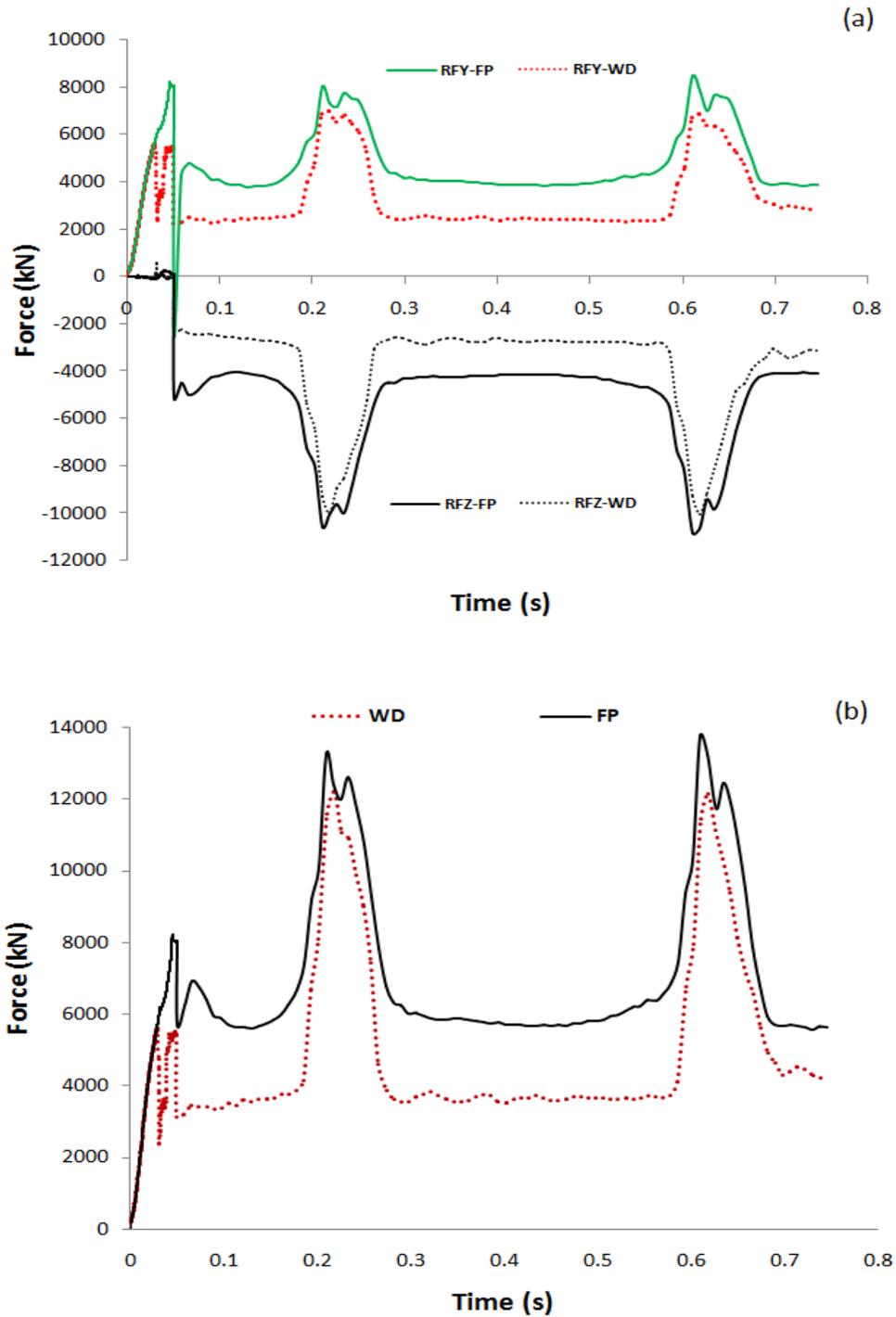
Figure 67: Impact between main floors the grounding force in Y (RFY) and Z (RFZ) direction, and (b) the resultant force.

Figure 67 shows the response of the structure when the grounding occurs between the main transverse floors followed by longitudinal tearing of the structure. The same behaviour as before is shown in Figure 67a and b, where

116

a larger force is generated without modelling rupture of the structure (FP) than when rupture ((WD) is modelled.

The difference between FP and WD failure modelling produces differences in the force in the range of 11- 40% for both. In Figure 22a, RFY and RFZ forces peak at 8.47MN and -10.84MN respectively for FP, and, 6.86MNand -10MN respectively for WD. The resultant maximum force for phase 1 and phase 2, shown in Figure 67b, are 8.2MN/ 13.76MN and 5.54MN/12.22MN for FP and WD respectively.
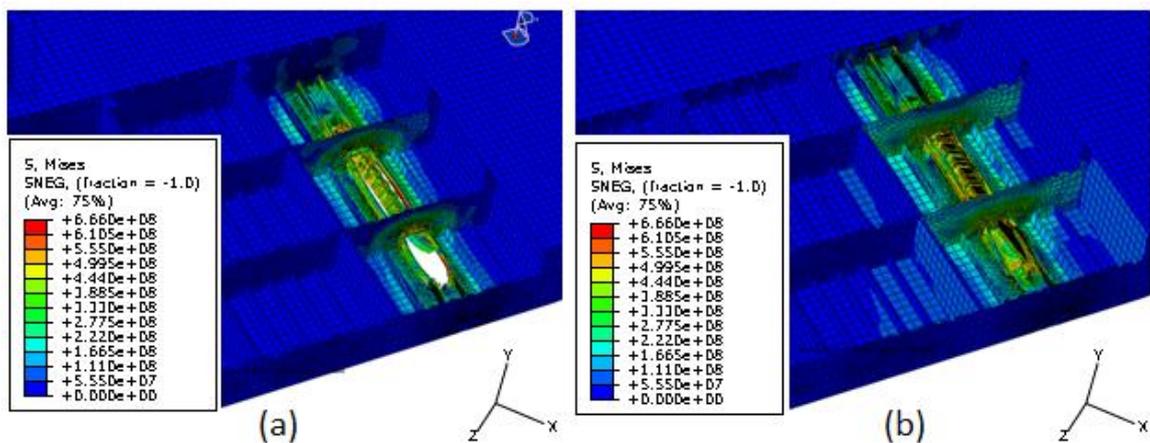
Figure 68: Impact between main floors, (a) with damage (b) without damage.

The failure mechanisms of the structure are clearly shown in Figure 68a and b. Figure 68a shows the failure of the structure during grounding and the plate tearing close to longitudinal stiffeners. Figure 68b shows the bottom plate elements stretching in the middle of a span between longitudinal bottom plate stiffeners without any rupture.

6.5. Discussion

In this analysis it has been demonstrated that a more rigid structure is less crashworthy than a more flexible structure when considering hull rupture. This phenomena is clearly demonstrated in Phase 1 of the simulation, where the

penetration of the indenter shows higher displacements before initiation of rupture when comparing model C with models A and B. This simulation also showed that not including material rupture (FP)always produces higher failure loads than when rupture is modelled (WD), where simulations demonstrate higher results by about 30-50% for Phase 1 and 11-35% for Phase 2.

The results in Phase 2 also show good correlation when compared to (Zilakos et al., 2009) where the maximum force for RFY-FP and RFZ-FP during crushing of the transverse floors demonstrates an almost constant level of force throughout the simulation irrespective of the number of transverse floors. The results obtained for RFY-FP and RFZ-FP simulations are also higher than (Zilakos et al., 2009), which is reasonable due to higher plastic material properties being used, (Zilakos et al., 2009) used 245MPa as the material yield stress where the current model is using properties as defined in chapter 4.

The analysis also found that estimated onset of material rupture in Phase 1 is very sensitive to the material failure model adopted, compared to phase 2. The differences between fully plastic and material failure models in Phase 1 clearly show significant differences as mentioned above. It has also been demonstrated that the effect of grounding is very localised in all simulations. This can be seen by observing the localisation of high stress contours which only occur in the area close to the impact location.

6.6. Summary

The purpose of this study was to use the finite element method to investigate grounding damage to ship structures. This was achieved by looking at available experimental data and calculations using FE analysis, and then applying the grounding methodology developed to study damage to the structure of ship bottoms. This is a very complex process and the calculations are dependent on mesh size, types of loading, crushing location, boundary conditions and the software that is being used in the analysis.

Although many studies have been conducted on this topic, their results show considerable variability. Therefore, a significant amount of discussion and explanation with regard to the accuracy and reliability of results is still required.

Overall, the results obtained from the FEA simulations produced very good agreement when compared to the experimental results of grounding damage by (Rodd, 1996) and the calculations by (Simonsen, 1997a). The grounding simulation also showed good correlation with previously published results (Samuelides et al., 2007; Zilakos et al., 2009) in terms of penetration force.

This demonstrates that FEA is an appropriate tool which can be used to investigate the local and global behaviour of a ship's structure during grounding, providing that good models for predicting material rupture are employed which should include appropriate scaling laws to take account of the mesh size sensitivity effect.

Numerical simulations are cheaper to run than experimental studies, but there is still a significant requirement to carry out good quality experimental studies. Results from such experiments are necessary for validating numerical simulation models in predicting structural responses during collision and grounding. The comparisons of experiments and numerical modelling studies will help establish suitable numerical models for carrying out future assessments of collision and grounding scenarios.

CHAPTER 7: COLLISION OF SHIP TO RIGIDWALL

7.1. Introduction

In the late 1990's, the double hull tanker become compulsory for new construction in order to prevent damage to the environment due to oil spill during collision. However, the crashworthiness of the side shell of ship did not seem to improve due to increase of ship size and large amount of kinetic energy carried by larger ships during collision.

Most of the previous researchers concentrated on side shell improvement of struck ship whereas less focus was placed on bow design of striking ship to absorb energy during collision. The buffer bow concept was proposed by The Association for Structural Improvement of Shipbuilding Industry (ASIS) in order to further decrease the oil spill probability as a next-step countermeasure. Buffer bow is expected to lessen the threat of the damage on the side hull of a struck ship by its collapsing advance (Endo et al., 2002). During the mid-1980's and early 1990's some of the researchers started to focus on the bow structure effect and design during collision, Cheung, Lee, JSRA, Ohnishi et al, looked mainly at the soft bow concept (Endo et al., 2002), investigated scale model of buffer bow, (Lehmann and Peschmann, 2002), introduced collapse mechanism of bulbous bow, (Suzuki et al., 2000) estimated the collapse strength of ship bow.

This chapter is very challenging, where most of the simulations were very costly in terms of simulation time, as well as processer and memory used capacity. The incidence of ship collisions and grounding has a significant contribution to oil spill, loss of life and environmental damage at sea. The costs incurred due to these accidental scenarios and the time taken for the polluted environmental area to recover to its original state is significantly large. In this paper the accidental loads and damage mechanism incurred on a ship's bow during a ship collision are analyzed using Nonlinear Finite Element methods in order to investigate the capability of ship's bow to absorb the force and energy generated during a collision event. The study investigates the effect of collision angle and ships speed, when looking at an

extreme collision event of a ship striking a rigid wall, a full ship model is employed in this investigation.

In this study, the capability of ship bow absorbing the impact force and energy during collision is investigated by introducing ship bow rigidity ratio which mainly focuses on the forward part of potential damage bow. The analysis involves using a full scale size of ship with velocity applied at the center of mass of the ship with 6 degrees of freedom allowed at all axis impact on rigid wall. The numerical simulation findings are used as the basis of a new simplified procedure for predicting damage response of the bow structure during collision events. The numerical results are also compared with more simple analytical calculations.

7.2. Structure Geometry

Ship structure is divided into two categories, consisting of rigid structure and deformable structure that are capable of absorbing collision force during collision (see Figure 69). The ship particulars and deformable structure material thicknesses are set according to Table 5 and Table 6.

Table 5: Vessel Particulars

Vessel Type	Bulk Carrier
Length	174.96 meters
Breadth	26.00 meters
Depth	15.50 meters
Maximum Draft	11.148 meters
Gross Tonnage	20362 metric tons
Net Tonnage	11438 metric tons
Ship displacement	34365 metric tons
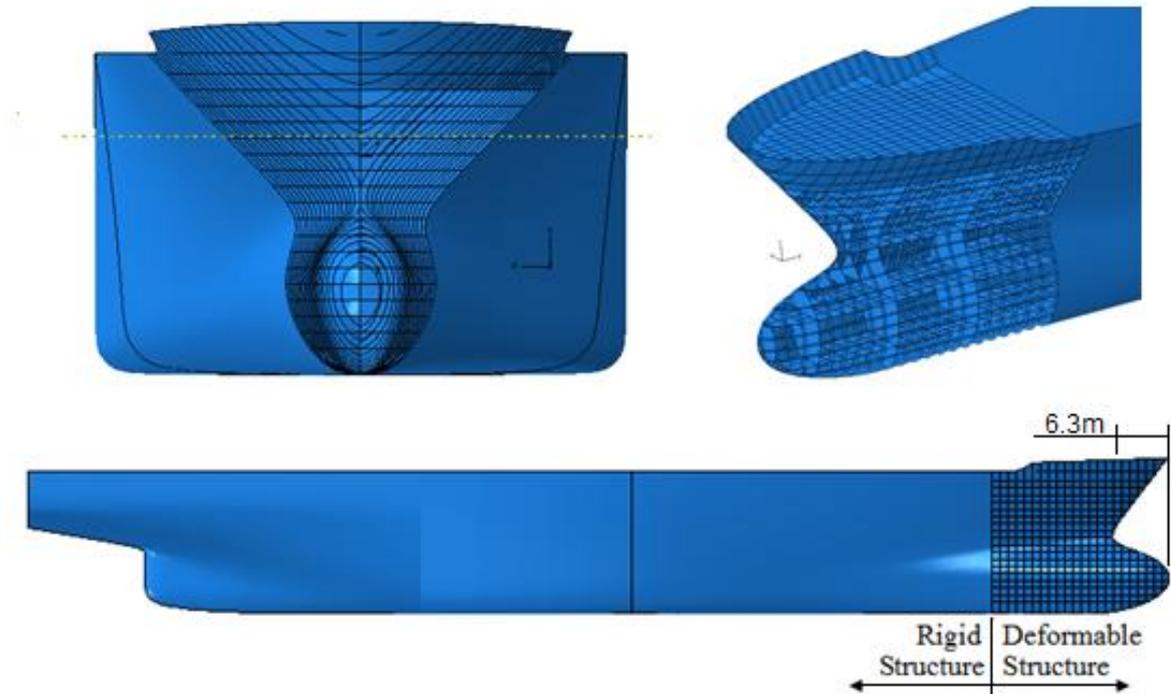
Figure 69: Ship Structure Geometry Model.

7.3. Collision Scenario

The simulations are setup according to Table 6, where the initial speed is initiated at center of mass at six degree of freedom and rigid wall set at standstill;

i)   Angle Collision (AC) - set at 300, 450, 600, 900 collision angles with constant speed, plate thickness and ship displacement.

ii)   Lateral Collision (LC)

   a. For different plate and stiffener thickness (LC-DT)

   b. For different initial speed just before collision occur (LC-DS)

   c. For different ship displacement (LC-DD)

Table 6: The Ship Collision Parameters.

Damage Condition		Initial	Collision Angle (0°)	Initial Speed (m/s)	Thickness (mm)	Ship displacement (kg)	Rigidity
Angle collision		AC-30	30	10	18	34,523, 896	0.045285
		AC-45	45	10	18	34,523, 896	0.045285
		AC-60	60	10	18	34,523, 896	0.045285
		AC-90	90	10	18	34,523, 896	0.045285
Lateral Collision	Different Thickness	LC-DT-10mm	90	5	10	34,523, 896	0.025158
		LC-DT-14mm	90	5	14	34,523, 896	0.035221
		LC-DT-16mm	90	5	16	34,523, 896	0.040253
		LC-DT-18mm	90	5	18	34,523, 896	0.045285
		LC-DT-20mm	90	5	20	34,523, 896	0.050316
	Different speed	LC-DS-2.5m/s	90	2.5	18	34,523, 896	0.045285
		LC-DS-5m/s	90	5	18	34,523, 896	0.045285
		LC-DS-7.5m/s	90	7.5	18	34,523, 896	0.045285
		LC-DS-10m/s	90	10	18	34,523, 896	0.045285
	Different Ship displacement	LC-DD-137Mkg	90	5	18	137,148,176	0.045285
		LC-DD-77Mkg	90	5	18	77,145,849	0.045285
		LC-DD-34Mkg	90	5	18	34,28,7044	0.045285
		LC-DD-8Mkg	90	5	18	8,571,761	0.045285

7.4. Simulation Results

7.4.1. Angle Collision

Figure 70 shows the crushing force against crushing time for different angle of attack collisions. The larger collision angle of attack produces higher impact force. The collision force also in this case followed Minorsky's prediction where larger collision angle of attack produce closed results and in this case more than 600. The time taken for ships to stop after collision or change direction are approximately 0.8s, 1.0s, 1.8s and 2.0s for AC-A30, AC-A45, AC-A60 and AC-A90 respectively.
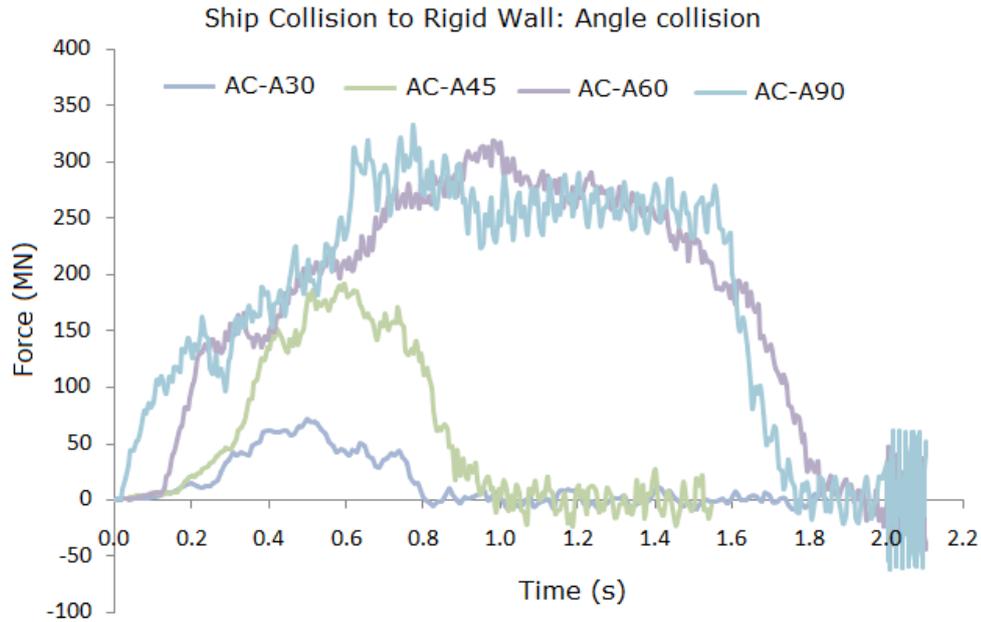
Figure 70: Force-Time of Angle Collision.

Figure 71 shows the crushing force in relation to crushing distance where ship's bow measured from forward part of bow to maximum crushing distance inward before ship fully stopped except for case AC-A30and AC-A45 which experienced sliding and changing course. The maximum crushing bow after collision are 8m, 9m, 8.5m and 9m for AC-A30, AC-A45, AC-A60 and AC-A90 respectively.
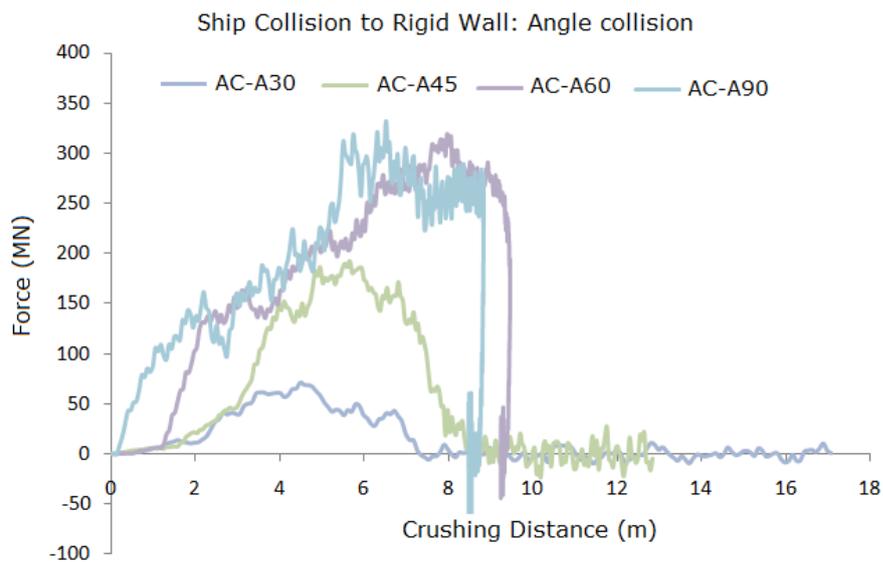
Figure 71: Force-Displacement of Angle Collision.

Figure 72 shows the dissipation of kinetic energy during collision, for AC-A30 and AC-A45 the ship keeps moving when kinetic energy stored is not fully converted or absorbed by rigid wall and damaged bow. For AC-A60 and AC-A90 the ship is fully stopped and bouncing back in the opposite direction, where kinetic energy is fully absorbed by rigid wall and damaged bow.
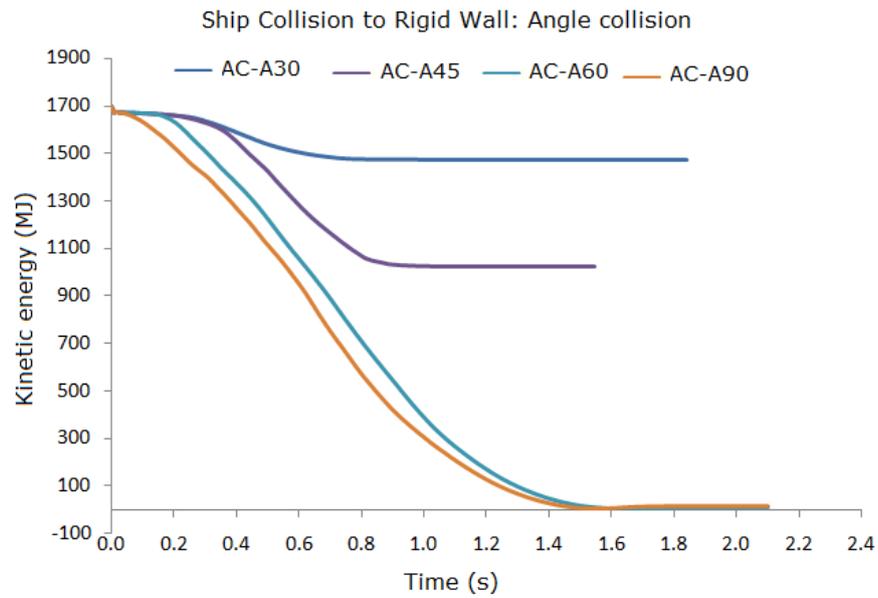
Figure 72: The Energy of Angle Collision

Collision Type	$\begin{array}{c}Y \quad X \\ \downarrow \\ Z\end{array}$	$\begin{array}{c}Y \\ \uparrow \\ X \longrightarrow Z\end{array}$	Stress Contour Level
AC-A30			
AC-A45			
AC-A60			
AC-A90			
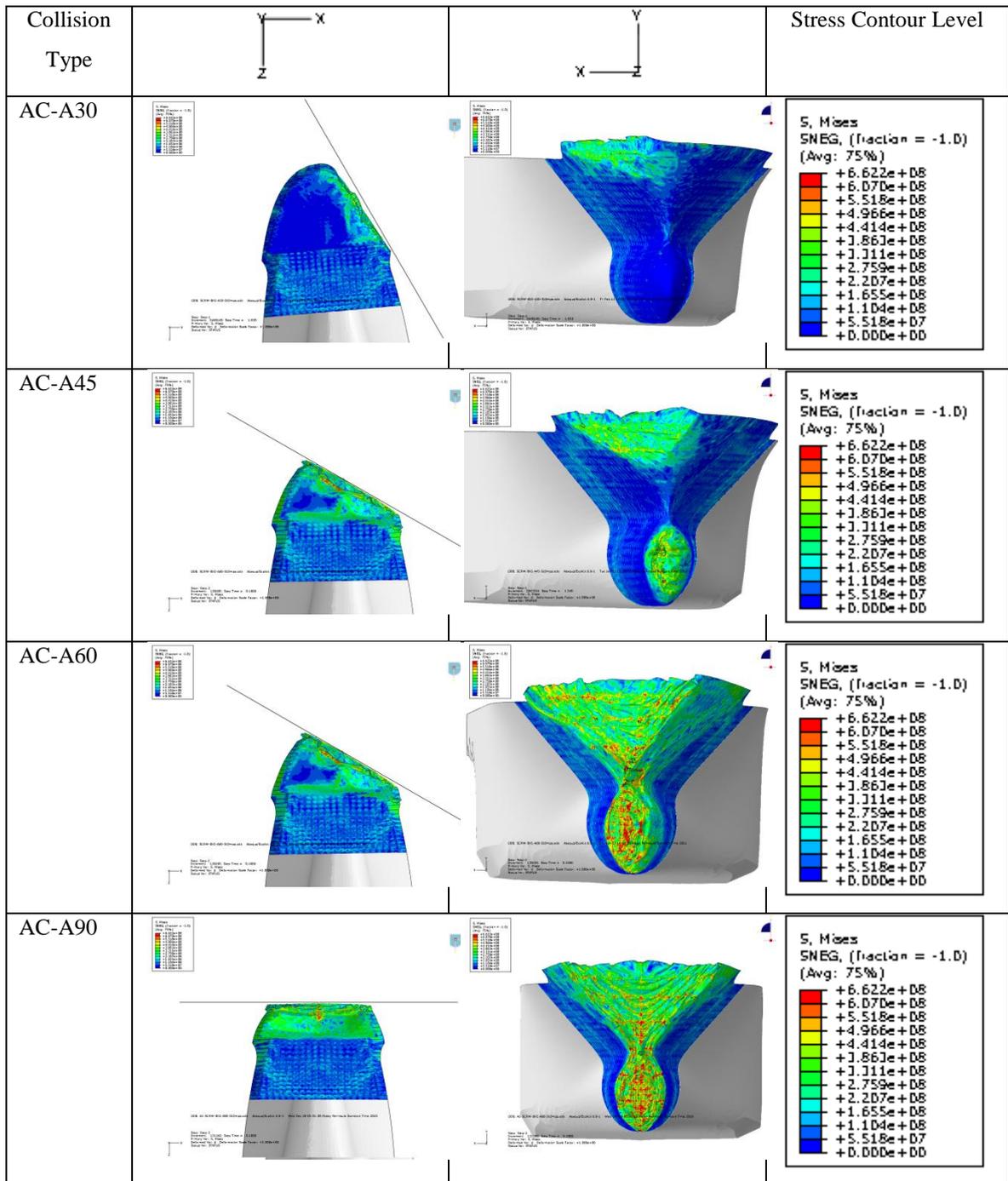
Figure 73: The crushing damage of Angel Collision.

Figure 73 shows the simulation results for angle collision where a small angle experienced a sliding effect and was hard to predict the crushing damage in perpendicular direction relative to the rigid wall. The ship tends to stop and bounces back in the opposite direction for larger angle collision when stored kinetic energy is fully absorbed by rigid wall and damaged bow.

7.4.2. Lateral Collision

Figure 74 and Figure 75 show the crushing force for lateral collision of ship to rigid wall where using different plate thicknesses at a constant collision speed of 5m/s. The force increased from 134MN, 137MN, 161MN, 146MN and 178MN for plate thickness 10mm, 14mm, 16mm, 18mm and 20mm respectively. The result indicates that increasing plate thickness leads to increase crushing force and less energy absorbed by damaged bow.

7.4.2.1. Different Thickness

Figure 73 also indicates the time for ship to completely stop after collision ranging from 1.42s, 1.54s, 1.61s and 1.89 for plate thickness 20mm, 18mm, and 16mm and 24mm respectively. For 10mm plate thickness the estimated time is about 2.1s due to ABAQUS job aborted before the step was finished. The results show that the crushing time is reduce when plate thickness is increased.
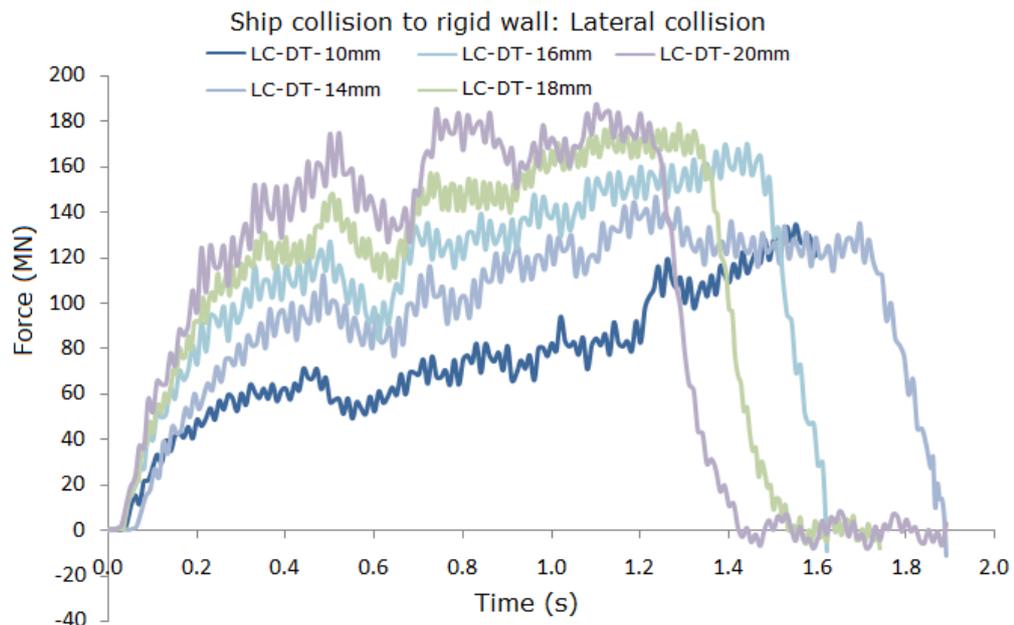
Figure 74: Force-Time of Lateral Collision for Different Forward Structure Thicknesses.

Figure 75 shows the crushing distance before ship stop after collision where large plate thickness shows less damage of ship bow. The crushing distance ranging from 5.98m, 4.78m, 4.27m, 3.85m and 3.5m for plate thickness 10mm, 14mm, 16mm, 18mm and 20mm respectively. The results show less crushing damage of bow when plate thickness is added.
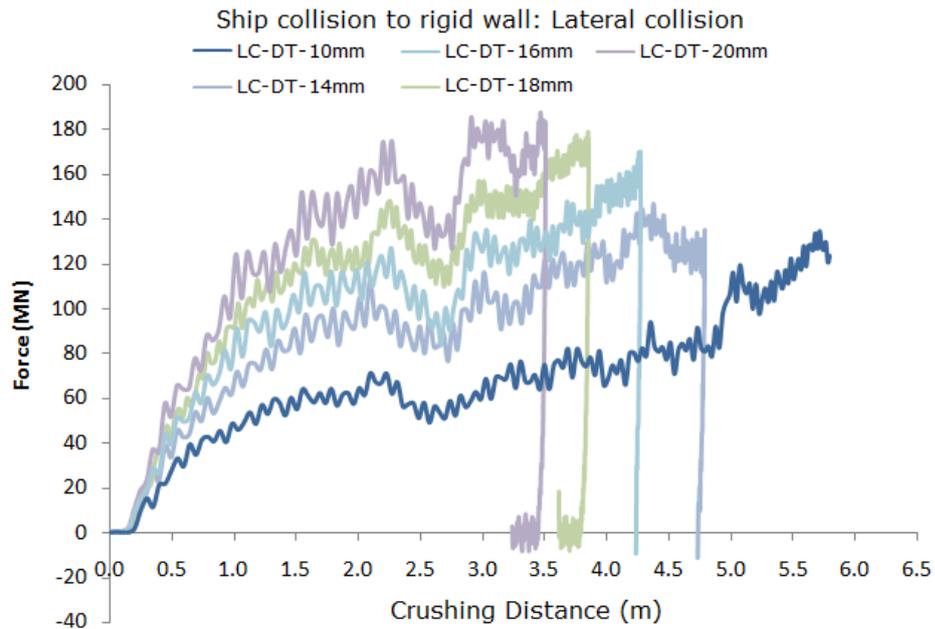
Figure 75: Force-Distance of Lateral Collision for Different Forward Structure Thicknesses.

Figure 76 shows the dissipation of kinetic energy after collision where thinner plate was able to prolong the collision time. This phenomenon shows that thinner plates are able to reduce damage of striking vessels and are capable of absorbing more energy during collision.
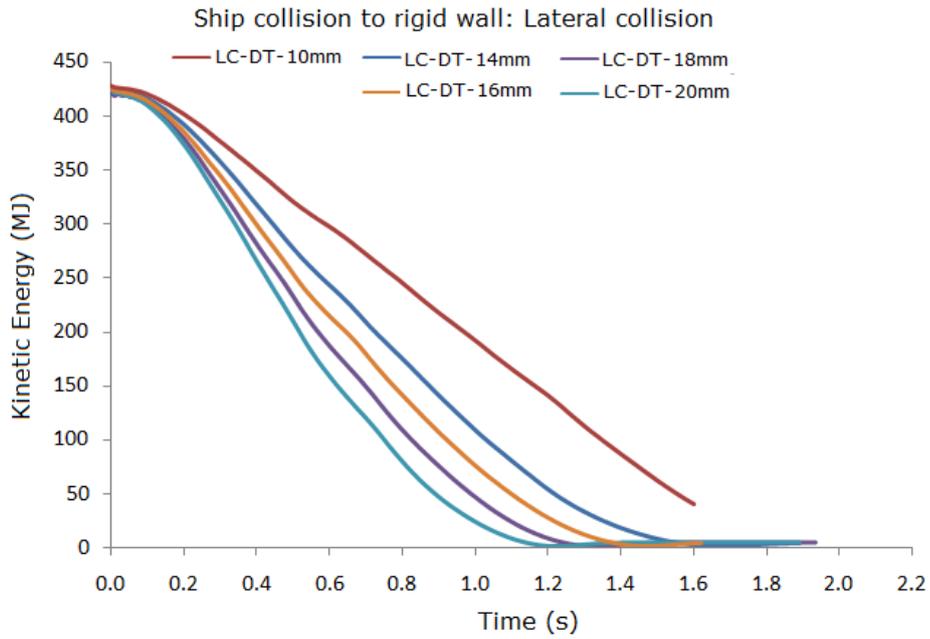
Figure 76: The Energy of Lateral Collision for Different Forward Structure Thicknesses.

Figure **77** shows the simulation results that depicted the damage of ship bow after ship collision to rigid wall. The results clearly indicate that LC-DT-10mm had severe ship bow damage after collision compare to others.

Collision Type	Y ↑ Z — X	Y ↑ X — Z	Stress Contour Level
LC-DT-10mm			S, Mises SNEG, (fraction = -1.0) (Avg: 75%) +6.622e+08 +6.070e+08 +5.518e+08 +4.966e+08 +4.414e+08 +3.863e+08 +3.311e+08 +2.759e+08 +2.207e+08 +1.655e+08 +1.104e+08 +5.518e+07 +0.000e+00
LC-DT-14mm			S, Mises SNEG, (fraction = -1.0) (Avg: 75%) +6.622e+08 +6.070e+08 +5.518e+08 +4.966e+08 +4.414e+08 +3.863e+08 +3.311e+08 +2.759e+08 +2.207e+08 +1.655e+08 +1.104e+08 +5.518e+07 +0.000e+00
LC-DT-16mm			S, Mises SNEG, (fraction = -1.0) (Avg: 75%) +6.622e+08 +6.070e+08 +5.518e+08 +4.966e+08 +4.414e+08 +3.863e+08 +3.311e+08 +2.759e+08 +2.207e+08 +1.655e+08 +1.104e+08 +5.518e+07 +0.000e+00
LC-DT-18mm			S, Mises SNEG, (fraction = -1.0) (Avg: 75%) +6.622e+08 +6.070e+08 +5.518e+08 +4.966e+08 +4.414e+08 +3.863e+08 +3.311e+08 +2.759e+08 +2.207e+08 +1.655e+08 +1.104e+08 +5.518e+07 +0.000e+00
LC-DT-20mm			S, Mises SNEG, (fraction = -1.0) (Avg: 75%) +6.622e+08 +6.070e+08 +5.518e+08 +4.966e+08 +4.414e+08 +3.863e+08 +3.311e+08 +2.759e+08 +2.207e+08 +1.655e+08 +1.104e+08 +5.518e+07 +0.000e+00

Figure 77: The Crushing Damage of Lateral Collision for Different Forward Structure Thicknesses.

7.4.2.2. Different Speeds

This section discusses the effect of ship collision for different speeds, constant plate thickness and ship displacement. The simulation speed ranged from 2.5m/s - 10m/s, a reasonable speed for ships in service before a collision might occur. Figure 78 shows ship collision force against collision time with maximum force generated (111MN, 171MN, 293MN and 332MN), collision duration (1.28s, 1.53s, 1.54s and 1.73s) and collision speed 2.5m/s, 5.0m/s, 7.5m/s and 10m/s respectively.
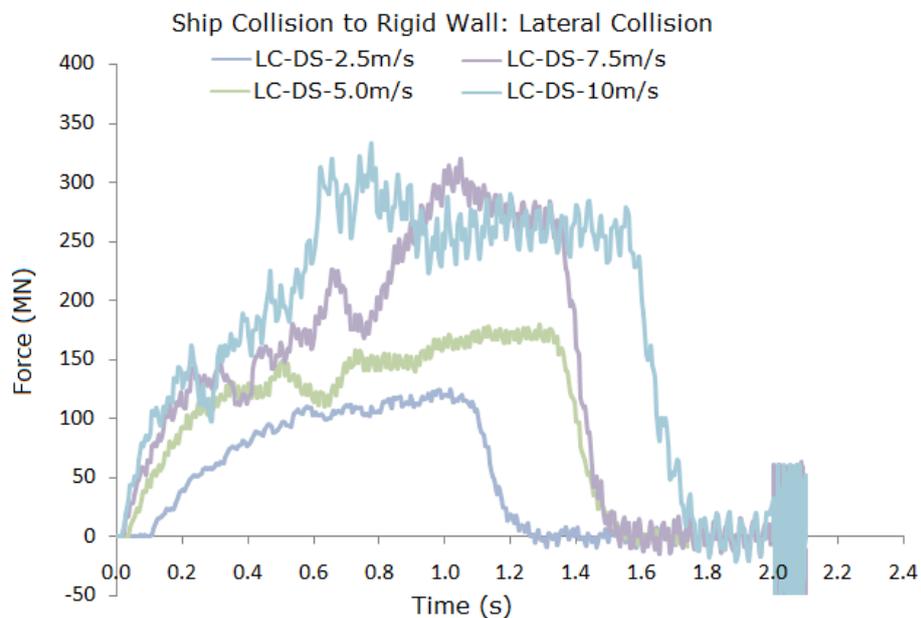
Figure 78: Force-Time of Lateral Collision for Different Speeds.

Figure 79 shows the force and crushing distance where all collisions seem to follow the same path of ship collision speed at 10m/s crushing. This occurs due to the simulation of same plate thickness, bow shape and size and also ship displacement. The crushing distance varies from 1.6m, 3.84m, 6.11m and 8.82m for ship collision speed 2.5m/s, 5.0m/s, 7.5m/s and 10m/s respectively.
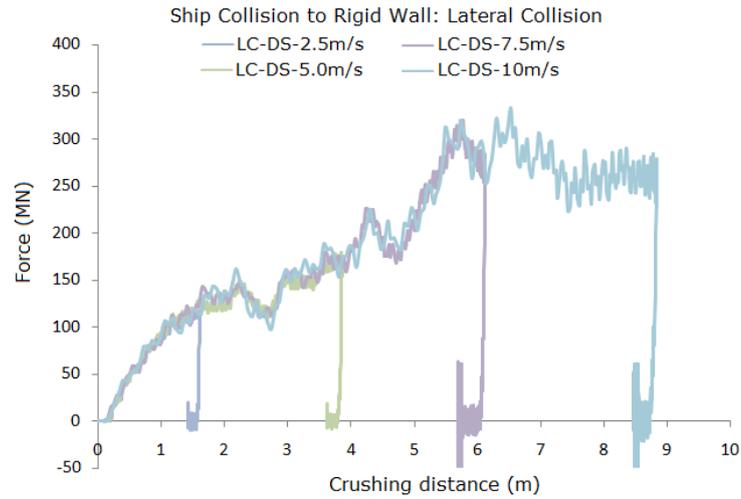
Figure 79: Force-Distance of Lateral Collision for Different Speeds.

Figure 80 shows the dissipation of kinetic energy for different speeds of ship collision to rigid wall where large kinetic energy produced a longer collision duration. The figure also indicates the dissipation of kinetic energy for different speeds where slow speeds LC-DS-2.5m/s are more tender compared to high speed collisions LC-DS-10m/s. This shows that high speed collisions produce high sudden impact force where displacement of ship remains constant. high speed collision will create more damage and produce higher inertia force against the direction of speed and are dangerous to the crews and loosen part and object are subject to severe damage.
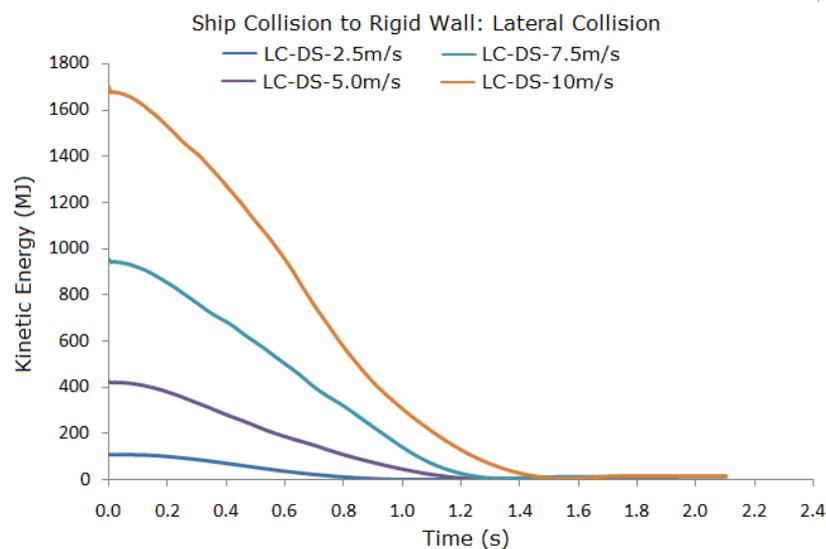
Figure 80: The Energy of Lateral Collision for Different Speeds.
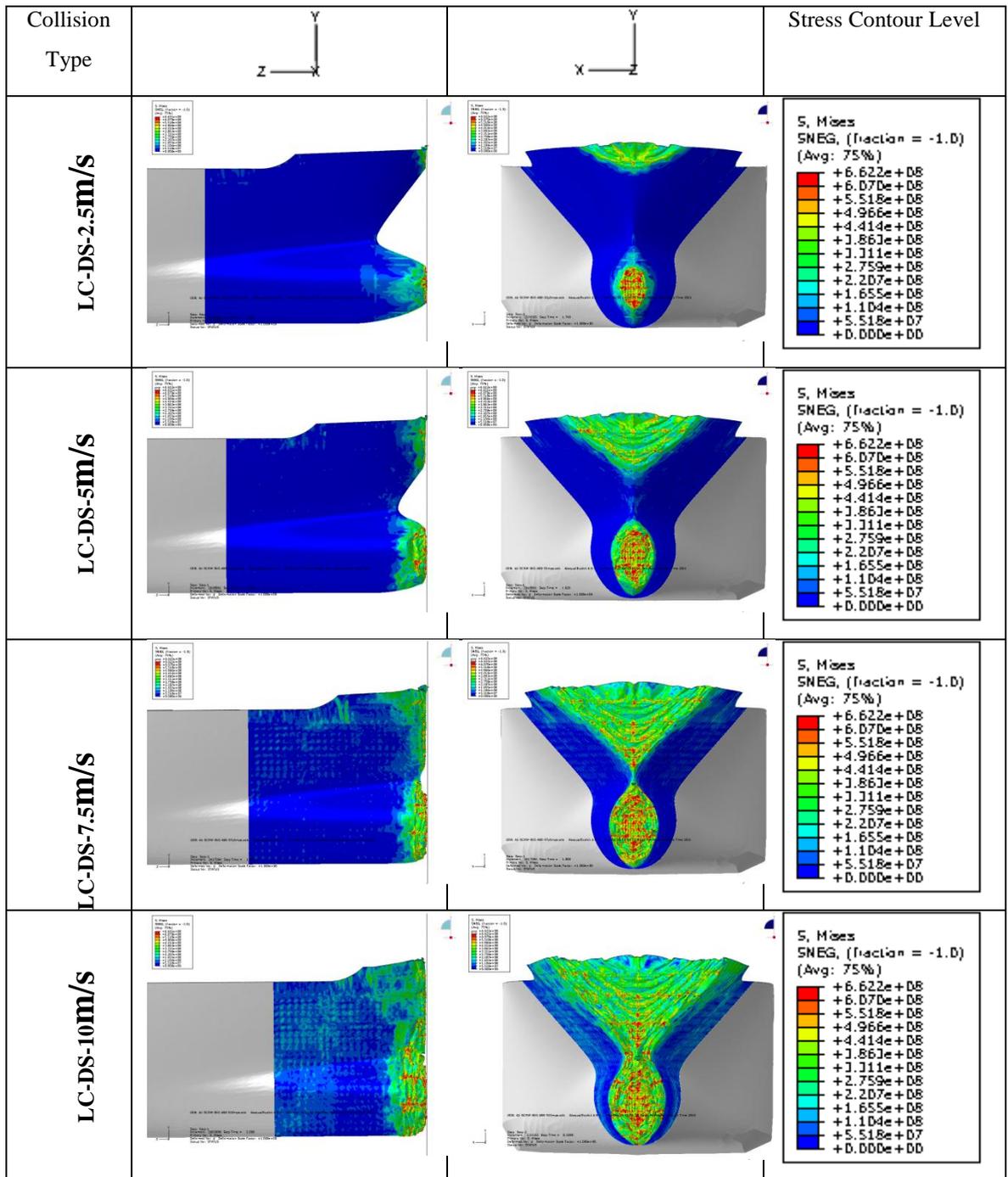
Figure 81: The Crushing Damage of Lateral Collision for Different Speeds.

Figure 81 shows the damage of lateral collision for different collision speeds. The damage of bow are predicted proportional to the increased speed of collision. The picture confirms the above discussion that the speed of a ship is main contribution of damage during ship collision.

7.4.2.3. Different Displacement

This section is to observe the effect of different ship displacement during collision where other variables such as collision speed and plate thickness are remain constant for in table 3. Figure 82shows the maximum force 301MN, 168MN, 146MN and 116MN for ship displacement 77MKg, 34MKg, 20MKg and 8MKg and collision duration 1.99s 1.57s, 1.06s and 0.58s respectively.
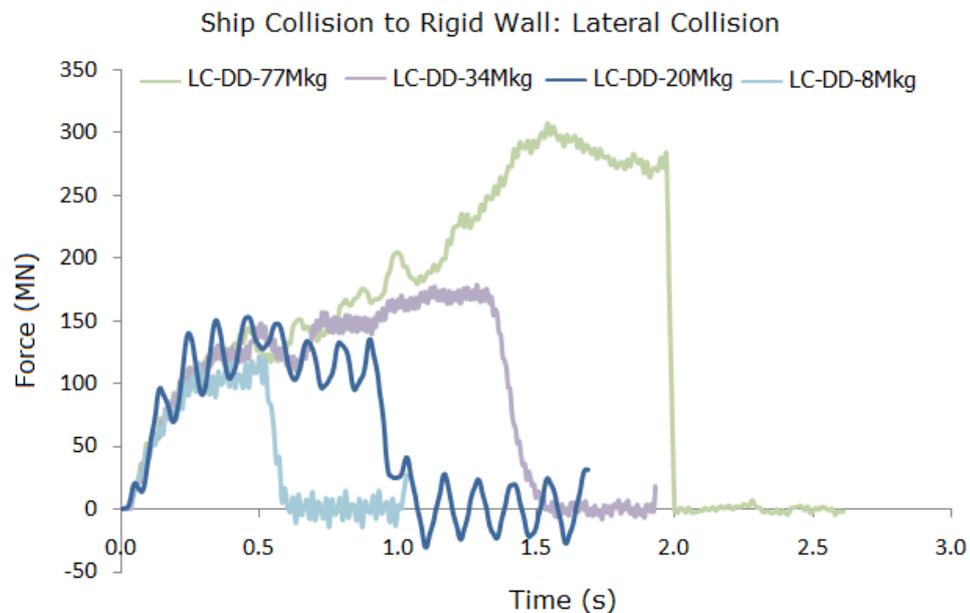
Figure 82: Force-Time of Lateral Collision for Different Displacement

Figure 83indicates that the force is gradually increased when the displacement of the ship increases. The path of the force gradient line also indicates that we can easily predict the impact force for the same ship when higher speed collision force is predicted. The crushing distances are 1.52m, 2.68m, 3.85m, 6.24m for ship model LC-DD-8Mkg, LC-DD-20Mkg, LC-DD-34Mkg, and LC-DD-77Mkg respectively.
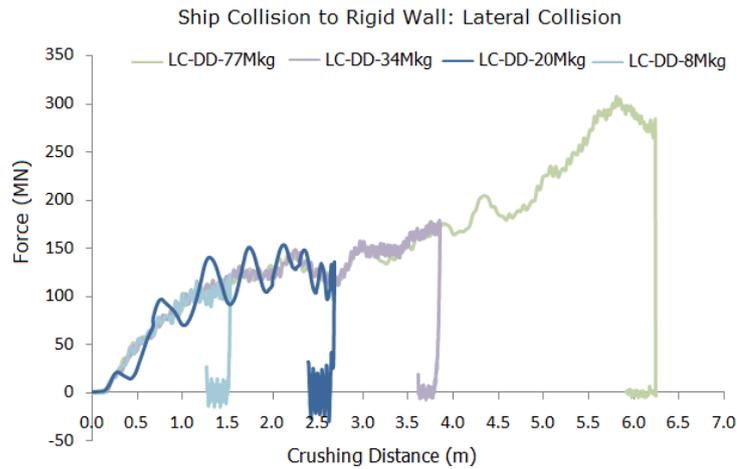
Figure 83: Force-Distance of Lateral Collision for Different Displacement.

Figure 84shows that kinetic energy experience almost same gradient of negative slope of energy dissipation before being fully absorbed by the rigidwall and damaged hull. This phenomena will help us to predict some kind of energy pattern for this kind of ship collision event when speed and thickness of plate remain constant.
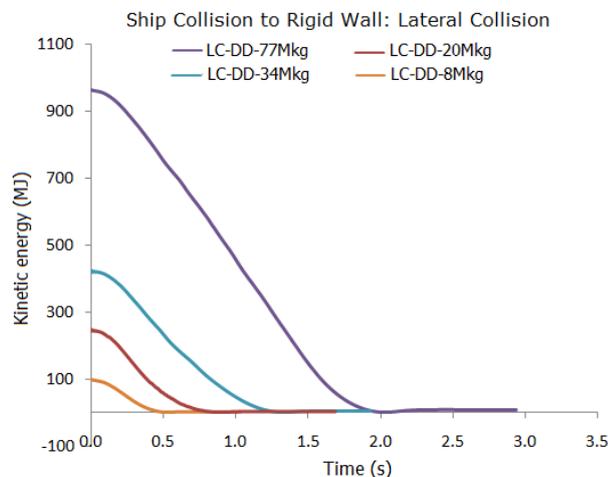
Figure 84: The Energy of Lateral Collision for Different Displacement.

Figure 85shows the same phenomenon as predicted where by increasing ship tonnage while the speed also plate thickness remain constant lead to an increase of ship bow damage. The figure also shows the cross section of ship damage where shell plating crumple together. This type of collision also produces minimal rupture to the shell due to shell plating being able to fold between them.

Collision Type			Stress Contour Level
LC-DD-8Mkg			
LC-DD-20Mkg			
LC-DD-34Mkg			
LC-DD-77Mkg			
LC-DD-77Mkg (Cut-Section)			
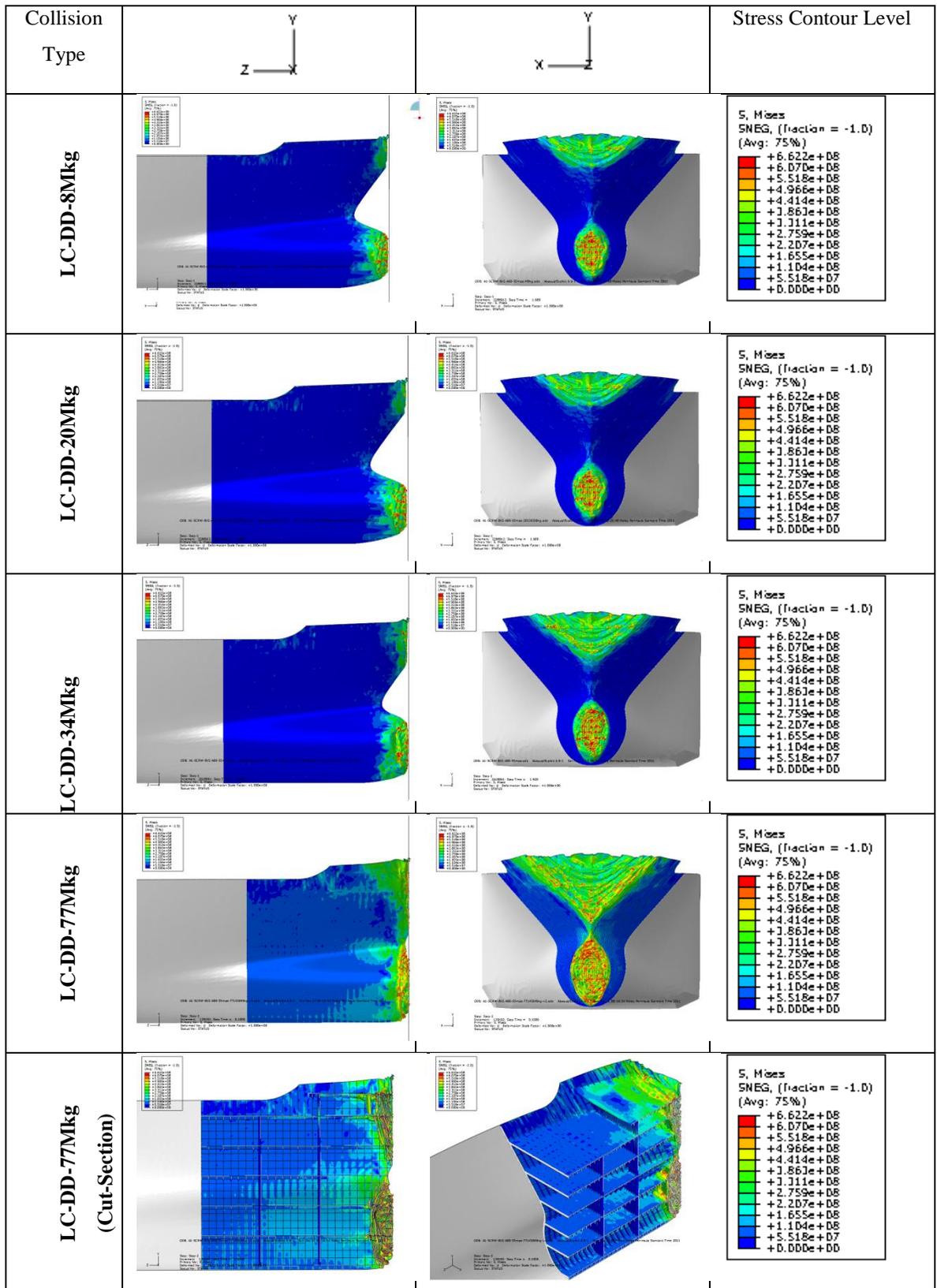
Figure 85: The crushing damage of Lateral Collision for Different Displacement.

7.5. Simplified Approach

The simplest and most conservative model, Figure 86a, is to assume that the ship structure remains perfectly elastic and the kinetic energy is completely transferred to the rigid wall for lateral collision and absorbed by the deformable structure. Figure 86b shows a simple elastic system, typically a spring with spring constant, K attached at the front of the rigid body with weight Mkg and moving with a velocity V struck to the rigid wall. The impact force F absorbed by spring and its equal and opposite reaction act to slowdown the object and compress the spring a maximum distance X_{max}. The calculations simply associate the work done absorbed by spring due to decreasing kinetic energy.
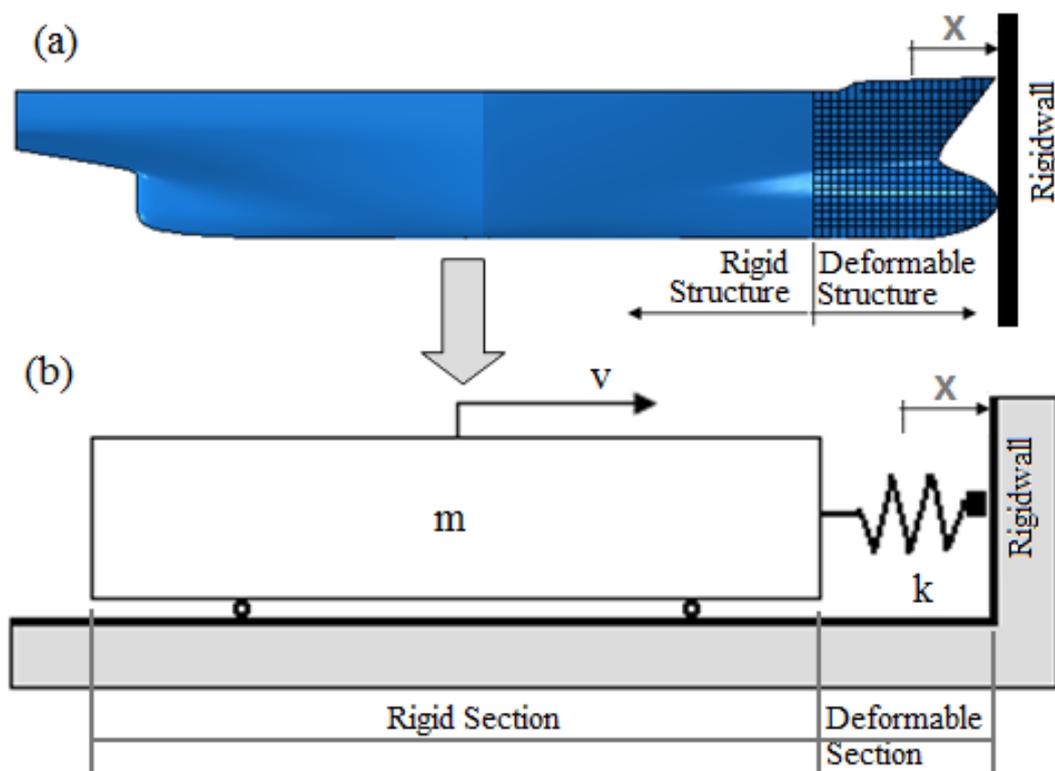
Figure 86: (a) Ship Collision Model (b) The Simplified Model of Ship Collision System.

$$\text{Kinetic energy } E_k = \frac{1}{2}MV^2 \qquad\qquad (7\text{-}8)$$

$$\text{Spring energy of deformation } E_s = \int_0^y F dx = \frac{1}{2} K x_{max}^2 \qquad (7\text{-}9)$$

A early assumption is that kinetic energy is absorbed by the spring when the ship starts to decelerate, then by equating (7-8) and (7-9) the kinetic energy to the spring energy,

$$E_s = E_k \qquad (7\text{-}10)$$

and

$$\frac{1}{2} K y_{max}^2 = \frac{1}{2} M V^2 \qquad (7\text{-}11)$$

Therefore

$$y_{max} = V \sqrt{\frac{M}{K}} \qquad (7\text{-}12)$$

Since the spring force, $F_{max} = K x_{max}$ $\qquad (7\text{-}13)$

$$F_{max} = \sqrt{2 K E_K} \qquad (7\text{-}14)$$

$F_{max} = V.\sqrt{KM}$ This is equal to Eurocode. $\qquad (7\text{-}15)$

As we know equation (7-14) is only true when equivalent stiffener K is specified for the model and not valid when the average thickness of the forward part of the ship structure is changed while the weight of the ship remains or is considered unchanged due to a small change in the weight of the ship (see LC-DT case Results). Thus, the prediction of crushing force is inaccurate at certain cases. Therefore, equation (7-15) is modified to generate better prediction results for crushing forces where the rigidity of the forward part and the average plate thicknesses role are included as a coefficient variable and introduced in equation (7-16);

$$F_{max} = t_{avg} R\eta V\sqrt{KM} \tag{7-16}$$

Where;

    Fmax = Maximum Crushing Force (N)

    M   = Ship displacement (kg)

    η = Efficiency

    t_{avg} = Average of plate thicknesses (mm)

    K   = Equivalent stiffener (N/m)

    V   = Ship collision speed (m/s)

    R   = Mass of effected area/ (volume of effect area x Density)

    Rigidity of structure range between 2.5% – 10%
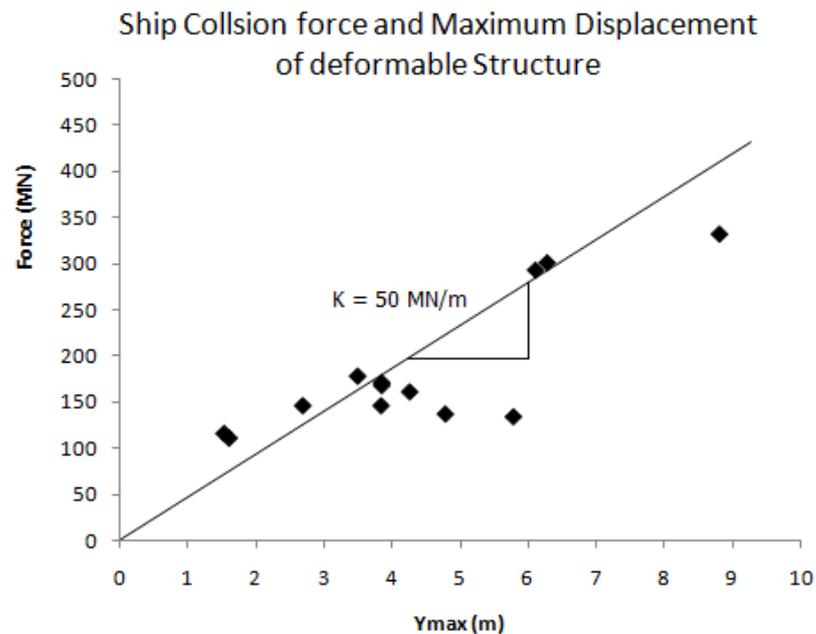
Figure 87: The Equivalent Stiffness

The regression of equivalent stiffener constant is taken from Figure 87generated from FE analysis about 50MN/m and the corresponding regulations in 1991-1 Eurocode 1 (ENV, 1994) equivalent stiffener are a bit smaller ranging from 5MN/m for inland waterway vessels and 15MN/m for sea going vessels(Fan et al., 2008)

Figure 88 shows the regression of rigidity value, when rigidity increase the crushing distance is reduced and knowing also the collision force is increasing proportionately
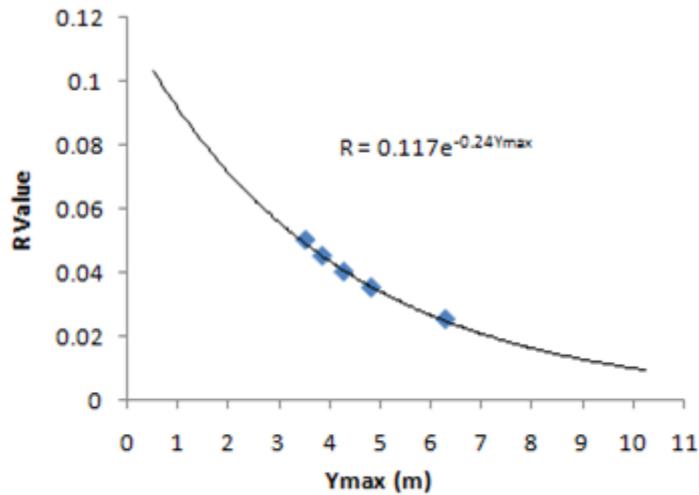
Figure 88: The Regression of Rigidity Variable for Bow Crushing Distance.

Figure 89 shows the efficiency of energy absorbed during collision in relation to coefficient friction for different materials and ship collision angles. The 0.35 coefficient of friction is used in equation (7-16) due to tight correlation between energy and force for the aspect of efficiency in prediction force of ship during collision.
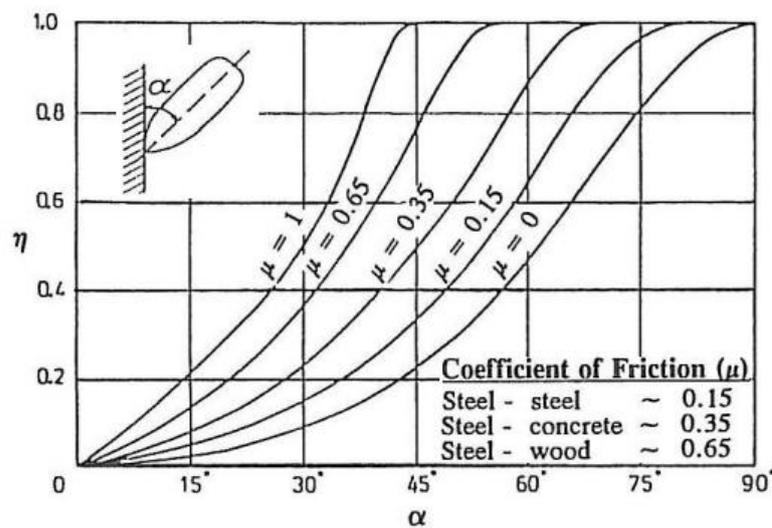
Figure 89: The efficiency of absorbed energy in relation to coefficient of friction and collision angle (Saul and Svensson, 1982).

Although a spring was used to illustrate the process, the actual elastic body could be any deformable structure for which the deformation can be estimated. This approach is conservative because it ignores damping, friction and any inelastic deformation or other energy absorption mechanisms. The approach produces reasonable results for assessing ship collision damage.

Table 7 shows the results of a simplified prediction compared with ASHTO, Woisin and Eurocode prediction. The prediction results for angle collision are show a good correlation between FEA results and current simplified prediction. In any occasion Pederson always shows high prediction results and Woisin shows very low prediction force when not adding a 50% margin. ASSTHO and Eurocode shows relatively good results but is not capable of capturing the effect of thickness of plate changes especially when compared to simulation results for case LC-DT. New approach prediction shows a good correlation when compared to FEA results where most of the cases produce errors of less than 30% unless in the case of LC-DT-10mm which produced a very high error of about 157%. The simplified formula also show thinner plate structure and low ship displacement generate less accurate results but in overall produce very promising results.

Figure 90 shows a relationship between ship collision forces against distance to the stopping of the ship after collision and rigidity effect for various ship tonnages using simplified formula discuss above. The negative slope of the graph shows an estimation of ship collision force and distance taken to stop after collision of ship. The positive slope of the graph shows the effect of rigidity of collision force of ship structure that refers to ship tonnage accordingly. The results of the graph are generated by using simplified formulas from equation (5-16) and equation in Figure 88. The graphs also show the ideal region for ship tonnage (10Mkg-200Mkg), rigidity values of forward ship structure (0.025-0.07) and distance taken to stop for ship after collision between 2.5m – 7m.

In the graph if we take case 1 scenario for 120Mkg ship tonnage and striking ship with speed 5m/s, the generated force for this collision = 401.38MN,

crushing distance for ship to completely stop before bouncing back to the opposite direction D1= 5.746m, rigidity value R1= 0.05746 and average thickness of forward ship structure = 20.76mm. For the case 2 scenario for 120Mkg ship tonnage and striking ship with speed 10m/s, the generated force for this collision = 399.32MN, crushing distance for the ship to completely stop before bouncing back to the opposite direction D2= 5.892m, rigidity value R2= 0.02868 and average thickness of forward ship structure = 18.17mm. For case 3, with an estimate ship collision force =692.15MN, the striking ship stop at crushing distanceD3=3.554m and R3=0.04988.

Table 7: The comparison of energy and force absorption.

Damage Condition	Rigidity	FEA Result				Efficiency (η)	Pedersen (MN)	ASSHTO (MN)	Woisin (+50%) (MN)	Eurocode (MN)	New Approach	
		Kinetic energy (MJ)	Plastic Energy (MJ)	Force (MN)	Crushing Distance (m)						Absorbed energy (MJ)	Collision Force (MN)
AC-A30	0.045285	1726	117	69	1.00	0.226	-	-	-	-	37	75
AC-A45	0.045285	1726	497	177	1.20	0.495	-	-	-	-	55	91
AC-A60	0.045285	1726	1568	313	2.00	0.867	-	-	-	-	210	210
AC-A90	0.045285	1726	1665	332	1.90	1.00	194	227	245	228	322	339
LC-DT-10mm	0.025158	432	410	134	6.20	1.00	194	113	245	114	162	52
LC-DT-14mm	0.035221	432	410	137	4.75	1.00	194	113	245	114	243	102
LC-DT-16mm	0.040253	432	410	161	4.25	1.00	194	113	245	114	284	134
LC-DT-18mm	0.045285	432	410	146	3.75	1.00	194	113	245	114	317	169
LC-DT-20mm	0.050316	432	410	178	3.40	1.00	194	113	245	114	355	209
LC-DS-2.5m/s	0.045285	108	103	111	1.50	1.00	194	57	245	57	63	85
LC-DS-5m/s	0.045285	432	415	171	3.80	1.00	194	113	245	114	322	169
LC-DS-7.5m/s	0.045285	971	929	293	6.00	1.00	194	170	245	171	762	254
LC-DS-10m/s	0.045285	1726	1667	332	8.80	1.00	194	227	245	228	1490	339
LC-DD-77Mkg	0.045285	964	948	301	6.75	1.00	194	169	367	170	854	253
LC-DD-34Mkg	0.045285	429	415	168	3.75	1.00	194	113	244	113	316	169
LC-DD-20Mkg	0.045285	257	243	146	2.60	1.00	194	87	189	88	170	131
LC-DD-8Mkg	0.045285	107	97	116	1.60	1.00	194	56	122	57	68	84
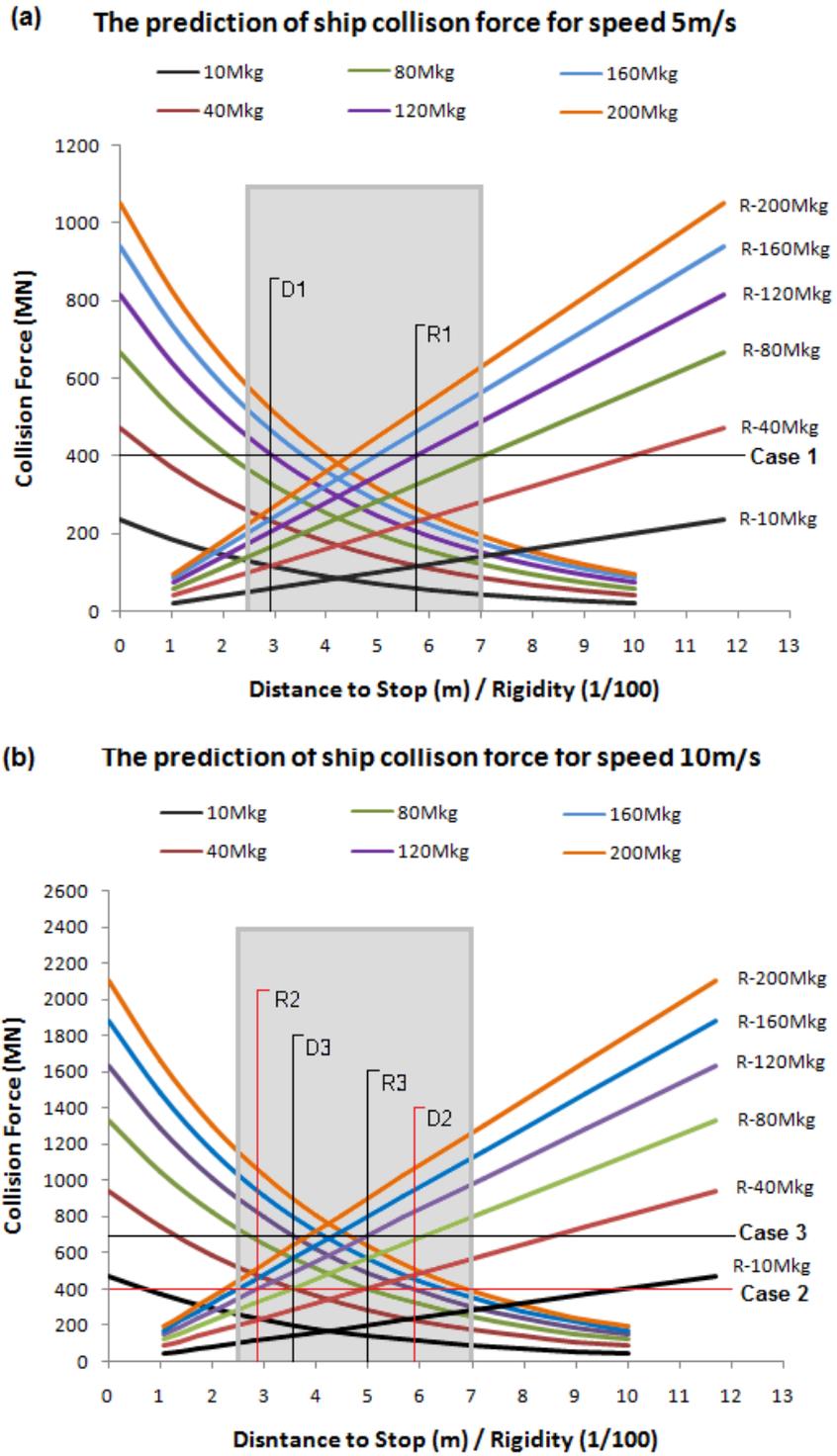
Figure 90: The Force, Crushing Distance, Ship Displacement and Rigidity Prediction of Ship Collision.

1. H. Svensson Newport bridge RI, USA, damage to ship

2. Newport bridge RI,USA, damage to pier

3. Simulation of ship damage at speed 10m/s
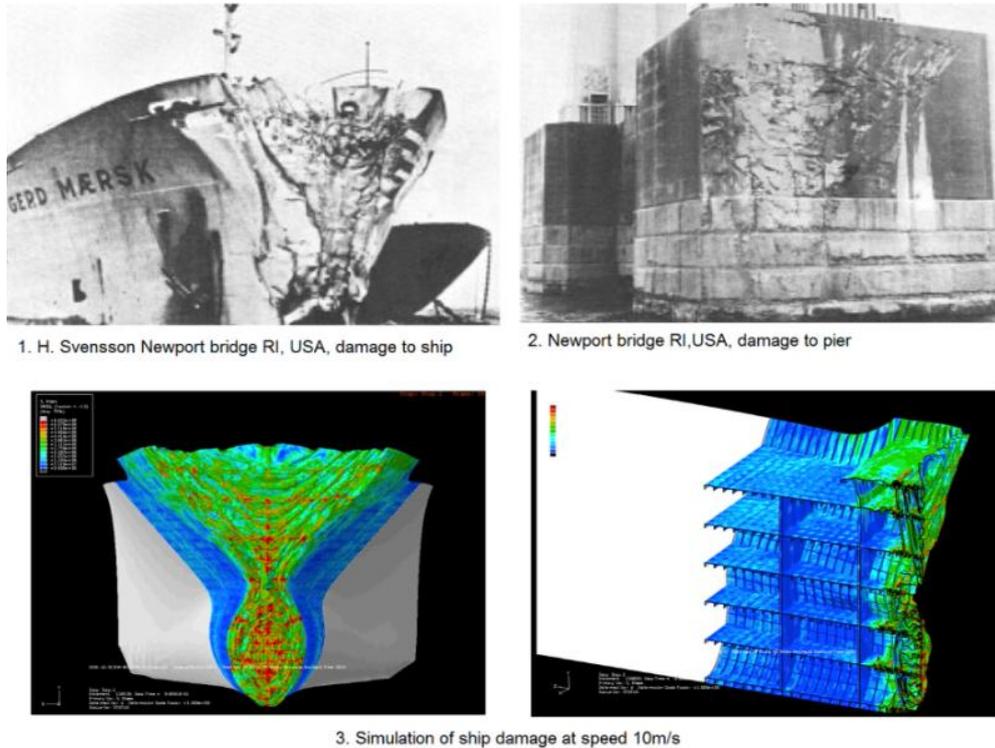
Figure 91: The Simulation Collision Damage and Actual Ship Collision Damage (Svensson, 2009).

7.6. Summary

The study shows that the FEA results produced are comparable with available empirical formula and show good agreement with (Woisin, 1979) only (Terndrup Pedersen et al., 1993b) shows significant differences. The simulation damage also gives a very convincing picture of damage when compared with actual incidents(Svensson, 2009) as illustrated in Figure 91.

The simplified method introduced also gives good agreement with the empirical formula when added rigidity value of forward part of ship structure and thickness of plate effect except when compared with (Terndrup Pedersen et al., 1993b). The introduced method is also capable of capturing the lateral

collision and angle collision effect when coefficient of efficiency of absorbed energy in relation to friction and collision angle is included. The introduced method is also valuable for predicting absorbed energy and impact forces in events of extreme collision and estimate the damage.

Overall, the results obtained from the FEA simulations of ship collision to rigidwall is acceptable and the simplified method introduced show good agreement as mentioned to predict ship collision damage.

CHAPTER 8: SHIP-SHIP COLLISION

8.1. Introduction

Generally, ship-ship collision modeling involves a very difficult coupled problem between the response of the water and the structural deformation of the ships and is also very costly. During a collision, kinetic energy is absorbed by structural deformation of the ships and by motion of the water (Ammerman and Daidola, 1996). However, study of previously published analyses that used a loosely coupled approach (Lenselink and Thung, 1993), showed the amount of kinetic energy that is dissipated in structural deformation is nearly the same whether or not the water is explicitly included in the analyses. Therefore, in this study the water is not explicitly modeled and struck ship is treated as a stationery ship. The effect of water is consider as added mass to the struck ship. Following the method of Minorsky (Minorsky, 1959), added mass is equal to 40% of the mass of the struck ship being used.

In this chapter, eighteen analyses were performed and this is an extension of the study from chapter 7. The studies are divided into 3 main sections which look at ;

    i) Control displacement of rigid bow collision to deformable ship side,
    ii) Energy dissipation of rigid body of ship collision to ship side and
    iii) Deformable of ship bow collision to deformable of ship side.

The control displacement collision is a setup where the displacement and time of bow penetration is set prior simulation analysis. The energy dissipation of ship-ship collisions are further divided into two categories which are lateral collision and angle collision of ship-ship interaction. These collision studies mainly monitor the force and energy dissipation until the kinetic energy fully absorbed or goes to zero. The deformable ship-ship collision is simulated only for lateral collision and at 50 degrees on inclination angle and it is a very expensive simulation.

The actual collision study is a replicate from an actual incident discussed in (AbuBakar et al., 2010)wherein 2001 a 34,365 DWT bulk carrier collided with

a 37,000DWT tanker carrying 33,000 tons of heavy fuel oil in the Baltic. During the incident the bow of the bulk carrier largely penetrated a ballast and a cargo tank whereas the bow of the bulk carrier suffered considerable damage. The damage was described in (THE REPUBLIC OF THE MARSHALL ISLANDS)as follows:

"The bow of the TERN penetrated approximately 5 meters into the double hull of the BALTIC CARRIER on the starboard side and holed the side shell plating between frames 43 and 60. The starboard #5 wing ballast tank and the #6 starboard cargo tank on the BALTIC CARRIER were opened vertically from the main deck to a point well below the waterline. The double bottom tanks located below the damaged ballast and cargo tanks remained intact. Damage to the TERN involved the bulwark, stem, and bow plating on both sides of the hull in way of the forepeak tank and deck storeroom, and included the collision bulkhead. The shank of the port anchor on the TERN was broken and the flukes were missing as a result of the impact from the collision"

The present work attempts to simulate a collision of two ships having the same particular dimensions as the ships involved in the incident. It is to be understood that since not all data needed for the simulation were available, the authors had to make assumptions that were mostly related to the structure of the collided ships.

8.1.1. Ship Particulars

Struck Ship (Baltic carrier)

Length	175.00 meters
Breadth	27.34 meters
Depth	16.70 meters
Maximum Draft	10.850 meters

Striking Ship (Tern)

Length	174.96 meters
Breadth	26.00 meters
Depth	15.50 meters
Maximum Draft	11.148 meters

8.1.2. Structure geometry

Figure 92: (a) Bulbous bow (b) Normal bow and (c) Mid-ship section details (not in scale).

8.2. Collision of Displacement Control

The main focus of control displacement collision of ships is to study the effect of the different bow collision and the effect of mesh sizes for a large volume of meshes in relation to the force and energy produce during collision. Two types of bow indentified where bulbous bow and normal bow as shown in Figure 93.
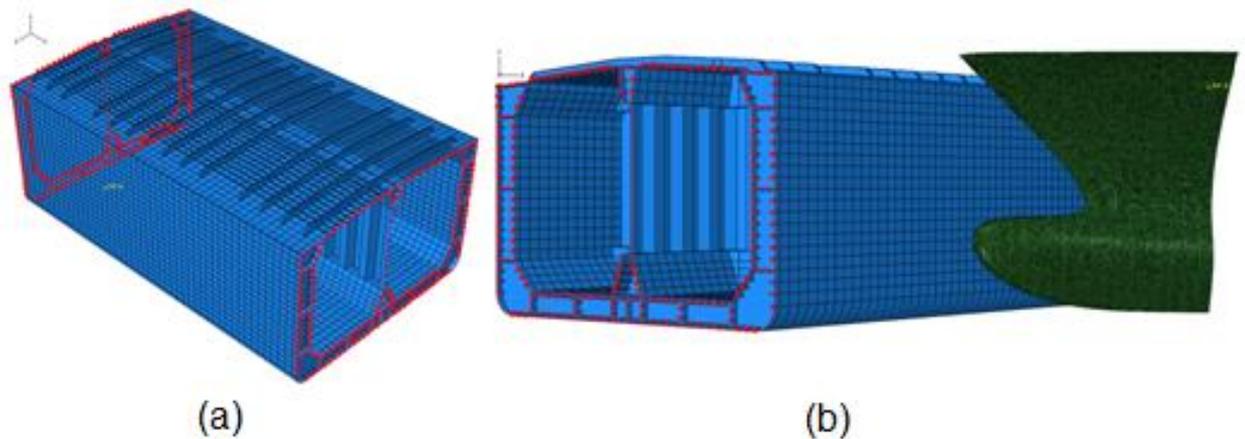
Figure 93: The boundary condition (red marks).

The geometry of the struck ship (double hulled tanker) and the geometry of the two alternative bow shapes used in the analysis are shown in *Figure 92* and Figure 93 respectively.

8.2.1. Simulation of Structural Response

The structural model chosen to represent the struck ship was that of a complete compartment plus half a compartment on either side to remove the influence of boundary condition effects from the area of interest.

Mesh sizes of 60mm and 80mm were chosen for the simulations carried out. The struck ship was assumed to be at rest with the striking bow having a relative speed of 10m/s and assumed to decelerate to an absolute stop when

maximum penetration was achieved. The actual collision between the two vessels was reported to have occurred at an angle of approximately 50 degrees, for this study,   collision angles of 50 and 90 degrees were investigated. The analysis utilised a structured quadrilateral dominated mesh for both fine mesh and coarse mesh regions and an unstructured mesh for the transition region.

The boundary conditions on the FE model were set as ENCASTRE (fully fixed) for both ends of compartment see Figure 93a and b. The impact point was set at a main transverse frame in the centre of the compartment for both collision scenarios considered using a rigid body representation of the bow.

8.2.2. Simulation Results

The lateral penetration and resultant force of rigid normal and bulbous bows, obtained from the FE simulations, are shown in **Figure 94**(a) and (b) respectively. In Figure 94a, the force on the bulbous bow BX, BY and BZ for 60mm and 80mm mesh size show good agreement with the scaling of FLD_0, this gives a level of confidence that the theoretical modelling of failure strain and characteristic element length can be successfully applied to a large structure.
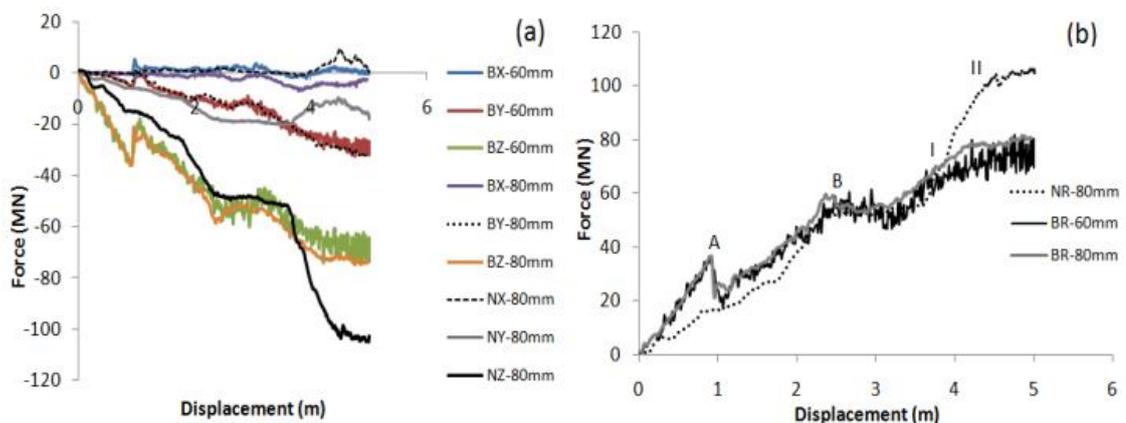
Figure 94: (a) Force - displacement of lateral penetration (b) resultant force - displacement of lateral penetration.
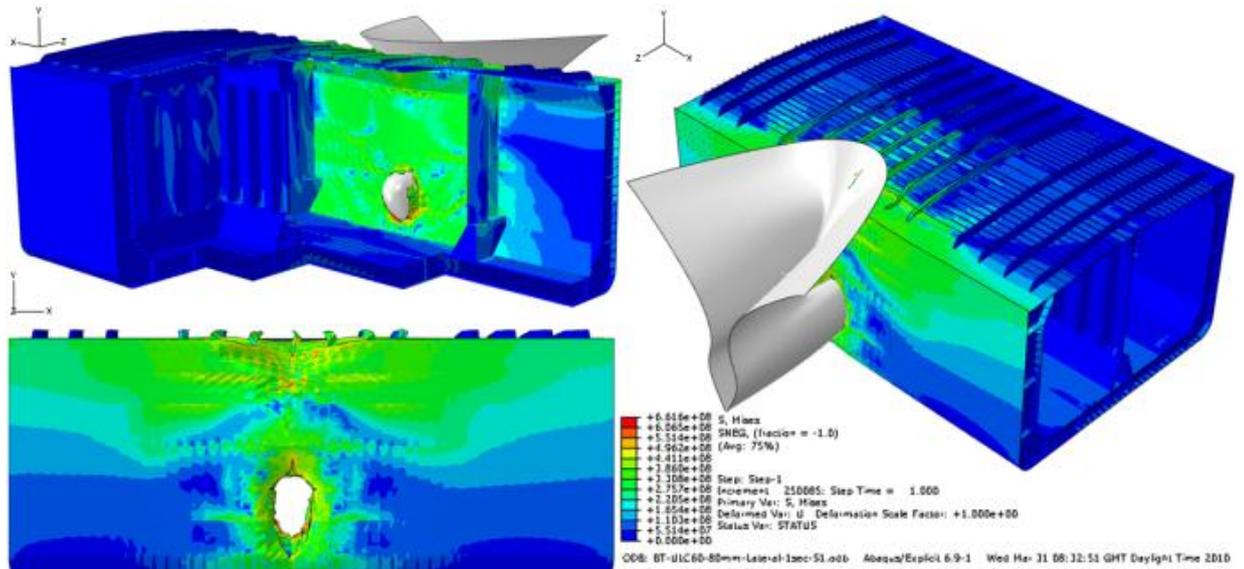
Figure 95: The lateral penetration of rigid body of bulbous bow penetrated to double side shell of Baltic tanker.

For the normal bow (NR-80), Figure 94 shows the vertical stem start to penetrate the outer shell at point I (3.67m, 59MN); at point II (4.52m, 106MN) it shows the outer shell onset of rupture.

For bulbous bow (BR-60mm and BR-80mm) the different mesh refinements give close results, where outer shell rupture is predicted at point A (0.97m, 25.88MN) and inner shell rupture at point B (2.7m, 56.12 MN).
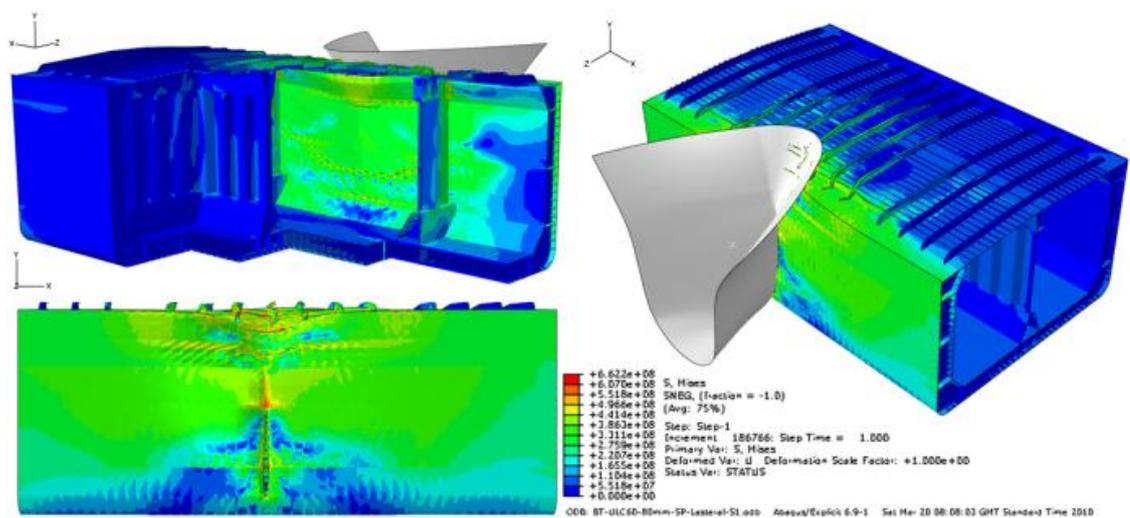
Figure 96: The lateral penetration of rigid body of normal bow penetrated to double side shell of Baltic tanker.

Figure 95 and Figure 96show the different deformation shapes produced by the penetration of a bulbous bow and a normal bow. The bulbous bow produces more severe damage compared to the normal bow at the same collision speed. The collision of the bulbous bow causes rupture of the inner hull which is not apparent during the collision with the normal bow.

The simulation with the normal bow produces a stress distribution, as shown in Figure 96. Figure 95 shows the same stress distribution for the bulbous bow. The bulbous bow stress distribution shows higher stress concentrations, as would be expected, than the normal bow. These results reinforce the idea that bulbous bows should be designed to absorb energy during a collision event to reduce the resulting levels of damage to the struck ship.

The Finite Element results for the forces produced during the 50 degree collision angle simulation are shown in Figure 97. Figure 97a shows the individual components of force with the resultant force being shown in Figure 97b. Results are presented in these figures for both the normal and bulbous bow simulations

These simulations attempt to replicate the actual collision incident of bulk carrier Tern with the Baltic oil tanker. These simulations were carried out to produce a penetration depth of 8.4m for a striking angle of 50^0 to side shell which is equivalent to a damage depth of 6.5m. This should provide damage levels equivalent to the actual damage suffered by the Baltic tanker.
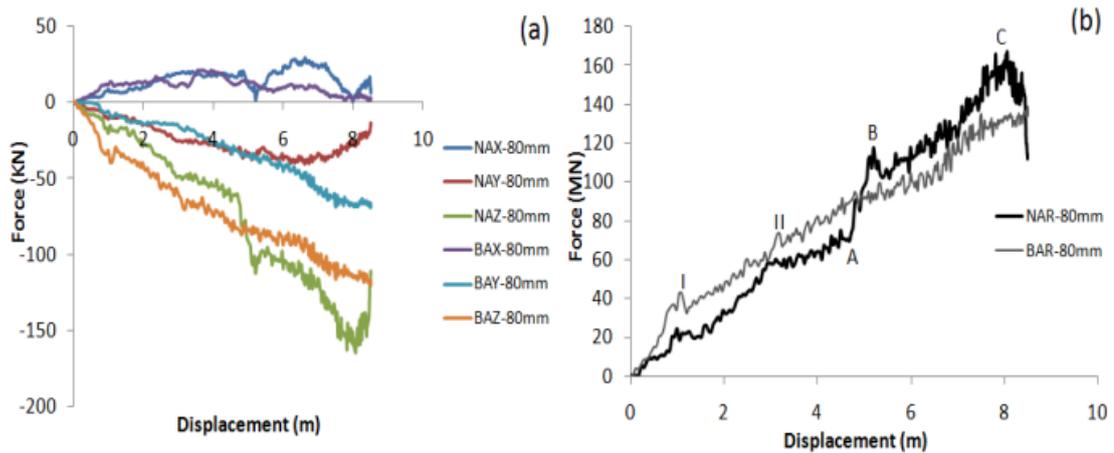
Figure 97: (a) Force - displacement of 50^0 collision angle. (b) Resultant force - displacement of 50^0 collision angle.

Figure 97a, shows the magnitude of the force acting during penetration for both bow forms in X, Y & Z direction, these results can be compared with the levels of damage shown in Figure 97b. The results for the bulbous bow show the outer shell and inner shell rupture at point I (1.1m, 42.5MN) and point II (3.2m, 73.14MN) respectively.

The curve of resultant force for the normal bow starts to increase at point A (4.7m, 76.85MN) when the flat vertical stem comes in contact with the side shell, with the rupture of outer shell and inner shell occurring at point B (5.23m, 112MN) and point C (8.16m, 156MN), respectively.

Figure 98 and Figure 99, show the severe levels of damage to both the outer shell and inner shell that occurs for both bow shapes. This is in line with the levels of damage that occurred during the actual collision incident. The damage levels produced from the simulation appear to be less severe than the actual damage due to the reduced level of penetration of inner shell and the unknown value of stem angle of the striking ship. The bigger the stem angle the more severe the level of damage that will occur during the collision when the bow is modelled as being rigid.
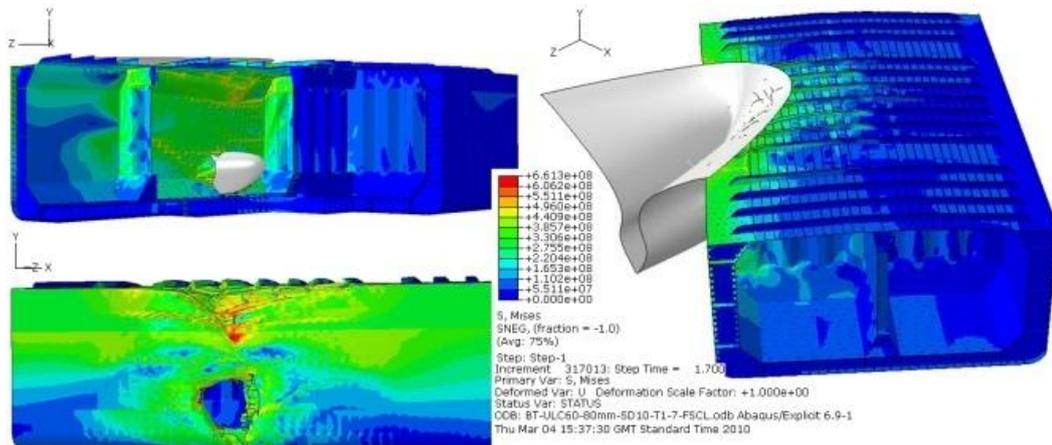
Figure 98: The rigid body of bulbous bow penetrated to double side shell of Baltic tanker at 50^0 collision angle.

These parameters are probably not the main contributors to the damage during collision of rigid body bow, others such as beam, depth and bulbous bow shape will have a significant influence on the levels of damage and the onset of rupture.

The energy dissipated during both the 90 and 50 degree collision scenarios are presented in Figure 100a and b respectively. The right-angle scenario always demonstrates larger levels of energy to rupture for both outer shell and inner shell.
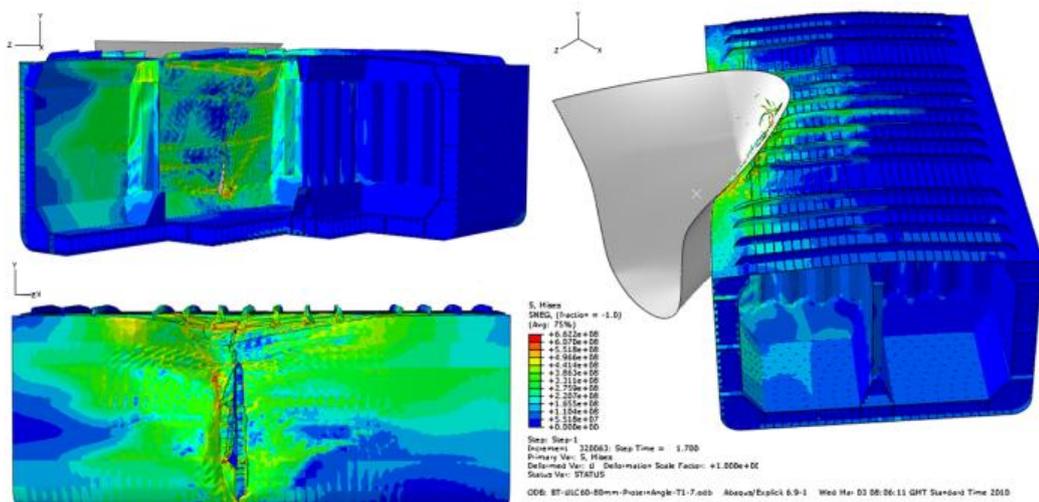
Figure 99: The rigid body of normal bow penetrated to double side shell of Baltic tanker at 50^0 collision angle.

The graphs for the 90 degree collision scenario for both normal and bulbous bow penetration energy, Figure 100a, for both mesh sizes BL-60mm and BL-80mm produce very similar results. The outer shell and inner shell of the struck ship ruptured at 17.7MJ and 85.7MJ, respectively during the collision with the bulbous bow. The outer shell of the struck ship ruptured at 184MJ with no rupture of the inner shell during collision with the normal bow. The collision penetration energy peak at 230 MJ for all meshes and both bow shapes using the same weight/displacement input parameters.
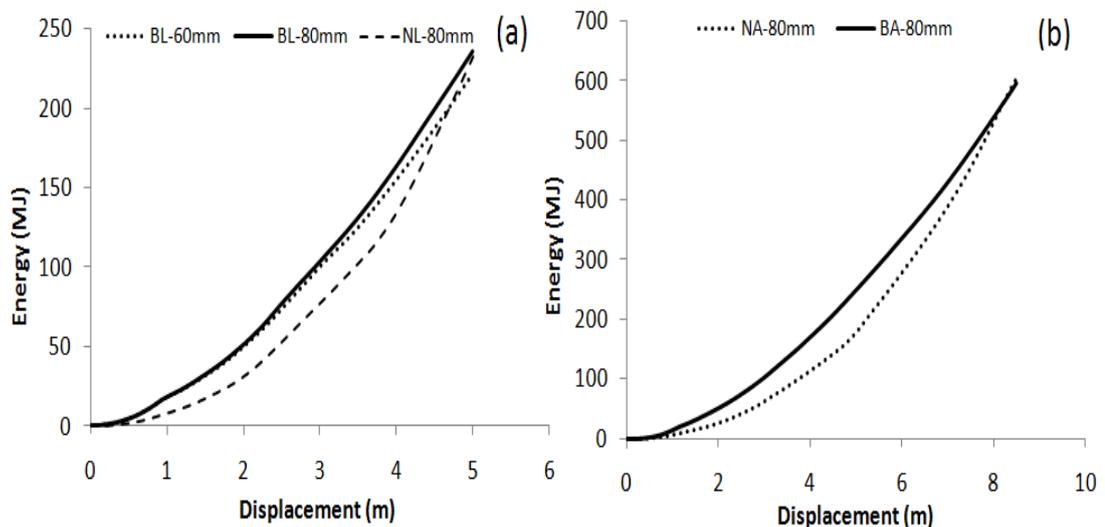
Figure 100: (a) The lateral penetration energy-displacement (b) The 50^0 collision angle penetration energy-displacement.

The results for the 50 degree collision angle simulation are presented in Figure 100b, the rupture of outer shell and inner shell occur for both types of bow collision simulations. Outer shell and inner shell ruptured at 202MJ, 556MMJ for the normal bow shape and 18.5MJ, 125MJ for the bulbous bow shape, respectively. The collision energy peaked at the same point for both collision scenarios with a peak of 600MJ.

8.3. Energy Dissipation Collision

The energy dissipation is a simulation of ships collision where the initial velocities of striking rigid body ship is set at centre of mass and degree of freedom of lateral movement and rotation are allowed in all X, Y and Z direction. The main ship dimension are taken from (THE REPUBLIC OF THE MARSHALL ISLANDS). The striking ship particulars is referred to section 8.1.1 and the struck ship structure geometry is refereed to *Figure 92*c. The simulation will observe the effect of lateral collision and angle collision that included different setup of collision angle, speed and displacement of ship (see Table 8).

Table 8: The rigid body of striking ship simulation matrix

Damage Condition		Initial	Ship Displacement (Mkg)	Initial Velocity (m/s)	Collision Angle (0^0)
Angle Collision		A90	34.29	10	90
		A70	34.29	10	70
		A50	34.29	10	50
		A30	34.29	10	30
Lateral Collision	Different Speed	DS-10m/s	34.29	10	90
		DS-7.5m/s	34.29	7.5	90
		DS-5.0m/s	34.29	5.0	90
		DS-2.5m/s	34.29	2.5	90
	Ship Displacement	DD-73.51Mkg	73.51	5	90
		DD-34.29Mkg	34.29	5	90
		DD-20.22Mkg	20.22	5	90
		DD-8.58Mkg	8.58	5	90
	Deformable Ship-ship Collision	DEF-A90	34.29	10	90
		DEF-A50	34.29	10	90

8.3.1. Angle Collision

Figure 101 and Figure 102show the force-displacement and Force-Time of rigid body striking ship, struck a deformable structure of ship side respectively. The rupture force, time and displacement for outer shell and inner shell indicate (A90=31.1MN, 0.09s, 0.9m), (A70=25.6MN, 0.072s, 0.72m), (A50=61.9MN, 0.108s, 1.08m), (A30=21.2MN, 1.11s, 10.84m) and (A90=58.4MN, 0.27s, 2.68m), (A70=78.1MN, 0.228s, 2.85 m), (A50=75.5MN, 0.36s, 3.52m), (A30=No rupture) respectively.

The rupture time for both outer and inner shell shows that larger collision angle employed less time to rupture the shell, except for A30 where no rupture took place. These phenomena occur when sliding of striking ship dominate at smaller collision angle instead of directly penetrating the struck ship at a large collision angle.

The rupture force shows that collision angles larger than 50^0 are closer to each other compared to collision angle at 30^0 and this is actually aligned with the prediction by (Minorsky, 1959) where the collision angle closer to a 90^0 angle of attack produces almost similar results in the prediction.

The maximum of penetration force for A90=106MN, A70=92.6MN, A50=98.89MN and A30=41.5MN and the striking ship are stopped before bouncing back at time and displacement as follows (A90= 5.4s, 28.83m), (A70=5.472s, 27.84m), (A50= 4.536s, 24.36m) where for A30 the striking ship kept moving due to most of her energy not being transferred to the struck ship.
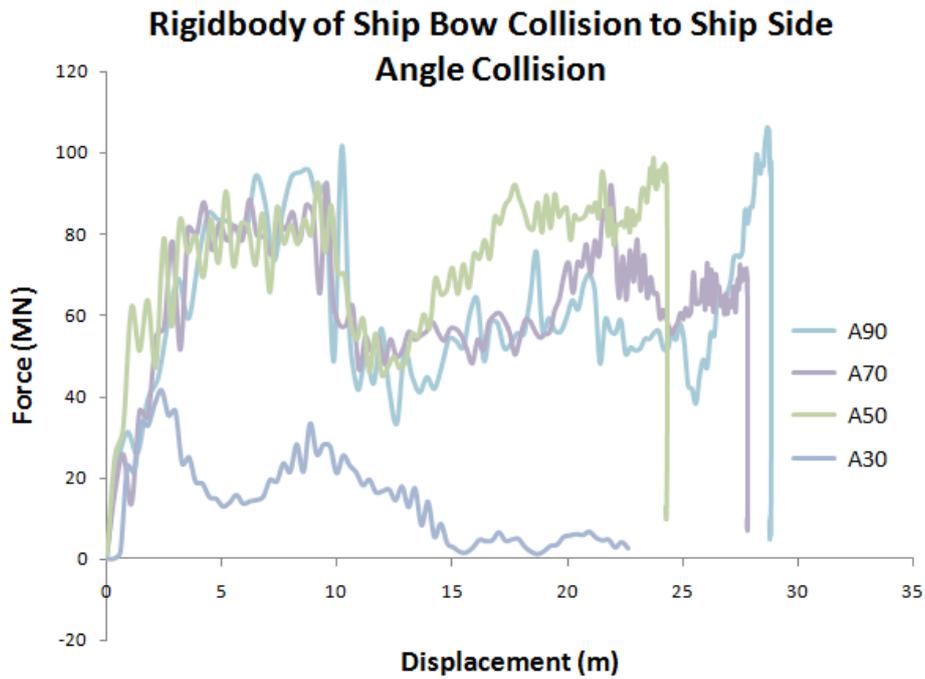
Figure 101: The Force-Displacement of rigid body of striking ship, struck to ship side for different angle setup.
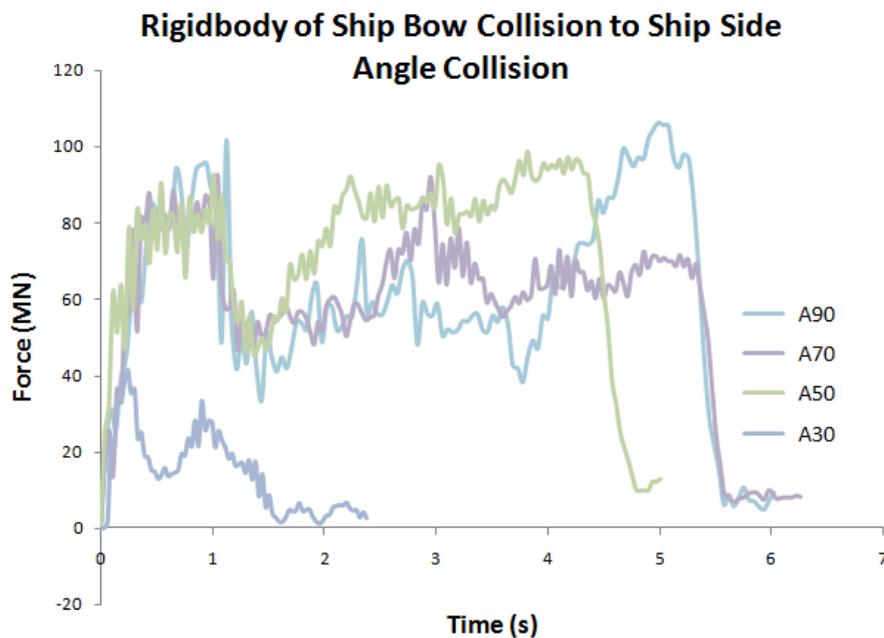
Figure 102: The Force -Time of rigid body of striking ship struck to ship, side for different angle setup.

Figure 103 and Figure 104 shows dissipation of energy of striking ship in relation of displacement and time respectively during collision. The kinetic energy is equal to the mass multiplied by the square of the speed, multiplied

by the constant 0.5, where the initial value 1710MJ before experience of degradation due to being absorbed by the struck ship. The graph also shows all the collision energy is fully absorbed by the struck ship except for A30. Striking ships for A90, A70 and A50 are stopped still completely before bouncing back in the opposite direction with some rotation for A70 and A50 striking ships. The A30 striking ship kept moving after the collision with a slight deviation with mild angle toward sliding each other as well settled at 1550MJ residual energy and kept ahead away with no contact between them.

The rupture energy, displacement and time for outer and inner shell initiated at (A90=13.6MJ, 0.09s, 0.9m), (A70=9.87MJ, 0.072s, 0.72m), (A50=30.2MJ, 0.108s, 1.08m), (A30=125MJ, 1.11s, 10.84m) and (A90=77.8MJ, 0.27s, 2.68m), (A70=95MJ, 0.228s, 2.85 m), (A50=170MJ, 0.36s, 3.52m), (A30=No rupture) respectively.

The graphs also show that more energy was needed to rupture the inner and outer shell when reducing the collision angle of attack of striking ship relative to struck ship. This indicates that the captain always needs to ovoid larger collision angle, especially lateral collision, to reduce severe damage for both vessels.
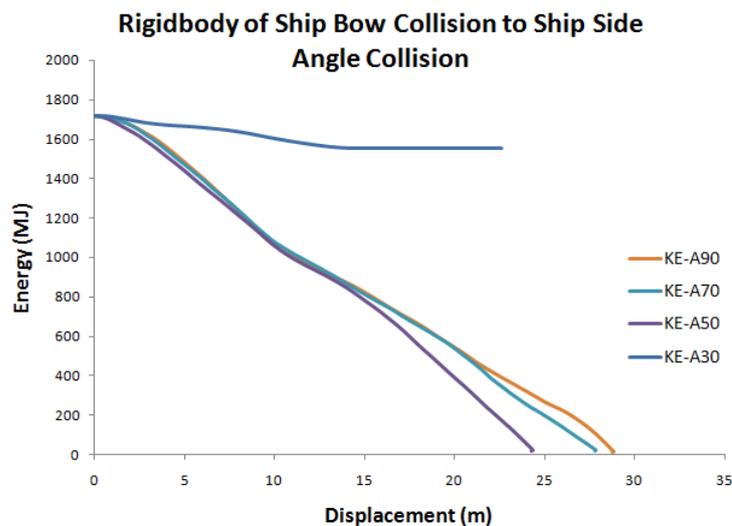
Figure 103: The Energy -Displacement of rigid body of striking ship, struck to ship side for different angle setup.
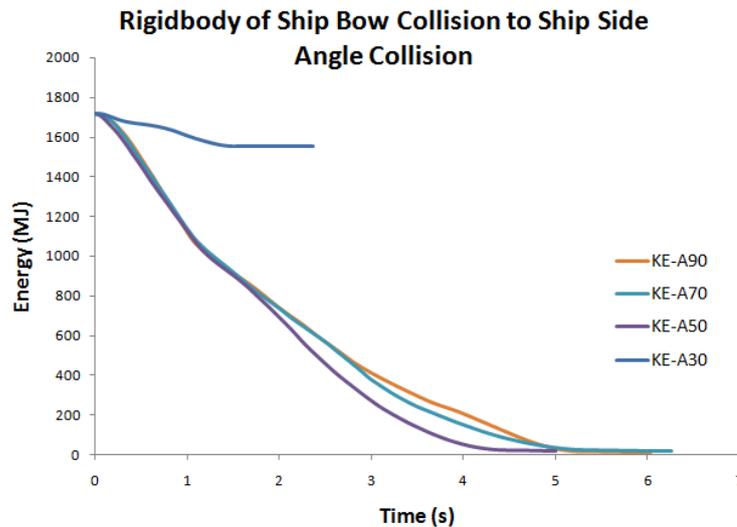
Figure 104:The Force -Displacement of rigid body of striking ship, struck to ship side for different angle setup.

Figure 105 - Figure 108, show, the damage condition of struck ship during collision for A90, A70, A50 and A30. Figure 105 shows that rigid body striking a ship at a 30^0 angle of attack smearing into struck ship and slides along the struck ship with some vertical inclination angle, clearly shown after time=1.02s. The initial rupture initiates at time=1.02s and graduals tears up the outer shell until both vessels start to separate at time =2.37s.

Figure 106indicates severe damage on struck ship at outer shell, inner shell, transverse watertight bulkhead, longitudinal watertight bulkhead and opening on the top deck of struck ship. At time=2.016s it is clearly shown that the striking ship rammed the struck ship and listed at port side before stopping at approximately time=4.28s and stayed intact with each other.

Figure 107shows the striking ship ram into struck ship and slightly list to port side at time =5.004s and stayed still and intact with struck ship starting at time=4.148s. The top deck of the struck ship ruptured almost two thirds of the beam of the ship. There was no damage at transverse watertight bulkhead however having severe damage at longitudinal watertight bulkhead with big opening.

Figure 108 shows the lateral collision of two ships where most of the energy produced by the striking ship was directed perpendicular to the struck ship. The striking ship rammed into the struck ship and the bow tore all of structure members along her course. Both inner and outer shell for both sides were torn by the striking bow also longitudinal watertight bulkhead was severely damaged by the collision. The striking ship sat still on the top deck of the struck ship at time= 5.04s also started to move in the opposite direction of collision course at time=5.625 after all kinetic energy had been absorbed by the struck ship.

SCRB-A30-10m/s
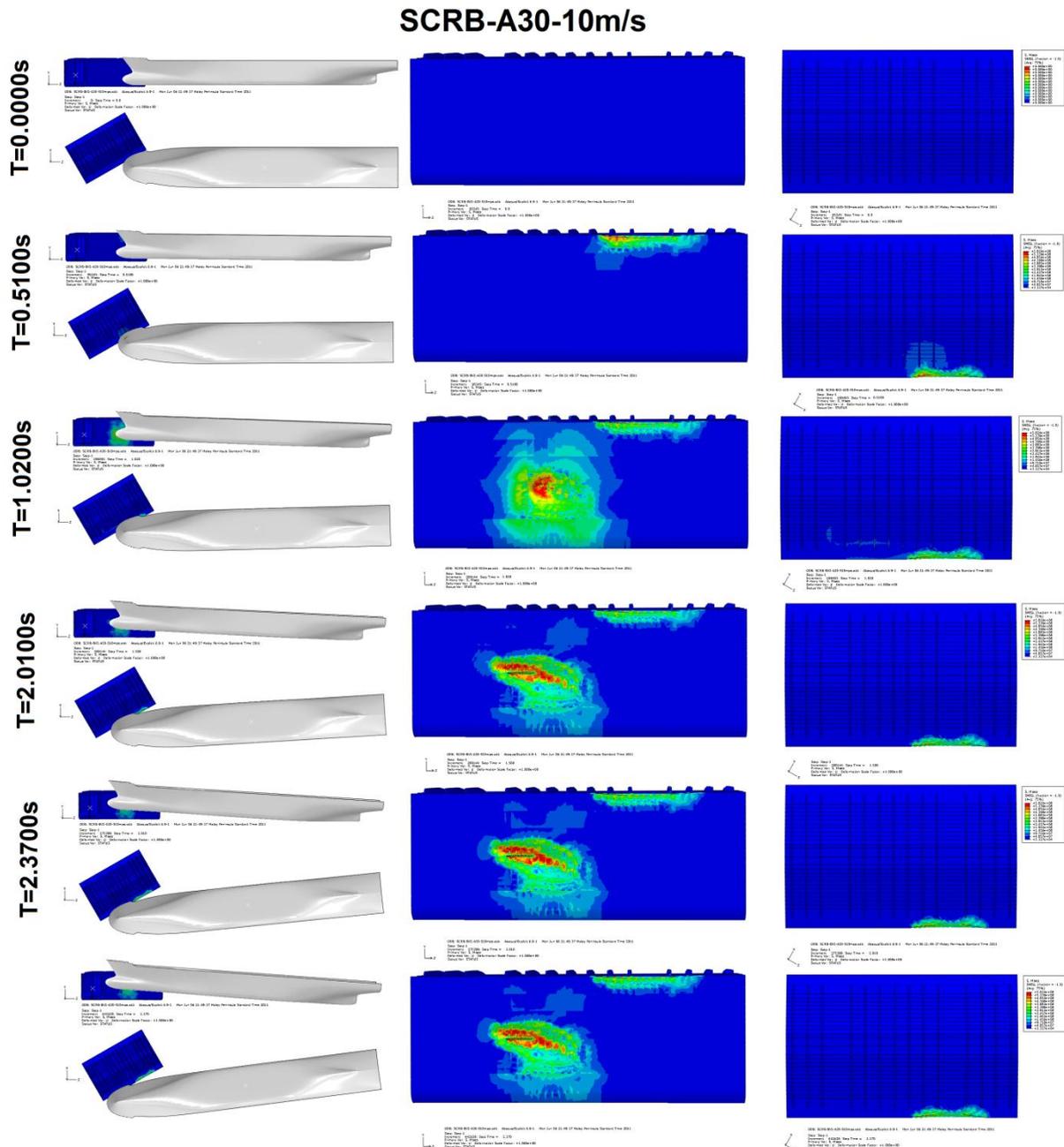
Figure 105: The damage condition of struck ship, striking by rigid body ship at 30^0 angle of attack.

SCRB-A50-10m/s
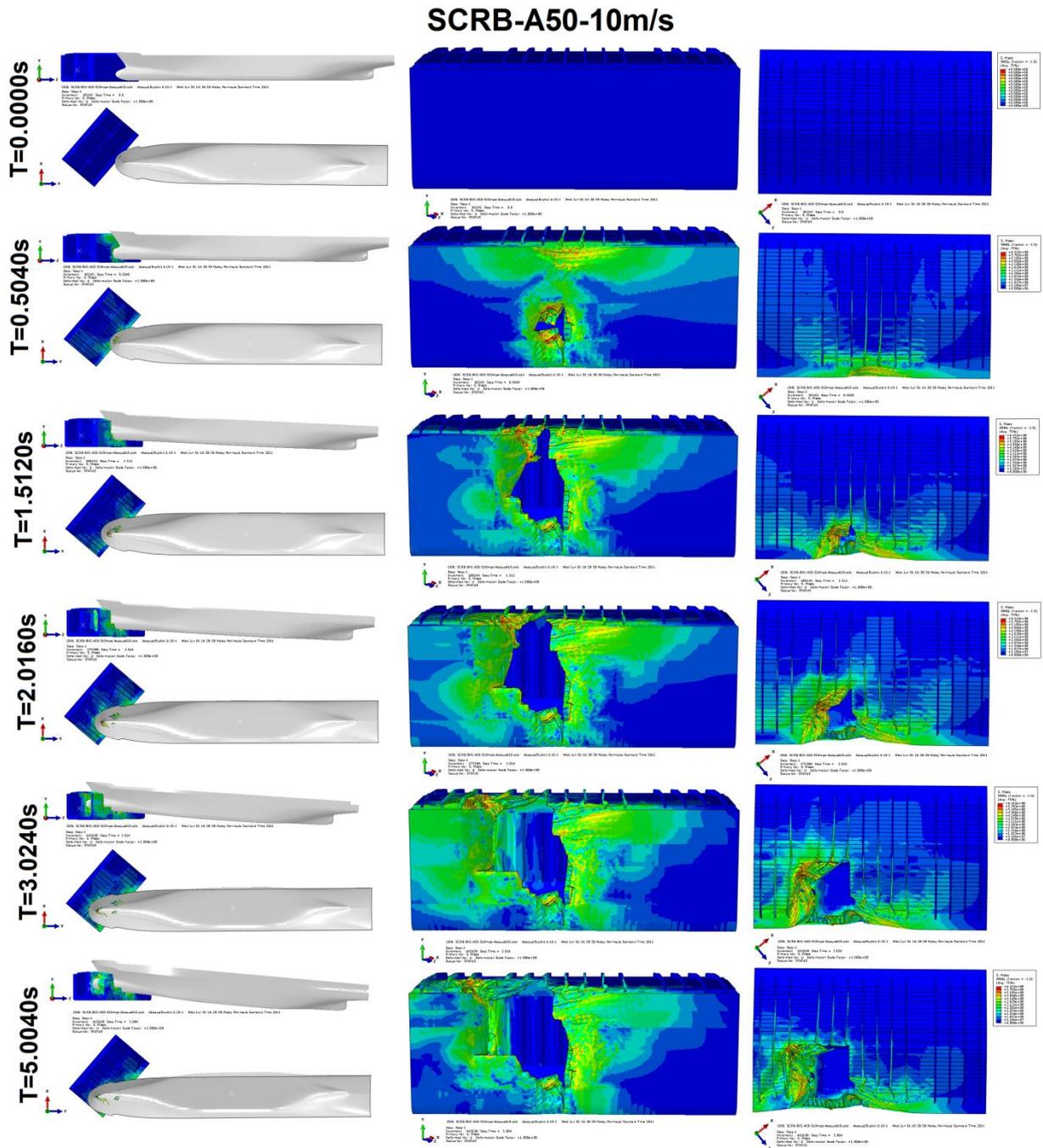
Figure 106: The damage condition of struck ship, striking by rigid body ship at 50^0 angle of attack.

SCRB-A70-10m/s
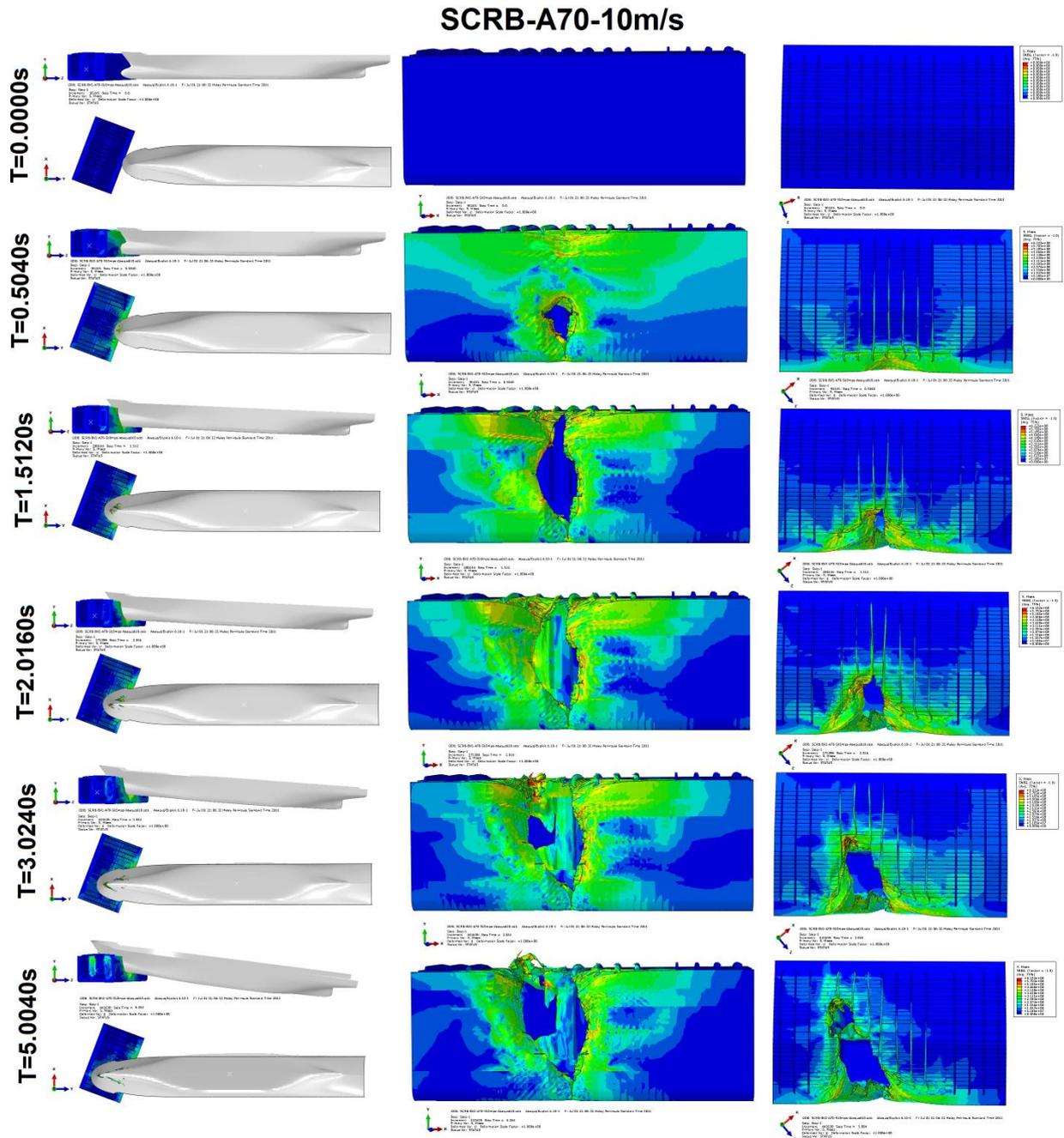
Figure 107: The damage condition of struck ship, striking by rigid body ship at 70^0 angle of attack.
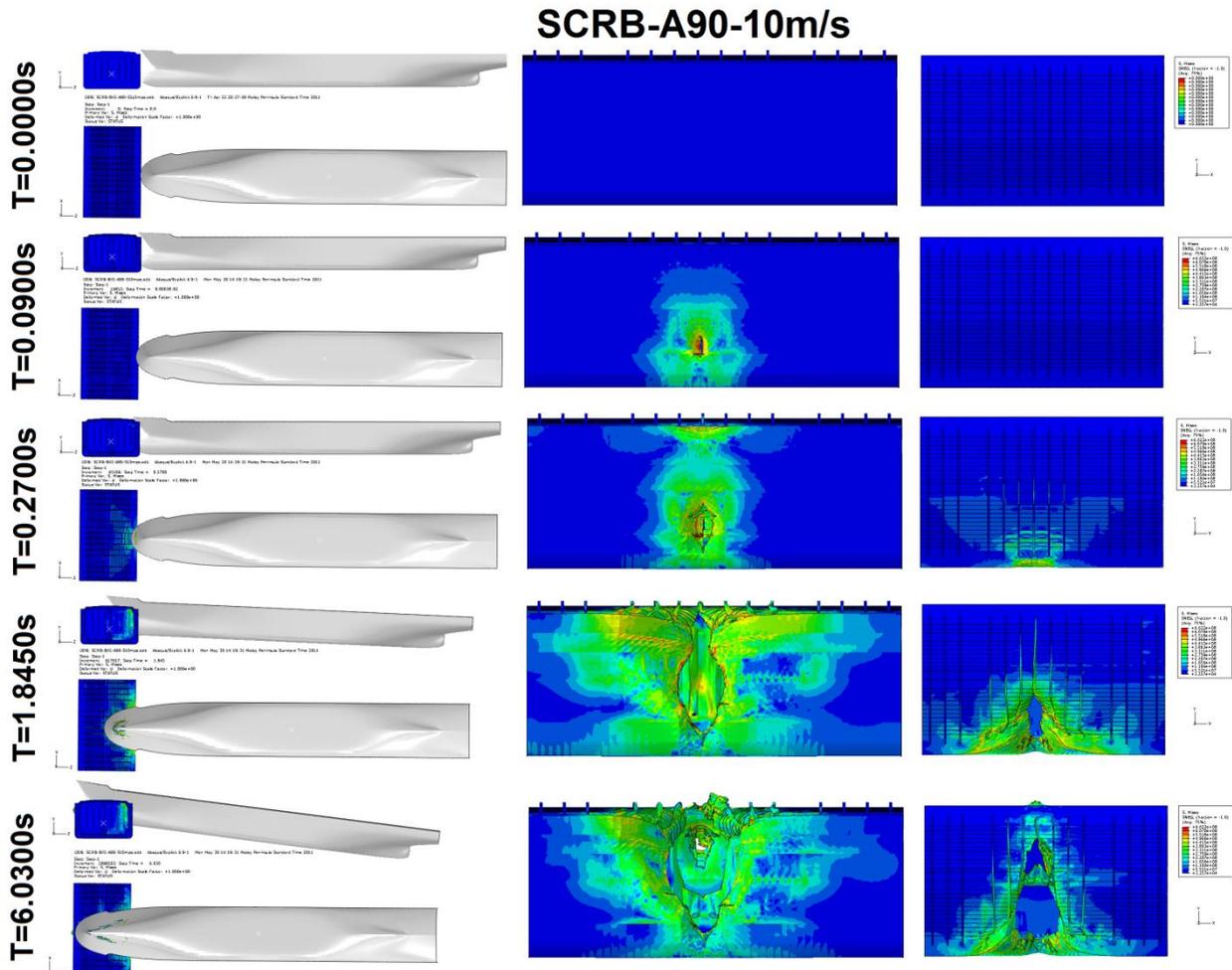
Figure 108: The damage condition of struck ship, striking by rigid body ship at 90^0 angle of attack.

8.3.2. Lateral Collision

The lateral collision analysis are divided into two simulation analysis which are rigid body of striking ship collide with deformable ship and both vessels are deformed during collision. The rigid body collision consists of different ships displacement and speed of striking ships. The deformable collision consists of 90 degree and 50 degree ship-ship collision. This analysis will show some understanding of the effect and behavior of rigid body and deformable collision and ship-ship interaction during collision. Most importantly, lateral collision is where most of the energy of the striking ship is directly absorbed

by the struck ship and severe damage for both vessels is likely to occur compared to an angle collision for the same striking energy employed.

8.3.3. Different Displacement

Figure 109 shows the Force-Displacement of striking ship with speed at collision = 5m/s. The graph shows that for most of the cases, the forces followed the same paths until peak at maximum penetration and the same applies to Figure 110.

The rupture force, displacement and time for outer and inner shell initiated at (73.51MKg=28MN, 0.15s, 0.749m), (34.29MKg =27.6MN, 0.18s, 0.893m), (20.22MKg =30.4MN, 0.16s, 0.794m), (8.57MKg =10.7MN, 0.18s, 0.879m) and (73.51MKg =57.1MN, 0.48s, 2.237m), (34.29MKg =58.8MN, 0.48s, 2.336m), (20.22MKg =52MN, 0.52s, 2.47m), (8.57MKg =55.4MN, 0.585s, 2.511m) respectively. The rapture of outer shell almost occur at same time for all cases within range 15-18s and force to rapture for outer shell within range 26-30.4MN. The case for 8.57MKG show less force to rupture, this is may be due step setting effect that influence the result. The penetration to rupture for outer shell ranging between 0.749-0.879m and for outer shell ranging from 2.237-2.511m. The force and time to rupture for outer shell ranging from 52 - 58.8MN and 0.48-0.585s. This phenomena show that the outer and inner shell able to withstand more less same resistant force before rupture.

Figure 109 and Figure 110 shows that on increasing the striking ship displacement and retain the ship's speed at 5m/s indicates that the penetration distance increases proportionally but not for penetration time. This phenomenon occurs due to the nature of the shape of the bow where further striking rate of the ship penetrated into struck ship, more contact areas are intact with the struck ship and this will increase the force and reduce the time as more resistance toward advance penetration in comparison with contact area and time.
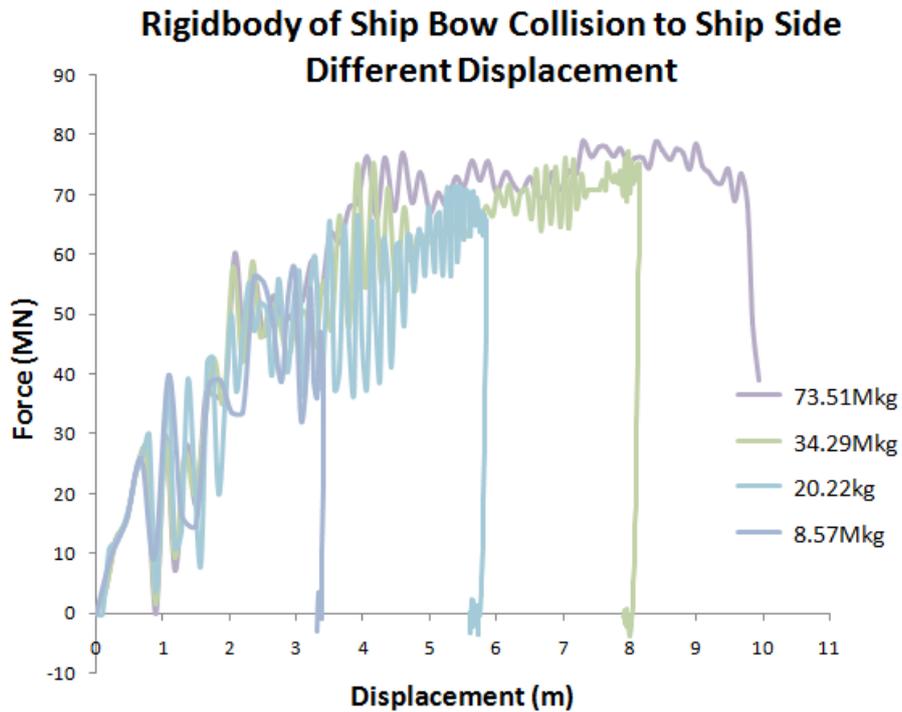
Figure 109: The Energy -Displacement of rigid body of striking ship, struck to ship side for different ship displacement setup.
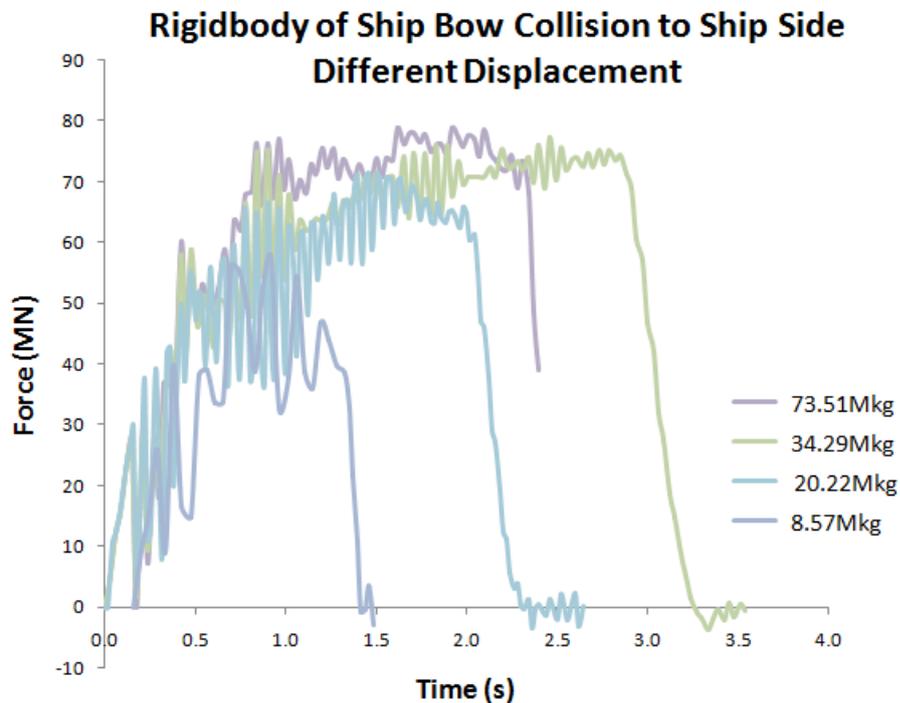
Figure 110:The Force -Time of rigid body of striking ship, struck to ship side for different ship displacement setup.

Figure 111 and Figure 112 show nice tender curve for striking ship dissipation of energy during collision for energy in respect with time and displacement respectively. The initial kinetic energy just before collision is 73.51Mkg=919MJ, 34.29MKg=429MJ, 20.22MKg=253MJ, and 8.57MKg=107MJ. The rupture force, displacement and time for outer and inner shell initiated at (73.51MKg=105MJ, 0.15s, 0.749m), (34.29MKg =135MJ, 0.18s, 0.893m), (20.22Mkg =115MJ, 0.16s, 0.794m), (8.57MKg =132MJ, 0.18s, 0.879m) and (73.51MKg =610MJ, 0.48s, 2.237m), (34.29MKg =591MJ, 0.48s, 2.336m), (20.22MKg =648MJ, 0.52s, 2.47m), (8.57MKg =651MJ, 0.585s, 2.511m) respectively. This show that the outer and inner shell able to absorbed energy before rupture ranging between 105-135MJ for outer shell and 591-651MJ for inner shell.

Both graphs also show that for case 73.51MKg, the simulation is terminated before the ship stopped still and all the kinetic energy had not yet fully converted or absorbed by the struck ship. The termination of the job occurred due to insufficient memory and was very costly to resubmit the job but the step is more than sufficient to make a good assumption of overall results when looking at Figure 109 and Figure 110 where the force was already in a state of decreasing and the striking ship had nearly stopped still.
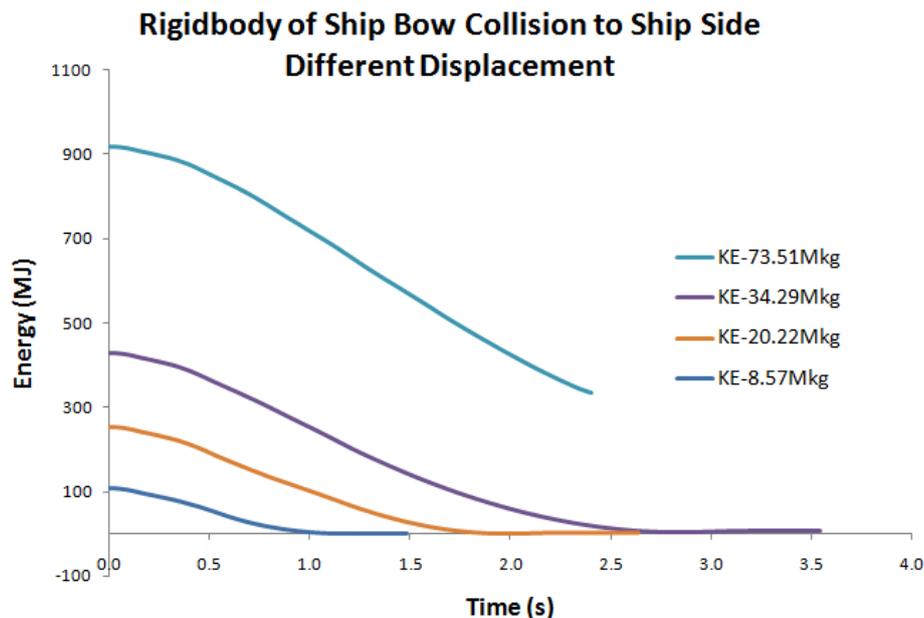
Figure 111: The Energy -Time of rigid body of striking ship, struck to ship side for different ship displacement setup.
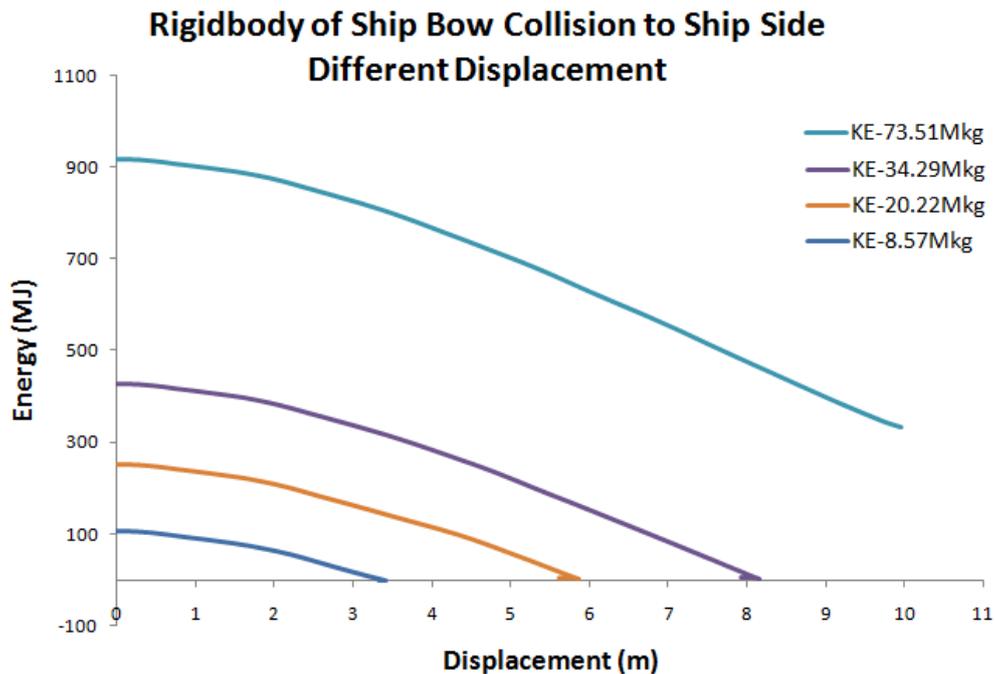
Figure 112: The Energy -Displacement of rigid body of striking ship, struck to ship side for different ship displacement setup.

Figure 113 shows the simulation analysis of striking ship with displacement 8.57MKg that ruptured the struck ship at time=0.18s and 0.585s for outer and inner shell respectively. There was no penetration at longitudinal watertight bulkhead. Based on the damage, the ship still had sea worthiness and was safe afloat. It shows that the ship still had structural integrity but lost her cargo due to the rupture occurring at the inner shell that spilled out all the oil from that compartment. The struck ship also did not experience severe damage on the top deck, only plastic deformation which is not significant.

Figure 114 shows the damage condition of the side shell of the struck ship with displacement of striking ship at 20.22MKg on outer and inner at time=0.16s and 0.52s respectively. Due to the low energy of the collision, the struck ship was not severely damaged on the top deck which only experienced plastic deformation.

The simulation also indicated that when larger displacements of striking ship were employed during collision while retaining the initial collision speed at 5m/s resulted in potentially increasing the damage of struck ships. Figure 115and Figure 116 show the severe damage on side shell for both cases 34.29MKg and 73.51MKg, where struck ship experienced a large opening on outer and inner shell. There was no damage on the top deck and longitudinal watertight bulkhead on 34.29MKg and 73.51MKg collision case. The Figure 115 and Figure 116 also indicate that the rupture initiated at the outer shell at time 0.18s and 0.15s. The inner shell ruptured at the same time at 0.48s due to stress concentration and step time that was small enough to capture the moment for collision 73.51MKg.
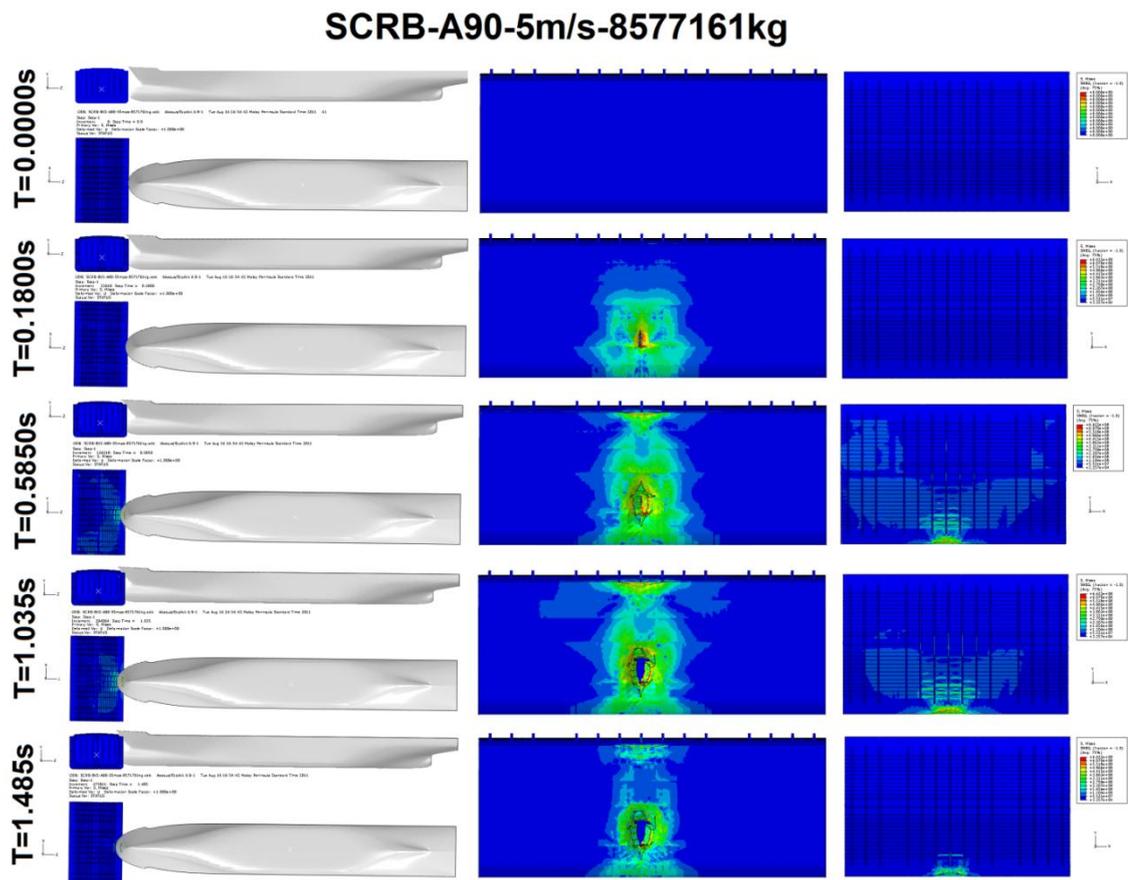
Figure 113: The damage condition of struck ship, striking by 8.6Mkg displacement of rigid body ship at 90^0 angle of attack.
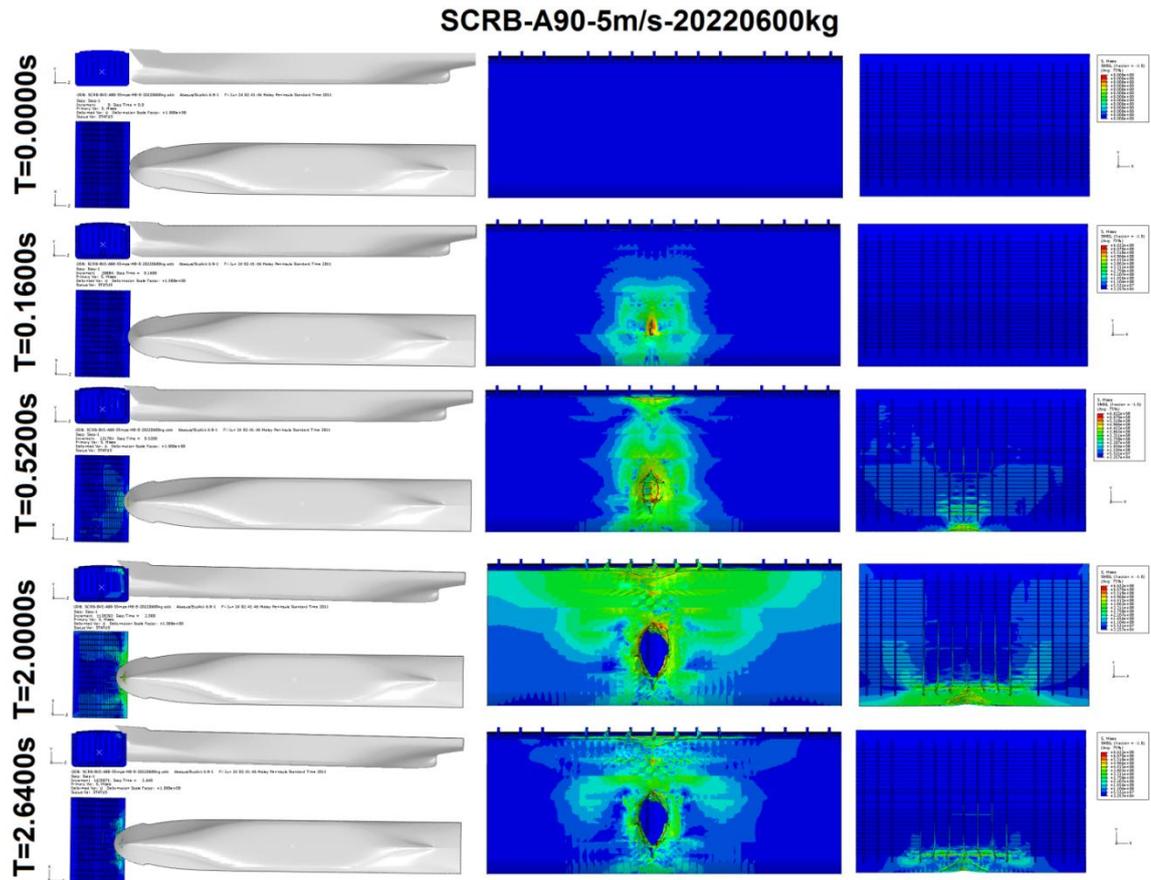
Figure 114 :The damage condition of struck ship, striking by 20.22Mkg displacement of rigid body ship at 90^0 angle of attack.

SCRB-A90-5m/s-34287044kg
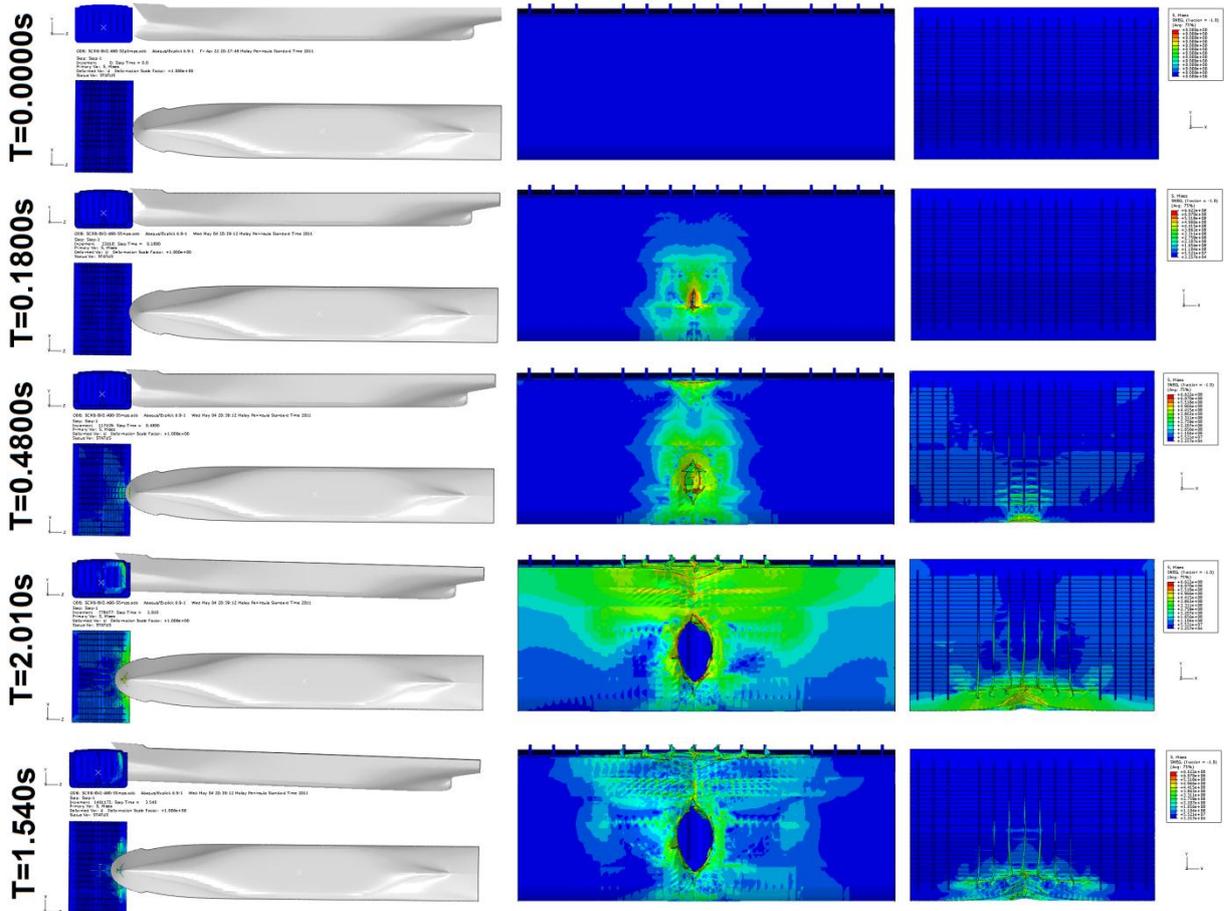
Figure 115:The damage condition of struck ship, striking by 34.29Mkg displacement of rigid body ship at 90^0 angle of attack.

SCRB-A90-5m/s-73512300kg
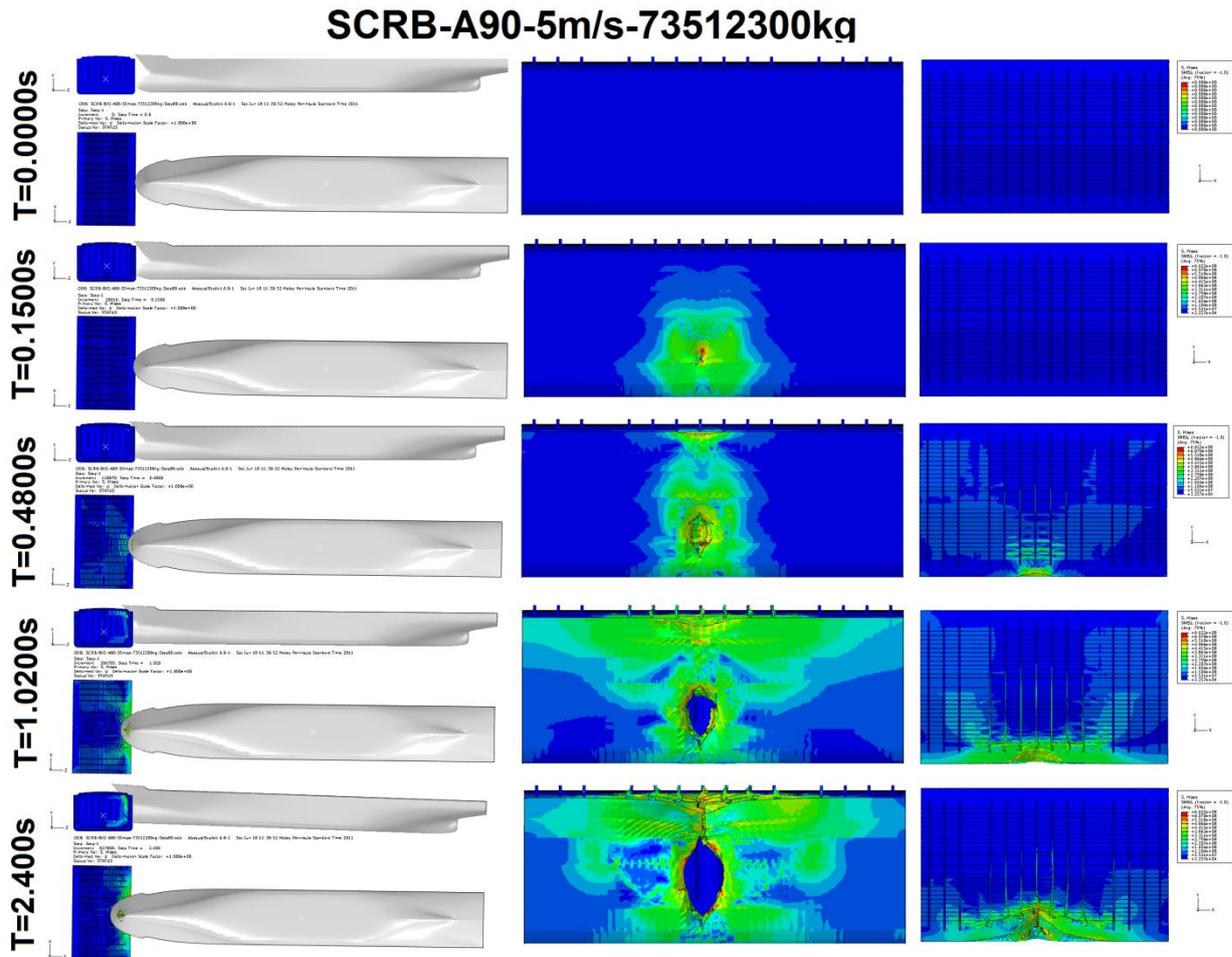
Figure 116:The damage condition of struck ship, striking by 73.51Mkg displacement of rigid body ship at 90^0 angle of attack.

8.3.4. Different Speed

In this section the analysis focuses and discusses ship-ship collision of with variable speeds of striking ship, while retaining a constant displacement as 34.29 MKg.

Figure 117 and Figure 118 show a Force-Displacement and Force-time of striking ship with 34.29MKg of ship displacement. The analysis were initiated at various speeds of striking ship deployed for ship-ship collision analysis. The rupture forces, displacement and time for outer and inner shell are (10m/s=31.1MN, 0.9m,0.1s), (7.5m/s=33.9MN, 0.9m, 0.12s), (5m/s=27.6MN, 0.9m, 0.18s), (2.5m/s=23.7MN, 0.7m, 0.28) and (10m/s=58.4MN, 2.68m,

0.27s), (7.5m/s=76.6MN, 2.67m, 0.36s), (5m/s=58.8MN, 2.34m, 0.48s), (2.5m/s=49.8MN, 2.41m, 1.1s) respectively. These show that the rupture of outer and inner shell indicate within ranges of 23.7MN-33.9MN for outer shell and 49.8MN-76.6MN for inner shell. The displacement and time of rupture also shows that proportional to speed of striking ship where is likely to occur in a real situation.

Figure 119 and Figure 120 show the kinetic energy versus time and displacement where the initial kinetic energy before collision occurs are 10m/s=1710MJ, 7.5m/s=964MJ, 5m/s=429MJ and 2.5m/s= 107MJ. The rupture energy for outer and inner shell takes place at (10m/s=13.6MJ, 0.9m,0.1s), (7.5m/s=13.8MJ, 0.9m, 0.12s), (5m/s=13.5MJ, 0.9m, 0.18s), (2.5m/s=8.85MJ, 0.7m, 0.28) and (10m/s=77.8MJ, 2.68m, 0.27s), (7.5m/s=76.7MJ, 2.67m, 0.36s), (5m/s=59.1MJ, 2.34m, 0.48s), (2.5m/s=58.3MJ, 2.41m, 1.1s) respectively. The rupture energy for outer shell are very close for all simulations where it is about the range of 13MJ-13.6MJ except for speed 2.5m/s which was less from the minimum range and about 8.85MJ. This is due to the effect of strain rate contribution but not significantly if we are looking at the differences of the results. The rupture energy for inner shell in range of 58.3MJ-77.8MJ and this indicates that the speed of striking ship is playing some role in the rupture of inner and outer shell.
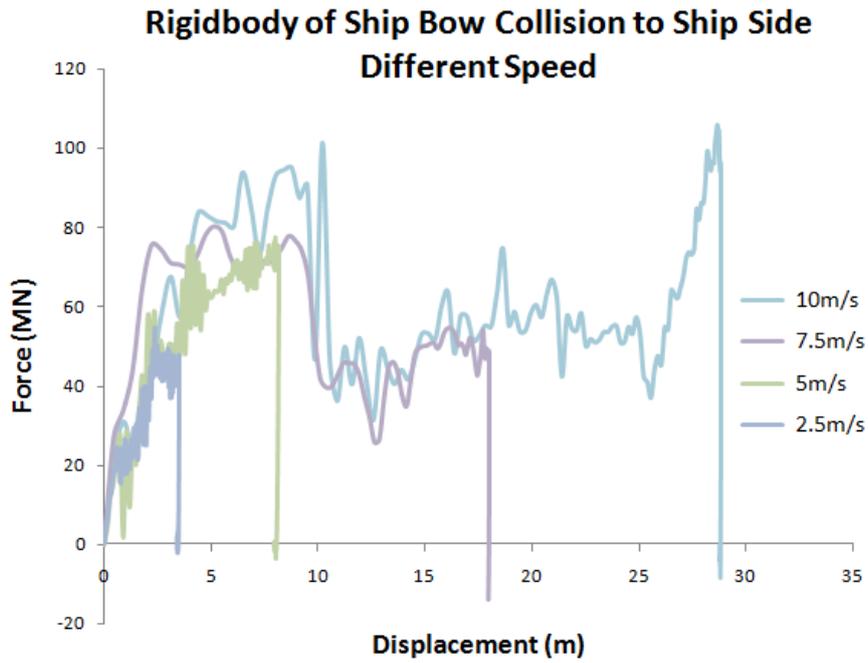
Figure 117 :The Force -Displacement of lateral collision of rigid body ship striking to ship side for various speeds.
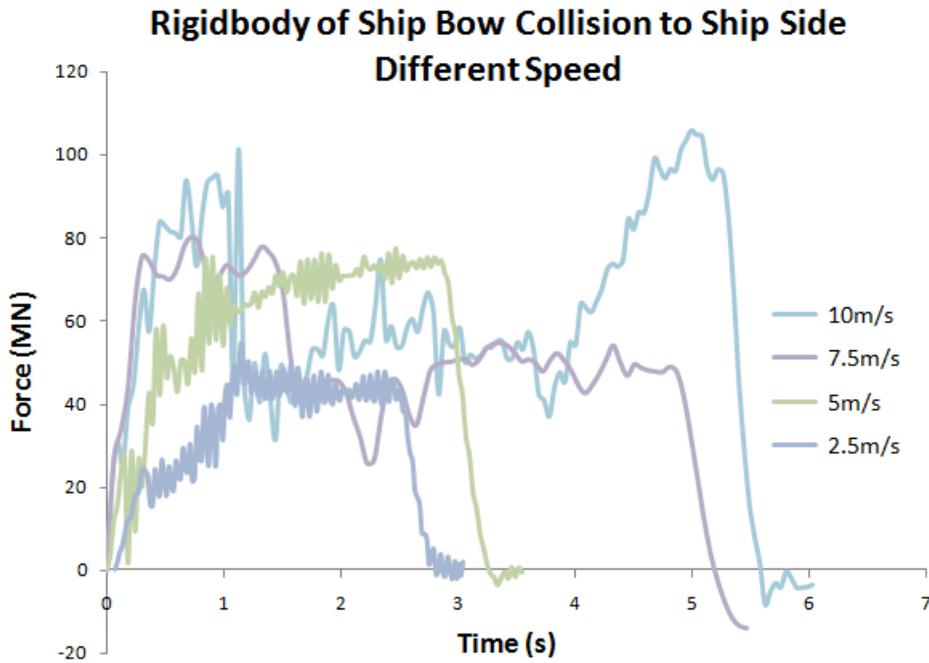
Figure 118 :The Force -Time of lateral collision of rigid body ship striking to ship side for various speeds.
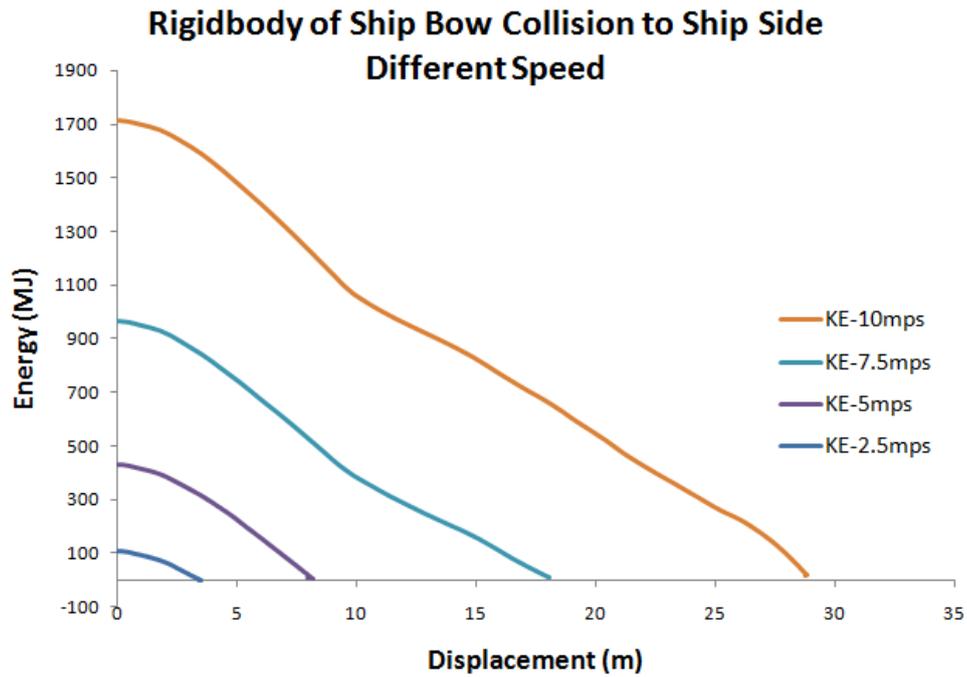
Figure 119 :The Energy -Displacement of lateral collision of rigid body ship striking to ship side for various speeds.
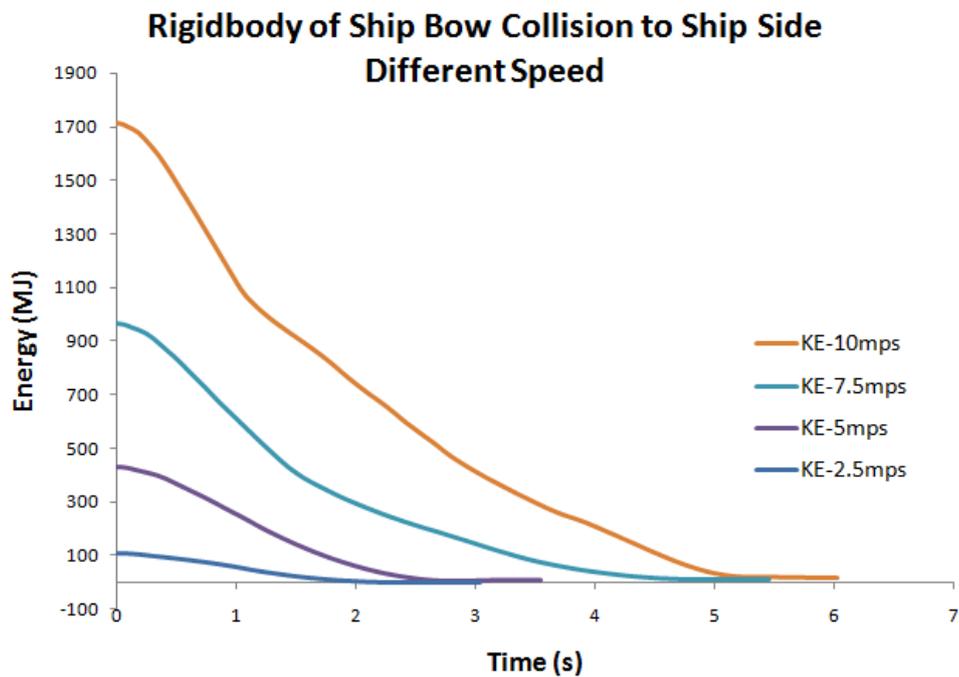
Figure 120:The Energy -Time of lateral collision of rigid body ship striking to ship side for various speeds.

As in Figure 121 - Figure 124, the damage condition of lateral collision for various speeds indicated that for collision speed at 2.5m/s (see Figure 121) there is no penetration at longitudinal watertight bulkhead and it also applies for collision speed at 5m/s (see Figure 122). Both of these collision speeds only rupture the inner and outer shell of struck ship and the stress is nicely spread toward both end of the compartment. The damage of struck ship is clearly seen for inner and outer shell at time=0.28s, 1.1s and time=0.18s, 0.48s for 2.5m/s and 5m/s respectively.

As for collision speed at 7.5m/s and 10m/s, both indicate that the penetration damage are get to longitudinal watertight bulkhead (see Figure 123 and Figure 124). For 10m/s collision, the striking ship is creates severe damage along her way that penetrate the way through of the struck ship. Figure 123 also shows the rupture of outer, inner and longitudinal watertight bulkhead at time = 0.12s, 0.36s and 53.18s respectively. Figure 124 also indicates the rupture damage for inner, outer, longitudinal and both inner and outer shell at opposite sides of struck ship where the rupture occurred at time=0.09s, 0.27s, 1.845s, 4.995s respectively.

The collision also indicates that there was no damage on the top deck of struck ship for collision speed at 2.5m/s and 5m/s but severe damage on top deck for collision speed at 7.5m/s and 10m/s. The striking ship also rammed into the struck ship with some inclination angle which was less for 2.5m/s and larger when the speed of collision are increased. The figures also shows minimal effect of boundary condition due to stress flow not being concentrated at both end of compartment where boundary condition are being sets. Based on observation, the lateral collision speed with kinetic energy at a range of 10.7MJ-40.9MJ with the displacement=34.29Mkg and speed 5m/s, still did not threaten the struck ship for current size of struck ship.

SCRB-A90-2.5m/s
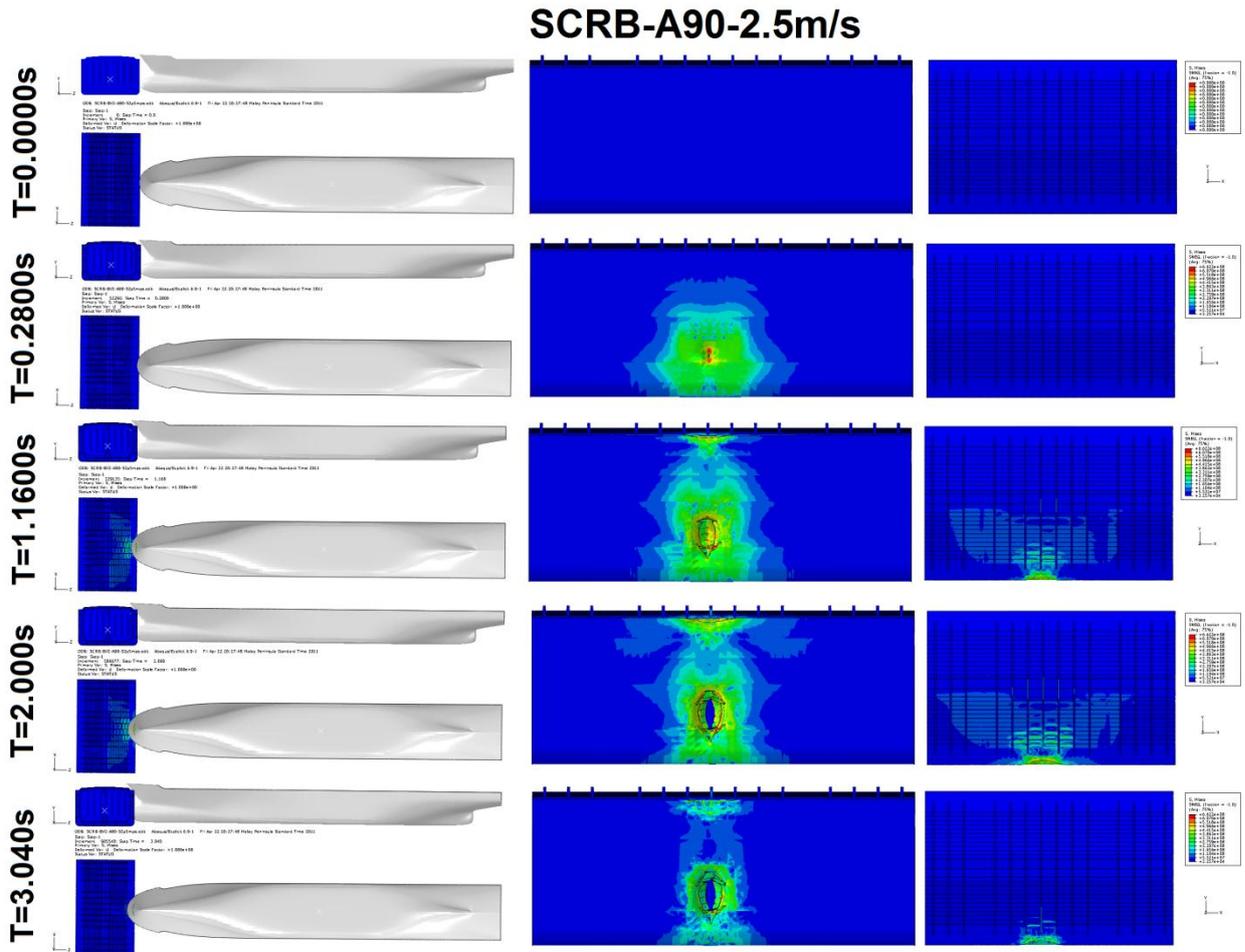


Figure 121:The damage condition of struck ship, striking by 34.29MKg displacement of rigid body ship at 90^0 angle of attack and 2.5m/s speed.
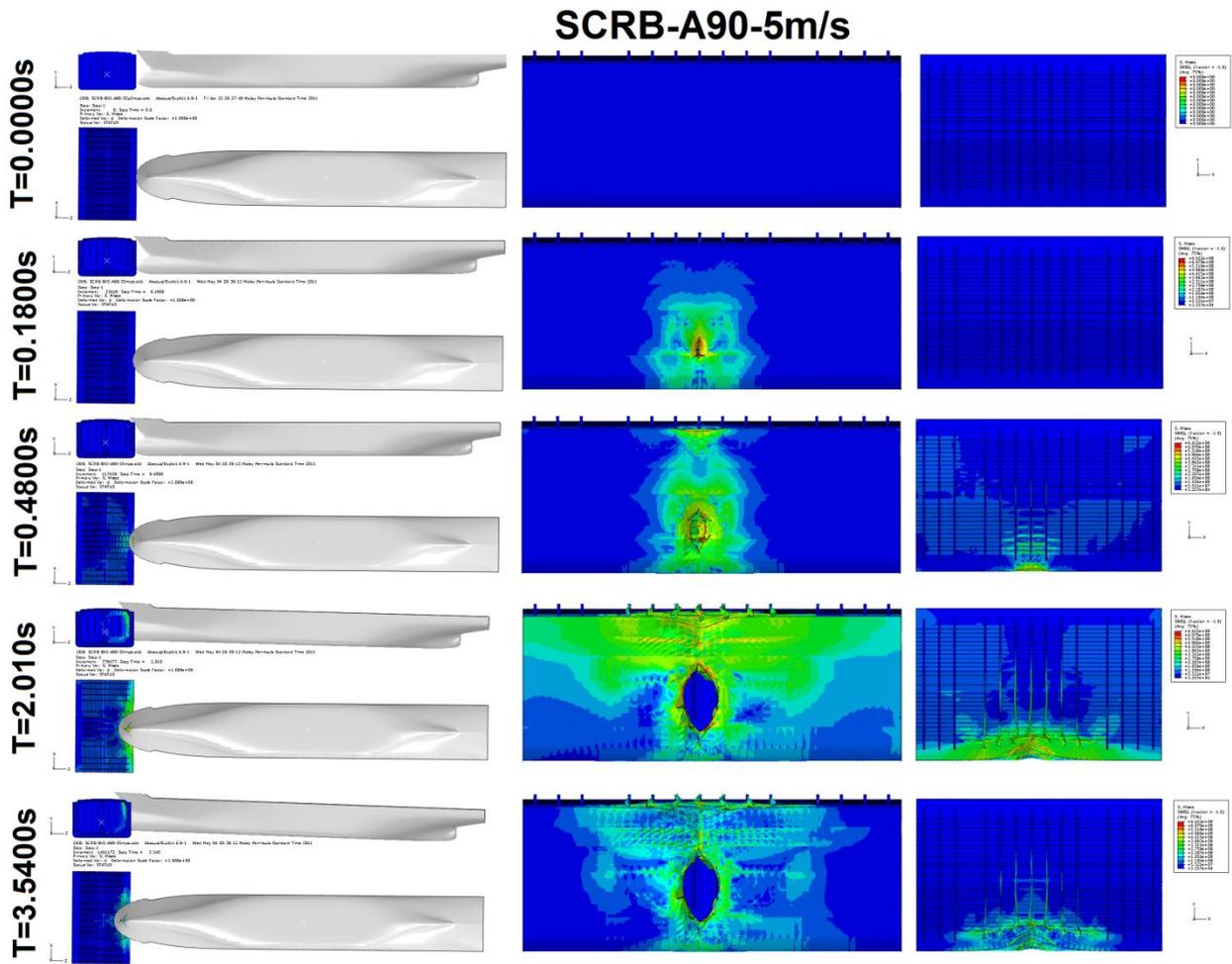
Figure 122:The damage condition of struck ship, striking by 34.29MKg displacement of rigid body ship at 90^0 angle of attack and 5m/s speed.
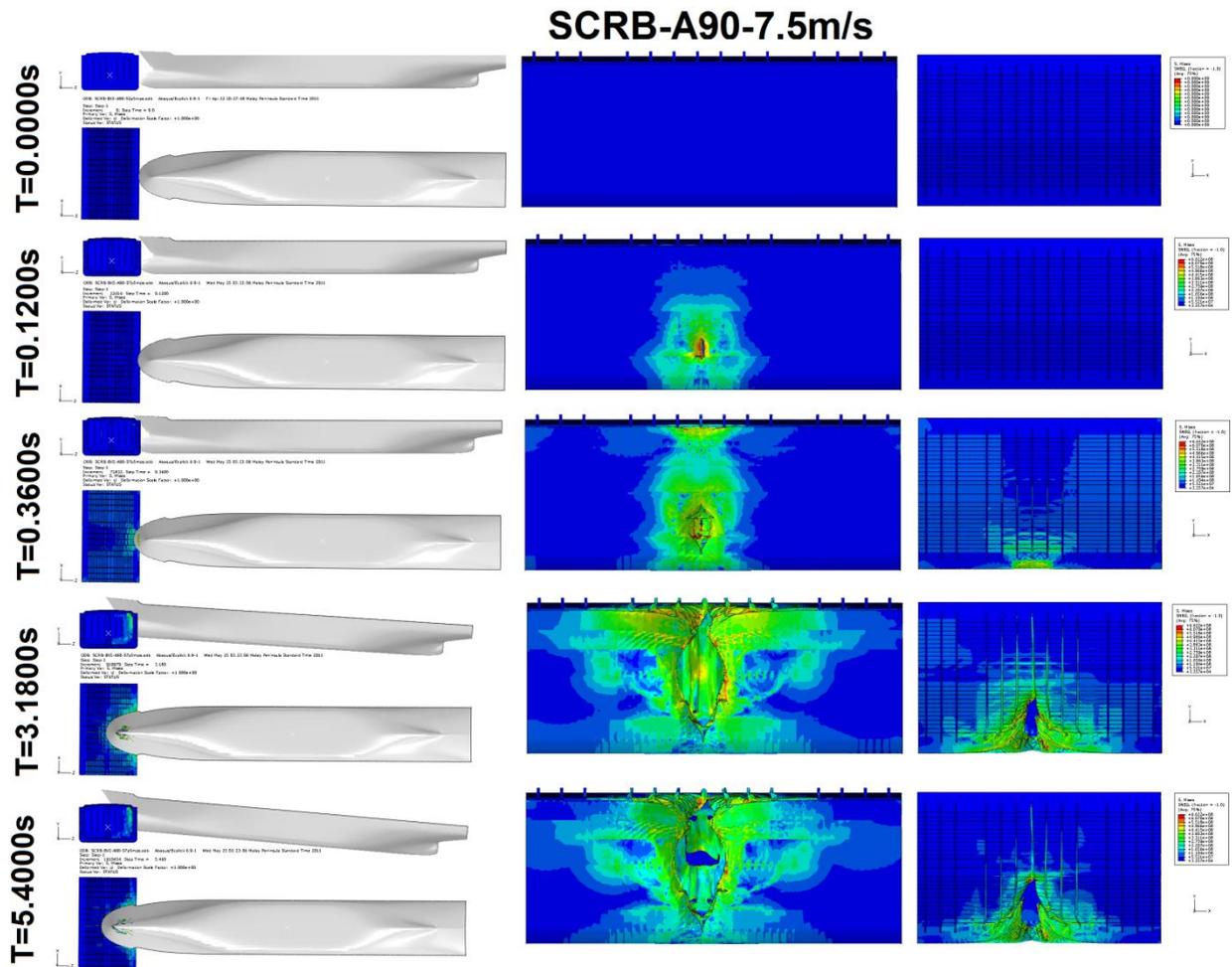
Figure 123 :The damage condition of struck ship, striking by 34.29MKg displacement of rigid body ship at 90^0 angle of attack and 7.5m/s speed.
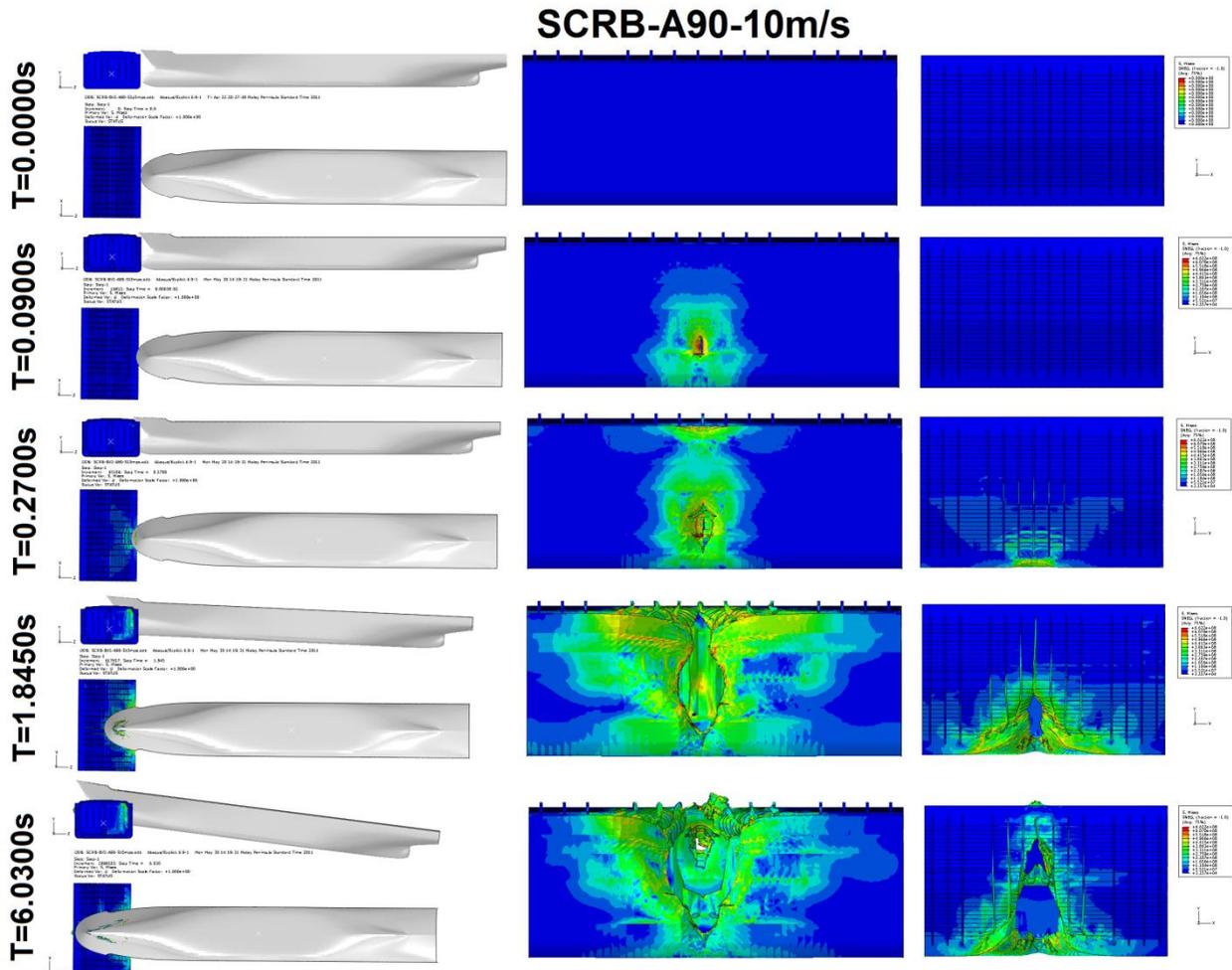
Figure 124 :The damage condition of struck ship, striking by 34.29MKg displacement of rigid body ship at 90^0 angle of attack and 10m/s speed.

### 8.3.5. Deformable of ship bow to ship side collision

Figure 125 and Figure 126 shows the Force-Displacement and Force-Time graphs for ship-ship collision for both deformable bow (SCdef) and rigid body bow (SCRB) collide with deformable ship side. For 50 degree and 90 degree angle of collision the rupture force for inner, outer shell and maximum penetration force of struck ship for deformable bow collision occur at (SCdef=45.4MN, 98.5MN, 136MN, and 34.2MN, 46.6MN, 144MN) and for rigid body collision take place at (SCRB=61.9MN, 75.5MN, 98.9MN and 31.1MN, 58.4MN, 106MN), respectively. The displacement and time to rupture for 50 degree and 90 degree collision (see Figure 125) also shown

that for outer shell rupture at (SCRB A50=1.077m, 0.11s, SCRB A90=0.9mm, 0.09s and SCdef A50=0.982m, 0.1s, SCdef A90=0.92m, 0.093s) and for inner shell rupture at (SCRB A50=3.522m, 0.36s, SCRB A90=2.678mm, 0.27s and SCdef A50=3.653m, 0.38s, SCdef A90=2.51m, 0.26s).

Figure 127 and Figure 128 show the kinetic energy generated by striking ship at 1710MJ before collision occurs and dissipated throughout the event. The energy, displacement and time to rupture for both 50 degree and 90 degree collisions shows outer shell rupture at (SCRB A50=30.2MJ, 1.077m, 0.11s, SCRB A90=13.6MJ, 0.9mm, 0.09s and SCdef A50=48.3MJ, 0.982m, 0.1s, SCdef A90=41.2MJ, 0.92m, 0.093s) and for inner shell rupture at (SCRB A50= 170MJ, 3.522m, 0.36s, SCRB A90=77.8MJ, 2.678mm, 0.27s and SCdef A50=222MJ, 3.653m, 0.38s, SCdef A90=97.4MJ, 2.51m, 0.26s).
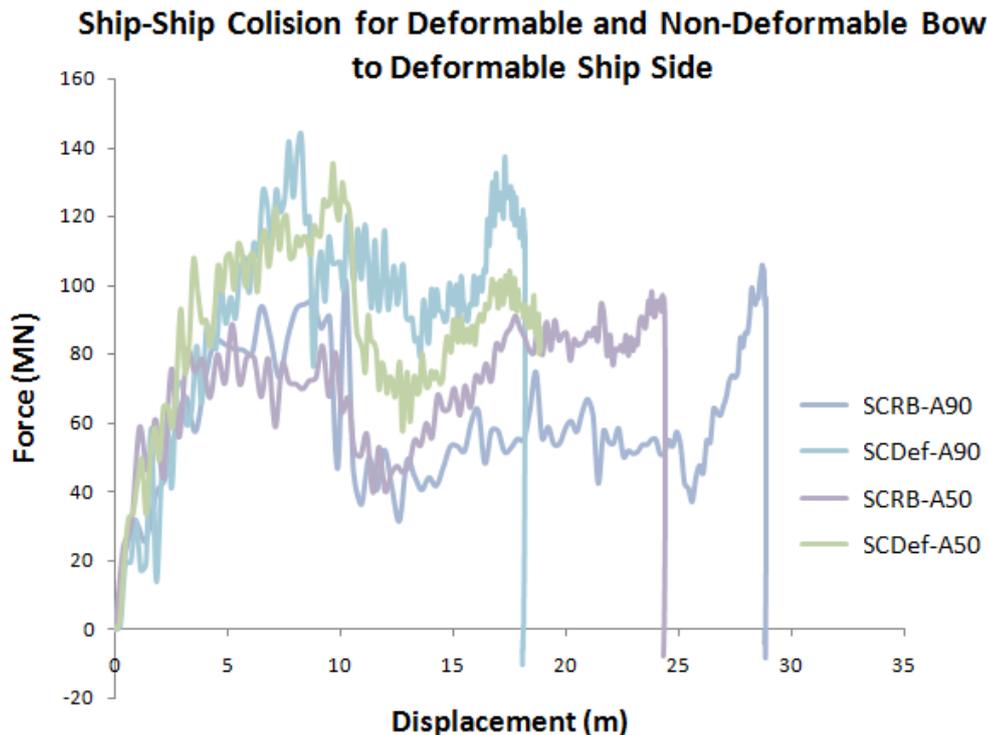
Figure 125 :The Force -Displacement of ship-ship collision for deformable and non-deformable bow to deformable ship-side.

This shows that there are higher forces absorbed by the struck ship, lesser time and smaller penetration damage to stop the striking ship after collision for deformable ship-ship collision compared to rigid body bow collision. It also shows that there is higher energy to rupture both outer and inner shell for deformable ship-ship collision compared to rigid body bow collision. This phenomena will help to prevent further damage of struck ship if the striking ship bow is designed to be more elastic instead of a rigid bow.
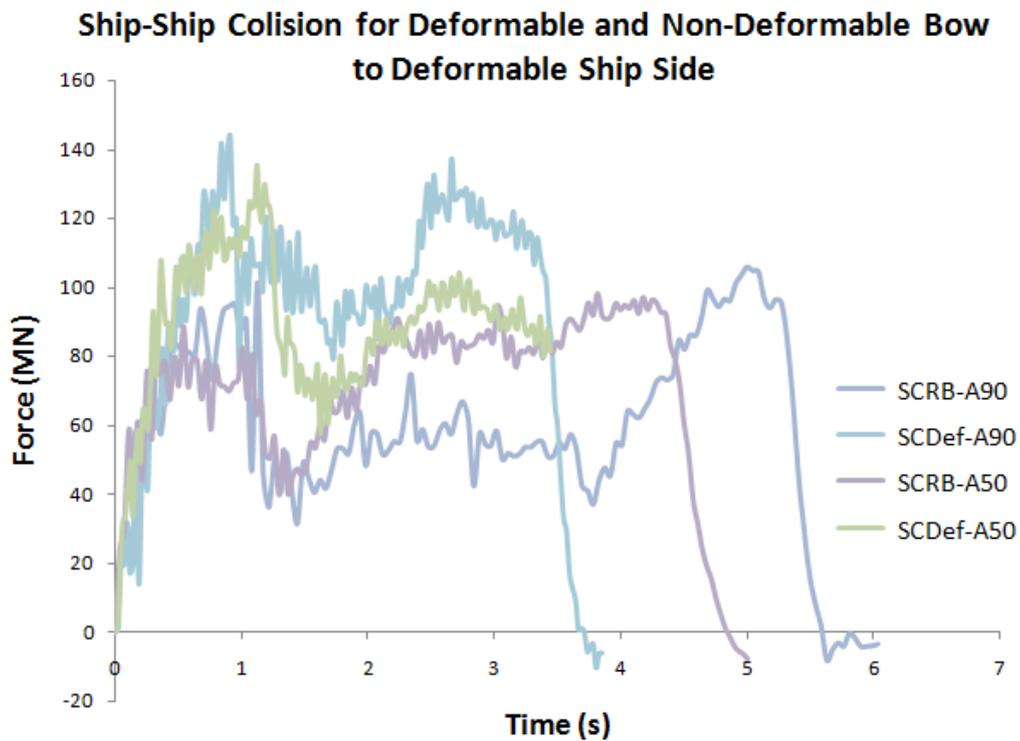
Figure 126 :The Force -Time of ship-ship collision for deformable and non-deformable bow to deformable ship-side.
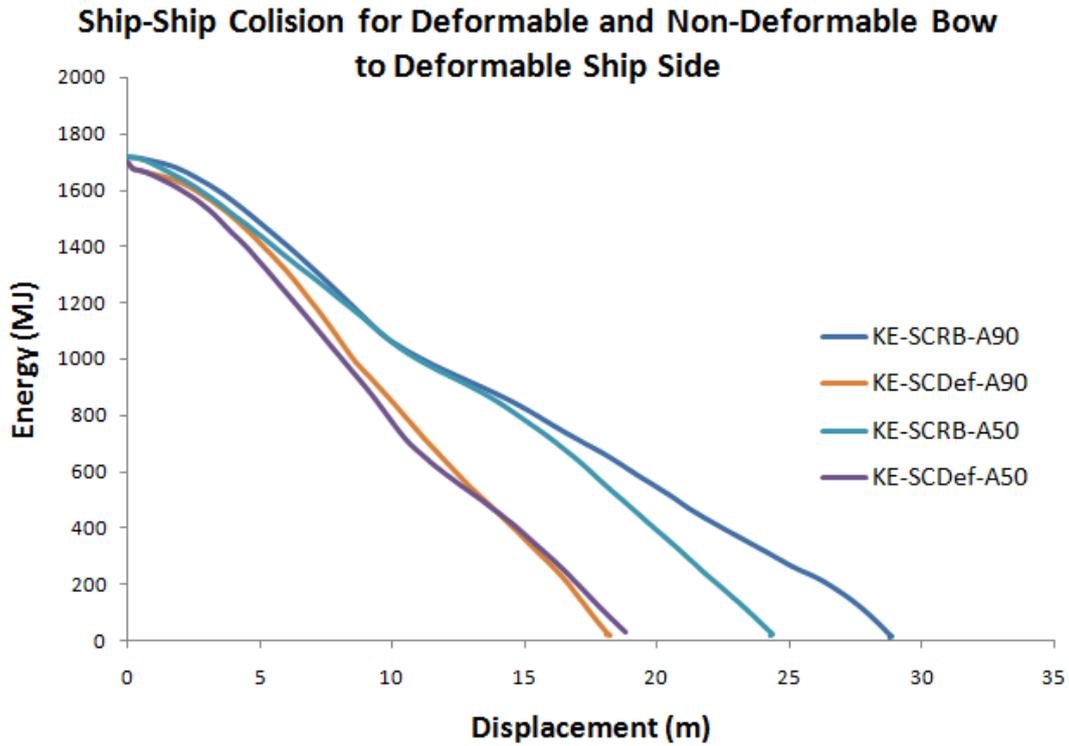
Figure 127 :The Energy -Displacement of ship-ship collision for deformable and non-deformable bow to deformable ship-side.
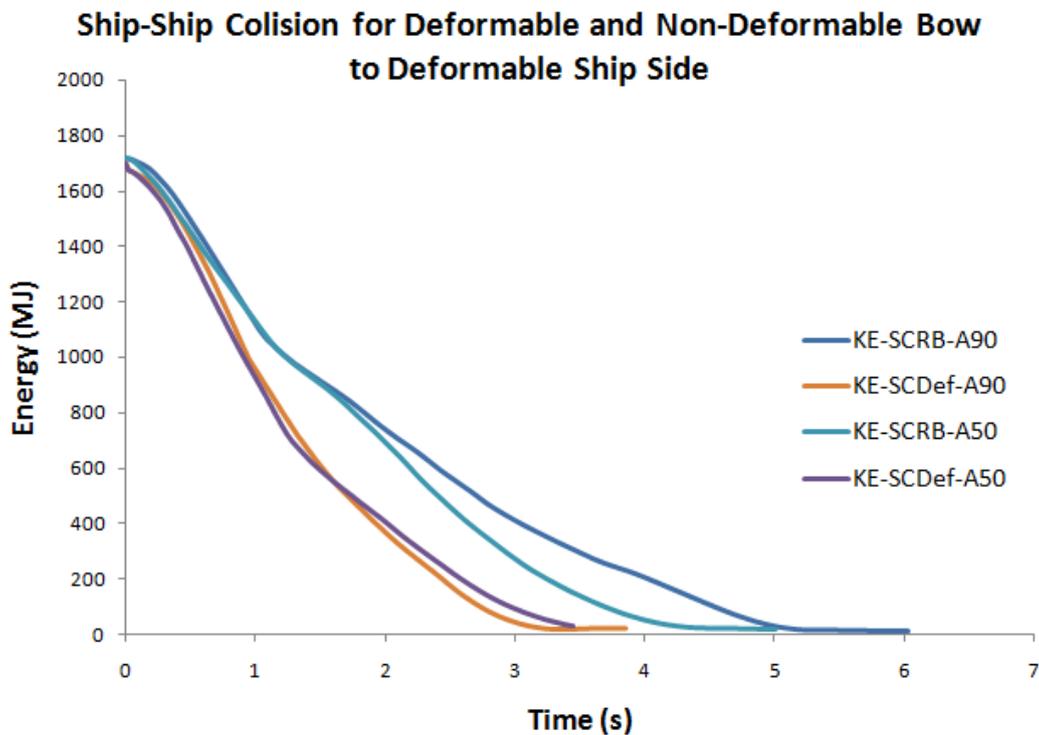
Figure 128:The Energy-Time of ship-ship collision for deformable and non-deformable bow to deformable ship-side.

Figure 129 and Figure 130show simulation damage of deformable collision of ship-ship for lateral collision and 50 degree collision. Figure 129, is 50 degree ship-ship collision and indicates that the struck ship had severe damage on the outer shell, inner shell, top deck and watertight transverse bulkhead. The damage of the inner shell and outer shell are clearly shown at Time= 0.1s for outer shell and 0.38 for inner shell. The striking ship listed to port side after inner shell rupture toward stop still. The striking bow shows no rupture, only plastic deformation at bulbous bow and forecastle deck.

Figure 130 shows a lateral collision and damage of struck ship as well as striking ship. The striking ship rammed into struck ship and seemed to have severe damage on forecastle deck where the forecastle deck was crushed also having a cut through by the top deck. As expected, the struck ship hada big opening on the side shell and top deck also ruptured at the longitudinal watertight bulkhead. The damage of the outer shell, inner shell and longitudinal watertight bulkhead occurred at Time=0.093s, 0.26s and 1.9s, respectively.

For rigidbody bow and deformable ship-ship collision, to some extent there are big differences of damage on struck ship. If we consider the opening on the struck ship and less damage of the deformable bow, where deformable collision both vessels are able to absorb the energy of impact during collision compare to rigid bow.

For lateral collision, deformable ship-ship collision showed outstanding achievement on absorbing the energy during collision compare to rigid bow collision. This is represented by looking at the damage of both struck ships that collided with rigid body ship and deformable ship bow. The deformable ship bow collision did not experience rupture on the opposite ship side the struck ship of the collision, but the rigid body ship collision struck through and rupture all the shell along the way of the struck ship until the opposite ship side.

SC-Def-A50-10m/s
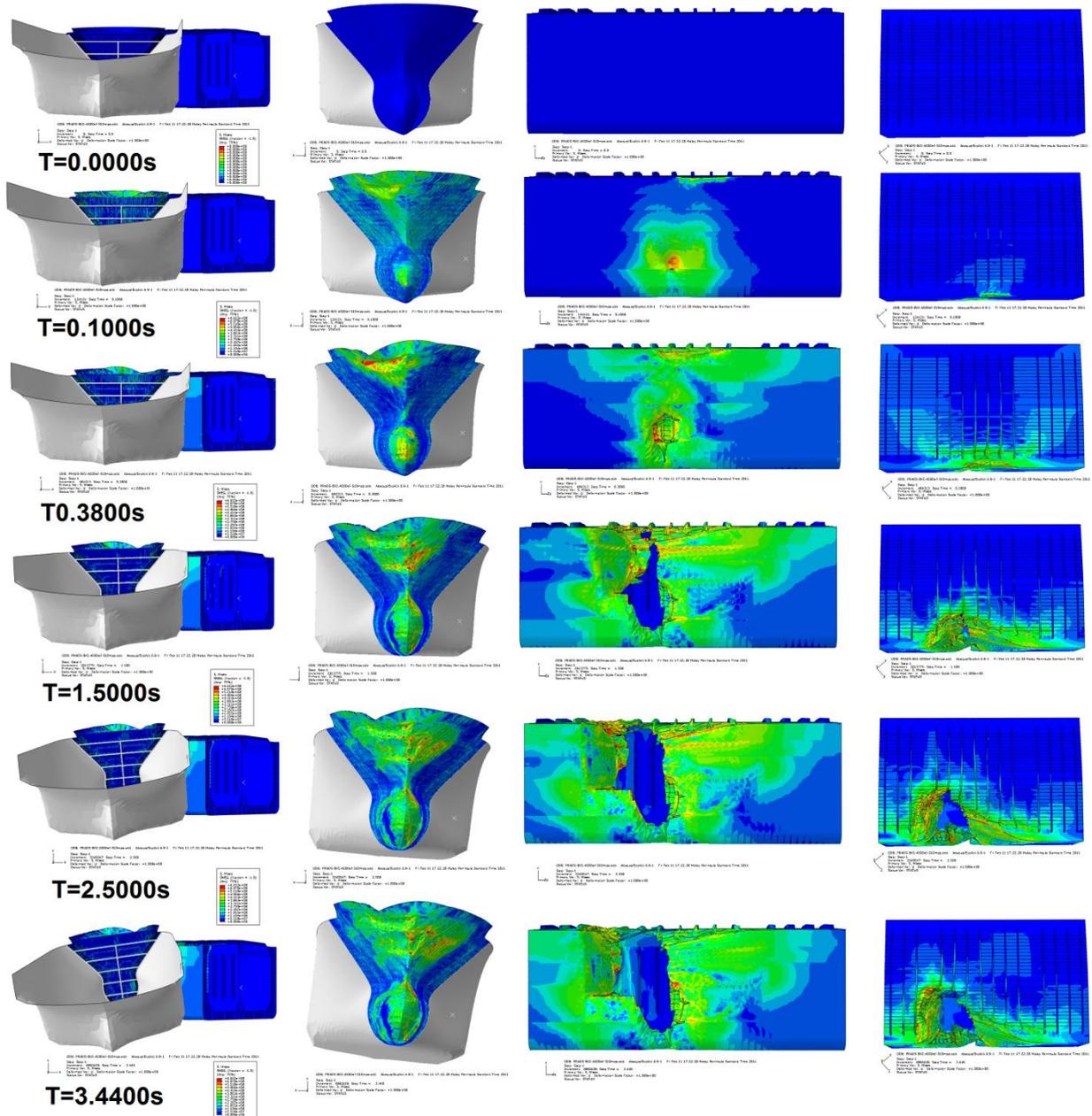
Figure 129 :The damage condition of ship-ship collision, striking by 34.29MKg displacement of ship at 50^{0} angle of attack and 10m/s speed.
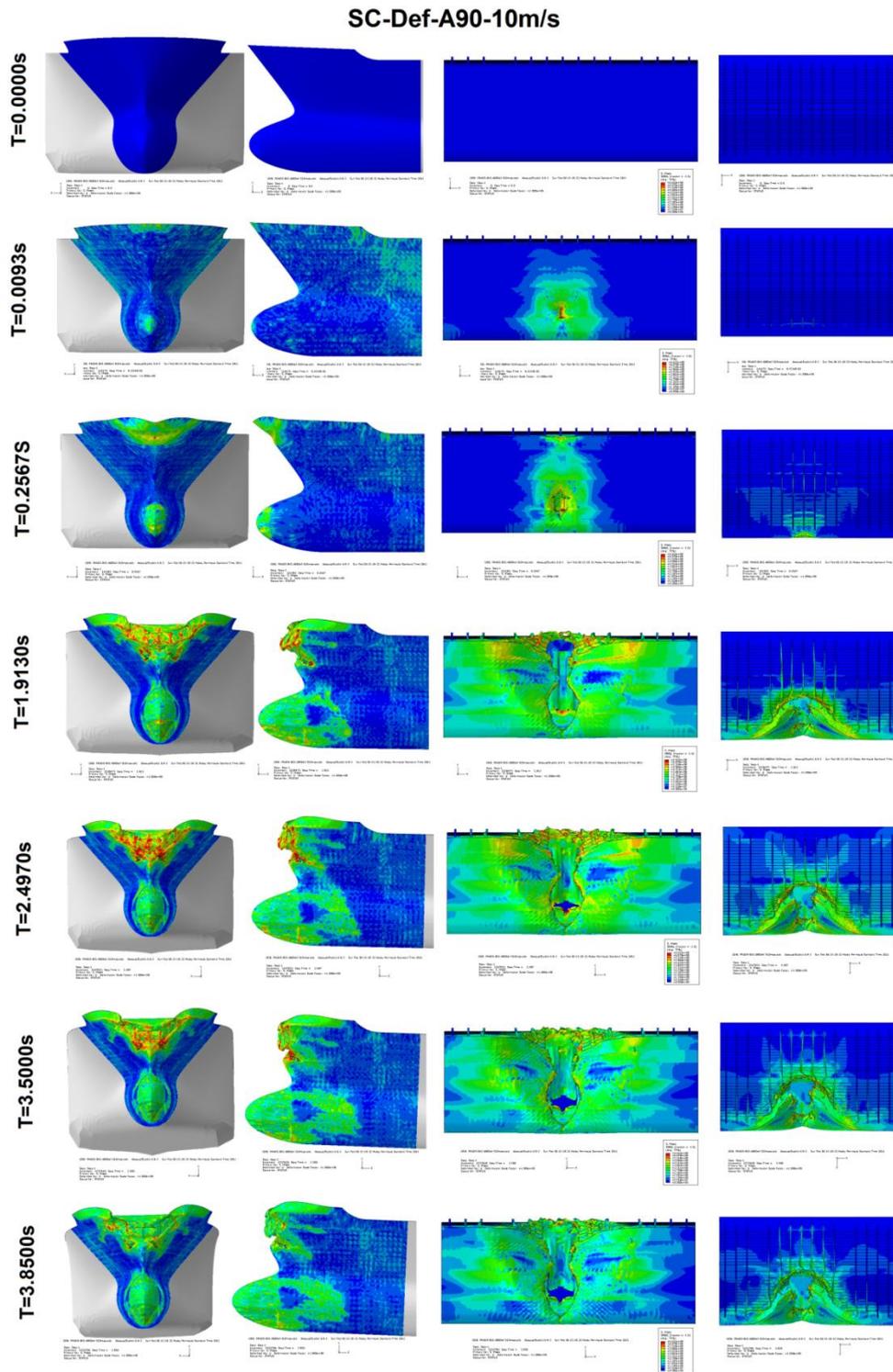
Figure 130 :The damage condition of ship-ship collision, striking by 34.29MKg displacement of ship at 90^0 angle of attack and 10m/s speed.

8.4. Simplified Approach

Based on the analysis done, most researchers such as (Karlsson, 2009, Hogström and Ringsberg, 2013, Ozguc et al., 2005)used displacement control analysis rather than running analysis using energy dissipation approach for ship-ship collision. The simplification structures for analysis without a complete striking ship with an actual ship displacement and the structure of struck ship only one or two compartments with half beam at midship. This is due to the analysis being very costly to replicate the actual size of a ship.

The current approach is an attempt to use actual ship displacement with full size of struck ship and two compartments of struck ship with full beam. Both methods, energy dissipation and control displacement approach are employed for the analysis of ship-ship collision.

As in chapter 7, the simplified analysis to predict maximum force and energy of rigid wall collision is introduced where the results are very promising. In this chapter some modification is establish for the prediction of force for energy dissipation in ship-ship collision.

For energy dissipation of rigid body collision, the conservative model (see Figure 131) and simple elastic system as shown in Figure 132 where the structure for rigidity calculation is only considered on shaded in grey area (see Figure 131) for struck ship. This is the part of structure most effected during collision overall. The section selection is also based on the overall damage and deformation that in FEA analysis where the selected section is deformed and ruptured without damage to the bottom structure and effects most of other half beam of the ship. The top deck also generates less resistance to the striking ship compared to side shell and easily ruptures after striking ship manages to rupture the side shell of the struck ship. The rigidity value R_s=0.0328 compute from equation (5-16). where, mass effected area=447290kg, Volume of effected area = length of compartment multiply (43.835m) by shaded area (1738m^2) see Figure 131.
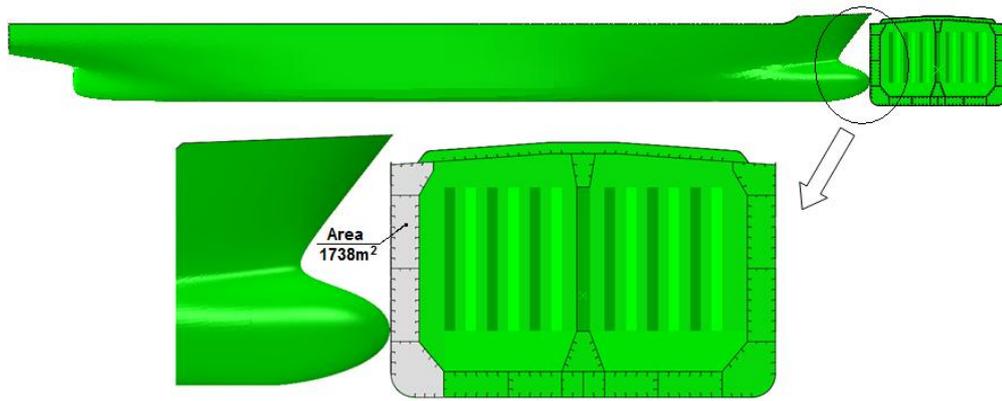
Figure 131: The energy dissipation for rigid bow collision model
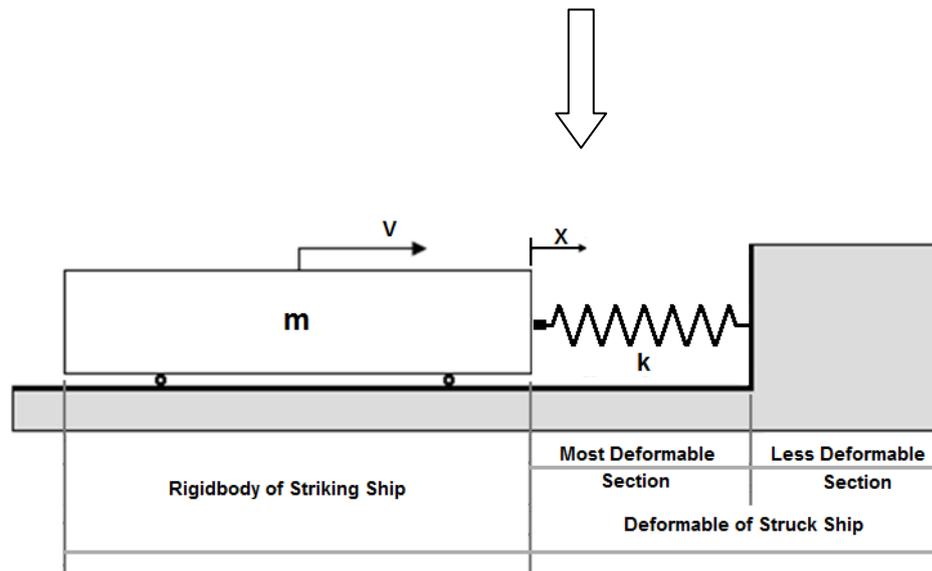
Figure 132: The simplified energy dissipation system of ship model for rigid bow.

Due to striking ship penetration into struck ship instead of crush as deformable bow collides to rigid wall, a new coefficient of bow shape (C_{bs}) is introduced. The coefficient of bow shape is to capture the contact area during penetration of rigid bow into struck ship. The coefficient is calculated based on the volume of penetrated bow into struck ship and divided with volume of rectangle that is able to contain the penetrated bow. In this case, the C_{bs} is estimated within range 0.35-0.65 depending on type of bow and shape. In the present analysis the value of C_{bs}=0.5 is adopted.

Figure 133: The simplified energy dissipation system of ship model for deformable ship-ship collision.
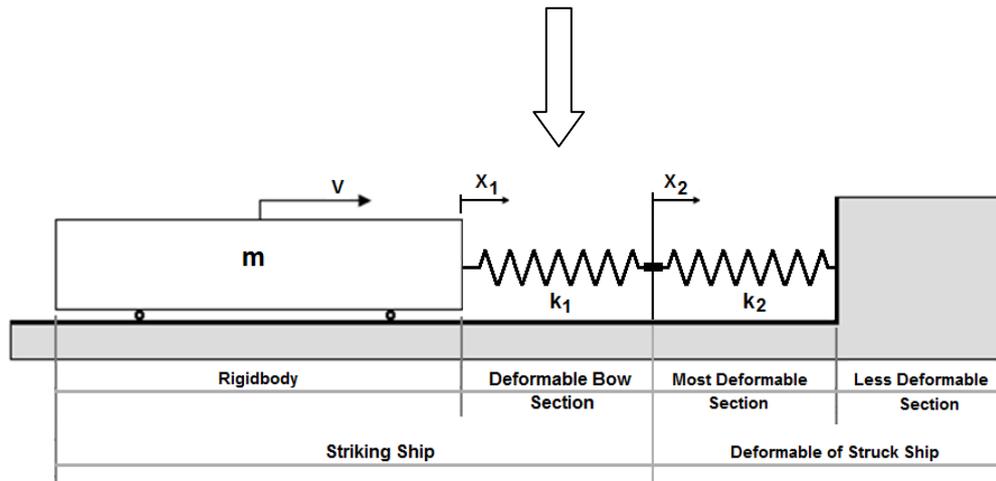
Figure 134: The simplified energy dissipation system of ship model for deformable ship-ship collision.

For energy dissipation of deformable collision, the conservative model is as in Figure 133 and simplified elastic system as shown in Figure 134. As simplification of the values of $k_1 + k_2 = k$ and $x_1 + x_2 = x$, due to the fact that most ship collisions are intact together during collision and act as one body. To compensate that the value of $R=R_b + R_s$ where combination of rigidity values for both structure are taken into account. Therefore the values k and x are assumed to be the same as discussed in chapter 7. The values of $R_b=0.0453$ from the previous chapter and $R_s=0.0328$ as calculated from Figure 131.

Therefore the new equation for rigid wall collision, rigid body of bow collision with deformable side shell and deformable ship-ship collision are as (8-1);

$$F_{max} = t_{avg}R\eta C_{bs}V\sqrt{KM} \begin{cases} \text{for rigid wall collision} & C_{bs} = 1 \text{ and } R = R_b \\ \text{for rigid body collision} & 0.35 \le C_{bs} \le 0.65 \text{ and } R = R_s \\ \text{for deformable collision } 0.35 \le C_{bs} \le 0.65 \text{ and } R = R_b + R_s \end{cases} \quad (8\text{-}1)$$

Where;

F_{max} = Maximum Crushing Force (N)

M = Ship displacement (kg)

η = Efficiency

C_{bs} = Coefficient of bow shape

t_{avg} = Average of plate thicknesses (mm)

K = Equivalent stiffener (N/m)

V = Ship collision speed (m/s)

R = Rigidity ratio

R_b = Rigidity ratio for deformable bow (Striking ship)

R_s = Rigidity ratio for deformable side shell (Struck ship)

Table 9 shows the summaries of the results for simulations analysis, prediction using simplified method and other available standards or approaches. Figure 135 shows the rupture energy and force for outer and inner shell of struck ship. The simplified results generated using equation (8-1) have also been tabulated and plotted along with Woisin, ASSTHO and Eurocode prediction results. The results plotted in Figure 136 show that Wiosin with 50% additional percentile always produces larger forces compared to others methods. Pederson generated too massive prediction forces for all cases, only tabulated in Table 9 and not plotted along with other methods. Eurocode prediction of maximum forces follow the nice pattern paths for all cases except for angle collision. The FEA and simplified method prediction gave very good correlation and promising results where most of the prediction nice follow the mode of FEA results.

Table 9 : The comparison results of ship-ship collision summary

Damage Condition	Collision Setup	Initial	Ship Displacement (M.kg)	Initial Velocity (m/s)	Collision Angle (0°)	η	Predicted Max Force	FEA Analysis Max Force	Eurocode K=10MN/m	Eurocode K=10MN/m	Wo sin (+50%)	AASTHO	Shell	Rupture Time(s)	Displacement (m)	Rupture Force (N)	Rupture Energy IE (J)	Rupture Energy KE (J)	KE
Angle Collision	1	A90	34.29	10	90	1	9.84E+07	1.06E+08	1.85E+08	2.27E+08	2.44E+08	2.26E+08	Outer	0.090003	0.898688	3.11E+07	1.30E+07	1.36E+07	1.71E+09
													Inner	0.270002	2.67738	5.84E+07	6.60E+07	7.78E+07	1.71E+09
	2	A70	34.29	10	70	0.98	9.64E+07	9.26E+07	1.85E+08	2.27E+08	2.44E+08	2.26E+08	Outer	0.072	0.719298	2.56E+07	9.11E+06	9.87E+06	1.71E+09
													Inner	0.288002	2.85164	7.81E+07	8.01E+07	9.50E+07	1.71E+09
	3	A50	34.29	10	50	0.65	6.40E+07	9.88E+07	1.85E+08	2.27E+08	2.44E+08	2.26E+08	Outer	0.108001	1.0786	6.19E+07	2.32E+07	3.02E+07	1.71E+09
													Inner	0.360002	3.52084	7.55E+07	1.24E+08	1.70E+08	1.71E+09
	4	A30	34.29	10	30	0.23	2.36E+07	4.15E+07	1.85E+08	2.27E+08	2.44E+08	2.26E+08	Outer	1.11	10.8416	2.12E+07	3.06E+07	1.25E+08	1.71E+09
													Inner	-	-	-	-	-	-
Deformable Collision	5	DEF-A90	34.29	10	90	1	2.34E+08	1.44E+08	1.85E+08	2.27E+08	2.44E+08	2.26E+08	Outer	0.083334	0.9170027	3.42E+07	4.05E+07	4.12E+07	1.70E+09
													Inner	0.296666	2.50062	4.66E+07	8.73E+07	9.74E+07	1.70E+09
	6	DEF-A50	34.29	10	50	0.65	1.32E+08	1.36E+08	1.85E+08	2.27E+08	2.44E+08	2.26E+08	Outer	0.1	0.981965	4.54E+07	4.28E+07	4.83E+07	1.70E+09
													Inner	0.38	3.65343	9.85E+07	1.73E+08	2.22E+08	1.70E+09
Different Speed	7	DS-10m/s	34.29	10	90	1	9.84E+07	1.06E+08	1.85E+08	2.27E+08	2.44E+08	2.26E+08	Outer	0.090003	0.898688	3.11E+07	1.30E+07	1.36E+07	1.71E+09
													Inner	0.270002	2.67738	5.84E+07	6.60E+07	7.78E+07	1.71E+09
	8	DS-7.5m/s	34.29	7.5	90	1	7.38E+07	8.05E+07	1.39E+08	1.70E+08	2.44E+08	1.69E+08	Outer	0.120002	0.897661	3.39E+07	1.33E+07	1.38E+07	9.64E+08
													Inner	0.360001	2.66033	7.66E+07	6.49E+07	7.67E+07	9.64E+08
	9	DS-5.0m/s	34.29	5	90	1	4.92E+07	7.74E+07	9.26E+07	1.13E+08	2.44E+08	1.13E+08	Outer	0.18	0.894817	2.76E+06	3.05E+07	1.35E+07	4.29E+08
													Inner	0.480001	2.33377	5.88E+07	8.76E+07	5.91E+07	4.29E+08
	10	DS-2.5m/s	34.29	2.5	90	1	2.46E+07	5.94E+07	4.63E+07	5.67E+07	2.44E+08	5.65E+07	Outer	0.280003	0.690241	2.37E+07	8.76E+06	8.85E+06	1.07E+08
													Inner	1.1	2.4106	4.98E+07	4.79E+07	5.83E+07	1.07E+08
Different Ship Displacement	11	DD-73.51M/kg	73.51	5	90	1	7.20E+07	7.90E+07	1.86E+08	1.66E+08	3.88E+08	1.65E+08	Outer	0.150002	0.748379	2.80E+07	1.04E+07	1.05E+07	9.19E+08
													Inner	0.480001	2.36599	5.71E+07	1.32E+07	6.10E+07	9.19E+08
	12	DD-34.29M/kg	34.29	5	90	1	4.92E+07	7.74E+07	9.26E+07	1.13E+08	2.44E+08	1.13E+08	Outer	0.18	0.894817	2.76E+06	3.05E+07	5.91E+07	4.29E+08
													Inner	0.480001	2.33377	5.88E+07	3.05E+07	5.91E+07	4.29E+08
	13	DD-20.22M/kg	20.22	5	90	1	3.78E+07	7.14E+07	7.11E+07	8.71E+07	1.88E+08	8.67E+07	Outer	0.160005	0.79373	3.04E+07	1.12E+07	1.15E+07	2.53E+08
													Inner	0.520001	2.46633	3.05E+07	3.46E+07	6.48E+07	2.53E+08
	14	DD-8.58M/kg	8.58	5	90	1	2.46E+07	5.76E+07	4.63E+07	5.67E+07	1.22E+08	5.65E+07	Outer	0.18	0.87927	1.07E+07	1.30E+07	1.32E+07	1.07E+08
													Inner	0.385001	2.51141	5.54E+07	5.33E+07	6.51E+07	1.07E+08

192

Figure 135: The comparison of FEA results for rupture forces and energies generated during collision.
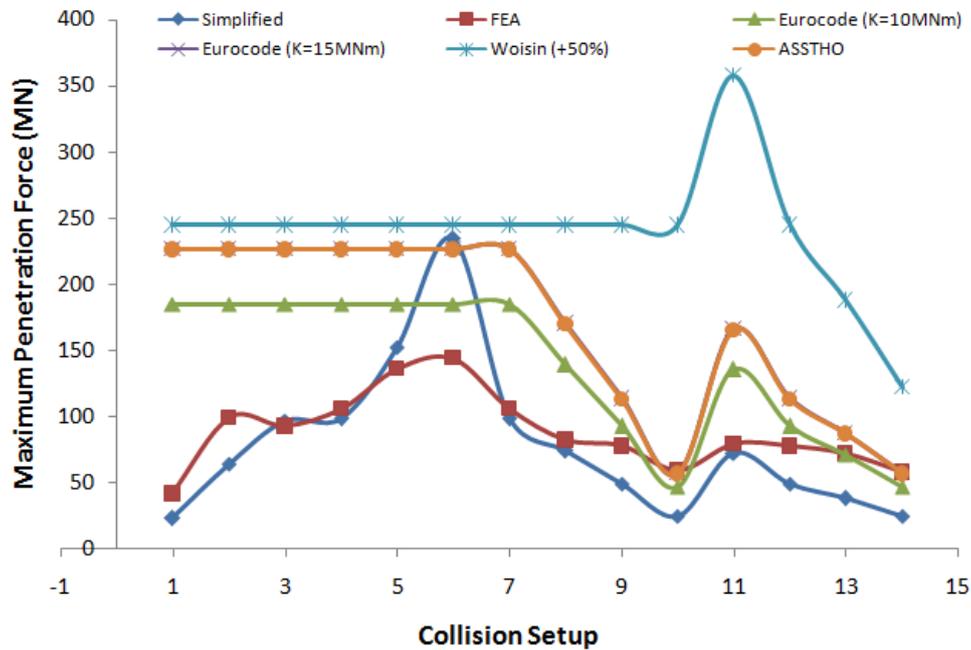
Figure 136: The comparison results of maximum collision forces generated during collision.

8.5. Summary
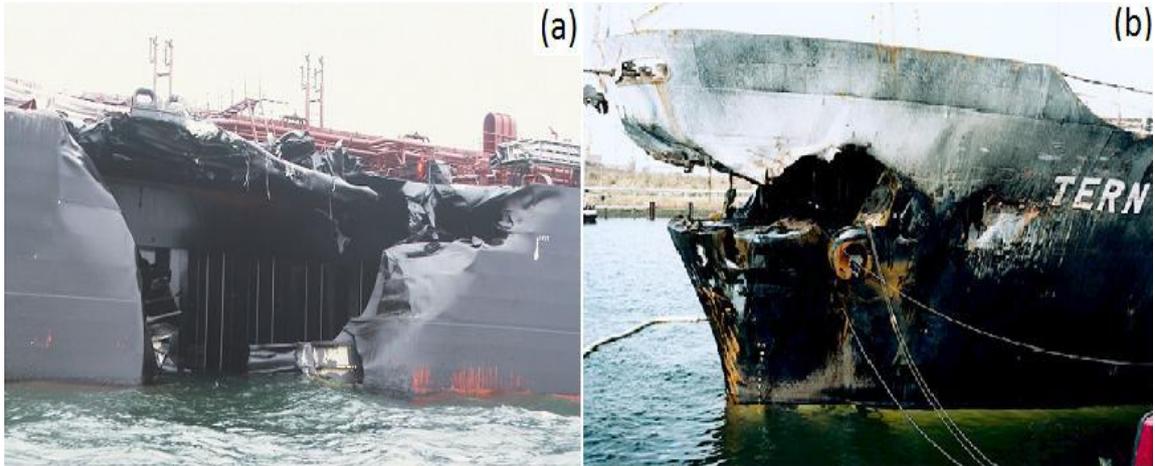
Figure 137: The collision damage of (a) Baltic Carrier and (b) Bulk Carrier Tern.

The analyses were carried out using both normal and bulbous bow shapes for control displacement ship-ship collision and only for bulbous bow for energy dissipation of ship-ship collision.

In all cases considered for control displacement of ship-ship collision the energy of the collision for the normal bow was larger than that for the bulbous bow during both outer shell and inner shell rupture. The energy settled at the same peak value during the collision simulation for both bow types using the same input parameter for weight of displacement.

Both rupture force and rupture energy for control displacement and energy dissipation of ship-ship collision show angle collision generated higher values compare to lateral collision. This happened where more distance of penetration needed to get larger contact in order to achieve ultimate stress concentration at side shell during penetration of striking into struck ship.

Overall, the average rupture force and energy for outer and inner shell of struck ship for lateral collision of ship-ship collision are 22.9MN, 57.2MN, 15.3MJ and 69.7MJ see Figure 135.

(Wang et al., 2006), with collision and grounding paper reported that, there is one set of regulations (Abramowicz, 1994), that are required for anyone navigating on the Rhine River. Side structures must absorb minimum collision energy of 22 MJ in gas tankers' side structures, when the scantlings are deviated from those prescribed in the rules. There are also reports of offloading shuttle tankers colliding with FPSOs in the North Sea. The most severe shuttle tanker impact so far involved energy of 37 MJ (BOMEL 1999). Moan et al (2002) reported that the critical energy for penetrating the wing tanker of an FPSO that is 40 m wide and 21 meters deep is about 8 to 18 MJ when the FPSO is struck by a 42,000 DWT tanker; 40 to 55 MJ when the FPSO is struck by a 18,000 DWT tanker; and 57 MJ when its engine room is penetrated by a tenderly moored shuttle tanker.

The maximum penetration force (see Figure 136) shows very good correlation between FEA and simplified calculation and some of the other methods for lateral collision of ship-ship collision.

The data also indicates that the rupture energy shows some close similarities, but many other influential factors, such as striking bow shape, position of collision, angle of collision, rigidity of structure play important roles. Therefore collision problems have to be treated separately as a case by case basis. There is no rigid formalized acceptance criterion for an ship-ship collision, especially ship structural designs. This is where FEA analysis takes place to evaluate for each complex problem of structure integrity due to collision and grounding events.

The differences in the actual damage and the predicted damage can be as a result of the assumptions being made about the shape of the bow of the striking ship; the modelling of the bow as being rigid and deformable, also the condition of the structure of both the struck and striking ships at the time of the collision. Also the assumption of idealised boundary conditions for the finite element model can affect the results produced and both figures for actual incident and FEA analysis which in Figure 137 for actual incident and

Figure 98, Figure 99, Figure 106 and Figure 129 for FEA simulation show some similarities on damage scale of striking and struck ship.

Even though, the analysis didn't take into account the effect of added mass during analysis which are (Minorsky, 1959) estimated $0.4M_b$ in sway motion, (Terndrup Pedersen and Zhang, 1998, Petersen and Pedersen, 1981) estimated (0.05-0.07 M_b in surge motion, 0.21 M_b in yaw motion and $0.85M_b$ in sway motion). However, the effect of added mass is reduced due to collision duration is very short, range between 1.5 - 5.6s and speed of striking ship between 5-10m/s.

In general, the results of the analysis carried out are interesting and give a good insight into the collision event. It is very difficult to validate with an actual collision event due to a lack of detailed information. The results of complex ship structure collision analysis are presented making a number of assumptions about the structure of the ships involved in the collision and the details of the collision.

CHAPTER 9: CASE STUDY FOR RESIDUAL STRENGTH AFTER DAMAGE

9.1. Introduction

This chapter is a case study of a box girder ultimate strength and residual strength after damage, solved using dynamic and static approaches. The chapter are divided into two sections which are damage analysis, and progressive collapse analyses of the damaged structures due to indentation of an artificial indenter.

The results of damage analysis will be focused on the load of the indenter that punches into the box girder with a constant velocity. The progressive collapse analyses is to compare the predictions of damaged box girder ultimate strength with and without residual stress using dynamic and static analysis and available methods.

The analysis will enable an author to understand the behavior of the solvers adopted and the reliability of the methods and techniques for FE analysis. The contents have already been discussed in (Benson et al., 2013).

9.2. Material and Structure Model Characteristics

9.2.1. Structure Model

The structure model is based on (Gordo and Soares, 2009), where replicate is from H200 model of experiment. The specimen length is = 1000mm, breadth = 800mm, depth = 600mm, span = 200mm, plate thicknesses = 4mm, stiffeners height = 20mm, and stiffener thicknesses = 4mm. The arrangement of the box girder structure model as shown in Figure 138.
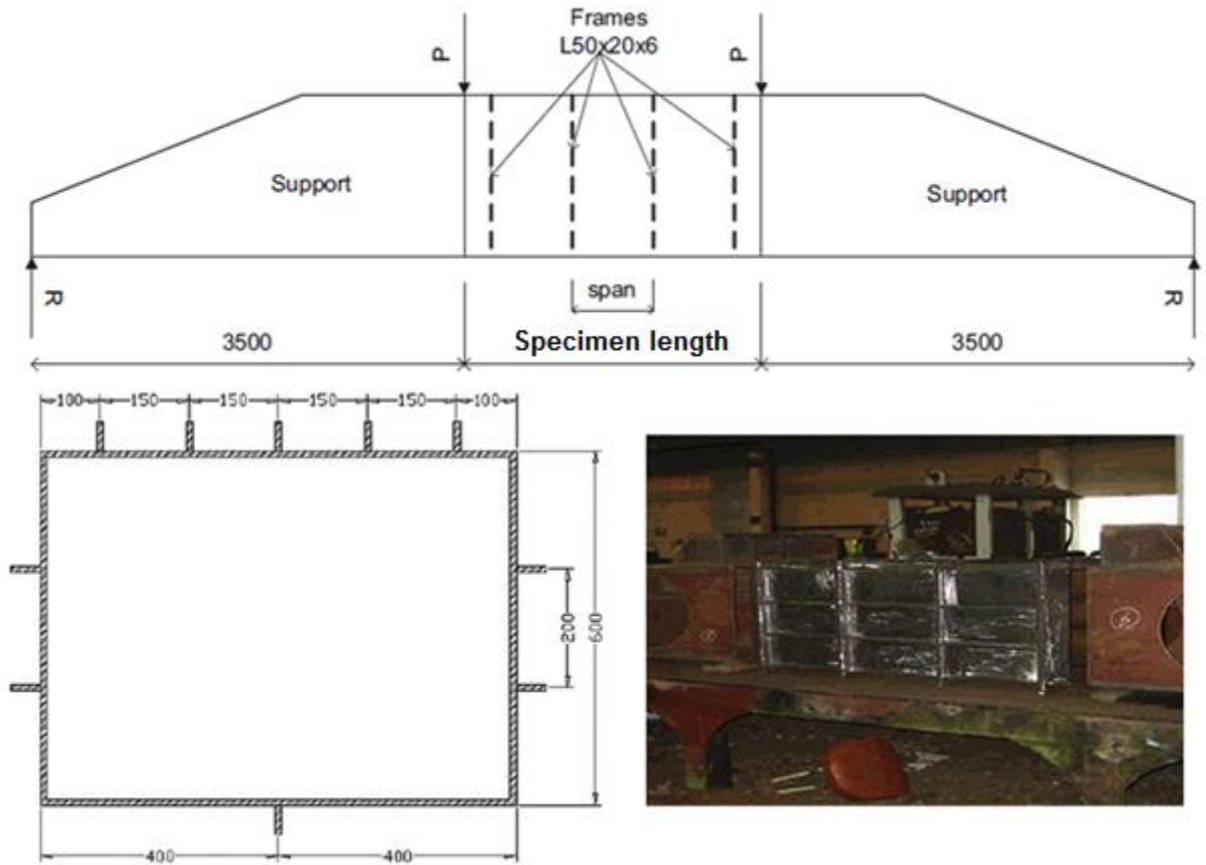
Figure 138 : Experimental setup (Gordo and Soares, 2009).

9.2.2. Material Properties

The material used is HTS 690 high tensile strength steel and taken from(Sedlacek and Müller, 2001) discussed previously in chapter 3.The principal material properties for structural analysis are the yield stress and the Young modulus which are set as 690 MPa and 211GPa, respectively. The constants for HTS 690 used in this study are based on the curve by (Sedlacek and Müller, 2001) as follows: K = 1250MPa, n = 0.12, e_{plat} = 0.0124, and σ_0= 745. The stress–strain curve is shown in Figure 139.
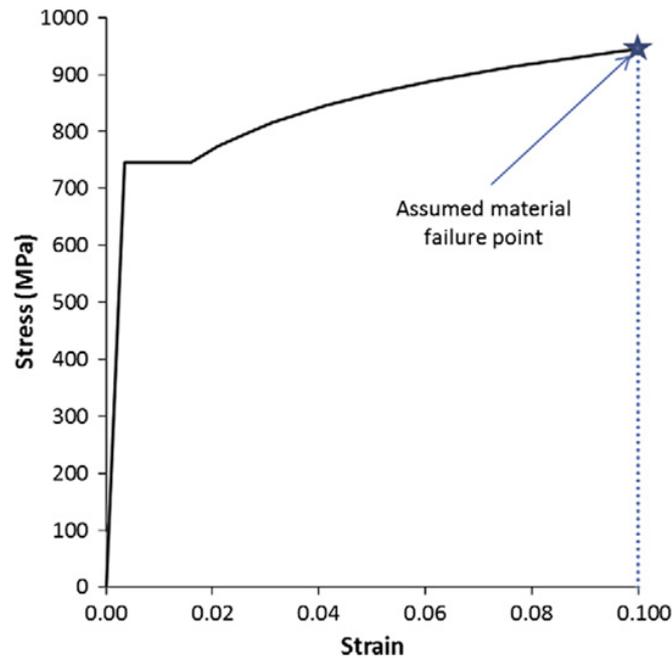
Figure 139: HTS 690 True Stress Strain Curve (Benson et al., 2013).

9.2.3. Material Failure

The material failure FLD model used is adopted from chapter 4 in conjunction with the material properties, parameters and material properties described in this chapter. The failure model permits the rupture of the box girder structure when the material exceeds the allowable or maximum strain in any direction of the shell elements during penetration of the indenter.

9.3. Simulation approach

The simulation is divided into two sections, which are indentation and progressive collapse of box girder due to bending load.

The simulation analysis was undertaken with three load steps:
- Step 1: penetration of the indenter into the box girder at 3 m/s and to a depth of 0.3 m.
- Step 2: retraction of the indenter at 3 m/s.

- Step 3: apply incremental bending moment up to and beyond the ultimate capacity.

Where Step 3 is completed using the dynamic solver a step time of 1 s was used to increment the applied curvature from zero to the post collapse region. The indenter is defined as a rigid body cylinder with a hemisphere tip. The indenter has a size of 0.75mheight and 0.35 m diameter. The FEM analysis used the dynamic explicit analysis capabilities of ABAQUS. Three different indentation scenarios were completed, damaging the bottom, the side and the top flanges of the box. In each case the indenter was targeted at the exact centre of the flange, Figure 140.

The penetration was sufficient to severely rupture the flange around the targeted area. The box boundaries are constrained in all six degrees of freedom for the end part of structure model. All other initial settings for the FEM analysis were the same as for the intact analyses, with superimposed average geometric imperfections. The indentation of the box girder at the top, bottom and side are completed in a separate simulation file before the subsequent bending moment analyses, using the restart capabilities of ABAQUS. This reduced the time cost of the various analyses considerably as multiple bending moment simulations could be completed using a single indentation simulation.
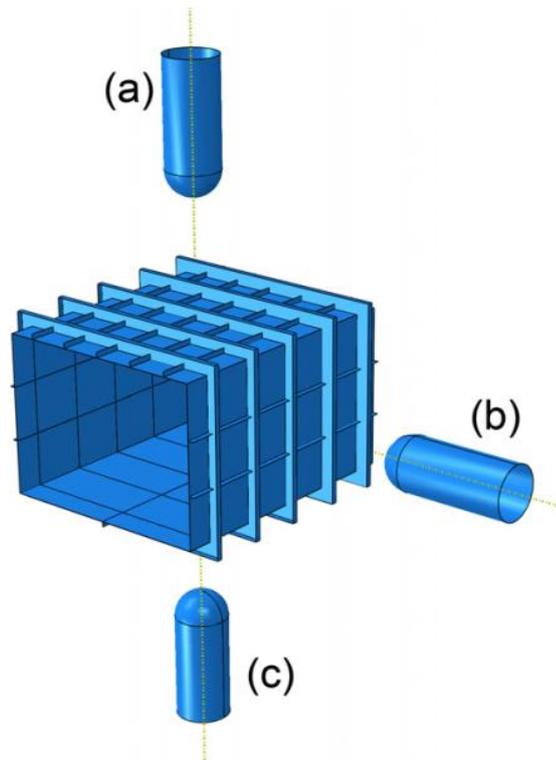
Figure 140: Indentation Orientation (a) Top Indentation, (b) Side Indentation and (c) Bottom Indentation(Benson et al., 2013).
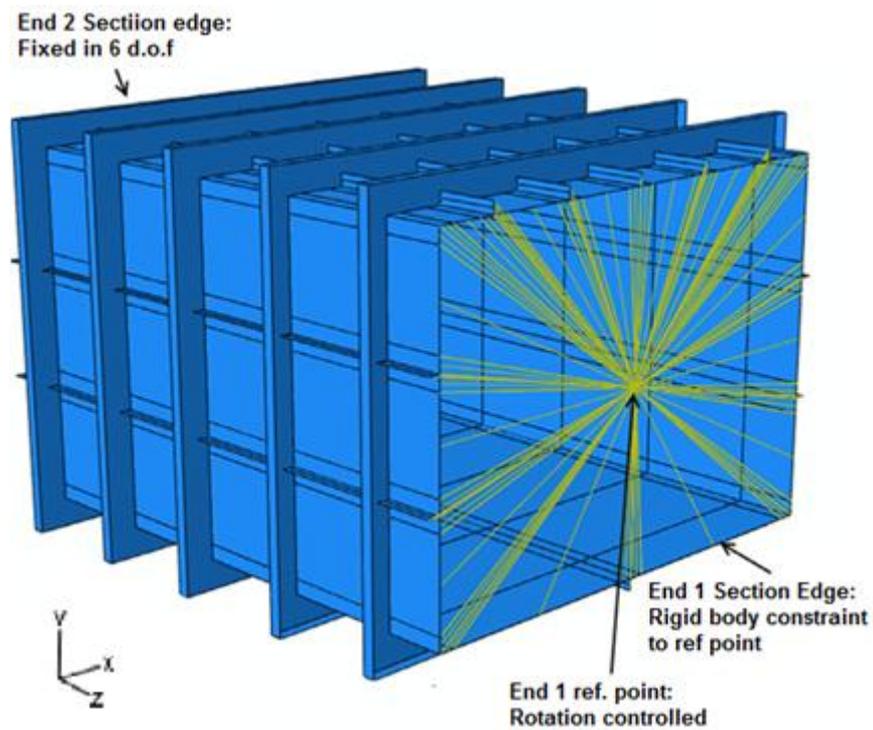
Figure 141 : H200 Boundary Conditions(Benson et al., 2013).

The bending moment is applied in the form of rotational at End 1 (see Figure 141) reference point. The rotational is applied in vertical and horizontal directions at different rotational ratio as stipulated in Table 10until the maximum bending moment is conceded. The arrangement of the rotational setup can be changed accordingly as far as satisfaction of the interaction table is achieved.

Table 10:   The ratio of rotational angle in radian.

Mode	Displacement (m)			Rotational (rad)		
	X-Axis	Y-Axis (Horizontal)	Z-Axis (Vertical)	X-Axis	Y-Axis (Horizontal)	Z-Axis (Vertical)
1	Allow	Allow	Allow	Allow	0.35	Allow
2	Allow	Allow	Allow	0.93	0.39	Allow
3	Allow	Allow	Allow	0.71	0.71	Allow
4	Allow	Allow	Allow	0.39	0.93	Allow
5	Allow	Allow	Allow	0.35	Allow	Allow
6	Allow	Allow	Allow	0.39	-0.93	Allow
7	Allow	Allow	Allow	0.71	-0.71	Allow
8	Allow	Allow	Allow	0.93	-0.39	Allow
9	Allow	Allow	Allow	Allow	-0.35	Allow

9.4. Indentation Results

9.4.1. Top Panel Damage

Figure 142shows the simulation stress plot of the ruptured panel and the displacement force graph for the top indentation of the box girder. The stress plot shows the stress state once the indenter has been removed. The maximum lateral penetration resistance force and displacement of the indentation are F = -579.5 kN and 83.9mmrespectively. The start of the rupture of the plate occurred at 86.93mm penetration after which the resistance force starts to decline. The rupture zone extends to the outermost

stiffeners on the top flange. The side flanges are highly stressed but do not exhibit significant out of plane deflection.

The stress plot shows the high residual stresses in the region around the ruptured hole. The box returns to an equilibrium state once the indenter is removed, which means the stresses are effectively locked into the structure subsequent to the impact. The residual stress is predominantly tensile in the area around the rupture with equilibrating compressive stresses of much lower magnitude occurring in the structure away from the hole. The residual stress reduces in magnitude across the side flanges and is very small in the bottom flange.
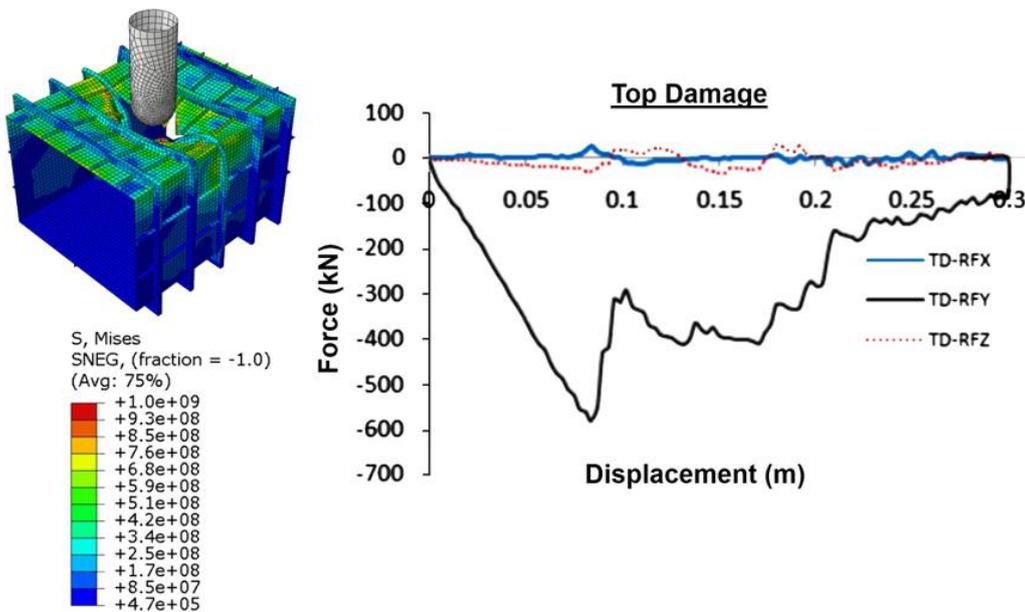
Figure 142: Force displacement of box girder for top indentation.

9.4.2. Bottom Panel Damage

Figure 143shows the simulation stress plot of the ruptured panel and the displacement force graph for the bottom indentation of the box girder. The graph of bottom damage shows the resistive force is proportional to the displacement until it reaches the maximum indentation force of F = 622.34 N and displacement of 89.9 mm. The rupture occurs almost immediately after the indentation force reaches its maximum value as shown in Figure 143.

The rupture takes place at about 3 mm of further penetration of the indenter after the maximum force has been reached and the force then sharply declines. The stress plot shows similar characteristics to the top damage model, with high tensile residual stresses in the area close to the rupture and equilibrating compressive stresses elsewhere. The rupture extends further than for the top panel, primarily because there are less stiffeners on the panel to resist the impact load. Significant distortion occurs across the whole bottom flange and into the side panels.
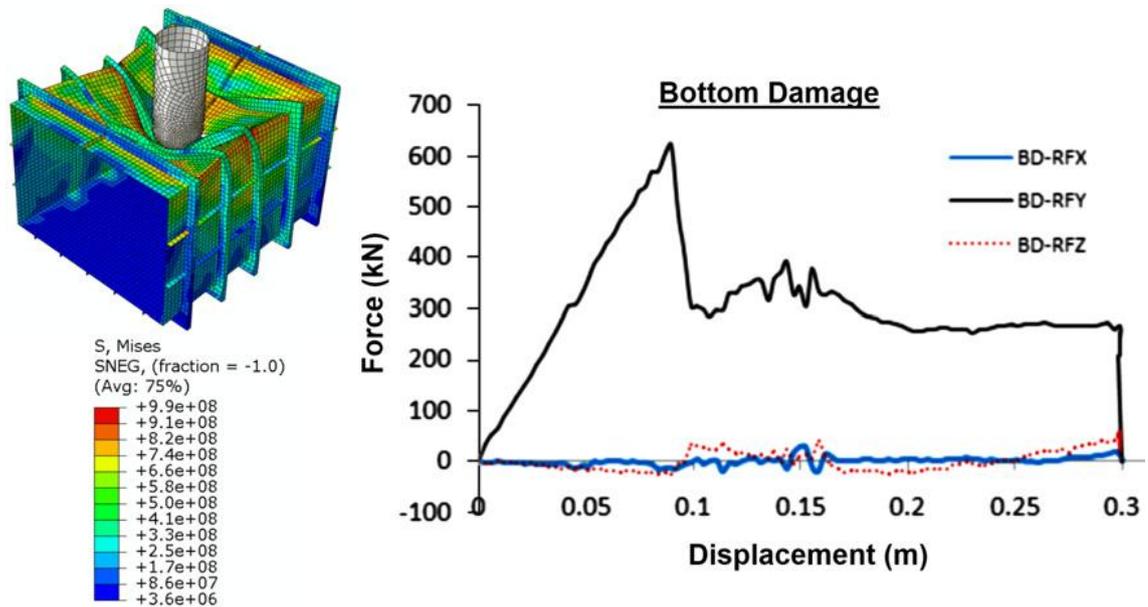
Figure 143: Force displacement of box girder for bottom indentation.

9.4.3. Side Panel Damage

Figure 144shows the simulation stress plot of the ruptured panel and the displacement force graph for the side indentation of the box girder. When placed under side damage, the transverse frame trips at 54mm after penetration of indenter and load F = -387.586 KN. This leads to a very sudden displacement with a corresponding drop in penetration force. The maximum indentation force and displacement for side damage peaks at F = -674.6 KN and 111mm respectively. The rupture initiates at 114.0mm and lower load is then required until the penetrator reaches the maximum indentation. With stress similar to the other damage models, the ruptured zone extends over

most of the side flange and significant distortion at the corners with the top and bottom panels are also exhibited.
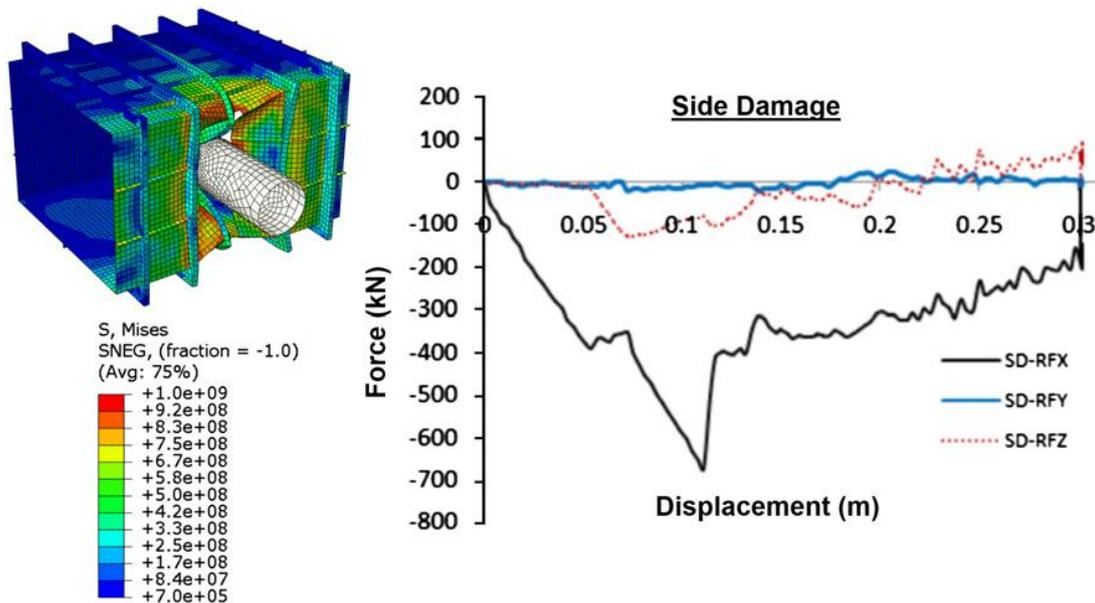
Figure 144: Force displacement of box girder for side indentation.

9.4.4. Comparison of Lateral Force of Box Girder to all the Side Shells.

Figure 145shows the comparison of lateral force for the three different damage scenarios. The top and bottom damage produces a very similar path of load displacement force. The side damage slightly deviates from the other lines at 54–70mmindentation. The side damage also produces a higher penetration force than the other cases. This happens because the indenter is targeted between the two longitudinal stiffeners and is thus capable of absorbing more energy and elongating more before rupture. In comparison, the top and bottom indentations are targeted directly at the central longitudinal. The top damage scenario produces a lower maximum load compared to side and bottom penetration. This occurs due to the additional rigidity of the top structure, meaning it is less capable of absorbing higher energy during indentation. This leads to higher stress concentration along the corner section and earlier rupture early compared to the other cases.
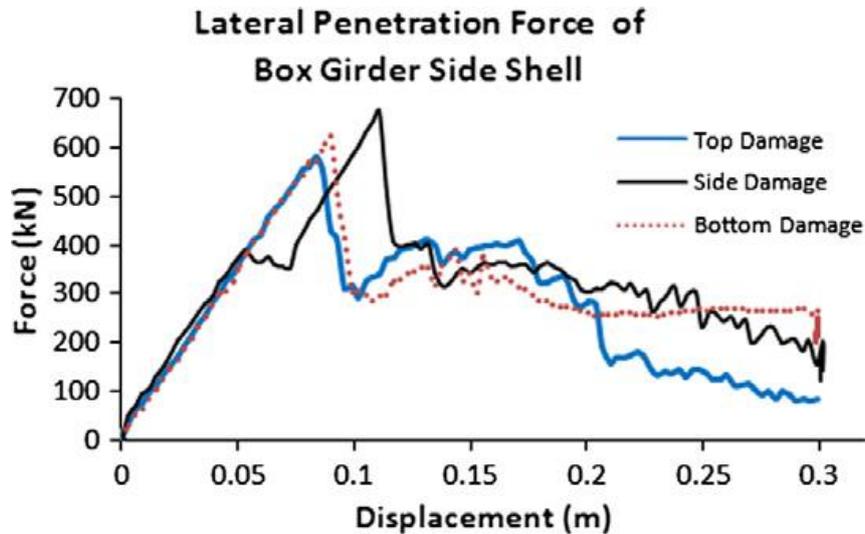
Figure 145: Force displacement of box girder for top, bottom and side indentation.

9.5. Ultimate Strength of Box Girder

The progressive collapse of box girder are simulated using explicit and implicit solver, where dynamics analysis was executed by the author and static analysis was executed by Benson as published in (Benson et al., 2013). The simulation results presented are partly shown in Figure 147 and in Figure 148 for interaction diagram for all conditions.

Figure 147 shows the progressive collapse of box girder after it experiences bending load in the form of rotational in mode 1 for top, side and bottom damage. The simulation will be repeated for all modes as in Table 10until the maximum bending moment is conceded. The interaction diagram of bending moment will be plotted to observe the behaviors for each damage simulations.

Figure 146 shows the comparison of experimental and simulation results where the collapse mechanism is closed imitation from simulation analysis. Figure 148a shows the interaction diagram for box girder without indentation processes. The results are compared with dynamic , static and (Smith, 1977) methods. The results show good agreement where dynamic FEM generated less values compared to static and Smith methods. This may have happened due to the influence of material failure embedded in the dynamic analysis

where there is no account for static analysis and Smith method. This analysis also shows Smith method predicted higher results compared to others in the first quadrant sector.

No	Experiment	Simulation
1		
2		
3		
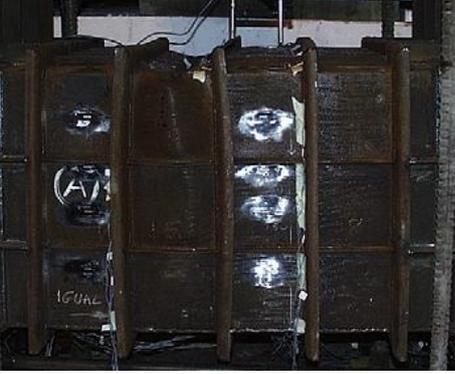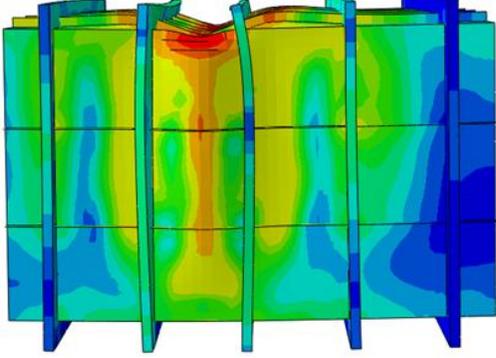
Figure 146 : The comparison of box girder damage for experimental (Gordo and Soares, 2009)and simulation analysis.

9.5.1. Interaction Diagram - Top Panel Damage

The interaction plots in Figure 148bshowsa significant reduction in ultimate capacity of the top damaged box compared to the intact strength in almost all cases. The reduction is most pronounced in the upper part of the interaction plot, where the box is under sagging bending moment. In this circumstance the damaged region is placed under compression in the plane load. This is predominantly taken by the upper parts of the box sides. Compared to the intact box, the compressive load portion of the cross section is also increased for the same curvature because the neutral axis is lower. These effects combine to cause much earlier buckling in the upper parts of the box, which corresponds to a much lower ultimate strength. The reduction in ultimate strength is less significant in the lower (hog) part of the interaction plot. The interaction plot also shows considerable differences between the FEM analyses where the residual stress due to damage is maintained (dynamic FEM with residual stress) and the equivalent analyses undertaken with no residual stresses included (static FEM). The simplified progressive collapse results show a close correlation to the static FEM.

Remarkably, under a predominant hogging bending moment the dynamic FEM ultimate strength results are greater than for the intact case, although the capacity is still much reduced in the upper quadrants of the interaction plot. These results suggest that the residual stresses in the structure, which are particularly high in the region adjacent to the ruptured zone, have a significant effect on the ultimate strength of the girder, in this case by increasing the capacity for all combinations of applied curvature. Both the static FEM and simplified progressive collapse results do not account for the influence of the residual stresses. The top damage box girder results from the static approach and the dynamic – zero residual stress approach are compared in Figure 148c. The results reiterate the findings from the intact analyses showing that the two solvers produce almost identical results so long as the initial conditions in the mesh are identical. This also shows conclusively that the differences between the static and dynamic results presented above are due to the residual stresses in the mesh resulting from the impact.

9.5.2. Interaction Diagram - Side Panel Damage

Interaction plots for the side damage scenario are presented in Figure 148d. The plot shows similar correlation between results as seen in the side damage scenario, which again reflects the dominance of the top flange in determining the overall strength of the girder.

9.5.3. Interaction Diagram - Bottom Panel Damage

Interaction plots for the bottom damage scenario are presented in Figure 148e. In comparison to the differences shown for the top damage case, the plot demonstrates a much closer correlation between the static FEM, dynamic FEM and simplified progressive collapse results. However, the dynamic FEM with residual stress results still shows higher ultimate strength than the equivalent zero stress static FEM when the box is predominantly under a hogging bending moment, which corresponds to the damaged region being placed under compressive load. The closer correlation between results is likely to be because the top flange, which in this scenario is left intact, is the dominant load bearing region of the structure. Therefore, the influence of the ruptured zone and the associated tensile residual stress field in the bottom flange has less influence on the overall strength of the box under longitudinal bending.

Mode	Orientation	Simulation
1	Top Damage	
1	Side Damage	
1	Bottom damage	

Figure 147 : Simulation bending moment after indentation (with residual stress).
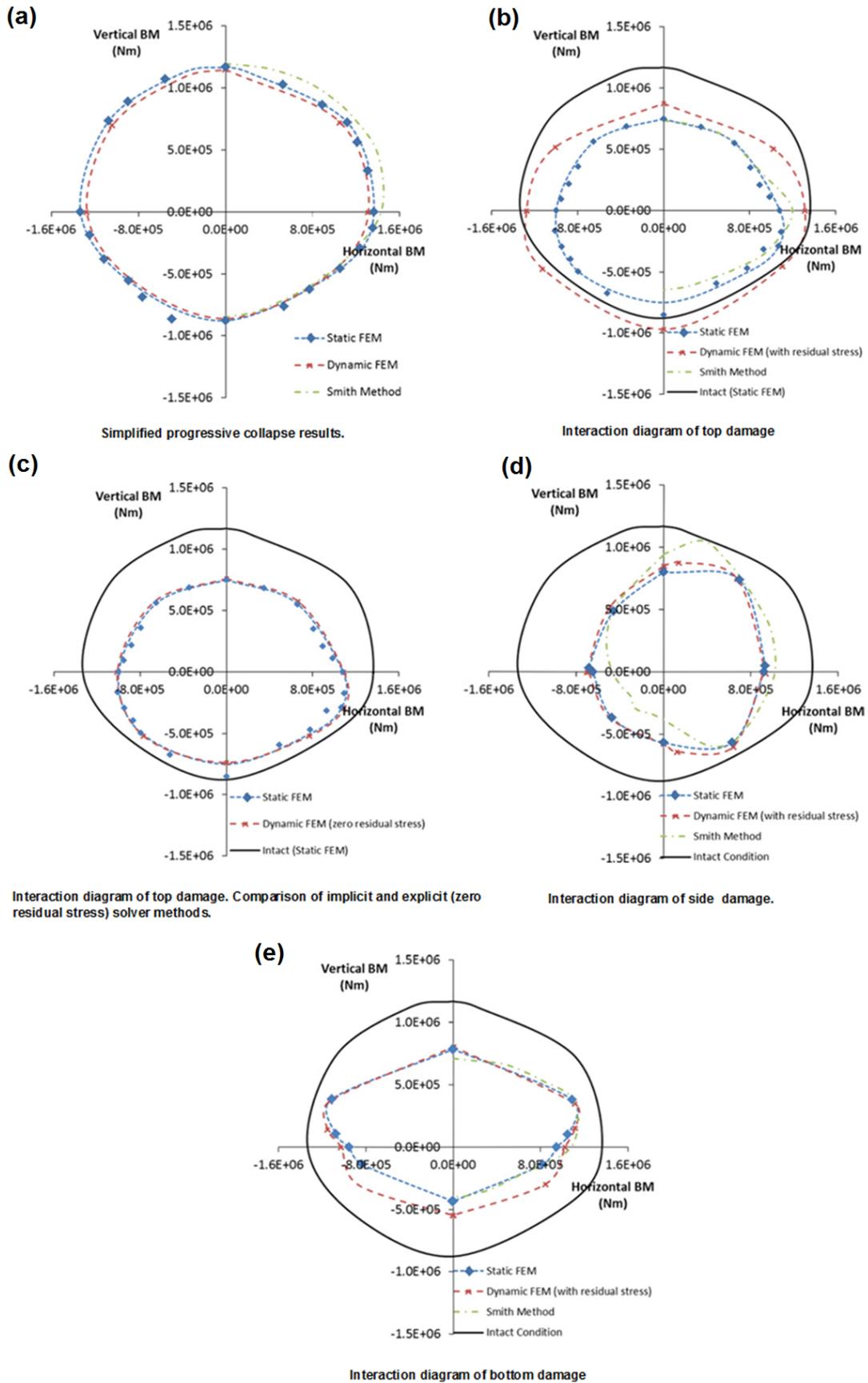
Figure 148 : Interaction diagram of progressive collapse of box girder (Benson et al., 2013).

9.1. Summary

The chapter discussed the progressive collapse of box girder ultimate strength with no indentation, with and without residual stress after indentation using dynamic and static FEM analysis. The result of box girder without indentation show very good agreement with experimental results by (Gordo and Soares, 2009) and simulation analysis. More important, the results of static and dynamic approaches produce almost identical behavior. The findings suggest that the quasi static approach is an acceptable solver method even when handling a highly non-linear post collapse scenario(Benson et al., 2013)

CHAPTER 10: CONCLUSIONS AND RECOMMENDATIONS FOR FUTURE WORK

10.1.   Conclusions

The main purpose of this thesis is to study the performances of ship collision and grounding with a rational investigation of an accidental load by addressing all various types of damage scenarios.

In fulfilling the objectives of present research work contributions, the thesis are focuses on four main separated tasks;

   i.   Rupture prediction

   ii.   Ship grounding analysis

   iii. Ship collision Analysis

   iv. Simplified approach

Furthermore, the present work also discussed the progressive collapse of box girder ultimate strength with no indentation, with and without residual stress after indentation using dynamic and static FEM analysis. The results of box girder without indentation shows very good agreement with experimental results by (Gordo and Soares, 2009) and simulation analysis. More important, the results of static and dynamic approaches produced almost identical behavior. The findings suggest that the quasi static approach is an acceptable solver method even when handling a highly non-linear post collapse scenario (Benson et al., 2013). This will often be true if the rupture didn't take place during the structure collapse.

10.1.1.   Rupture prediction

Rupture prediction is closely related to the prediction of an accidental load of ship collision and grounding. The rupture is often subject to a loss in resistance of ship deformation before significant damage occurs. Therefore,

the rational accuracy to predict rupture is very important before further investigations on ship collision and grounding analysis take place.

Most of the work in this section discussed some characteristic of material properties, material failure, mesh convergence study and some aspect need to be considered for running analysis in order to reduce cost. The material used isotropic approximation, FLD material failure, using five thickness integration Simpson rules, validated with experimental data and also compared to available FE analysis such as RTCL and BWH approaches.

As is normal FEA, the accuracy of the solution depends on the material properties, material failure, element type and mesh size. Given the limitations of the element formulations, finer meshes normally produced more realistic and accurate results. This is because a finer mesh usually gives a better representation of stress concentrations and also gives a better prediction of the strain in the element, hence providing a better prediction of the onset of failure.

The present FLD approach was compared to a series of experimental tests carried out by (Alsos and Amdahl, 2009) under quasi-static conditions, which were compared with FEA simulations (Alsos et al., 2009) using both RTCL and BWH damage evolution criteria. The current approach of FEA simulations only require simple damage input parameters. The attraction of the FLD approach to modeling material rupture is that it is very simple to construct the material failure diagram, which can account for both local necking and material rupture based on the simple tensile testing of materials. However the results produced are consistent and reliable when compared to the actual experimental results.

The validation of material failure to predict rupture using FLD approach extended to examination and was compared with experimental lateral crushing of buffer bow studied by (Yamada and Endo, 2005). The experimental and simulation models were used in research project by ASIS launched in 2001. The project is sponsored by the Japanese Ministry of Land

Infrastructure and Transport (MILT). The project is executed by the National Maritime Research Institute (NMRI) using several types of model. The results produced generate are as promising, consistent, reliable and close to experimental results.

Most important, the scaling law for FLD material failure was introduced where the relationship between onset failure (see Figure 40) at plane strain with mesh sizes for high tensile steel and mild steel marine grade.

Overall the current method demonstrates good convergence FEA results and generated nice correlation when compared to experimental results.

10.1.2.   Ship Grounding Analysis

Even though many studies have been conducted on this area, their results show considerable variability. Therefore, a significant amount of discussion and rationalization with regards to the accuracy and reliability of results is still required.

The ship grounding analysis were investigated by looking at available experimental data and calculations using FE analysis, and then applying the grounding methodology developed to study damage to the structure of ship bottoms. This is a very complex process and the calculations are dependent on mesh size, types of loading, crushing location, boundary conditions and the software that is being used in the analysis.

Overall, the results obtained from the FEA simulations produced very good agreement when compared to the experimental results of grounding damage by (Rodd, 1996) and the calculations by (Simonsen, 1997a). The grounding simulation also showed good correlation with previously published results (Samuelides et al., 2007; Zilakos et al., 2009) in terms of penetration force.

This demonstrates that FEA is an appropriate tool which can be used to investigate the local and global behaviour of a ship's structure during grounding, provided that good models for predicting material rupture are employed which should include appropriate scaling laws to take account of the mesh size sensitivity effect.

Numerical simulations are cheaper to run than experimental studies, but there is still a significant requirement to carry out good quality experimental studies. Results from such experiments are necessary for validating numerical simulation models in predicting structural responses during collision and grounding. The comparison of experiments and numerical modelling studies will help establish suitable numerical models for carrying out future assessments of collision and grounding scenarios.

10.1.3. Ship Collision Analysis

To investigate the behavior of a ship's accidental damage, rigorous non linear analysis were performed for structural failure due to ship collision in various scenarios;

These were achieved by investigating;

   i.   Deformable of ship bow collided with rigid wall

  ii.   Deformable bow collided with deformable double skin of side shell using displacement control.

 iii.   Deformable bow collided with deformable double skin of side shell using energy dissipation approach.

The deformable bow of ship collided with rigid wall is an extreme accidental load that may be subject to a ship colliding with the foundation of a rigid concrete pier, large static structure, etc. This study found that most of the kinetic energy was transferred to plastic deformation energy with damage of ship bow.

The study showed that the FEA results produced are comparable with available empirical formula and show good agreement with (Woisin, 1979) only (Terndrup Pedersen et al., 1993b) showed significant differences. The simulation damage also gave a very convincing picture of damage when compared with the actual incident as experienced by Gerd Maersk colliding with bridge pier on February 19, 1981 as illustrated in (Svensson, 2009).

Overall, the results obtained from the FEA simulations of ship collision to rigid wall is acceptable and the collision angel are playing an important role in the gradient of the ship bow damage. The rigidity ratio of ship bow determines the significant of damage and crushable distance of the ship bow by the rigid wall.

The deformable bow collided with deformable double skin of side shell using displacement control. The analyses were carried out using both normal and bulbous bow shapes due to control displacement ship-ship collision and only for bulbous bow for energy dissipation of ship-ship collision.

Both, rupture force and rupture energy for control displacement and energy dissipation of ship-ship collision showed angle collision generated higher values compare to lateral collision. This happened where large distance of penetration and larger contact area at side shell during penetration of the striking ship into the struck ship. This approaches is considerably acceptable even though the actual collision did not occurs at same condition where at a large collision angle, ship tend to slide each other.

The deformable bow collided with deformable double skin of side shell using energy dissipation approach. The analysis is close to actual incidents where striking ship is set free in all directions and struck ship is in stand still. Even though, the collision didn't take into account the effect of coupling with hydrodynamic forces but an assumption was made for added mass forces. This will enhance the reliability of the accidental load prediction compare to others scenarios. The disadvantages of this approach is very high cost in terms of memory used, calculation time, storage of the machine and capability

of CPU should be taken into consideration. Most of the calculations took between 25-70 days to finish, the time span depended on how powerful the machine and number of elements used.

The data also indicates that the rupture energy shows some close similarities, but many other influential factors, such as striking bow shape, position of collision, angle of collision, rigidity of structure play an important role. Therefore collision problems have to be treated separately on a case by case basis. There is no rigid formalized acceptance criterion for an ship-ship collision, especially ship structural designs. This is where FEA analysis take place to evaluate for each complex problem of structure integrity due to collision and grounding events.

In general, the result of the analysis carried out are interesting and give a good insight into the collision event. It is very difficult to validate with an actual collision event due to a lack of detailed information. The results of complex ship structure collision analysis are presented making a number of assumptions about the structure of the ships involved in the collision and the details of the collision.

10.1.4.   Simplified Approaches

The simplified approaches formulae is modified from Eurocode formulation and was established based on ship collision analysis, where three main assumption were made referring to the condition;

  i.   Ship collided to rigid wall where forward part of ship bow is deformed during collision.
  ii.   Rigid body ship collided to deformable struck ship
  iii. Both striking and struck ship are deformed

From later formulation discussed in chapter 7 in equation (7-16), there is no coefficient of bow shape. But in chapter 8, due to the striking ship penetrating

into the struck ship instead of crush as deformable bow collides onto a rigid wall, the coefficient of bow shape (C_{bs}) is introduced in equation (8-1). The coefficient of bow shape is to capture the contact area during penetration of rigid bow into struck ship. The coefficient is calculated based on the volume of penetrated bow into struck ship and divided with the volume of the rectangle that contains the penetrated bow. In this case, the C_{bs} is estimated within the range 0.35-0.65 and depending on the type of bow and shape.

For the first condition, C_{bs} = 1, due to full force and total deformation only occurs to the striking ship and rigidity ratio =R_b due to undeformed rigid wall. For the second condition, C_{bs} within ranges 0.35-0.65 and rigidity ratio is calculated accordingly. For the last condition, C_{bs} is estimated in ranges of 0.35-0.65 depending on how rigid the striking bow is, and rigidity ratio is a combination of both values, which are striking and struck ship.

The simplified formula is as below;

$$F_{max} = t_{avg}\, R\eta C_{bs} V\sqrt{KM} \begin{cases} \text{for rigid wall collision} & C_{bs} = 1 \text{ and } R = R_b \\ \text{for rigid body collision} & 0.35 \leq C_{bs} \leq 0.65 \text{ and } R = R_s \\ \text{for deformable collision} & 0.35 \leq C_{bs} \leq 0.65 \text{ and } R = R_b + R_s \end{cases}$$

Where; F_{max} = Maximum Crushing Force (N), M=Ship displacement (kg), η= Efficiency, C_{bs}= Coefficient of bow shape, t_{avg} =Average of plate thicknesses (mm), K=Equivalent stiffener (N/m), V=Ship collision speed (m/s), R= Rigidity ratio, R_b=Rigidity ratio for deformable bow (Striking ship), and R_s=Rigidity ratio for deformable side shell (Struck ship)

The simplified method introduced also gives good agreement with the empirical formula when you added rigidity value of forward part of ship structure and thickness of plate effect, except when compared with (Terndrup Pedersen et al., 1993b). The introduced method is also capable of capturing the lateral collision and angle collision effect when a coefficient of efficiency of absorbed energy in relation to friction and collision angle is included. The

introduced method also valuable for predicting absorbed energy and impact force in events of extreme collision.

10.2.   Recommendations For Future Work

The present work of this thesis is considerably sufficient to cover most of aspects of study of ship collision and grounding analysis. Even though there was less concentration on establishment simplified approach on prediction of ship grounding accidental load. This is due to costly analysis being required for both ship collision and grounding. The main focus of this research was the prediction of material rupture, investigation of ship collision and grounding analysis and the introduction of simplified approaches based on empirical studies by other researchers and combination of FEA results gained from analysis.

However, due to limited time to conduct further investigations, it is therefore recommended that some aspects are taken into consideration to enhance the practices such as;

Include more types of material instead of using only steel grade S235-EN10025 for mild steel and S355JR-EN10210 for high tensile steel to predict rupture. Generate material failure scaling law for other material types and make them readily available to be used with further validation.

The future analysis of ship collision and grounding should be extended to full scale of striking and struck ship as currently we only used two compartments of struck ship. However the current simulation managed to avoid stress flow concentrated on boundary conditions which are a good practice to adopt for all types of FEA simulations.

It is recommended that future studies include imperfection of the structure and hydrodynamic effects by any means. This will replicate to the nearer, the actual incident of ship collision and grounding. The limitation of degree of

freedom of struck ship in current analysis could be extended and replace by spring force and validated for better and reliable results.

Finally, the enhancement of the FE analysis and suggestions proposed are currently dictated by the capability of the machine and complicity of calculation formulation and FEA model setup. The moderation of study approaches is necessary to produce reliable accurate, and ideal results.

REFERENCES

AASTHO 1994. Guide specifications and commentary for vessel collision design of highway bridges.

ABAQUS ABAQUS Analysis User's Manual, Version 6.8, Dassault Systèmes Simulia Corporation.

ABAQUS, V. 6.9 online documentation. *SIMULIA Inc*.

ABRAMOWICZ, W. 1994. Crush resistance of T, Y and X sections. Joint MIT-Industry program on tanker safety. Report no. ADNR,(2005), Part.

ABUBAKAR, A., DOW, R., TIGKAS, I. G., SAMUELIDES, M. S. & SPYROU, K. J. Investigation of an actual collision incident between a tanker and a bulk carrier. 2010. 201-211.

ABUBAKAR, A. & DOW, R. S. Simulation of Ship Grounding Damage using the Finite Element Method. *International Journal of Solids and Structures*.

ALSOS, H. S. & AMDAHL, J. 2007. On the resistance of tanker bottom structures during stranding. *Marine Structures,* 20**,** 218-237.

ALSOS, H. S. & AMDAHL, J. 2009. On the resistance to penetration of stiffened plates, Part I - Experiments. *International Journal of Impact Engineering,* 36**,** 799-807.

ALSOS, H. S., AMDAHL, J. & HOPPERSTAD, O. S. 2009. On the resistance to penetration of stiffened plates, Part II: Numerical analysis. *International Journal of Impact Engineering,* 36**,** 875-887.

ALSOS, H. S., HOPPERSTAD, O. S., TÖRNQVIST, R. & AMDAHL, J. 2008. Analytical and numerical analysis of sheet metal instability using a stress based criterion. *International Journal of Solids and Structures,* 45**,** 2042-2055.

AMDAHL, J. 1983. Energy absorption in ship-platform impacts.

AMDAHL, J. & KAVLIE, D. 1992. Experimental and numerical simulation of double hull stranding. *DNV-MIT Workshop on Mechanics of Ship Collision and Grounding*.

AMDAHL, J. & KAVLIE, D. Design of tankers for grounding and collision. Proceedings of Int'Conference on Technologies for Marine Environment Preservation, Tokyo, Japan, 1995. 167-174.

AMDAHL, J., KAVLIE, D. & JOHANSEN, A. 1995. Tanker grounding resistance.

AMMERMAN, D. J. & DAIDOLA, J. C. 1996. A comparison of methods for evaluating structure during ship collisions. Sandia National Labs., Albuquerque, NM (United States).

ASHBY, M., GANDHI, C. & TAPLIN, D. 1979. Overview No. 3 Fracture-mechanism maps and their construction for fcc metals and alloys. *Acta Metallurgica,* 27**,** 699-729.

BATHE, K. J. 1996. Solution of equilibrium equations in dynamic analysis. *Finite Element Procedures***,** 768-837.

BENSON, S., ABUBAKAR, A. & DOW, R. S. 2013. A comparison of computational methods to predict the progressive collapse behaviour of a damaged box girder. *Engineering Structures,* 48**,** 266-280.

BLOY, M. 2002. Samuel Plimsoll's Merchant Shipping Act (1876): http://www.victorianweb.org/history/plimsoll.html.

BRAMFITT, B. L. 2012. The RMS titanic: 100 years later. *Iron and Steel Technology,* 9**,** 178-186.

BRESSAN, J. D. & WILLIAMS, J. A. 1983. The use of a shear instability criterion to predict local necking in sheet metal deformation. *International Journal of Mechanical Sciences,* 25**,** 155-168.

BROWN, A. J. 2002. Modeling structural damage in ship collisions. *Ship Structure Committee Report, SSC-422.*

CERUP-SIMONSEN, B., TÖRNQVIST, R. & LÜTZEN, M. 2009. A simplified grounding damage prediction method and its application in modern damage stability requirements. *Marine Structures,* 22**,** 62-83.

CHEN, D. 2000. *Simplified ship collision model.* Virginia Polytechnic Institute and State University.

DEVANNEY, J. 2010. The strange history of tank inerting. *Saatavissa http://www. c4tx. org/ctx/pub/igs. pdf. Viitattu,* 18**,** 2010.

DNV 1981. Det Norske Veritas: Impact loads from boats, DNV, Technical Note TNA 202.

DNV 1996. Det Norske Veritas: Rules for classification of ship part 5, chapter 9-oil storage and production vessels.

DNV 1999. Det Norske Veritas: Rules for classification of ship part 5, chapter 3 - Oil carriers.

DUDDECK, F. 2008a. Lecture notes for "Vehicular Crashworthiness". *Queen Mary University of London, 2008.*

DUDDECK, F. 2008b. Multidisciplinary optimization of car bodies. *Structural and Multidisciplinary Optimization,* 35**,** 375-389.

EGGE, E. & BÖCKENHAUER, M. 1991. Calculation of the collision resistance of ships and its assessment for classification purposes. *Marine Structures,* 4**,** 35-56.

EHLERS, S. 2009a. A procedure to optimize ship side structures for crashworthiness. *Proceedings of the Institution of Mechanical Engineers Part M: Journal of Engineering for the Maritime Environment,* 224**,** 1-11.

EHLERS, S. 2009b. Strain and stress relation until fracture for finite element simulations of a thin circular plate. *Thin-Walled Structs*.

EHLERS, S. & VARSTA, P. 2009. Strain and stress relation for non-linear finite element simulations. *Thin-Walled Structures,* 47**,** 1203-1217.

ENDO, H., YAMADA, Y., KITAMURA, O. & SUZUKI, K. 2001. Model test on the collapse strength of the buffer bow structures. *Proceedings, 2nd International Conference on Collision and Grounding of Ships (ICCGS 2001), Copenhagen, Denmark, July 1-3,* 145-153.

ENDO, H., YAMADA, Y., KITAMURA, O. & SUZUKI, K. 2002. Model test on the collapse strength of the buffer bow structures. *Marine Structures,* 15**,** 365-381.

ENV 1991. Eurocode 1: Basis of Design and Action on Structures, Part 1: Basis of Design. CEN/CS,.

FAN, W., YUAN, W. C. & FAN, Q. W. 2008. Calculation method of ship collision force on bridge using artificial neural network. *Journal of Zhejiang University: Science A,* 9**,** 614-623.

FAULKNER, D. 2004. Shipping safety: a matter of concern. *Proceedings of IMarEST-Part B-Journal of Marine Design and Operations,* 2004**,** 37-56.

GERMANISCHER-LLOYD 1997. Rules for classification and construction, I-Ship technology part 1-Seagoing ships, Chapter 1 Hull structures, section 33.

GORDO, J. & SOARES, C. G. 2009. Tests on ultimate strength of hull box girders made of high tensile steel. *Marine Structures,* 22**,** 770-790.

GUEDES SOARES, C., BITNER-GREGERSEN, E. & ANTÃO, P. 2001. Analysis of the frequency of ship accidents under severe North Atlantic weather conditions. *Proceedings of the design & operations in abnormal conditions II. Royal Institution of Naval Architects (RINA), London*.

HARRISON, O. An overview of the Exxon Valdez oil spill. International Oil Spill Conference, 1991. American Petroleum Institute, 313-319.

HILBER, H. M., HUGHES, T. J. R. & TAYLOR, R. L. 1977. Improved numerical dissipation for time integration algorithms in structural dynamics. *Earthquake Engineering & Structural Dynamics,* 5**,** 283-292.

HILL, R. 1952. On discontinuous plastic states, with special reference to localized necking in thin sheets. *Journal of the Mechanics and Physics of Solids,* 1**,** 19-30.

HILL, R. 1991. A theoretical perspective on in-plane forming of sheet metal. *Journal of the Mechanics and Physics of Solids,* 39**,** 295-307.

HIROTA, K., TAKEDA, S., TADA, M., NAKAGAWA, T. & HASHI, Y. 2007. World's first development and application of HTSS (high tensile strength steel) with yield stress of 47 kgf/mm2 to actual ship hull structure. *Mitsubishi Heavy Industries Technical Review,* 44**,** 28-33.

HOGSTRÖM, P. & RINGSBERG, J. W. 2013. Assessment of the crashworthiness of a selection of innovative ship structures. *Ocean Engineering,* 59**,** 58-72.

HOOPUTRA, H., GESE, H., DELL, H. & WERNER, H. 2004. A comprehensive failure model for crashworthiness simulation of aluminium extrusions. *International Journal of Crashworthiness,* 9**,** 449-464.

HSE 1990. Health and Safety Executive: Offshore installation - Guidance on design construction and certification, 4th Edition.

HUTCHINSON, J. W. & NEALE, K. W. 1978. Sheet necking-III. Strain-rate effects. *Mechanics of Sheet Metal Forming***,** 269-285.

IMO The Origins of the International Maritime Organization.

IMO Prevention of Pollution by Oil, http://www.imo.org/blast/mainframe.asp?topic_id=231.

IMO 1966. International Convention on Load Lines, 1966;

 http://www.imo.org/ourwork/safety/stabilityandsubdivision/pages/loadlines.aspx.

IMO 1972. Convention on the International Regulations for Preventing Collisions at Sea, 1972 (COLREGs).

IMO 1978. International Convention on Standards of Training, Certification and Watchkeeping for Seafarers.

IMO 2004. International Convention for the Control and Management of Ships' Ballast Water and

 Sediments adopted in 2004.

IMO 2011. *Construction Requirements for Oil Tankers*.

IMO 2012a. *Rescue at Sea - A guide to principles and practice as applied to migrants and refugees*.

IMO 2012b. International Shipping Facts and Figures – Information Resources on Trade, Safety, Security,

 Environment,

 http://www.imo.org/KnowledgeCentre/ShipsAndShippingFactsAndFigures/TheRoleandImportanc

 eofInternationalShipping/Documents/International%20Shipping%20-

 %20Facts%20and%20Figures.pdf.

IMO. 1998. Surviving Disaster: Life-saving at Sea. The Organization.

IOPCF 2005. The report of International Oil Pollution Compensation Fund.

J . AMDAHL , I . ZILAKOS , M . SAMUELIDES , TAN-HOI NGUYEN & TOULIOS, M. 2009. Simulation of the

 response of double bottoms under grounding actions using finite elements. *Proceedings of

 MARSTRUCT 2009, Second International Conference on Marine Structures-Analysis and Design of

 Marine Structures, Lisbon.*, 305–311.

JIE, M., CHENG, C. H., CHAN, L. C. & CHOW, C. L. 2009. Forming limit diagrams of strain-rate-dependent

 sheet metals. *International Journal of Mechanical Sciences,* 51, 269-275.

JOHNSON, B. 1999. English in the Global Maritime Distress and Safety System. *World Englishes,* 18, 145-157.

JOHNSON, G. R. & COOK, W. H. 1985. Fracture characteristics of three metals subjected to various strains,

 strain rates, temperatures and pressures. *Engineering fracture mechanics,* 21, 31-48.

KARLSSON, U. B. 2009. Improved collision safety of ships by an intrusion-tolerant inner side shell. *Marine

 Technology,* 46, 165-173.

KEELER, S. P. & BACKOFEN, W. A. 1963a. Plastic instability and fracture in sheets stretched over rigid

 punches. *ASM TRANS Q,* 56, 25-48.

KEELER, S. P. & BACKOFEN, W. A. 1963b. Plastic instability and fracture in sheets stretched over rigid

 punches. *Trans. ASM,* 56, 25-48.

KIERKEGAARD, H. 1993. Ship Collisions with Icebergs *PhD Thesis, DTU*.

KITAMURA, O. 1997. Comparative study on collision resistance of side structure. *Marine Technology,* 34,

 293-308.

KUROIWA, T. Numerical simulation of actual collision and grounding experiments. International Conference on Design and Methodologies for Collision and Grounding Protection of Ships, San Francisco, 1996.

LEHMANN, E. & PESCHMANN, J. 2002. Energy absorption by the steel structure of ships in the event of collisions. *Marine Structures,* 15**,** 429-441.

LENSELINK, H. & THUNG, K. G. 1993. Numerical simulations of the Dutch-Japanese full scale ship collision tests. *3rd International Symposium on Structural Crashworthiness and Failure*.

LIU, G.-R. 2009. *Mesh free methods: moving beyond the finite element method*, CRC.

LLOYDS 1999. LLOYDS Register of Shipping: Rules and regulations for the classification of floating offshore installation, part 4, Chapter 3.

LUOMA, E. 2009. Oil Spills and Safety Legislation. *Publications from the Centre for Maritime Studies, University of Turku, Finland*.

MCDERMOTT, J. F., KLINE, R. G., JONES, E., MANIAR, N. & CHIANG, W. 1974. Tanker structural analysis for minor collisions.

MCEWEN, N. 1999. The Telegraph Office Magazine Volume II, Issue 1,"'SOS,' 'CQD' and the History of Maritime Distress Calls"; http://www.telegraph-office.com/pages/arc2-2.html.

MINORSKY, V. U. 1959. An analysis of ship collisions with reference to protection of nuclear power plants. *Journal of Ship Research,* 3**,** 1-4.

MOORE, W. H. & ROBERTS, K. H. Safety management for the maritime industry: the international safety management code. Proceedings of the 1995 International Oil Spill Conference. Washington, DC American Petroleum Institute, 1995.

MSRC 2012. Marine spill response corporation. *Oil and Gas Journal,* 110**,** S1-S2+S4-S12.

NAAR, H., KUJALA, P., SIMONSEN, B. C. & LUDOLPHY, H. 2002. Comparison of the crashworthiness of various bottom and side structures. *Marine Structures,* 15**,** 443-460.

NORSOK 1999. NORSOK Standards: Design of steel structures-Actions and action effects, N-003, Revision 1.

NPD 1990. Norwegian Petroleum Directorate-Acts, Regulations and provisions for the petroleum activity.

OZGUC, O., DAS, P. K. & BARLTROP, N. D. P. 2005. A comparative study on the structural integrity of single and double side skin bulk carriers under collision damage. *Marine Structures (In Press)*.

PAIK, J., AMDAHL, J., BARLTROP, N., DONNER, E., GU, Y., ITO, H., LUDOLPHY, H., PERDERSEN, P. & UDO, W. G.(2003), Committee Report V. 3: Collision and Grounding. 15th International Ship and Offshore Structures Congress. 11-15.

PAIK, J. K. & PEDERSEN, P. T. 1996. Modelling of the internal mechanics in ship collisions. *Ocean Engineering,* 23**,** 107-142.

PAIK, J. K., THAYAMBALLI, A. K. & YANG, S. H. 1998. Residual strength assessment of ships after collision and grounding. *Marine Technology,* 35**,** 38-54.

PAINE, R. T., RUESINK, J. L., SUN, A., SOULANILLE, E. L., WONHAM, M. J., HARLEY, C. D., BRUMBAUGH, D. R. & SECORD, D. L. 1996. Trouble on oiled waters: lessons from the Exxon Valdez oil spill. *Annual Review of Ecology and Systematics***,** 197-235.

PETERSEN, M. J. & PEDERSEN, P. T. Collisions between ships and offshore platforms. Offshore Technology Conference, 1981. Offshore Technology Conference.

QUEK, S. & LIU, G. 2003. *Finite Element Method: A Practical Course: A Practical Course*, Butterworth-Heinemann.

REARDON, P. C. & SPRUNG, J. 1996. Validation of Minorsky's ship collision model and use of the model to estimate the probability of damaging a radioactive material transportation cask during a ship collision. *International Conference on Design and Methodologies for Collision and Grounding Protection of Ships, San Francisco*.

RITCHIE, W. 1995. Maritime oil spills—Environmental lessons and experiences with special reference to low-risk coastlines. *Journal of Coastal Conservation,* 1**,** 63-76.

RODD, J. L. 1996. Observations on conventional and advanced double hull grounding experiments. *Int. Conf. on Designs and Methodologies for Collision and Grounding Protection of Ships***,** 131-1313.

ROGERS, J. D. TITANIC LECTURE NOTES, University of Missouri-Rolla, http://web.mst.edu/~rogersda/american&military_history/titanic%20lecture%20notes.pdf.

ROMHANJI, E. & POPOVIĆ, M. 2006. Problems and prospect of Al-Mg alloys application in marine constructions. *Metalurgija,* 12**,** 297-307.

SAJDAK, J. A. 2004. *Analyses of Ship Collisions: Determination of Longitudinal Extent of Damage and Penetration.* Virginia Tech.

SAMUELIDES, M. S., VOUDOURIS, G., TOULIOS, M., AMDAHL, J. & DOW, R. 2007a. Simulation of the behavior of double bottoms subjected to grounding actions. *International Conference on Collision and Grounding of Ships; International Conference for Collision and Groundings ICCGS2007, September 2007*.

SAMUELIDES, M. S., VOUDOURIS, G., TOULIOS, M., AMDAHL, J. & DOW, R. 2007b. Simulation of the behaviour of double bottoms subjected to grounding actions. *Proceedings of the 4th International Conference on Collision and Grounding of Ships (ICCGS)*.

SAUL, R. & SVENSSON, H. 1982. On the theory of ship collision against bridge piers. *IABSE Proc.,* P-51**,** 29-38.

SCHWEIZERHOF, K., NILSSON, L. & HALLQUIST, J. 1992a. Crashworthiness analysis in the automotive industry. *International Journal of Computer Applications in Technology,* 5**,** 134-156.

SCHWEIZERHOF, K., NILSSON, L. & HALLQUIST, J. O. 1992b. Crashworthiness analysis in the automotive industry. *International Journal of Computer Applications in Technology,* 5**,** 134-156.

SEDLACEK, G. & MÜLLER, C. 2001. High strength steels in steel construction. *Niobium: Science & Technology, TMS: The Minerals, Metals & Materials Society, Orlando, Florida*.

SEMIATIN, S. 2006. *ASM Handbook, Volume 14B: Metalworking: Sheet Forming*, ASM International (OH).

SIMONSEN, B. C. 1997a. Mechanics of ship grounding. *Mechanics of Ship Grounding*.

SIMONSEN, B. C. 1997b. Ship grounding on rock—I. Theory. *marine Structures,* 10**,** 519-562.

SIMONSEN, B. C. 1997c. Ship grounding on rock—II. Validation and application. *Marine Structures,* 10**,** 563-584.

SIMONSEN, B. C. 1999. Theory and validation for the collision module.

SIMONSEN, B. C. & PEDERSEN, P. T. 1997. *Mechanics of ship grounding.* Technical University of DenmarkDanmarks Tekniske Universitet, Department of Mechanical EngineeringInstitut for Mekanisk Teknologi.

SMITH, A. & MEAD, L. The oil industry international oil spill response centres: What future? , 2005. 9944-9947.

SMITH, C. S. 1977. Influence of local compressive failure on ultimate longitudinal strength of a ship's hull. *Proceedings of the International Symposium on Practical Design Shipbuilding***,** 73-79.

STONE, R. M. 2012. *Stress-Strain Relationships, OPTI 222-Mechanical Design in Optical Engineering, Optical Science Center***,** 17-23.

SUZUKI, K., OHTSUBO, H. & SAJIT, C. 2000. Evaluation method of absorbed energy in collision of ships with anti-collision structure. *Proceedings of the SSC/SNAME/ASNE Symposium 2000 Ship Structures for the New Millennium*.

SUZUKI, K., OHTSUBO, H. & SAJIT, K. 1999. Evaluation of Absorbed Energy in Collision of Ships–The Effectiveness of Minorsky's Formula in Anti-Collision Structure. *Journal of the Society of Naval Architects of Japan,* 186**,** 311-317.

SUZUKI, S., MURAOKA, R., OBINATA, T., ENDO, S., HORITA, T. & OMATA, K. 2004. Steel products for shipbuilding. *JFE technical report,* 2**,** 41-46.

SVENSSON, H. 2009. Protection of bridge piers against ship collision. *Steel Construction,* 2**,** 21-32.

SYSTÈMES, D. 2010. Abaqus 6.10: Analysis User's Manual. *Providence, RI: Dassault Systèmes Simulia Corp*.

TERNDRUP PEDERSEN, P., VALSGAARD, S., OLSEN, D. & SPANGENBERG, S. 1993a. Ship impacts: bow collisions. *International Journal of Impact Engineering,* 13**,** 163-187.

TERNDRUP PEDERSEN, P., VALSGÅRD, S., OLSEN, D. & SPANGENBERG, S. 1993b. Ship impacts: Bow collisions. *International Journal of Impact Engineering,* 13**,** 163-187.

TERNDRUP PEDERSEN, P. & ZHANG, S. 1998. On Impact mechanics in ship collisions. *Marine Structures,* 11**,** 429-449.

THE REPUBLIC OF THE MARSHALL ISLANDS, D. O. T. M. A.-T. R. O. T. M. I. and the Report of Investigation in the Matter of the Collision between the Tankship BALTIC CARRIER (O.N. 1430) and the Bulk Carrier TERN in the Baltic Sea on 29 March 2001, PUBLISHED BY THE OFFICE OF THE MARITIME ADMINISTRATOR , 20 May 2002.

TOFFOLI, A., LEFÈVRE, J. M., BITNER-GREGERSEN, E. & MONBALIU, J. 2005. Towards the identification of warning criteria: Analysis of a ship accident database. *Applied Ocean Research,* 27**,** 281-291.

TOREM, A. 1991. The Exxon Valdez: A Lesson Learned?; http://environs.law.ucdavis.edu/issues/14/2/articles/torem.pdf.

TØRNQVIST, R. 2003. *Design of crashworthy ship structures.* Technical University of Denmark Kgns Lyngby,, Denmark.

UK-HSE 2009. Memorandum of Understanding between the Health and Safety Executive, the Maritime and Coastguard Agency and the Marine Accident Investigation Branch for health and safety enforcement activities etc at the water margin and offshore.

USCG 2011. Report of the International Ice Patrol in the North Atlantic.

VAN DER VEGTE, G. & MAKINO, Y. 2004. Numerical simulations of bolted connections: the implicit versus the explicit approach. *Connections in Steel Structures V-Amsterdam-June*.

WANG, G., JI, C., KUJALA, P., GAB LEE, S., MARINO, A., SIRKAR, J., SUZUKI, K., PEDERSEN, P., VREDEVELDT, A. & YURIY, V. Committee Report V. 1: Collision and Grounding. Proceedings of the 16th International Ship and Offshore Structures Congress, 2006.

WANG, G., JI, C., KUJALA, P., LEE, S., GAB, M. A., SIRKAR, J., SUZUKI, K., PEDERSEN, P., VREDEVELDT, A. & YURIY, V. Report of Committee V. 1 Collision and Grounding. Proceedings of the 16th international ship offshore structures congress. 1-61.

WANG, G. & OHTSUBO, H. Deformation of ship plate subjected to very large load. PROCEEDINGS OF THE INTERNATIONAL CONFERENCE ON OFFSHORE MECHANICS AND ARCTIC ENGINEERING, 1997. AMERICAN SOCIETY OF MECHANICAL ENGINEERS, 173-180.

WANG, G. & OHTSUBO, H. Impact load of a supply vessel. The Proceedings of the... International Offshore and Polar Engineering Conference, 1999. International Society of Offshore and Polar Engineers.

WANG, G., OHTSUBO, H. & ARITA, K. 1998. Large deflection of a rigid-plastic circular plate pressed by a sphere. *Journal of applied mechanics,* 65**,** 533-535.

WANG, G., SPENCER, J. & CHEN, Y. 2002. Assessment of a ship's performance in accidents. *Marine Structures,* 15**,** 313-333.

WIERZBICKI, T. 1991. Joint MIT-Industry Program on Tanker Safety. Massachusetts Institute of Technology, Cambridge, MA.

WILLMS, R. & DER DILLINGER HÜTTENWERKE, A. High strength steel for steel constructions. Nordic Steel Construction Conference–NSCC, 2009. 597-604.

WILSON, E. L. 2002. Three-dimensional static and dynamic analysis of structures A physical approach with emphasis on earthquake engineering. *Computers and Structures*.

WIŚNIEWSKI, K. & KOŁAKOWSKI, P. 2003. The effect of selected parameters on ship collision results by dynamic FE simulations. *Finite Elements in Analysis and Design,* 39**,** 985-1006.

WOISIN, G. 1979. Design against collision. *Proc. of Int. Symposium on Advances in Marine Technology,* 309-336.

WOISIN, G. 1979. Design Against Collision. *International Symposium on Advances in Marine*

Technology Trondheim, Norway.

WRIGGERS, P. 2008. *Nonlinear finite element methods,* Springer.

YAMADA, Y. & ENDO, H. 2005. Collapse mechanism of the buffer bow structure on axial crushing. *International Journal of Offshore and Polar Engineering,* 15.

YAMADA, Y., ENDO, H. & PEDERSEN, P. T. Numerical study on the effect of buffer bow structure in ship-ship collision. Proceedings of the International Offshore and Polar Engineering Conference, 2005 Seoul. 604-611.

YANG, P. & CALDWELL, J. 1988. Collision energy absorption of ships' bow structures. *International journal of impact engineering,* 7**,** 181-196.

YU, H. & JEONG, D. 2010. Application of a stress triaxiality dependent fracture criterion in the finite element analysis of unnotched Charpy specimens. *Theoretical and Applied Fracture Mechanics,* 54**,** 54-62.

ZHANG, A. & SUZUKI, K. 2005. Numerical simulation the bottom structure grounding test by LS-DYNA. *5th European LS-DYNA Users Conference*.

ZHANG, X. 2011. Development and Outlook of Advanced High Strength Steel in Ansteel. *Advanced Steels.* Springer.

ZHIQIANG, H., JØRGEN, A. & LIN, H. 2011. Verification of a simplified analytical method for predictions of ship groundings over large contact surfaces by numerical simulations. *Marine Structures,* 24**,** 436-458.

ZILAKOS, I., TOULIOS, M., SAMUELIDES, M., NGUYEN, T. H. & AMDAHL, J. Simulation of the response of double bottoms under grounding actions using finite elements. Proceedings of MARSTRUCT 2009, 2nd International Conference on Marine Structures-Analysis and Design of Marine Structures, 2009. 305-311.